



Extracellular Electron Transfer of *S. oneidensis* MR 1: Fundamentals and Applications

Zheng, Zhiyong

Publication date:
2019

Document Version
Publisher's PDF, also known as Version of record

[Link back to DTU Orbit](#)

Citation (APA):
Zheng, Z. (2019). *Extracellular Electron Transfer of S. oneidensis MR 1: Fundamentals and Applications*. Technical University of Denmark.

General rights

Copyright and moral rights for the publications made accessible in the public portal are retained by the authors and/or other copyright owners and it is a condition of accessing publications that users recognise and abide by the legal requirements associated with these rights.

- Users may download and print one copy of any publication from the public portal for the purpose of private study or research.
- You may not further distribute the material or use it for any profit-making activity or commercial gain
- You may freely distribute the URL identifying the publication in the public portal

If you believe that this document breaches copyright please contact us providing details, and we will remove access to the work immediately and investigate your claim.

Extracellular Electron Transfer of *S. oneidensis* MR-1: Fundamentals and Applications

Zhiyong Zheng

Ph.D. Thesis

Department of Chemistry

Technical University of Denmark

November 2019

Extracellular Electron Transfer of *S. oneidensis*

MR-1: Fundamentals and Applications

Ph.D. Thesis

November 15th, 2019

Zhiyong Zheng

zhizhe@kemi.dtu.dk

Main supervisor

Prof. Jingdong Zhang

Co-supervisors

Assoc. Prof. Hans E. Mølager Christensen

Prof. Jens Ulstrup

Department of Chemistry

Technical University of Denmark

Preface and Acknowledgments

The thesis is submitted for the degree of Doctor of Philosophy (Ph.D.) in the Department of Chemistry, Technical University of Denmark (DTU). The work was carried out at the NanoChemistry group, Department of Chemistry, DTU, under the supervision of Prof. Jingdong Zhang, Assoc. Prof. Hans E. Mølager Christensen, and Prof. Jens Ulstrup. The project was financially supported by the China Scholarship Council (No.201606130019), DTU Chemistry, Danish Agency for Science, Technology and Innovation (Establishment of Danish-USA-Chinese network on theranostic nanomaterials for cancer), and Otto Mønsted foundation.

First and foremost, I would like to express my sincere gratitude to my supervisor Prof. Jingdong Zhang and co-supervisors Assoc. Prof. Hans E. Mølager Christensen and Prof. Jens Ulstrup for all the continuous support, patient guidance, and consistent encouragement. I would like to thank Assoc. Prof. Hans E. Mølager Christensen for his supervision in the first two years. The supervisors' guidance helped me in all the time of my research, and their advice on both research and on my career is invaluable and helps me grow up as a scientist.

Besides my supervisors, I would like to thank Prof. Feng Zhao and Assoc. Prof. Yong Xiao from Institute of Urban Environment, Chinese Academy of Sciences, as well as Dr. Ranran Wu from Tianjin Institute of Industrial Biotechnology, Chinese Academy of Sciences. Their valuable comments, suggestions, and revisions for my manuscripts and the abstracts of conferences, as well as the support for my research, are more than appreciated.

My sincere thanks also go to Assoc. Prof. Lixin Ma, Prof. Ping Yu, Ms. Li Ean Lee, Dr. Ran Li, and Mr. Thomas L. Zhou from the University of Missouri for the great help during my external research stay at the University of Missouri (USA). I learned quantities of knowledge about medical research at the University of Missouri. The external research stay indeed broadened my research field and scientific horizon. The great efforts and support in my research and my applications from Assoc. Prof. Lixin Ma, Prof. Ping Yu is greatly appreciated.

I would like to thank all of the group members in the NanoChemistry group for their support and suggestion in my research and life in general. They created a friendly and active atmosphere, helped me to adjust my life and work in Denmark, gave me valuable suggestions in course selection, and provided considerable collaborations and useful comments for my research. All the joyful moments in life, hardworking in laboratories and offices are memorable.

I also would like to thank many people at DTU, especially at the Department of Chemistry. For example, laboratory technicians David Frej Nielsen, Betina Margrethe

Farrington Roesdahl, Johanne Marie Nielsen, Marie Koefoed, Ph.D. coordinator Mette Hansen, and receptionist Jette Berg Nestén for their great help to me during the last three years. The patience training and timely support of scanning electron microscope and transmission electron microscope from the DTU Nanolab is really appreciated.

A special thanks to my family: my parents and my brothers for their great and firm support, consistent understanding and assistance. Finally, I would like to thank all of my friends who have been supporting me to pursue my goals.

November 2019, Kgs. Lyngby

Zhiyong Zheng

Abstract

Bioelectrochemical systems (BESs) offer attractive applications in environmental remediation, energy harvesting, sensing, and organic and inorganic chemical synthesis. Fundamental studies of BESs not only hold promise for better performance of BES applications but are also crucial for the understanding of processes in nature. These processes, mainly extracellular electron transfer (EET), alter and affect the biogeochemical cycles.

In this Ph.D. project, *S. oneidensis* MR-1 (MR-1), an extensively investigated electrochemically active bacterium (EAB), was chosen as a tool to probe the EET process, which is essential in BESs. An opposite process of the outward EET, inward EET of MR-1 was here discovered. In inward EET, MR-1 catalyzes specific electrooxidation of redox molecules and exhibits asymmetric cyclic voltammograms. The electrocatalysis is highly selective and efficient. Among twelve redox molecules studied, only molecules with high midpoint potential and negative electrostatic charge(s) show electrocatalysis. $[\text{Fe}(\text{CN})_6]^{4-}$ as a representative of these molecules was chosen for deeper studies.

Further studies reveal that the formation of Pd nanoparticles (NPs) blocked the electrocatalysis systematically. On the other hand, the depletion of MtrC and OmcA, two crucial cytochromes c for outward EET, and inactivation of MR-1 did not deprive the ability of MR-1 of inward EET. A model coupling the oxidation of $[\text{Fe}(\text{CN})_6]^{4-}$ and $[\text{Fe}(\text{CN})_6]^{4-/3-}$ as catalytic mediator is hence proposed.

MR-1 was also applied in the biosynthesis of nanomaterials. Biosynthesis of nanomaterials can undertake a dual-task: bioremediation and biorecovery. To bridge the current gaps between laboratory investigations and practical applications, the effects of Cu(II) and different media were explored. The pre-culture in Cu(II) showed no critical inhibition of the bioremediation of Pd(II), and relatively high removal efficiency was achieved. However, pre-incubation of Cu(II) apparently altered the morphologies of the recovered nanomaterials. Inclusion of phosphate can increase the recovery efficiency of Pd(II), but only with limited enhancement.

Abstract-Danish

Bioelektrokemiske systemer (BESs) frembyder attraktive anvendelsesmuligheder inden for miljøgenopretning, energioptagelse, sensing, såvel som i organisk og uorganisk kemisk syntese. Basale studier af BESs har betydning ikke alene for mere effektive BES anvendelser, men er også afgørende for forståelsen af fundamentale naturprocesser. Centrale processer er her især ekstracellulær elektrontransport (EET), der på afgørende vis kontrollerer de biogeokemiske cyklusser.

I det foreliggende ph.d. projekt er den bredt undersøgte elektrokemisk aktive bakterie (EAB), *S. oneidensis* MR-1 (MR-1), valgt som teststamme for essentielle BES EET processer. Herunder er en modgående process i forhold til normalt udadgående EET, indadgående EET of MR-1, blevet opdaget. I indadgående EET, katalyserer MR-1 specifik electrooxidation af redoxmolekyler, afspejlet i asymmetriske cykliske voltammogrammer. Elektrokatalysen er yderst effektiv og selektiv. Blandt tolv undersøgte redoxmolekyler, udviste alene molekyler med højt midpunktpotential og negativ elektrostatisk ladning elektrokatalyse. Blandt disse udvalgte $[\text{Fe}(\text{CN})_6]^{4-}$ som repræsentant for videre studier.

Videre studier viste, at dannelse af Pd nanopartikler (NPer) systematisk blokerer elektrokatalysen. Til gengæld førte hverken udfasning af de to centrale cytochromer *c* i udadgående EET, MtrC and OmcA, eller inaktivering af MR-1, til blokering af MR-1's evne til at medvirke i indadgående EET. Dette har ført til opstilling af en model, der kobler oxidation af $[\text{Fe}(\text{CN})_6]^{4-}$ til $[\text{Fe}(\text{CN})_6]^{4-/3-}$ som katalytisk mediator.

MR-1 blev også anvendt i biosyntese af nanomaterialer. Biosyntese af nanomaterialer kan udøve en dobbeltrolle: bioremediering og biologisk genudvinding. For bedre at kunne sammenknytte laboratorieundersøgelser med praktiske anvendelser, blev effekten af tilsat Cu(II) og af forskellige medier undersøgt. Præ-kultivering i tilstedeværelse af Cu(II) viste ikke kritisk inhibering i Pd(II) bioremediering, og forholdsvis høj genoptagelseseffektivitet. Til gengæld førte præ-inkubation med Cu(II) tilsyneladende til ændret morfologi af de genoptagne nanomaterialer. Inklusion af fosfat kan øge effektiviteten af Pd(II) genoptagelse, om end kun i mindre grad.

Motivation and project objectives

Motivation

The microbial activities between bacteria and minerals play an essential role in biogeochemical cycling through metal mobilization, metal immobilization, and mineral transformations, *etc.* One of these activities is extracellular electron transfer (EET), in which microbes exchange electrons with external redox compounds, electrodes or even other microorganisms. As an electrochemically active bacteria, *Shewanella oneidensis* MR-1 (MR-1) transport electrons from the cells to extracellular electron acceptors, such as thiosulfate, fumarate, nitrate, Mn(IV) oxides, and Fe(III) (hydro)oxides.

In addition to outward EET, the inward electron transfer, *i.e.*, microbes take electrons from electron donors in the environment and transport the electrons into cells, has been reported. The outward electron transfer of MR-1 can be reversed in the OmcA–MtrCAB pathway, *i.e.*, OmcA–MtrCAB respiratory pathway can transport electrons from electrodes into the cells. However, whether MR-1 can directly take electrons from inorganic/organic compounds is unknown. There are more than 39 genes relevant to cytochromes *c* in the genome of MR-1, but only a small fraction of cytochromes *c* has been discovered in the outward EET.

The study of EET not only can help us to understand the role and function of MR-1 in the environment but also optimize relevant applications, for example, the biosynthesis of nanomaterials. The biosynthesis of nanomaterials by microbes can realize metal remediation and recovery and numerous studies have been reported. However, more efforts are needed to fill the gaps between the experiments in labs and practical application in reality.

Project objectives

The project aims at studying the EET process of MR-1 and exploring the biosynthesis of nanomaterial by MR-1. Different possible forms of EET of MR-1, including inward EET, will be investigated using a number of methods in electrochemistry, advanced microscopies, chemistry, and microbiology. The biosynthesis of various nanomaterials also will be attempted. The results will provide useful information about the electrocatalytic behavior of bacteria and broaden the synthesis of nanomaterials.

Synopsis

The main purpose this three-year Ph.D. project is to study the fundamentals of the extracellular electron transfer (EET) of *S. oneidensis* MR-1 (MR-1) and explore the bioremediation and biorecovery of metals such as Pd(II).

The Ph.D. thesis consists of six chapters, including the introduction of research field, methodologies, experimental details, results and discussion, and conclusion and perspectives.

Chapter 1 is a general introduction to bioelectrochemical system (BESs), including concepts, theory, and typical applications. The overview of BESs is presented first, including the function of microbial activity in the environment. The concept of EET is then introduced and detailed. An important application of BESs, *i.e.*, biosynthesis of nanomaterials by microbes, was reviewed. The section [1.3 Biosynthesis of nanomaterials by *S. oneidensis* MR-1](#) has been included in the book chapter *Bacterially generated nanocatalysts and their applications*. in *Novel catalyst materials for bioelectrochemical systems: Fundamentals and applications*. American Chemical Society, 2019 (in press).

Chapter 2 briefly introduces methodology and techniques applied in this Ph.D. project, including electrochemical techniques, microscopic techniques, and microscopic techniques. Fundamental principles of these applied methods and techniques are presented to premise the discussions of the following chapters.

Chapter 3 describes the electrooxidation of certain redox molecules catalyzed by MR-1. The role of extracellular polymeric substances, *in vitro* cytochrome *c*, and riboflavin are explored. The dependence of the electrocatalysis on the scan rate of CV and $[\text{Fe}(\text{CN})_6]^{4-}$ concentration. **Chapter 4** further studies the mechanism of electrocatalysis. The effect of the formation of Pd nanoparticles, MtrC and OmcA, and cellular respiration are investigated. A model of the electrocatalysis is proposed, which combines the catalytic electrooxidation of $[\text{Fe}(\text{CN})_6]^{4-}$ by MR-1, and a mediated EET process by $[\text{Fe}(\text{CN})_6]^{4-/3-}$. Notably, the mediated EET proceed both with and without the outer membrane bound cytochromes *c* MtrA and OmcA. **Chapter 3** and **Chapter 4** are included in the article *Electrons selective uptake of a metal-reducing bacterium *Shewanella oneidensis* MR-1 from ferrocyanide* published in *Biosens. Bioelectron.*, 2019.

Chapter 5 studies the effect of Cu(II) on the bio-remediation of Pd(II), and the influence of Cu(II) and media to the morphologies of the nanomaterials hybrids obtained are discussed. The presence of Cu(II) have only minor effect on the remove efficiency of Pd(II), and a remove efficiency as high as 89.8% is achieved, although Cu(II) is reported as a inhibitor to microbes. Pd nanoparticles (Pd NPs) are observed in the presence and absence of Cu(II), but the structure is clearly different. Relatively large Pd NPs accumulate in the

periplasm and the outer membrane of MR-1 in the absence of Cu(II), while smaller Pd NPs accumulate only in the periplasm in the presence of Cu(II) leading comparatively smooth cellular surface. A mechanism for the inhibition of Cu(II) to the Pd(II) reduction by MR-1 is suggested: Cu(II) does not inhibit the sorption of Pd(II) by MR-1, but the growth, accumulation, and transport of Pd NPs in the periplasm. The inclusion of phosphate in medium is not essential, because resulting increase of Pd(II) recovery is minor but with a potential precipitation of Cu(II), which is undesired for Cu(II) recovery.

Chapter 6 summarizes the conclusions of the entire Ph.D. thesis and give perspective of the fundament and application of BESs.

Acronyms and instructional notes

6C-HS: 6-Mercaptohexanoic acid

ABTS: Azino-di-[3-ethylbenzthiazoline sulfonate (6)]

AFM: Atomic force microscopy

BESs: Bioelectrochemical systems

bya: billion years ago

CE: Counter electrode

CSAFM: Current-sensing atomic force microscopy

CV: Cyclic voltammetry

DIET: Direct interspecies electron transfer

DMMB: 1,9-Dimethyl-methylene blue zinc chloride double salt

DP: Carbonized hybrids of *S. oneidensis* MR-1 cells and Pd NPs

DPA: Carbonized hybrids of *S. oneidensis* MR-1 cells and PdAu alloy

DPV: differential pulse voltammetry

DPARH: Carbonized hybrids of *S. oneidensis* MR-1 cells, PdAu alloy with reduced graphene oxide

DTU: Technical University of Denmark

EAB: Electrochemically active bacteria

EDS, EDX: Energy-dispersive X-ray spectroscopy

EELS: Electron energy loss spectroscopy

EET: Extracellular electron transfer

EFTEM: Energy-filtered transmission electron microscopy

EPS: Extracellular polymeric substances

E_{HW}: Half-wave potential

E_p: Peak potential

FcCA: Ferrocenecarboxylic acid

Fc(CA)₂: 1,1'-ferrocenedicarboxylic acid

FcMeOH: Hydroxymethylferrocene

FcNH₂: Aminoferrocene

FTIR: Fourier transform infrared spectroscopy

GCE: Glassy carbon electrode

GO: Graphene oxide

Gt: Gigaton

HEPES: Sodium 4-(2-hydroxyethyl)-1-piperazineethanesulphonic acid

HREM, HRTEM: High-resolution transmission electron microscopy

ICP-OES: Inductively coupled plasma optical emission spectroscopy

ICP-AES: Inductively coupled plasma atomic emission spectroscopy

IET: Interspecies electron transfer

LB: Luria broth

MEC: microbial electrolysis cells

MFC: Microbial fuel cell

MR-1: *Shewanella oneidensis* MR-1, also *S. oneidensis* MR-1

DIET: Direct interspecies electron transfer

MOPS: 3-(N-morpholino)propanesulfonic acid

Mt: megaton

NP: Nanoparticle

OCV: Open circuit voltage	STEM: Scanning transmission electron microscopy
ORR: oxygen reduction reaction	MR-1: <i>S. oneidensis</i> MR-1
PBS: Phosphate buffer solution	SPM: Scanning probe microscopy
PCB: Polychlorinated biphenyls	STC: Small tetraheme cytochrome
PV: Polyviologen	STEM: Scanning transmission electron microscopy
ppm: Parts per million	STM: Scanning tunneling microscopy
ppt: Parts per thousand	TEM: Transmission electron microscopy
RE: Reference electrode	TGA: Thermogravimetric analyses
RF: Riboflavin	t-PSA: Total prostate-specific antigen
RhB: Rhodamine B	UV-Vis: Ultraviolet–visible spectroscopy
SAED: Selected area electron diffraction	WE: Working electrode
SCE: Saturated calomel electrode	XPS: X-ray photoelectron spectroscopy
SEM: Scanning electron microscopy	XRD: X-ray diffraction
SHE: Standard hydrogen electrode	
SMC: Soil microbial carbon	
SOC: Soil organic carbon	

Instructional notes

Acronyms of terms ending in -microscopy, -chemistry, -voltammetry or -spectroscopy, refer to -microscope, -chemical, -voltammogram and –spectrum/spectra, as well. Abbreviations are used in plural form by adding “s”.

Contents

Preface and Acknowledgments	I
Abstract	III
Abstract-Danish.....	IV
Motivation and project objectives	V
Synopsis	VI
Acronyms and instructional notes	VIII
Chapter 1 Overview of bioelectrochemical systems	1
1.1 Bioelectrochemical systems.....	1
1.1.1 Microbes and the environment	1
1.1.2 Cellular respiration and current	4
1.1.3 Application of bioelectrochemical systems	7
1.2 Extracellular electron transfer (EET).....	13
1.2.1 Introduction	13
1.2.2 Short-range direct EET.....	17
1.2.3 Long-range direct EET.....	19
1.2.4 Mediated EET	19
1.3 Biosynthesis of nanomaterials by <i>S. oneidensis</i> MR-1	21
1.3.1 Introduction	21
1.3.2 Biosynthesis mechanism of nanocatalysts.....	23
1.3.3 Characterization of biogenic nanocatalysts	26
1.3.4 Classes of biogenic nanocatalysts	30
1.3.5 Applications of Biogenic Nanocatalysts.....	33
1.3.6 Outlook.....	40
1.4 Conclusions	41
Chapter 2 Methodology.....	42
2.1 Electrochemical techniques	42
2.1.1 Cyclic voltammetry	42
2.1.2 Differential pulse voltammetry.....	45
2.1.3 Chronoamperometry.....	46
2.2 Microscopic techniques	48
2.2.1 Scanning electron microscopy.....	48

2.2.2	Transmission electron microscopy	49
2.2.3	Atomic force microscopy	51
2.3	Spectroscopic techniques	52
2.3.1	Ultraviolet-visible spectroscopy.....	52
2.3.2	Energy-dispersive X-ray spectroscopy.....	53
2.3.3	Inductively coupled plasma optical emission spectroscopy	54
Chapter 3	Selective electrooxidation catalyzed by <i>S. oneidensis</i> MR-1	56
3.1	Introduction	56
3.2	Experimental Section	57
3.2.1	Chemicals.....	57
3.2.2	Culture and collection of <i>S. oneidensis</i> MR-1.....	58
3.2.3	Electrochemical measurements.....	58
3.2.4	Extraction of extracellular polymeric substances.....	59
3.2.5	Coating of cytochrome <i>c</i> on gold electrodes.....	59
3.2.6	Coating of riboflavin on GCE.....	59
3.2.7	AFM mapping of the cells.....	59
3.3	Results and discussion.....	59
3.3.1	Electrooxidation of $[\text{Fe}(\text{CN})_6]^{4-}$ catalyzed by MR-1 is highly selective and efficient	59
3.3.2	The key factors in MR-1 for $[\text{Fe}(\text{CN})_6]^{4-}$ electrocatalysis	68
3.3.3	The dependence of electrocatalysis on CV scan rate.....	70
3.3.4	The dependence of electrocatalysis on $[\text{Fe}(\text{CN})_6]^{4-}$ concentration	70
3.4	Conclusions	73
Chapter 4	Electrons uptake by <i>S. oneidensis</i> MR-1	74
4.1	Introduction	74
4.2	Experimental section	75
4.2.1	Chemicals.....	75
4.2.2	Culture and collection of <i>S. oneidensis</i> MR-1.....	76
4.2.3	Electrochemical measurements.....	76
4.2.4	Formation of Pd NPs on MR-1	76

4.2.5 Formation of Pd NPs on GCE	76
4.2.6 Preparation of inactive MR-1	76
4.2.7 Morphology characterization.....	77
4.2.8 Cell growth monitoring	77
4.3 Results and discussion	77
4.3.1 The formation of palladium NPs on MR-1 block the $[\text{Fe}(\text{CN})_6]^{4+}$ electrocatalytic oxidation.....	77
4.3.2 The effect of MtrC, OmcA, cellular respiration	82
4.3.3 The mediating effect of $[\text{Fe}(\text{CN})_6]^{4/3-}$ without extracellular electron donors is limited	85
4.3.4 The direct EET between MR-1 and the electrode is feeble	90
4.3.5 Electron uptake mechanism by MR-1	91
4.4 Conclusions	97
Chapter 5 Co-recycling of metals by <i>S. oneidensis</i> MR-1.....	98
5.1 Introduction	98
5.2 Experimental section	100
5.2.1 Chemicals	100
5.2.2 Removal of Pd and Cu by MR-1	100
5.2.3 Measurement of reduced Cu and Pd.....	100
5.2.4 Preparation of Cu, Pd, and CuPd NPs by MR-1.....	100
5.2.5 Characterizations of biosynthesized NPs	101
5.3 Results and discussion	101
5.3.1 Co-removal of Cu and Pd.....	101
5.3.2 Effect of Cu(II) and the medium on the biorecovery of Pd(II).....	104
5.4 Conclusions	125
Chapter 6 Conclusions and perspectives	126
Bibliography.....	129
Appendix.....	149

Chapter 1

Overview of bioelectrochemical systems

This chapter presents an introduction of bioelectrochemical systems, including principles and applications. Half part of this chapter has been accepted as a book chapter in “Novel Catalyst Materials for Bioelectrochemical Systems: Fundamentals and Applications” by the American Chemical Society co-authored by Y. Xiao, F. Zhao, J. Ulstrup, and J. Zhang.

1.1 Bioelectrochemical systems

1.1.1 Microbes and the environment

Microbes, or microorganisms, are microscopic organisms that are too small to be seen by naked eyes (1). Microbes include all single-celled organism, such as archaea, bacteria, and protists, and some multicellular organisms, such as some fungi and some algae. Viruses also belong to microbes (2). The size of microbe can range from 16 nm, a virus *Circoviridae* (3), to as large as 300 μm , *Thiomargarita namibiensis* (4). Microbes are often living in microbial communities, which are groups of microorganisms that share a common living space.

The soil community is crucial to the function of the earth (5). Life mainly consists of carbon and is keeping alive by taking energy from the reactions related to carbon. Six kingdoms are involved with the carbon cycle: plants, bacteria, archaea, protists, fungi, and animals, as shown in Figure 1.1. Plants fix carbon from the atmosphere through photosynthesis effect, and the other fives, *i.e.*, heterotrophic soil organisms, are responsible for the carbon turnover (5). Apparently, microbes, especially bacteria, are playing a key role in the process and involved every soil functions except mechanical shredding. The numerous species intake and release carbon and nutrients at every moment and regulate every aspect of our planet including the evolution of multicellular life forms. Plenty of key processes are proceeding exclusively by microbes, such as methanotrophy, methanogenesis, nitrification, and nitrogen fixation, *etc.* (5, 6). Therefore, it is expected the similar latitudinal trend between the soil organic carbon and the soil microbial carbon in the terrestrial ecosystems (5) (Figure 1.2).

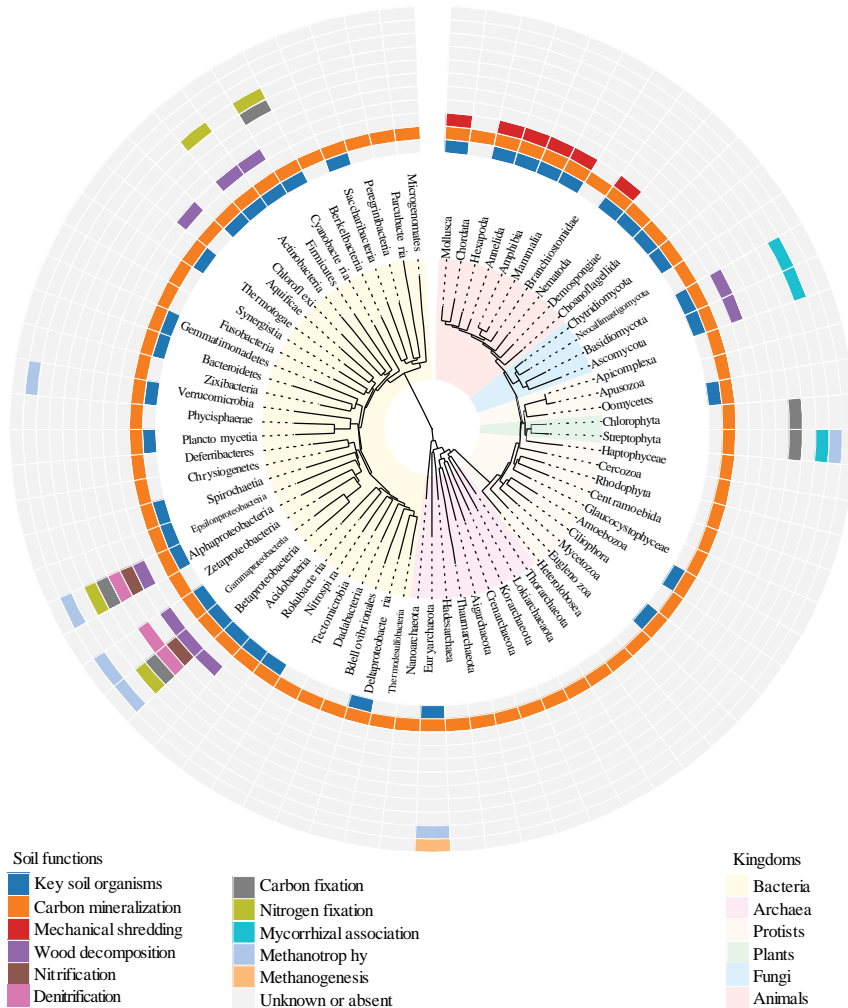


Figure 1.1. The function of soil biota. Soil organisms span all domains of life. The phylogenetic distribution of 12 common functions that are performed by soil organisms. Colored blocks indicate the performance of a particular function by at least one species in the respective taxonomic group. Colors on the branches of the phylogenetic tree indicate the different kingdoms. From (5). Reprinted with permission from AAAS. The *S. oneidensis* MR-1 studied in the Ph.D. thesis belongs to gammaproteobacterial.

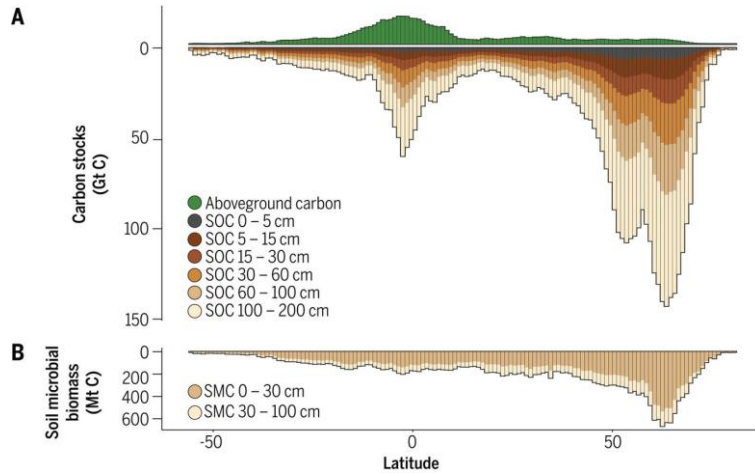


Figure 1.2. Latitudinal trends in organic matter across terrestrial ecosystems. (A) The latitudinal patterns of terrestrial carbon stocks, both aboveground plant biomass (green) and soil carbon stocks (brown). (B) The same latitudinal trend in soil microbial biomass, revealing similar patterns to that observed in soil carbon. Gt: gigaton, Mt: megaton, SOC: soil organic carbon, SMC: soil microbial carbon. From (5). Reprinted with permission from AAAS

Apart from the terrestrial biosphere, microbes also influence the hydrosphere. The essential source of dissolved organic matter, which is the overall majority in the pool of organic matter in aquatic habitats, is the leakage from photosynthetic algae (6). The turnover of organic matter (*i.e.*, degradation or mineralization) is mainly done by free-floating bacteria in the surface ocean (7).

As the first life forms on earth, microbes keep shaping this planet. In fact, about 80% of life's history on earth is occupied by microbes exclusively, as shown in Figure 1.3. Microbes presented on earth about 4 billion years ago even if there is no oxygen existing in the atmosphere (1). After that, microbes are laboring to conduct a series of biogeochemical process to advance the revolution of the earth. For example, *cyanobacteria* started the process of oxygenating at least 2.7 billion years ago (8). As a more efficient greenhouse gas than CO₂, the content of methane is regulated by methanogenesis and methane oxidation which is carried by different microbes, for example, phylum *Euryarchaeota* and *Methyloirabilis oxyfera* respectively (9, 10).

On the other hand, microbes respond to the changes in the environment. For example, when soil was polluted by Cr(VI), the microbial diversity, which represents one of the key indicators of microbial communities, decrease significantly compared to that of free of Cr(VI) pollution (11). The nitrogen cycle has been interrupted and nitrogen was accumulated caused by the agricultural practice by the human, as one of consequence, coastal anoxia is predicted to increase to restore the nitrogen cycle (12).

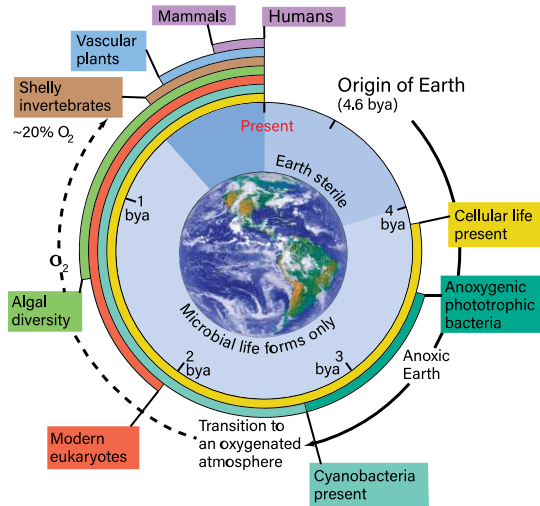


Figure 1.3. Life evolution on earth. In the beginning, no life form was on earth. Cellular life appeared by 3.8 billion years ago (bya). Cyanobacteria started to produce oxygen about 3 bya, and current oxygen levels in the atmosphere were reached 0.5 to 0.8 bya. reproduced from ref. (1). The image of Earth is produced by M. Jentoft-Nilsen, F. Hasler, D. Chesters (NASA/Goddard) and T. Nielsen (Univ. of Hawaii)/NASA Headquarters.

1.1.2 Cellular respiration and current

A proton-motive force is vital for microbes to grow and remain alive, and the generation of proton motive force involves the cellular respiration of microbes (13). Cellular respiration can be categorized into aerobic respiration and anaerobic respiration (1). Briefly, for aerobes, they obtain energy by intaking and oxidizing biological fuels (e.g., glucose, lactate, acetate) and simultaneously respiring and reducing oxygen; For anaerobes, the oxygen is replaced with other electron acceptors, such as NO_3^- , S^{2-} , Fe(III) compounds or Mn(IV) compounds; For facultative anaerobes, they behave as aerobes in the presence of oxygen and anaerobes in the absence of oxygen. Note that, in anaerobic respiration, some of the electron acceptors cannot be ingested by microbes due to big size, poor solubility, or the lack of transport pathway, etc.

In certain circumstances, for example, at the bottom of the ocean, oxygen is limited while Mn(IV) oxides and Fe(III) oxides are abundant, so facultative anaerobes and anaerobes have to use these external electron acceptors. To do so, the microbes have to transport intracellular electrons outside of the cells. Moreover, some microbes (e.g., chemoautotroph) can take electrons from external electron donors. The flow of electrons creates current between microbes and external redox partners.

Microbes gain energy through this electron exchange behavior, and the magnitude of energy is determined by the potential difference between the electron donor and acceptor. Theoretically, the energy gain ΔG (kJ mol^{-1}) can be described by the equation (14) (1.1):

$$\Delta G = -nFE_{emf} \quad (1.1)$$

Where n is the number of electrons transferred in the redox reaction; F is the Faraday's constant (96485 C mol^{-1}); E_{emf} is the potential difference between the electron donor and electron acceptor (V).

Different redox potentials (E_0') of aerobic and anaerobic respiration are listed in Figure 1.4. Microbes will try to maximum energy input by selecting the most electropositive redox couple within their abilities. Note that the $\text{O}_2/\text{H}_2\text{O}$ is the most electropositive redox couple ($+0.82 \text{ V}$ vs. standard hydrogen electrode, SHE), therefore, facultative anaerobes will prefer anaerobic respiration as long as oxygen is available (1). Because oxygen is an outstanding candidate for electron acceptor, the competition for oxygen is also fierce and it can be devoured quickly. Additionally, due to the poor solubility of oxygen in water, the concentration of oxygen decreases with depth in the ocean. For example, oxygen can be as low as $20 \mu\text{mol kg}^{-1}$ in 1000 m in the North Pacific Ocean, in contrast, it is about $200 \mu\text{mol kg}^{-1}$ in the upper part of the ocean (15).

The electron transfer triggers redox reactions in nature. As shown in Figure 1.1, half of the soil functions, *i.e.*, nitrification, denitrification, nitrogen fixation, methanogenesis, carbon fixation, methanotrophy, are actually redox reactions. Additionally, redox reaction also involved in the sulfur cycle, iron cycle, manganese cycle, which are all critical cycles in biogeochemistry. Therefore, microbes are playing a substantial role in these processes.

In summary, anoxic habitats are ubiquitous in nature, in which facultative anaerobes and anaerobes create current between the cells and external redox partners by facilitating the electron transfer from electron donors to electron acceptors. The electron donors and electron acceptors can be intracellular and extracellular respectively, or *vice versa*. Therefore, electrons can be transferred from or to the microbes. The electron transfer dominates biogeochemical cycling.

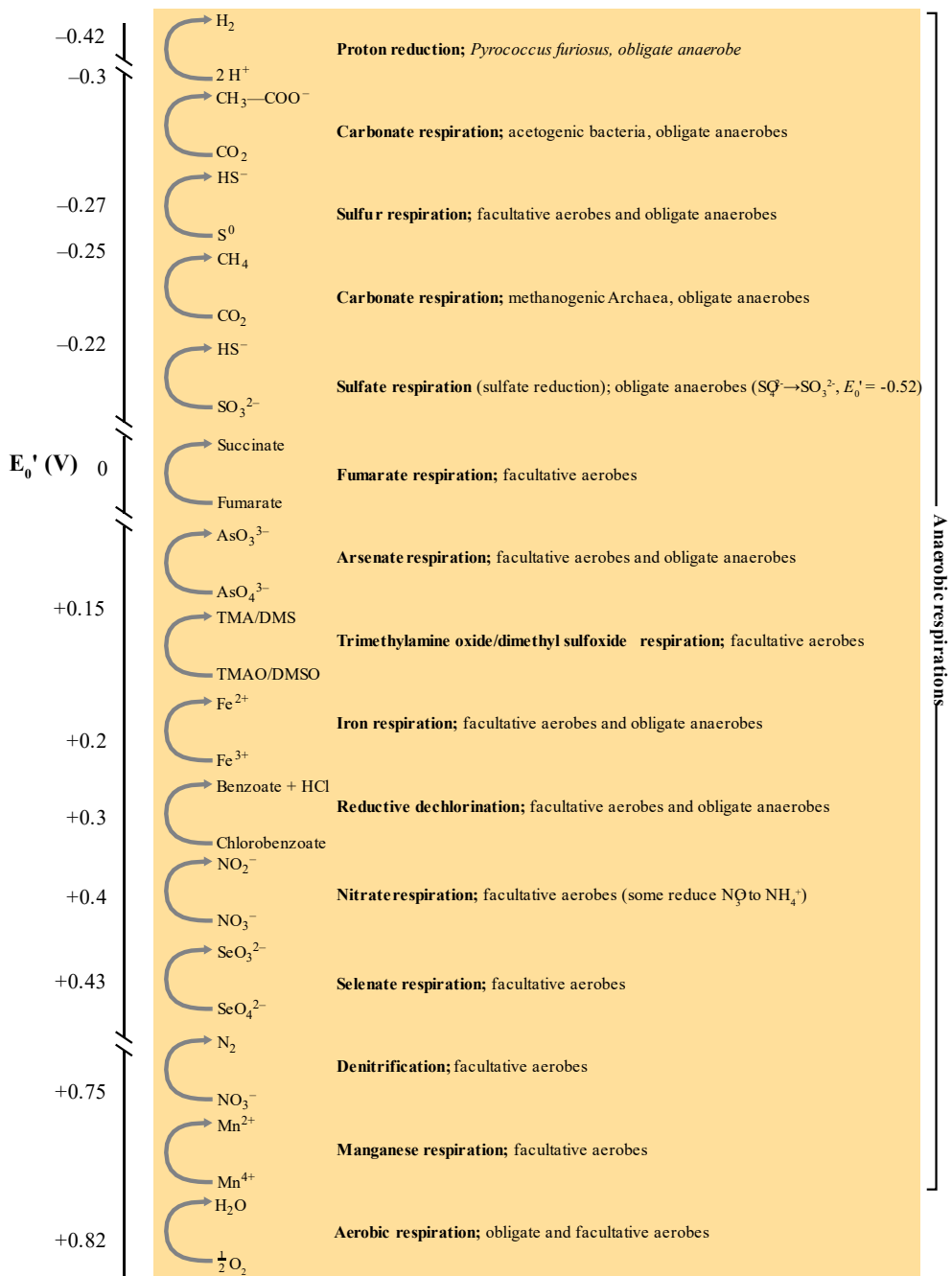


Figure 1.4. Aerobic and major forms of anaerobic respiration. The redox potentials (vs. SHE) are based on the reactions in neutral pH. From ref. (1) with permission. Reprinted by permission of Pearson Education, Inc., New York, New York.

1.1.3 Application of bioelectrochemical systems

Bioelectrochemical systems (BESs) are unique systems integrated energy harvesting or chemical production, waste removal using biocatalysts (16-19). Broadly, the biocatalysts can be microbes or enzymes (17), as shown in Figure 1.5. The thesis will focus on microbial BESs.

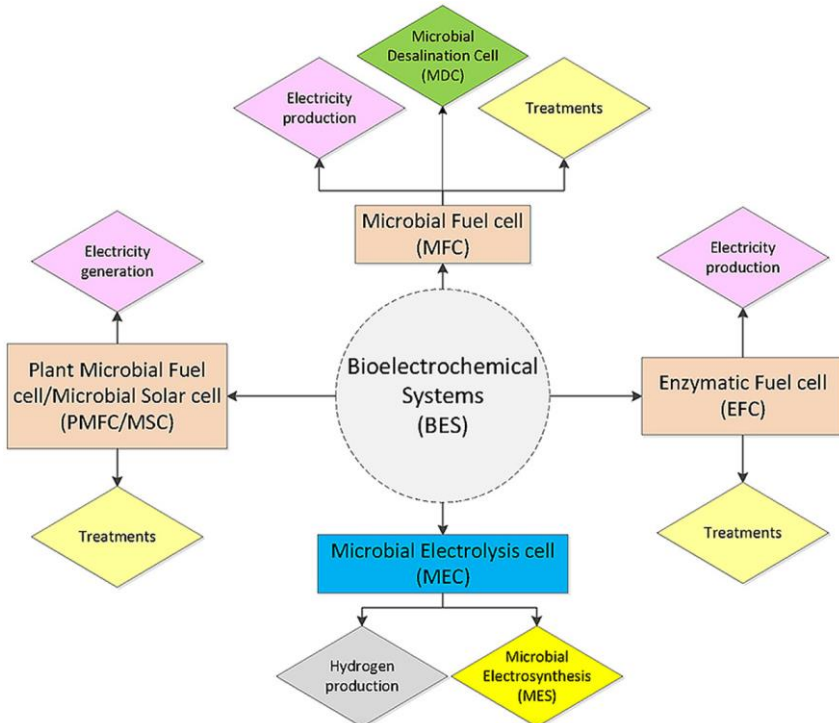


Figure 1.5. Representative of different bioelectrochemical systems (BESs). Reproduced from ref. (17) with permission.

A brief scheme of BESs is shown in Figure 1.6. Normally, BESs composed of two chambers separated with an exchange membrane: one chamber with an anode and one with a cathode. The anode is inhabited with heterotrophic bacteria film where oxidation reactions occur (20). Correspondingly, the electrons conducted by external circuit trigger reduction reaction at the cathode. The cathode can be biotic or abiotic, in which the former is clothed with autotrophic bacteria and the cathode is termed “bio-cathode” (21). The abiotic cathode is immersed in high-potential redox substances (22) (e.g., $K_4[Fe(CN)_6]$) or loaded with catalysts to oxygen reduction reaction (ORR) (e.g., Pt) and exposed in the air which is single-chamber BESs with air cathode (23). Additionally, the separating membrane is absent in some cases (24).

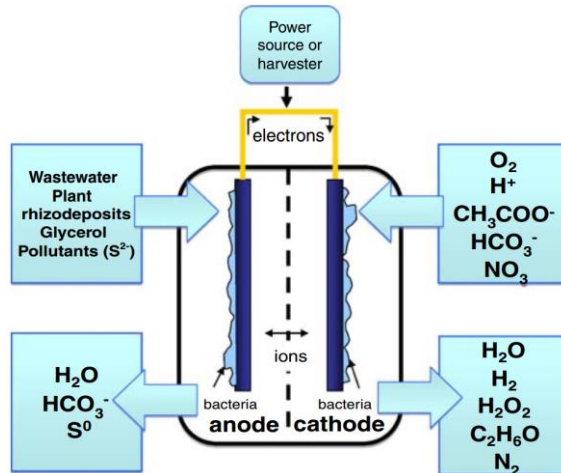


Figure 1.6. Typical inputs and outputs in BESs. The membrane between anode and cathode is not indispensable. Reproduced from ref. (19) with permission. C₂H₆O indicates ethanol.

The most two attractive advantages of BESs for application are the accelerated oxidation/reduction reactions and the generated current. An external power supply can be employed if the oxidation/reduction reactions are desired (Figure 1.6). Different applications of BESs emerged since the twentieth century (Figure 1.7).

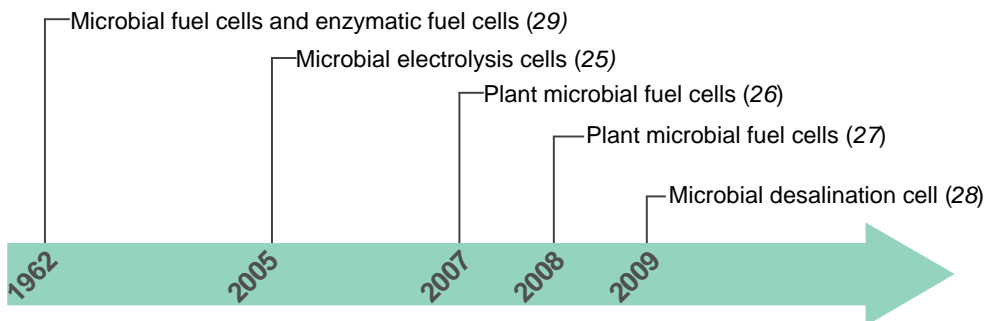


Figure 1.7. Timeline of revolution of BESs (25-29).

Microbial fuel cell (MFC) is a device using microbes as catalysts to harvest energy from the oxidation of organic and inorganic matters (29). MFC probably is the first application of BESs and the base of various other applications of BESs and provoked extensive attention to this versatile technique. The generation of current originates from the potential difference between the cathode and anode (Figure 1.8).

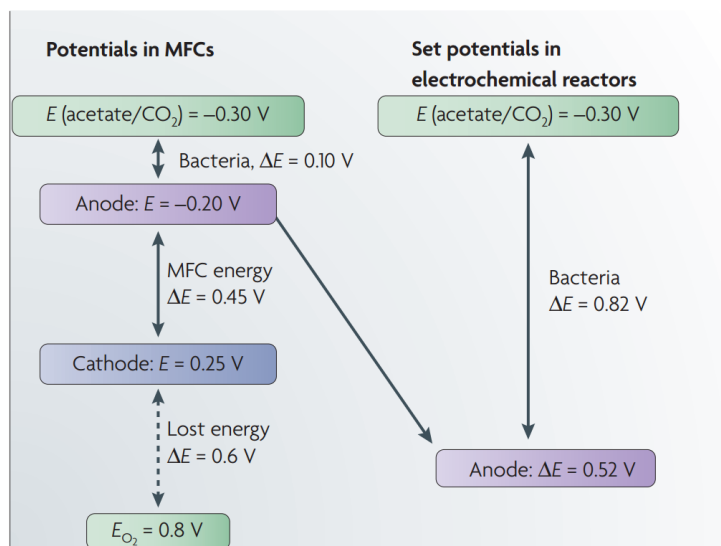


Figure 1.8. Potentials in MFCs. Reproduced from ref. (30) with permission.

The optimization of anode microbes, electrode material, and ORR catalysts in cathodes is important for good performance of MFCs. Microbes act as catalysts on anodes as mentioned before, and anode with mix cultures is much more efficient than that with pure cultures (17). *Shewanella* and *Geobacter* species are widely studied and the presence of *Geobacteraceae* is often linked with good performance of MFCs (31), but *Shewanella* is not. The possible reason for the absence of *Shewanella* in BESs with high power density probably related to the different metabolism and EET strategies compared to *Geobacter*. For example, the common substrate for *Shewanella* is lactate, while the normal carbon source is glucose, acetate, etc. Moreover, *Shewanella* needs redox mediator to guarantee efficient EET which may be limited in BESs. Anode electrodes provide residence to microbes and meanwhile act as current collectors. The following properties are desired for a suitable electrode material: (i) good biocompatibility, including hydrophilicity to facilitate the formation of biofilm; (ii) high electroconductivity; (iii) high specific area; (iv) good chemical and mechanical stability to guarantee long-term operation; (v) acceptable price (32). The common electrode materials include carbon materials, such as graphite rod (33), graphite fiber brush (34), carbon cloth (35), carbon paper (36), and carbon felt (37), carbon nanotubes (38), to metals, such as modified stainless steel (39) and gold film (40). Bio-cathode electrode materials are similar to anode materials, and the materials for air cathodes significantly vary with that for anode electrodes. For example, to prevent biofouling, antibiotic instead of biocompatibility electrode materials are more preferable for air cathode. Moreover, air cathode materials also should be impermeable to water to avoid the blocking of the contact between air and ORR catalysts. Most of ORR catalysts in air cathodes can be classified into three groups: Pt, metal oxides, and transition metal macrocycle-based catalysts (14). Pt is a benchmark material for ORR; however, the high

price limited its usage. Metal oxides, especially transition metal oxides show promising ORR activity. For example, PbO_2 shown better performance than Pt as an ORR catalyst in a salt-bridge based MFC (41) and $\beta\text{-MnO}_2$ can be an alternative ORR catalyst for the scaling up of MFC (42). Transition metal macrocycle, such as cobalt tetramethoxyphenylporphyrin (CoTMPP) (43, 44), iron phthalocyanine (44), and manganese(II) phthalocyanine (45) are all good ORR catalysts and much cheaper than Pt. On the other hand, although the aforementioned non-Pt catalysts show good ORR activity and, in some cases, even outperformed Pt, their long-term stability need to be verified.

Different configurations of MFCs have been reported as presented in Figure 1.9. The most common design is “H” type MFCs (Figure 1.9A-C and F), in which the anodic chamber and the cathodic chamber is separated with a cation exchange membrane and anode and cathode are immersed in electrolytes. The membrane is to facilitate cation exchange to keep electroneutrality and can be replaced with a salt bridge as shown in Figure 1.9A, which will low the cost but lead to higher resistance. The operation of MFC can be batched (Figure 1.9B) or continuously flowed (Figure 1.9C). If oxygen was chosen as the electron acceptor for the cathode, the “H” type MFC may not be the best option because, in this case, the air has to be aerated into the catholyte. The feasibility will be compromised by the poor solubility of oxygen in water and the required power to aeration. The better design is to expose one side of the cathode to air and the other side to the electrolyte, as shown in Figure 1.9E. This design can improve the performance of the cathode, but it also faces the challenge to prevent leakage of water in long-term operation.

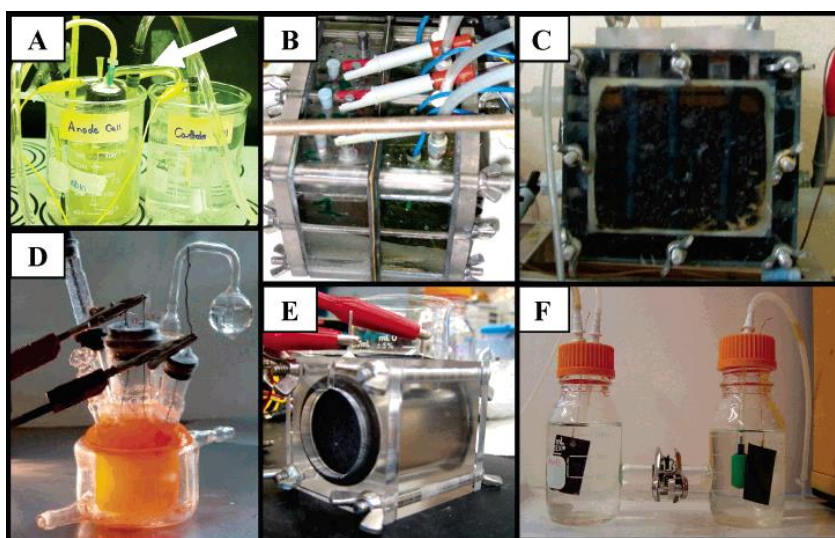


Figure 1.9. Different forms of MFCs: (A) easily constructed MFC with a salt bridge (indicated by an arrow) (46); (B) four batch-type MFCs with separated chambers (47); (C) similar with B except with a continuous flow-through anode and close anode–cathode placement (48); (D) photoheterotrophic

type MFC (49); (E) single-chamber, air-cathode MFC (50); (F) two-chamber H-type system including anode and cathode chambers with gas sparging (36). Reproduced from ref. (51) with permission.

To advance the studies of MFCs in labs into practical application, it is essential to scale up MFCs. The volume of MFCs in labs often are in milliliter scale, and the successful lab demonstrations are not transferable to larger and pilot scale, for example, liter scale or larger (52). The gap between lab-scale MFCs to pilot scale MFCs are the main differences in the following two aspects.

The hydraulic and electrical design of pilot MFCs system is notably different to that of lab-scale MFCs. One method to MFCs scaling up is adopting MFC stacks, as presented in Figure 1.10. MFC stacks can flexibly increase the working volume of the system. For example, the unit of MFC stacks system is about 14 L and the overall working volume is 1500 L. The anolyte is organic wastewater with chemical oxygen demand of 780 mg L⁻¹ and the catholyte is inorganic wastewater with total inorganic carbon of 100 mg L⁻¹. The chemical oxygen demand is removed by more than 70% and the energy harvest is more than 5 W m⁻³. However, MFC stack is not as efficient and stable than independent MFCs (53), and the overall performance is normally limited by the unit with the worst performance (54). One solution is to design controllers for every unit both in electricity and hydraulics, and operating status (*e.g.*, voltage) of each unit should be monitored. In this way, the unit with the poorest performance can be isolated or removed from the system to stabilize the system. Moreover, the combination of series and parallel connection in electricity and hydraulics also need to be considered before the operation or modified during operation. Problems such as voltage reversal and contact voltage losses have been reported in air-cathode MFC stack (55).

The cost should be considered in pilot MFCs. The main capital cost of pilot MFCs consists of electrode material, exchange membrane, and lift and circulating pumps, and the ORR catalysts in the air cathode, or aerator for biocathodes. To low the cost, expensive materials in lab-scale MFCs (*e.g.*, Nafion exchange membranes and Pt catalysts) may not be preferable. For liter-scale MFCs, the mechanical strength of the shell of chambers and membrane is much important due to potential high water pressure. Alternative ORR catalysts, instead of Pt catalysts, is preferable (45), and biocathode can be attractive if denitrification treatment is required (56, 57). The widely used K₃[Fe(CN)₆] as an electron acceptor in the cathode of lab-scale MFCs is not practical since it is expensive and harmful to the environment. The running cost of MFC stacks mainly is electric power for circulation and aeration. Varied from lab-scale MFCs, the operations of MFC stacks (*e.g.*, replacing anolyte and catholyte) should be automated as much as possible. Note that the prior goal of MFC stacks is the treatment of sewage, instead of the generation of current.

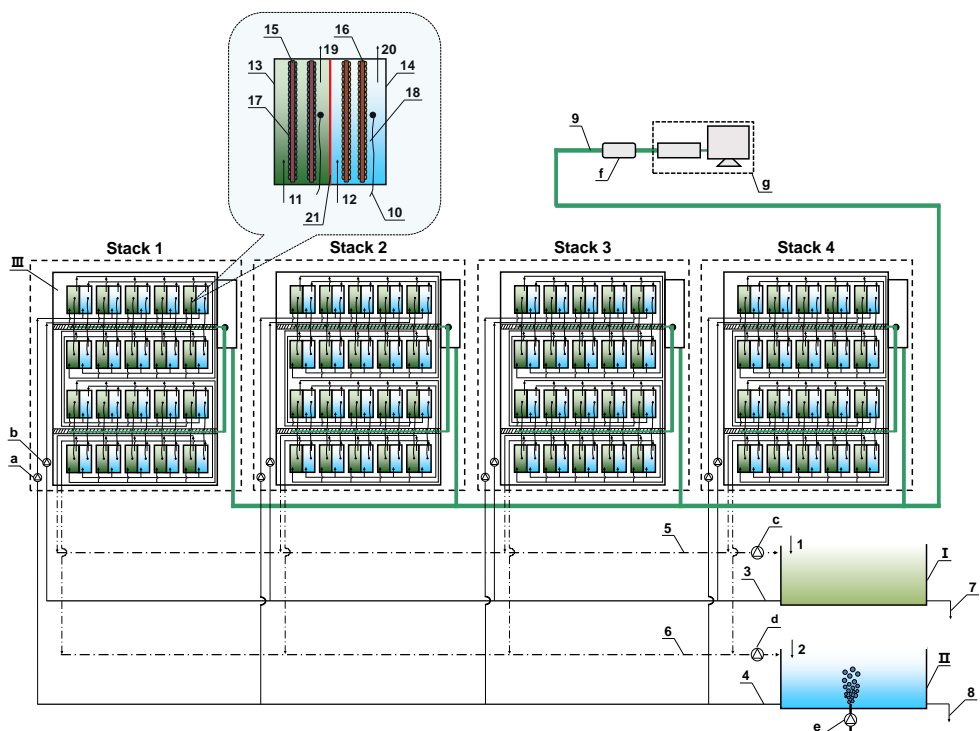


Figure 1.10. A pilot biocathode MFCs system with a the working volume of 1500 L. (I), anodic tank; (II), cathodic tank; (III), MFC stack; (1), inlet of anodic tank; (2), inlet of cathodic tank; (3), anolyte inflow; (4), catholyte inflow; (5), anolyte outflow; (6), catholyte outflow; (7), discharge of anodic tank; (8), discharge of cathodic tank; (9), electricity cable; (10), electricity wire for MFC; (11), inflow of anodic chamber; (12), inflow of cathodic chamber; (13), anodic chamber; (14), cathodic chamber; (15), anode; (16), cathode; (17), aerobes; (18), anaerobes; (19), outflow of anodic chamber; (20), outflow of cathodic chamber; (21), exchange membrane; (a), circulating pump of anolyte; (b), circulating pump of catholyte; (c), lift pump of anolyte; (d), lift pump of catholyte; (e), aerator; (f), electric loading; (g), data acquisition system. Adapted from ref. (58).

Another important application is microbial electrolysis cells (MECs) which can produce high-yield hydrogen from microbial oxidation of organic matters with the aid of external power supply (59, 60). Different to MFCs, the reduction in the cathode of MECs is the main goal and thus external power is applied to overcome thermodynamic limitations. Compared to direct electrolysis, MEC is more efficiently and mild (59). Some energetically unfavorable reactions, which are unlikely happen in MFCs, are achieved, for example, the production of methane (61, 62), ethanol (63), formic acid (64, 65), and acetate (66), etc. These BESs producing chemical substance other than hydrogen are also termed “microbial electrosynthesis” (17). More applications of BESs have been reported. For example, microbial desalination cells can additionally perform *in situ* desalination (28, 67), microbial solar cells can harvest solar energy with the help of photoautotrophic

microbes and higher plants (68), and sediment microbial fuel cell can ameliorate acidic soil (69). Additionally, various biosensors based on BESs are running to monitor acetate (70), CO (71), ammonia (72, 73), volatile fatty acids (74, 75), dissolved oxygen (76), etc.

1.2 Extracellular electron transfer (EET)

1.2.1 Introduction

The fundamental of BESs is the process of extracellular electron transfer (EET), in which EAB exchange electrons with external redox partners, including redox molecules/minerals, electrochemical electrodes, and other EAB (77, 78). The EET between EAB and redox molecules/minerals is akin to that between EAB and electrochemical electrodes except that some redox molecules are soluble. The EET between different species is drawing much attention recently. Note that the EET can occur between the same species and different species, and the latter is also termed “interspecies electron transfer” (IET). EET can also be categorized into outward EET and inward EET (Figure 1.11). Outward EET is the process in which EAB transfer electrons from the cells to extracellular redox partners (*e.g.*, Figure 1.11A), and inward EET proceed in the opposite direction (*e.g.*, Figure 1.11B). Outward EET often take place at the anode in BESs and inward EET at the cathode. The major achievements of outward EET and inward EET are summarized in Figure 1.12. Outward EET will be shortened as EET unless stated otherwise.

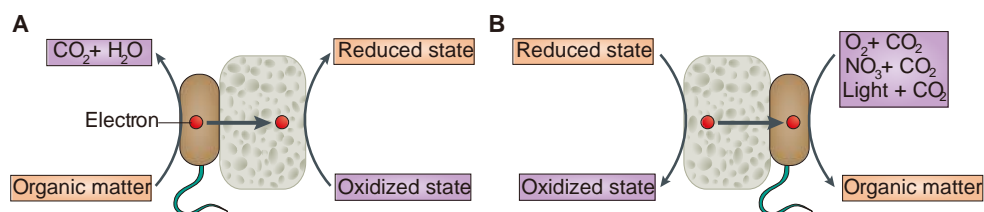


Figure 1.11. Electrical interaction between microbes and minerals. (A) In outward EET, microbes use minerals that contain metal ions as terminal electron acceptors for respiration; (B) In inward EET, microbes use minerals that contain metal ions as electron and/or energy sources for growth. Similar EET can happen when the minerals are replaced with other redox partners, such as redox molecules and other EAB. Reproduced from ref. (79) with permission.

Three pathways of outward EET have been reported (Figure 1.13). The first pathway is short-range direct EET, in which EAB exchange electrons with external redox partners *via* redox proteins in the outer cell membrane, such as cytochromes *c* OmcA and MtrC. The second pathway is long-range direct EET. EAB develop conductive appendices (also termed as “pili”, or “nanowires”) to reach redox partners when nutrients are limited. The last pathway is mediated EET, in which EAB secrete redox mediators (*e.g.*, flavins,

pyocyanin) to shuttle EET (77). Note that, in all these three pathways, the transferred electrons are subjected to “hopping” in extracellular polymeric substances (EPS) clothing the bacteria (80).

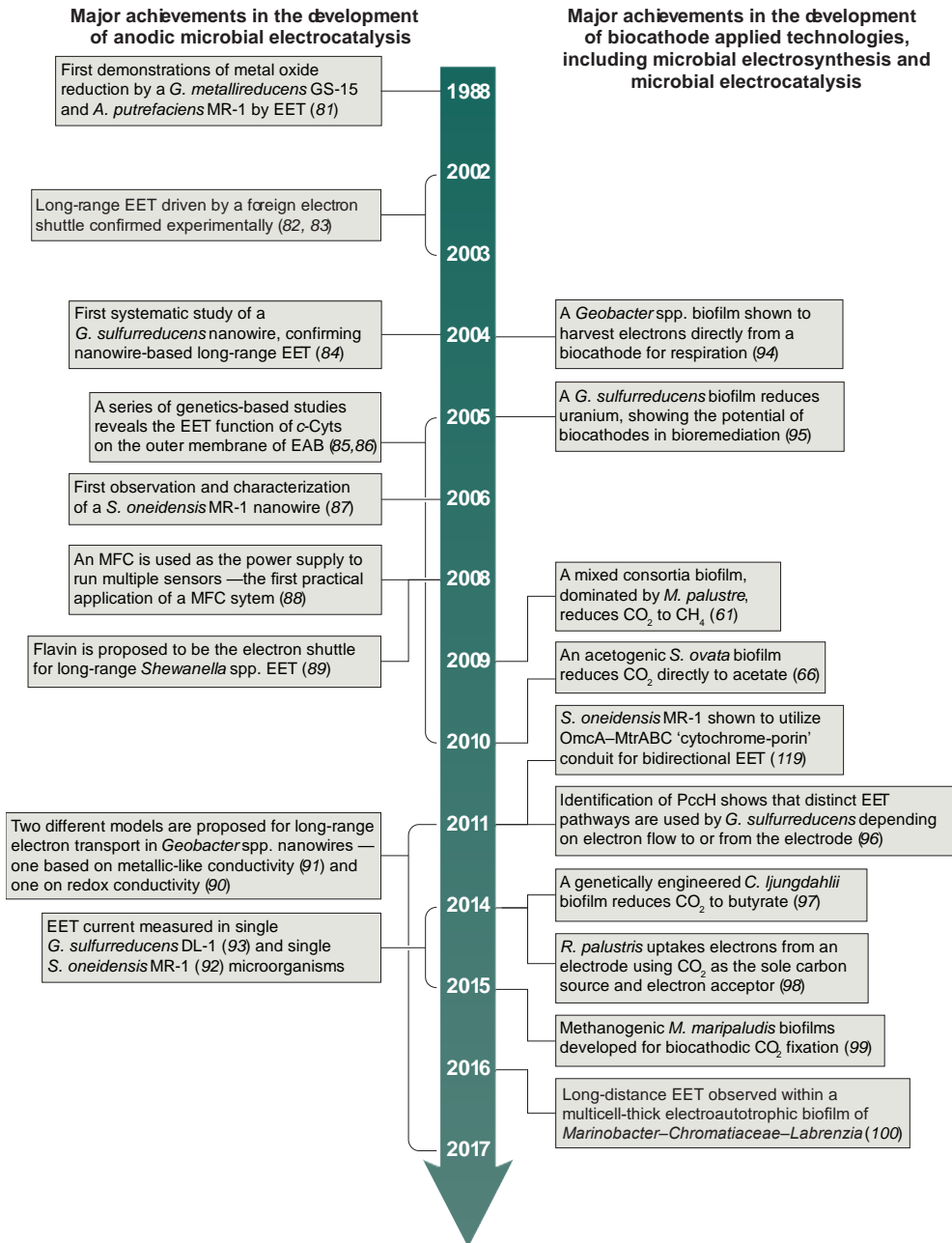


Figure 1.12. Timeline showing recent major achievements in anodic and cathodic microbial

electrosynthesis and electrocatalysis research. A. putrefaciens, Alteromonas putrefaciens; C. ljungdahii, Clostridium ljungdahlii; c-Cyt, c-type cytochrome; EAB, electrochemically active bacteria; EET, extracellular electron transfer; G. metallireducens, Geobacter metallireducens; G. sulfurreducens, Geobacter sulfurreducens; MFC, microbial fuel cell; M. maripaludis, Methanococcus maripaludis; M. palustre, Methanobacterium palustre; Mtr, metal reduction; OmcB, outer-membrane c-type cytochrome B; R. palustris, Rhodospseudomonas palustris; S. oneidensis, Shewanella oneidensis; S. ovata, Sporomusa ovata. (81-93) (61, 66, 80, 87, 94-100). Adapted from ref. (101) with permission.

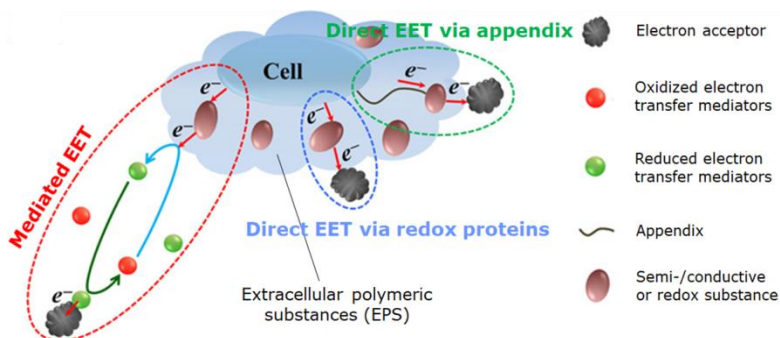


Figure 1.13. Three pathways of outward EET. Adapted from ref. (80).

Interspecies electron transfer (IET) can happen between bacteria (102-105), and bacteria and archaea (105). IET can be completed through diffusive electron carriers (e.g., H_2 and formate) and is called “mediated interspecies electron transfer” (MIET) (102). IET can also be completed through conductive materials (e.g., pill/nanowires and outer membrane cytochromes *c*) and is called “direct interspecies electron transfer” (DIET) (106). DIET is believed to be more efficient than MIET because the former needs fewer steps and conductive materials are more effective than electron carriers in transferring electrons (107, 108).

Plenty of microbes contribute the current generation in BESs, however, only part of them have been illuminated the ability to process EET. For example, *Geobacter sulfurreducens* (93), *Shewanella oneidensis* (80), *Pseudomonas aeruginosa* (47), *Bacillus subtilis* (109), and so on. Among these microbes, *Geobacter sulfurreducens* and *Shewanella oneidensis* are model EAB which are widely studied to explore the mechanism of EET, and *Shewanella oneidensis* is cable of use all the three pathways aforementioned, while the mediated EET is absent in *Geobacter sulfurreducens* (110-113).

S. oneidensis MR-1 is a facultatively aerobic Gram-negative bacterium (114), 2~ 3 μm in length and about 0.5 μm in diameter (Figure 1.14). *Shewanella* was first classified in 1931 as belonging to the *Achromobacter* genus (115). Several reclassifications have followed until 1985 when the new name *Shewanella* was assigned to the genus to honor Dr. James M. Shewan’s prolific contribution in fishery microbiology (116). *Shewanella oneidensis*

MR-1 was first discovered in Oneida Lake, New York, 1988 in relation to Mn^{4+} reduction and named as *Alteromonas putrefaciens* MR-1 (81). This bacterium was re-named as *Shewanella putrefaciens* MR-1 before finally named as *Shewanella oneidensis* MR-1 after the lake where it was discovered (117). The term “MR” is the abbreviation for “manganese reducer”.

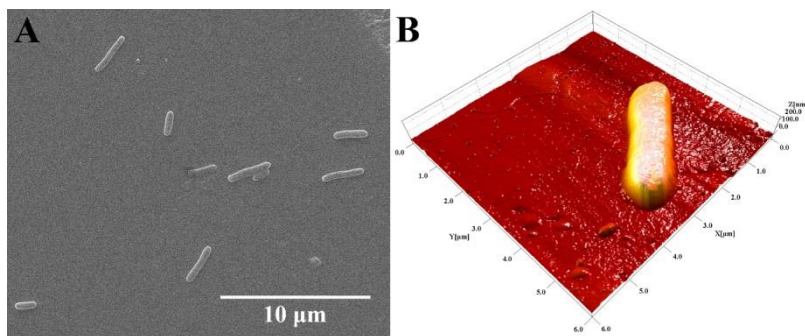


Figure 1.14. Morphology of *S. oneidensis* MR-1. (A) Scanning electron microscopy and (B) atomic force microscopy images of *S. oneidensis* MR-1.

The genome of *S. oneidensis* MR-1 is composed of 4,969,803 base pairs (114), including 76 base pairs involving EET process according to information from the National Center for Biotechnology Information (NCBI) database (Figure 1.15). Products of the 76 are cytochromes, hydrogenases, reductases, flavodoxins, etc. It has been reported that there are 39 cytochrome *c* in *S. oneidensis* MR-1 including 8 decaheme-cytochromes *c* (114). The vital genes in OmcA–MtrCAB pathway are summarized in Table 1.1. Note that among the 39 cytochromes *c*, only 6 of them (MtrA, MtrC, OmcA, CymA, small tetraheme cytochrome, and FccA) have been well documented in the EET process and fewer have been fully investigated in the synthesis of nanomaterials.

Table 1.1. Important genes in OmcA-MtrCAB pathway

Locus tag	No. of haems	Location in the cell	Reference for <i>S. oneidensis</i> MR-1
SO_1776	- ^a	Outer membrane	MtrB
SO_1777	10	Periplasm	MtrA
SO_1778	10	Outer membrane	MtrC
SO_1779	10	Outer membrane	OmcA
SO_4591	4	Periplasm	CymA

a. MtrB is not a cytochrome *c* and contains no haem.

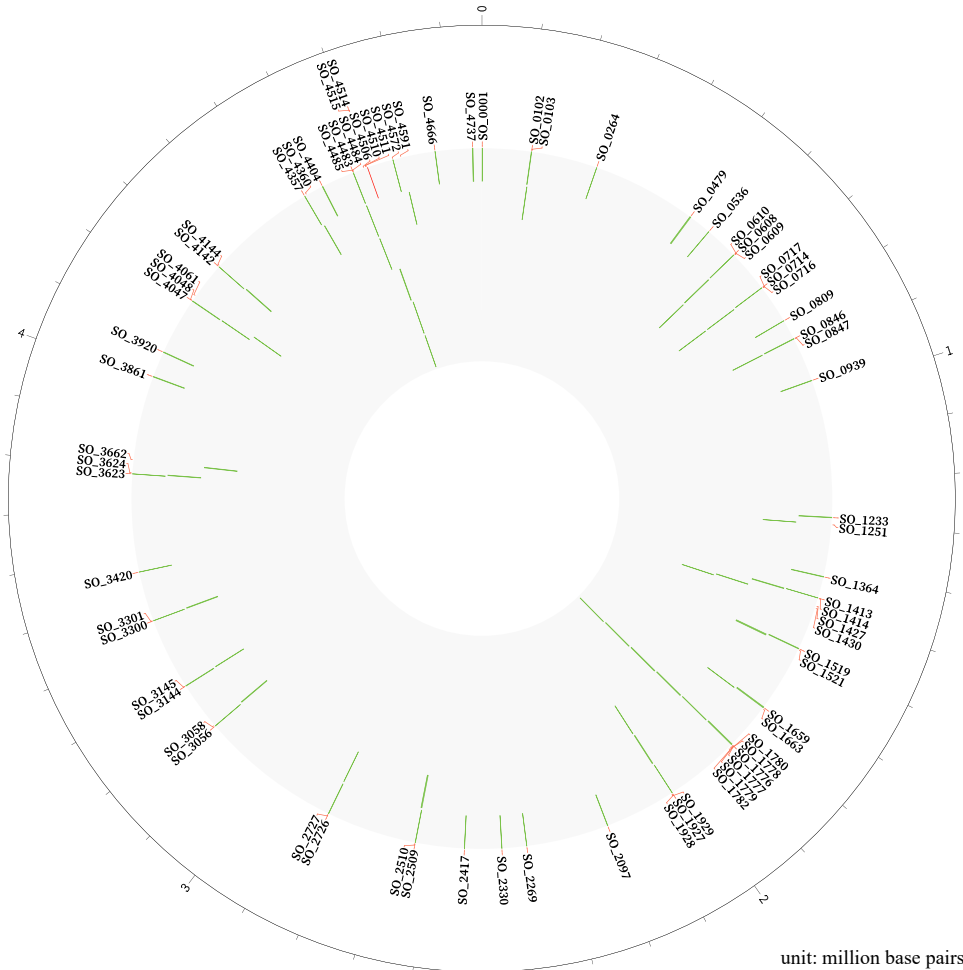


Figure 1.15. Circular representation of the *Shewanella oneidensis* MR-1 chromosome sequence related to EET process. The sequence originated from GenBank (accession numbers AE014299).

1.2.2 Short-range direct EET

The short-range direct EET proceed when microbes directly contact with extracellular redox partners *via* the cell membrane without any diffusive redox mediator. Redox proteins bounded in outer membranes, such as multiheme cytochromes *c*, are needed to accomplish this EET pathway. The short-range direct EET is very efficient. However, it is also limited because a short distance is required between the redox proteins on outer membranes and external redox partners (113). Therefore, only the microbes on the surface of redox partners can contribute EET in this way.

A brief cell membrane structure of *S. oneidensis* MR-1 is shown in Figure 1.16. Six cytochromes *c*, *i.e.*, MtrA, MtrC, OmcA, CymA, small tetraheme cytochrome (STC), and FccA, and one β barrel porin MtrB concern the short-range direct EET of *S. oneidensis* MR-1 (78). The electrons from oxidation of quinol are transferred to CymA and transmitted to MtrA with the help of small tetraheme cytochrome as well as FccA. The MtrA wrapped by MtrB relays the electrons to the complex of MtrC and OmcA where electrons are finally transported to extracellular redox partners.

MtrC and CymA are crucial to the EET of *S. oneidensis* MR-1 and the EET can decrease by 90% and 80% respectively with the absence of them (118-120). The electron transfer in multiheme cytochromes *c* is achieved through the chain of hemes. For example, ten heme are contained in MtrF (a homolog of MtrC) and they are arranged in “staggered-cross” formation with a distance between 4~11 Å to conduct electron transfer (121, 122). The solvent-exposed haems contained in cytochromes *c* (*e.g.*, MtrC and OmcA) might be responsible for the interfacial electron transfer between the cytochromes *c* and redox partners (121, 122).

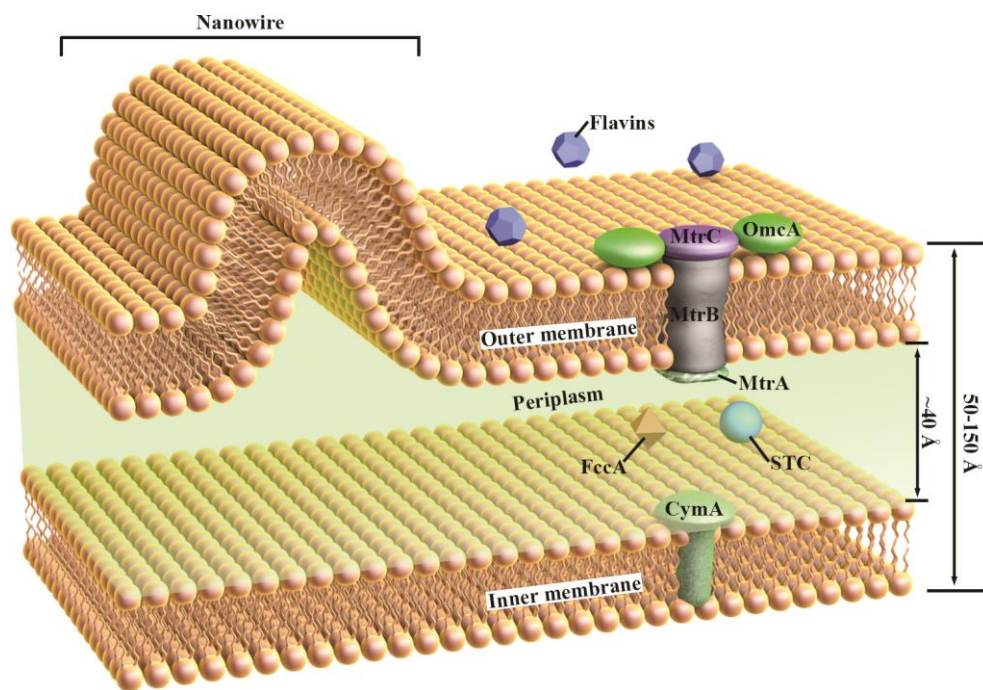


Figure 1.16. EET mechanisms operative in *S. oneidensis* MR-1

1.2.3 Long-range direct EET

EAB can also develop appendices-like structures called “nanowires” to accomplish long-range direct EET. Unlike to short-range direct EET, the long-range direct EET can achieve EET up to tens of micrometers (87, 123).

The nanowires of *S. oneidensis* MR-1 are 50 to 150 nm in diameter and tens of micrometers or longer in length (87) and reported as extensions of the outer membrane containing MtrC and OmcA, as shown in Figure 1.16 and Figure 1.17 (87, 124). More nanowires are produced when electron acceptors are limited and agitation is low (85, 87, 124, 125). The nanowires behave as a semiconductor and multistep redox hopping *via* cytochromes *c* is proposed as conductance model along the nanowires (101, 124). The electron transport rate along the nanowires is 1×10^9 /s at 0.100 V of potential biased and the resistivity is $1 \Omega \cdot \text{cm}$ (125). The mutant that has been knocked MtrC and OmcA can still produce nanowires, but the conductivity across and along the nanowire is poor (87, 125).

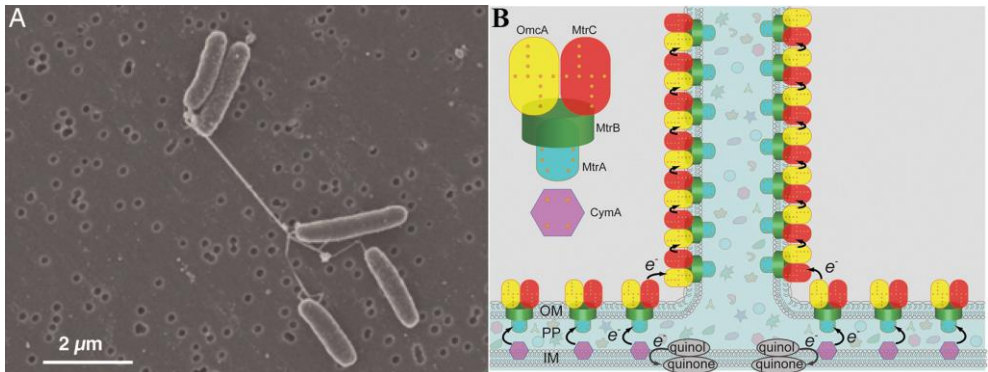


Figure 1.17. Nanowires of *S. oneidensis* MR-1. (A) SEM of the nanowires. Reproduced from ref. (87). Copyright (2006) National Academy of Sciences. (B) Proposed structural model for the nanowires. Reproduced from the ref. (124).

Other microbes can also develop nanowires. For example, nanowires are observed in *Geobacter* and a further study shows that the nanowires are metallic conductivity due to amino acid sequence (84).

1.2.4 Mediated EET

An alternative EET strategy for EAB, especially the outer layer of the biofilm in BESs, is using soluble redox mediators, or redox shuttles, to wire EET. A good candidate for efficient redox mediator should possess following features: good aqueous solubility, bio-refractory, benign to microbes, reusable, acceptable price, fast electron transfer with electrode and microbes (86, 126, 127). Redox mediators can be endogenous and exogenous (Figure 1.18). Examples of endogenous redox mediators are phenazines secreted by

Pseudomonas aeruginosa (128), quinones by *Lactococcus lactis* (129), hydroquinone by *E. coli* K-12 (130), and flavins by *S. oneidensis* MR-1 (89, 131, 132) and by *Bacillus* sp. WS-XY1 and *Pichia stipitis* (133). Examples of exogenous redox compounds are $K_3[Fe(CN)_6]$ (78), neutral red (134), humic substances (135, 136), etc. Notably, all iron-reducing bacteria and archaea can reduce humics according to the existing studies (136, 137). Notably, a low concentration of redox mediators can effectively accelerate EET because redox mediators can be cycled many times (127). Some microbes can use the mediators produced by other species, for example, *S. oneidensis* MR-1 can employ phenazines produced by *Pseudomonas aeruginosa* (128).

The mediated EET dominates EET process of *S. oneidensis* MR-1 and contributes more than 70% EET (80, 89, 125, 138). The process of mediated EET is similar to the short-range direct EET except that the electrons are not directly transmitted to terminal electron acceptors but oxidized flavins, mainly riboflavin (RF) and flavin mononucleotide (FMN), by OmcA and MtrC (Figure 1.16). FMN is a precursor of RF and a part of FMN is spontaneously transformed into RF when FMN is transported across the outer membrane of *S. oneidensis* MR-1. FMN can freely diffuse across the outer membrane while RF cannot (139). Studies show that flavins are easy to adsorb on the surface of Fe(III) and Mn(IV) (hydr)oxides as well as (89) with outer membrane bounded-cytochromes *c* (132). Moreover, flavins can chelate with soluble Fe(III) and increase local Fe(III) concentration, therefore, further enhance EET (89).

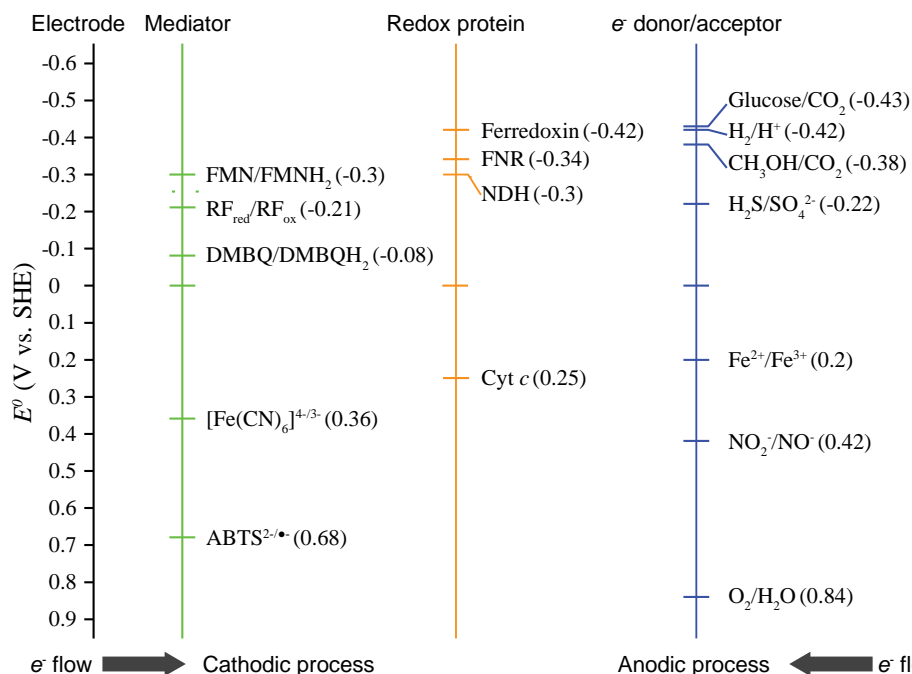


Figure 1.18. Thermodynamics of mediators, redox proteins on cell membranes, and electron flow

donors/acceptors. Values in parentheses indicate the redox potentials (pH 7.0, 25°C), which originated from ref. (1, 89, 140). ABTS, 2,2'-azino-bis(3-ethylbenzothiazoline-6-sulphonic acid); Cyt *c*, cytochrome *c*; DMBQ, 2,6-dimethyl-1,4-benzoquinone; FMN, flavin mononucleotide; FNR, ferredoxin—NADP(+) reductase; NDH, NADH dehydrogenase; RF, riboflavin.

1.3 Biosynthesis of nanomaterials by *S. oneidensis* MR-1

1.3.1 Introduction

Nanomaterials have been defined as “materials with any external dimension in the nanoscale or having internal structure or surface structure in the nanoscale.” “Nanoscale” is defined as a “length range approximately from 1 nm to 100 nm” (141). Nanocatalysts, therefore, refer to catalysts in the nanoscale. Compared to bulk counterparts, nanocatalysts offer a wealth of advantages, such as high activity, economy in atomic consumption, high selectivity, and stability. Due to these unique properties, nanocatalysts are attracting wide attention, and numerous nanocatalysts for a range of applications in clean energy technology and chemical industry have emerged.

Different methods to produce nanomaterials have been developed. Physical methods include ion implantation (142), vapor deposition (143), pulsed laser deposition (144), and mechanical techniques (145). The nanomaterials produced using physical methods are morphologically well controlled and environmentally friendly, but the methods are also limited by high complexity, low yield, and low efficiency (146). Chemical methods, such as ion exchange (147), sol-gel deposition (148), hydrothermal reactions (11, 149), and chemical co-precipitation (150), produce high yields and can synthesize uniformly dispersive and narrow-sized nanomaterials in solution, but are demanding regarding experimental conditions, fraught by side reactions, and potentially harmful to the environment. Recently, green synthesis using non-toxic chemicals such as starch has emerged for platinum (151) and gold nanoparticles (NPs) (152).

The biosynthesis methods are eco-friendly and non-toxic. Different biological reactive agents react with metal ions and form corresponding NPs intra- or extracellularly (153). The biosynthesized nanomaterials also benefit from excellent biocompatibility, mild experimental conditions, low cost, high yield, and good scalability. The biosynthesis processes are very attractive because they can be accomplished using bacteria, fungi, plant extracts, and DNA (154, 155).

Due to fast growth, low cost, and established genetic manipulation, bacterial biosynthesis of nanomaterials has been widely investigated. Bacterial biosynthesis of nanomaterials is simple and straightforward. Bacteria are cultured in nutritionally rich media (*e.g.*, Luria broth) to obtain sufficient numbers of bacterial cells. The bacterial cells are then washed with water or a 0.9% NaCl aqueous solution to remove secretion. The cell pellet

is then resuspended in a deoxygenated defined medium, such as M9 medium (156, 157), 3-(N-morpholino)propanesulfonic acid buffer (158, 159), sodium 4-(2-hydroxyethyl)-1-piperazineethanesulfonic acid (HEPES) buffer (160-163), a 0.9% NaCl aqueous solution, or even distilled water (164, 165). Phosphate buffer solution, which is widely used in other applications of bioelectrochemical systems (166), is rarely chosen because most metal ions precipitate with phosphate. The redox properties of the medium should also be considered. Maintaining neutral pH is not essential since many bacteria can survive in high concentrations of metal ions due to the extracellular electron transfer (EET) process (167); for example, *Lysinibacillus* sp. ZYM-1 can produce Se NPs over a range of pH 5 to 9 (168). Finally, depending on nanomaterial and synthesis conditions (*i.e.* bacteria or medium), the target nanomaterials are synthesized within a few minutes, several hours, or even days after introducing metal ions into the medium (mainly as an electron acceptor) of specific bacteria.

Moreover, the biosynthesis process of nanomaterials by bacteria can achieve environmental remediation and material recycling at the same time. For example, *Cupriavidus necator* and *Pseudomonas putida* can remove Pd(II) from waste materials and the recycled Pd(0) nanomaterials were found to be able to catalyze Suzuki–Miyaura reactions ($R_1 - BY_2 + R_2 - X \xrightarrow[\text{Base}]{\text{Pd}(0)} R_1 - R_2$) (169). The C-C bond formation was also catalyzed using the Pd(0) NPs produced by *C. necator* and *Cupriavidus metallidurans* from an acidic leachate containing several heavy metals including Pd(II) (170). The remediation by bacteria can be very efficient. *C. necator*, *P. putida*, and *Paracoccus denitrificans* removed 80%, 100%, and 100% of Pd(II), respectively. The Pd(0) nanomaterials obtained catalyzes dihydrogen production from hypophosphite (171).

Depending on extracellular or intracellular biosynthesis, different separation methods (*e.g.*, centrifugation, sonication, and freeze-thawing) can be employed to obtain the separated nanomaterials (172). Separation of nanomaterials from bacterial cells is not generally required. Nanomaterial-bacteria hybrids offer several advantages compared to the separated nanomaterials. Aggregation is avoided in biosynthesized nanomaterials. Aggregation of nanomaterials has been a problem in applications, and different surfactants or stabilizing agents (*e.g.*, polyethylene glycol) are used to solve the problem. However, the addition of surfactants often contributes to the decreased performance of the nanomaterials. Bacterial cells act as a supporter and framework in nanomaterial-bacteria hybrids, in which the formation sites for nanomaterials are uniformly distributed on the bacterial cell surfaces (*e.g.*, the outer cell membrane) to efficiently prevent aggregation in this way. Additionally, the yield is increased compared to the separated nanomaterials. For small-sized NP materials (*e.g.*, quantum dots), it is a challenge to retain samples during concentration and purification without aggregation. In contrast, nanomaterials generated by bacteria are attached on or enclosed in the cells. Concentration and purification can thus be accomplished straightforwardly by

centrifugation. Other functions are also introduced via chemical doping elements. The main elemental composition of bacterial cells includes carbon (C), hydrogen (H), oxygen (O), nitrogen (N), phosphorus (P), and sulfur (S), in which N, P, and S are essential doping elements for catalysts. These elements can be doped into the nanomaterials in subsequent processes (156). After the formation of the nanomaterials, obtained or separated nanomaterials from the nanomaterial-bacteria hybrids can be used as electrocatalysts (173), in biosensors (174) and electrosynthesis (175, 176), as adsorbents (163), and as photothermal agents (162) without further treatment. Besides, further treatment (e.g., carbonization, hydrothermal processing, and microwave heating) can be implemented to enhance the electroconductivity and structure of the nanomaterials.

A variety of bacteria have been employed in the biosynthesis of nanomaterials, including *Saccharomyces cerevisiae* (177), *Bacillus subtilis* (178), *Shewanella* spp. (156, 164, 173), and *Escherichia coli* (179). As one of several models of electrochemically active bacteria (EAB) in bioelectrochemical systems, *Shewanella oneidensis* MR-1 has gained particular attention in the biosynthesis of various nanomaterials, including metal, metalloid, and inorganic compounds.

As a dissimilatory metal-reducing bacterium, *S. oneidensis* MR-1 is able to reduce anaerobically various metal ions, for instance, Au(III) (164), Pd(II) (157, 173), Pt(IV) (156), and Ag(I) (180), and form the corresponding metallic nanomaterials. The metal ions are electron acceptors in bacterial biosynthesis, and this process correlates with the EET process (Figure 1.13).

Much attention has been given to the biosynthesis of nanomaterials, and several studies have summarized these developments (181-187). The present chapter provides a general view of metallic and non-metallic nanocatalysts synthesized by bacteria. In particular, the mechanism of bacterial NP biosynthesis with focus on *S. oneidensis* MR-1 is discussed. Characterization methods of the catalytic NPs are described, their applications summarized, and new prospects and challenges of biosynthesized nanocatalysts envisioned.

1.3.2 Biosynthesis mechanism of nanocatalysts

Metal ions and metal complexes are often positively charged while there are numerous negatively charged sites on the bacterial cell membrane due to the presence of glycoconjugates and surface groups such as carboxylate groups (188, 189). There are, however, also positively charged sites on the cell surface caused by positively charged proteins, which attract negatively charged metal complexes. As shown in Figure 1.19, target ions are captured from the environment by electrostatic interactions. The ions are then extracellularly converted into elemental metals by redox molecules on the outer membrane (e.g., cytochromes and enzymes). Alternatively, the ions are transported

through the outer membrane, interact with redox molecules, and intracellularly transformed into nanocatalysts in the periplasm (158, 164, 173, 188, 190).

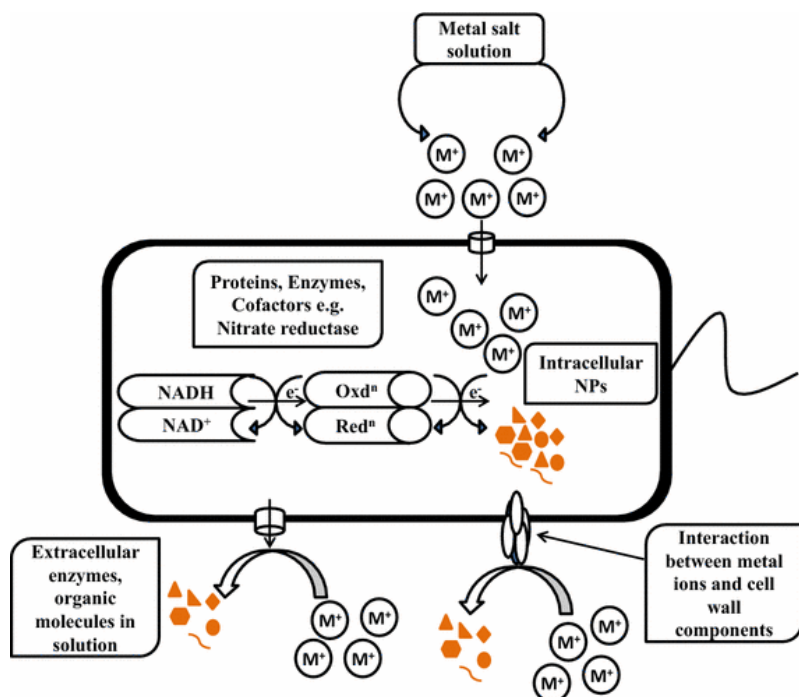


Figure 1.19. Three possible microbial synthesis mechanisms of nanocatalysts. Reproduced from ref. (188) with permission.

The exact routes for bacterial nanocatalyst biosynthesis are very complex and vary depending on the bacteria and ions. Presently, focus is on the mechanism of bacterial biosynthesis of nanocatalysts by the representative bacterium (*S. oneidensis* MR-1). This bacterium can reduce a variety of metal ions and EET of this particular species has been well studied.

The cell membrane of *S. oneidensis* MR-1 is shown schematically in Figure 1.20. The formation of nanocatalysts correlates with the precipitation and bioreduction of metal ions by EAB (191). Metal ions precipitate on or within the bacterial cell because the metal concentration exceeds the stoichiometry per reactive sites on or in the cell. That means that a small amount of soluble metals can be associated with cell surface or inside the cell, while high metal concentration can cause precipitation on the reactive sites (192). Although three EET pathways for *S. oneidensis* MR-1 have been proposed, the short-range direct EET prevails in the biosynthesis of nanocatalysts compared to the other two pathways. Nanowires are unlikely to be formed in the biosynthesis, in which abundant

metal ions are present as electron acceptor and are usually formed only when electron acceptors are limited (87). In the mediated EET pathway, *S. oneidensis* MR-1 excretes flavins, which mediate the EET between the cells and external electron acceptors (89). However, biosynthesis of nanocatalysts by flavins is hampered since their midpoint potentials are in the range -0.2 to -0.25 V compared to the standard hydrogen electrode (89). Different cytochromes *c* (e.g., MtrC, MtrA, and OmcA) are involved in the short-range direct EET and form the OmcA–MtrCAB pathway (80, 193). Electrons from oxidized quinol are first delivered to CymA, where the electrons are then carried to MtrA using FccA and a small tetraheme cytochrome (STC). This is followed by electron transport successively through MtrA, MtrB, and MtrC, which constitutes a complex penetrating the outer cell membrane. Finally, outer membrane cytochromes *c* MtrC and OmcA directly relay the electrons to metal ions (79, 85, 101). MtrA and OmcA are therefore important for the biosynthesis of metallic nanocatalysts and strongly affect the size of the nanocatalyst particles (159). Nonetheless, the presence of MtrA and OmcA is not indispensable for the formation of all nanomaterials since a mutant without MtrA and OmcA (*S. oneidensis* MR-1 $\Delta omcA/mtrC$) can also synthesize nanocatalysts such as Ag (159), Se(IV) (160), and Au (164) NPs. The nanocatalysts synthesized by the mutant can differ in size and antibacterial activity from those synthesized by the wildtype, making controlling synthesis by gene technologies possible (159). The ability of *S. oneidensis* MR-1 $\Delta omcA/mtrC$ to synthesize extracellular nanocatalysts indicates that other reactive sites are present, but the details regarding these sites remain to be explored.

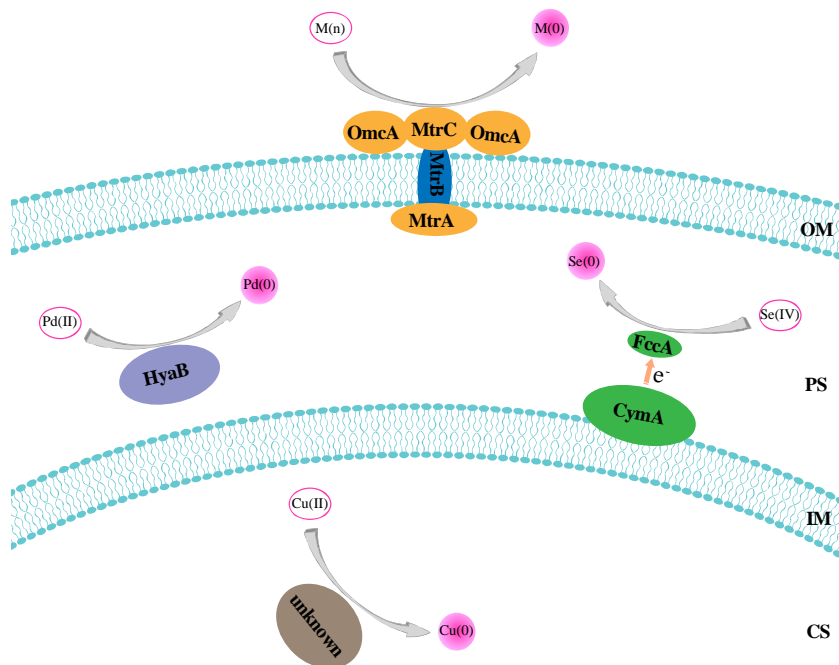


Figure 1.20. Schematic view of cell membrane structure of *S. oneidensis* MR-1 and main synthesis sites of metallic and metalloid nanomaterials. $M(n)$ = Tc(VII), Ag(I), U(VI), and Au(III). OM: outer membrane; PS: periplasm; IM: inner membrane; CS: cytoplasm. Note that the indicated sites are the primary sites for the metals and metalloids, but other sites are also possible. For simplicity the quinol and other structures are not presented.

Moreover, some studies show that MtrC and OmcA play an important role in the reduction of Fe(III), Cr(VI), Tc(VII), Ag(I), Au(III), and U(VI) (159, 167, 194, 195), while other studies imply that hydrogenases, specifically [NiFe]-hydrogenase HyaB, are responsible for the reduction of Pd(II) (161). Two main hydrogenases are present in the genome of *S. oneidensis* MR-1: HydA and HyaB (196). HydA is a periplasmic [Fe-Fe] hydrogenase, which is involved in dihydrogen formation, while HyaB is a bifunctional periplasmic [Ni-Fe] hydrogenase responsible for either the formation or oxidation of dihydrogen (196). The Pd(II) complex, normally $[PdCl_4]^{2-}$, has to penetrate the outer cell membrane in order to be reduced by HyaB, but only limited information about the mechanism of how $[PdCl_4]^{2-}$ is transported through the outer membrane is available. On the other hand, abundant Pd NPs were also found on the outer membrane (173).

The OmcA-MtrCAB pathway, nitrate and nitrite reductase, and hydrogenase are reported to have little effect on the reduction of SeO_3^{2-} to Se(0). In the periplasm, CymA relays electrons from quinol to fumarate reductase FccA, which further reduces SeO_3^{2-} to Se(0) (160). Different from Au, Pd, or Pt NPs with uniform and small size, the Se NPs are apparently bigger and more widely dispersed in size.

Apart from the formation of nanocatalysts in the outer membrane and the periplasm of *S. oneidensis* MR-1, Cu particles are also found to be dispersed in the cytoplasm and periplasm. In the reduction of Cu(II), MtrC, OmcA, MtrF, MtrABCDEF, DmsE, S04360, and CctA did not play a role. The reduction of Cu(II) could happen intracellularly, with possible unidentified reductases involved (158). Tellurium (Te) nanomaterials were also observed in the cytoplasm and periplasm (197, 198), but detailed mechanisms are not clear.

In summary, various electron transport pathways in *S. oneidensis* MR-1 provide different biosynthesis mechanisms. Different enzymes and 42 cytochrome *c* species are present in the genome of the bacteria, and only some of them have been studied (e.g., MtrC, OmcA, MtrB, CymA). The three established EET pathways dominate the reduction of insoluble Mn(IV) and Fe(III) (hydro)oxides, but different EET processes operate for other soluble metal ions (Figure 1.20).

1.3.3 Characterization of biogenic nanocatalysts

In the bacterial synthesis of nanocatalysts, it is important to follow the formation process. The defined medium changes to pale yellow after bacterial cells (e.g., *S. oneidensis* MR-1)

are resuspended into the medium. The medium can change to a specific color or the color of the metal ions fade as the nanocatalysts are formed, which means that the formation of some nanocatalysts can be followed directly with UV-Vis spectroscopy. For example, the absorption peak around the wavelength of maximum absorbance (λ_{\max}) of 411 nm disappears when Pd nanocatalysts are formed (173). A peak at $\lambda_{\max} = 530$ nm appears within 24 h in the biosynthesis of Au nanomaterial using *S. oneidensis* MR-1 (167). For Ag nanomaterials, a peak at $\lambda_{\max} = 418$ nm emerges in the colorless AgNO_3 solution containing *S. oneidensis* MR-1 after 48 h (180). CuS NPs form simultaneously with the appearance of a peak at $\lambda_{\max} = 1100$ nm (162). Moreover, since λ_{\max} is strongly linked with the size or the structure of nanomaterials, the evolution of nanomaterials can be monitored by UV-Vis spectroscopy. For example, a spectral red shift indicates an increasing amount of CdS quantum dots (177).

Electron microscopy technologies are crucial for visualization of the precise size and morphology as well as the structure of the nanocatalyst NPs. The most common of these technologies are SEM and TEM. The SEM and TEM sample preparations are similar, and fixation (usually by glutaraldehyde) and dehydration (*e.g.*, gradient ethanol dehydration) are required to maintain the original structure of the bacterial cells (20, 156, 173, 177). A relatively low voltage (5–20 kV) is applied in SEM of biological samples to avoid destroying the samples (199). SEM can image a large enough area for nanomaterial-bacteria hybrids, and the resolution can reach 1 nm. The diameter of bacterial cells can be several hundred nanometers, but slicing is not required if the inside structure of the cells is not addressed. Advanced SEM technologies have emerged and provided much more information. For example, in Figure 1.21, “3D” images were constructed with serial block-face SEM, confirming the presence of Cu NPs inside the *S. oneidensis* MR-1 cells (158). TEM is very powerful for observing both the morphology and structure of the nanomaterials, but ultra-thin sections of the nanomaterial-bacterial hybrids must be sliced if the inside of the cells is to be mapped (158, 164) since the electron beam of the TEM cannot penetrate samples thicker than 100 nm. The surface facets of the nanocatalysts are key factors for their performance, and the extraordinary nanometer-to-atomic TEM resolution makes the acquisition of such information possible, particularly the structure of the crystal lattice (156, 162). Coupled with energy-dispersive X-ray spectroscopy (EDS), TEM can map not only the morphology of the nanocatalysts, but also the elemental composition, which is essential for the characterization of alloys and core-shell NPs. For example, the EDS mapping displayed in Figure 1.22 shows clearly overlapping Pd, Au, P, and S peaks, indicative of a doped alloy (156).

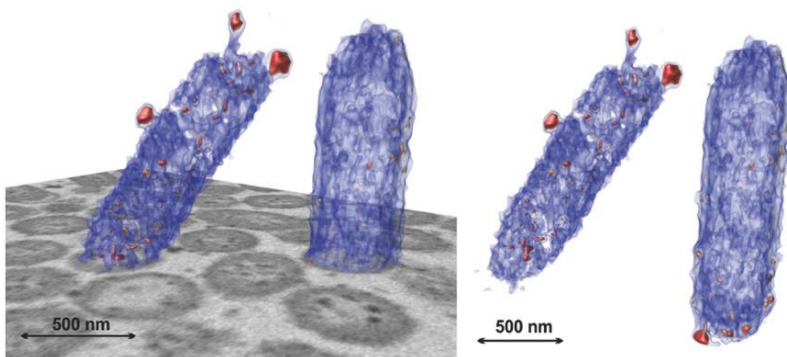


Figure 1.21. “3D” images reconstructed with serial block-face scanning electron microscopy. The red dots are Cu NPs, and blue indicates a cell. Reproduced from ref. (158). with permission.

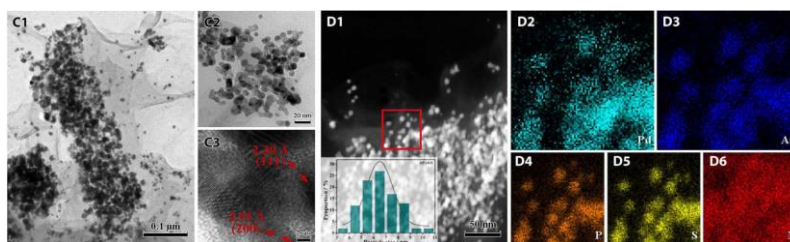


Figure 1.22. TEM and corresponding EDS mapping of PdAu alloy biosynthesized by *S. oneidensis* MR-1 with subsequent hydrothermal treatment. Reproduced from ref. (156).

Another versatile technique is AFM. The resolution of AFM can also reach the nanometer level, and, AFM is therefore, suitable for precise imaging of nanomaterials (180). The sample preparation of AFM is simple with a small number of samples immobilized and spread out on a flat surface. Fixation, dehydration, coating with metal layer, and slicing are not needed, which minimizes sample destruction. AFM can be conducted in ambient atmosphere and even in solution. In addition, 3D images can be readily constructed from AFM measurements (Figure 1.14A). AFM can provide physical properties and information other than size and morphology. For instance, Figure 1.23 shows a comparison between the topographic and current-sensing AFM (CSAFM) images of *S. oneidensis* MR-1 cells coated with Pd NPs that are apparently different from pristine *S. oneidensis* MR-1 cells. Compared with the dark area in pristine *S. oneidensis* MR-1 cells, the brightness of the cells coated with biosynthesized Pd nanocatalysts reflects higher conductivity, since the brightness in CSAFM images indicates the current flow between the AFM tip and the substrate (173).

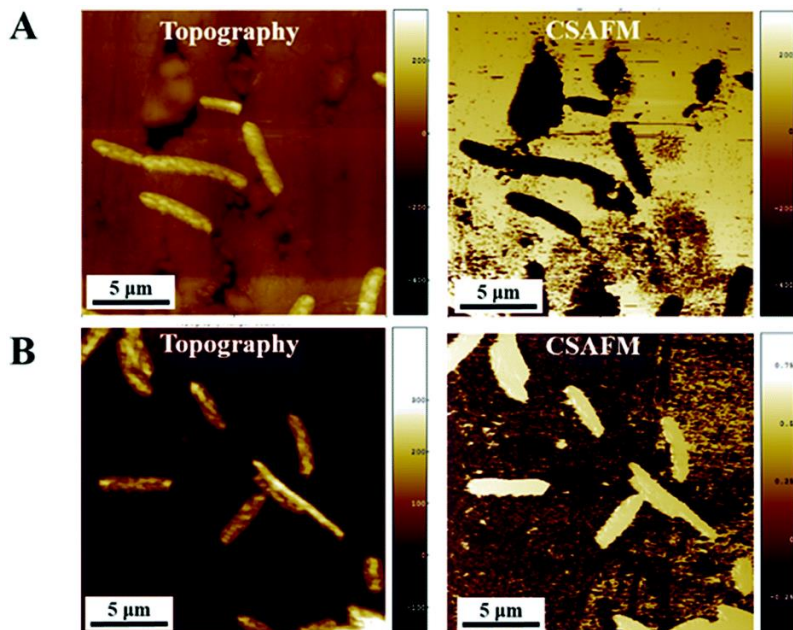


Figure 1.23. Representative topographic (left) and current-sensing AFM images (right) of *S. oneidensis* MR-1 (A) and *S. oneidensis* MR-1 coated with biosynthesized Pd nanocatalysts (B). Reproduced from ref. (173) with permission.

EDS in SEM and TEM can show the elemental composition but does not give other information, such as chemical and electronic state of the elements. X-ray photoelectron spectroscopy (XPS) is helpful in achieving this additional information. XPS is a qualitative and semiquantitative analysis method for chemical surface elements including the chemical and electronic states. For example, a peak belonging to Se_{3d} emerged in Se nanospheres synthesized by MR-1 (174). In another study, the ratio of Pd, Au, P, N, and S elements (32.28:10.83:4.32:47.09:5.48) was obtained using XPS (156).

The qualitative and semiquantitative information from XPS analysis is highly valuable, but XPS is limited only to the surface of the sample (*e.g.*, 20 nm into samples). This is not comprehensive enough for bulk materials (*i.e.* nanomaterial-bacterial hybrids), which are hundreds of nanometers in diameter. To get the crystal structure on or within nanomaterial-bacterial hybrids, X-ray diffraction (XRD) analysis, in which the penetration of the X-ray can be several millimeters, is practical. For example, both peaks belonging to Au and Pd were observed in the PdAu alloy (156, 165). Nonetheless, XRD analysis alone is not sufficient to confirm the phase analysis since the XRD pattern of different crystals can be very similar and it is difficult to analyze when different crystals co-exist. Moreover, signals are weak if the nanocatalysts are amorphous or the metals are highly dispersed in the nanomaterials. If possible, XRD, EDS, TEM, and XPS analysis should all be considered (156, 162).

The biosynthesized nanocatalysts are different from their chemically synthesized analogues. Bacterial cells are normally covered with EPS, and organic substances can participate in the formation of the nanocatalysts. To quantify these substances, thermogravimetric analyses (TGA) can be employed. For example, the weight loss is caused by thermal decomposition of adsorbed organic substances in nanomaterials synthesized by bacteria when the temperature was increased from 100°C to 400 °C during TGA, while the weight loss from 400 to 800 °C is due to decomposition of intracrystalline organic substances (165, 200).

1.3.4 Classes of biogenic nanocatalysts

1.3.4.1 Metals and alloys

Much attention has been given to the biosynthesis of metallic nanomaterials, (especially noble metal nanomaterials) due to the considerable economic benefits of metal recovery (182). A variety of noble metal ions, such as Au(III), Pt(IV), Pd(II), and Ag(I), can be recovered by bacteria (156, 180, 201, 202). The local size of the nanomaterials depends on experimental conditions, but typically the microstructures of noble metal nanomaterials are small (*i.e.*, in ranges from a few to tens of nanometers) and uniform. Biogenic Pt NPs synthesized by *Shewanella algae* (202) are about 5 nm. Au and Pd NPs synthesized by *S. oneidensis* MR-1 are 5–30 nm (164) and 3–10 nm (173), respectively. The size of Ag NPs is similar to that of Pd NPs (*i.e.*, about 2–10 nm in diameter) (180).

The recovery of noble metal ions is very high within a relatively short treatment time. For example, a recovery of 99.6% of Pd(II) was achieved by *S. oneidensis* MR-1 ($OD_{600} = 2.0$) overnight when 50 mg/L of Pd(II) was used as an electron acceptor and dihydrogen as an electron donor (157). The recovery remains high at high concentrations of Pd(II). For instance, only 0.1 mg/L remained in the solution when 1000 mg/L of Pd(II) was introduced (157). Au (III) removal can be visually observed within 30 min indicated by the color change from pale yellow to purple when *S. oneidensis* MR-1 is exposed to 100 mg/L of $[AuCl_4]^-$ (164). Similarly, about 90% of $[PtCl_6]^{2-}$ was removed by *S. algae* in 60 min (202).

Other metal ions can also be reduced by bacteria, forming corresponding metal NPs. The Cu NPs synthesized by *S. oneidensis* MR-1 are relatively larger than the noble metal NPs just noted, with a typical size range of 20 to 40 nm (158). The recovery of Cu(II) is also high, with 70% after 3 h, 91% after 24 h, and 100% after 96 h. The core of the NPs is Cu(0), while the surface is Cu₂O due to oxidation caused by exposure to oxygen in the air (158). Co NPs of 4-8 nm in length were formed in the outer membrane of *S. putrefaciens* CN32 after the cells were exposed to 195 mg/L of Co²⁺ in pH 3 for 24 h. Moderate recovery of 21% was achieved with an initial concentration of 210.745 mg/L. The limited recovery may be due to the short lifespan of the bacteria under these experimental conditions (203).

The ability of EAB to reduce various metal ions offers an approach for the synthesis of alloys. A highly dispersed PdAu alloy was synthesized on the cell surface of *S. oneidensis* MR-1 after successive addition of $[\text{AuCl}_4]^-$ and $[\text{PdCl}_4]^{2-}$. As shown in Figure 1.22, NPs of this alloy are quite small, with an average diameter of 5 nm (156). An extracellular PdAu alloy is also formed when a higher concentration of $[\text{PdCl}_4]^{2-}$ and $[\text{AuCl}_4]^-$ are used as electron acceptors; for example, a nanocomposite of PdAu alloy and Fe_3O_4 with a NP size of 3–15 nm was obtained from *S. oneidensis* MR-1 after 1 mM of $[\text{PdCl}_4]^{2-}$ and 1 mM of $[\text{AuCl}_4]^-$ were introduced into the medium containing akaganeite for 48 h (165).

1.3.4.2 Metal and metalloid sulfides

EAB can also reduce sulfur and thiosulfate to sulfide (204), producing metal sulfides when specific metal ions, sulfur, and thiosulfate as electron acceptors are present simultaneously. For example, brown-colored CuS NPs with a uniform size of about 5 nm are formed extracellularly, when *S. oneidensis* MR-1 is incubated in a HEPES-buffered mineral medium containing 1 mM of $\text{Na}_2\text{S}_2\text{O}_3$, CuCl_2 , and 20 mM of lactate. The Cu:S ratio was 0.94:1 analyzed from XPS results (162). In another study, CuS nanorods with 17.4 nm and 80.8 nm in diameter and length were embedded in the *S. oneidensis* MR-1 cell membrane, forming a complex hollow shell structure (163).

S. oneidensis MR-1 can synthesize Ag_2S NPs of 53.4 ± 12.4 nm. The size of the NPs decreased to 27.6 ± 6.4 nm when MtrC and OmcA were knocked out (159). In contrast, another study showed that the presence of *S. oneidensis* MR-1 cells is not required to form Ag_2S NPs (205). These authors inferred that the complex $\text{Na}_3[\text{Ag}(\text{S}_2\text{O}_3)_2]$ caused precipitation of Ag_2S . However, MtrC, OmcA, and MtrB from *S. oneidensis* MR-1 can stabilize Ag_2S NPs. The native cell structure stabilizes rather than forms Ag_2S NPs, which means larger Ag_2S NPs are formed in the absence of *S. oneidensis* MR-1 cells (205). Smaller Ag_2S NPs can also be obtained from the same bacterium. For example, Ag_2S NPs smaller than 8 nm attached to TiO_2 nanotubes have been produced by *S. oneidensis* MR-1 (206).

FeS can also be formed abiotically. For example, poorly crystalline FeS can be obtained by mixing 0.57 M of FeCl_2 and 1.1 M of Na_2S (207). Different from abiotic FeS with bulk and irregular forms, the biogenic FeS synthesized by *S. putrefaciens* CN32 is mainly comprised of 100-nm NPs. Moreover, the biogenic Fe:S ratio was 2.3, which is different from that of abiotic FeS with a ratio of 1.3 (208).

CdS NPs (“quantum dots”) with an average diameter of 2 nm can be synthesized by *S. cerevisiae* via yeast cells cultured in 0.1 mM of CdCl_2 and 0.05 mM of Na_2S for one day. Notably, the size of the CdS quantum dots increases with longer culture times (177). Much larger CdS NPs (about 15 nm in diameter) synthesized by *S. oneidensis* MR-1 have also

been reported (209). Moreover, the addition of ionic liquid can modify the CdS NPs from agglomerated and irregular shapes to highly ordered spherical structures (209).

Biosynthesis also provides morphologies that are not available from chemical synthesis. AsS nanotubes that are 20–100 nm in diameter and about 30 μm in length were produced extracellularly by *Shewanella* sp. strain HN-41 in a medium containing As(V) and $\text{S}_2\text{O}_3^{2-}$. The nanotube composition nine days after inoculation was As_2S_3 , which transformed to AsS after two to three weeks (210).

Notably, the addition of metal and sulfur or thiosulfate is sometimes not needed. Some bacteria are able to synthesize metal sulfide-based nanomaterials even in groundwater. Natural biofilms of *Desulfobacteraceae* can, for example, synthesize 2–5-nm ZnS NPs by accumulating a Zn concentration that is 10^6 times over ground water level (211).

The biosynthesis of other metal sulfides is also reported, such as MnS (212), but the application of these metal sulfides as catalysts is rarely reported. We therefore do not include detailed discussion of these biogenic metal sulfides.

1.3.4.3 Metal oxides and metal hydroxides

Fe_3O_4 NPs were obtained under anaerobic conditions by transforming akaganeite to magnetite by culturing *S. oneidensis* MR-1 with lactate as an electron donor for 48 h. The Fe_3O_4 NP size was 3–15 nm in diameter (165). Larger Fe_3O_4 NPs with a diameter of 26–38 nm can be acquired from *Shewanella* sp. HN-41 using a similar method (213).

In contrast, another study reported that the transformation of akaganeite by *Shewanella* sp. HN-41 depends on the amount of akaganeite precursors and Fe(II) in the solution. Akaganeite nanorods that are about 5 nm in width and 20 nm in length were used as precursors and electron acceptors. When 30-mM akaganeite was introduced after 10 days, magnetite NPs up to 100 nm diameter appeared. However, goethite nanowires 15 nm in width and 500 nm in length appeared instead (214).

UO_2 NPs formed when *S. oneidensis* MR-1 cells were inoculated in 250 μm of uranyl acetate and 10 mM of sodium lactate under anaerobic conditions. The UO_2 NPs are quite small, only 1–5 nm in diameter. The NPs appeared in three forms, in which some, densely packed with EPS, were complex structures, similar to glycocalyx. This indicates that EPS (possibly with a redox substance inside) plays an important role in the formation of UO_2 NPs (195).

1.3.4.4 Metalloids

Apart from metals and metal compounds, the biosynthesis of metalloid nanomaterials by EAB have been extensively studied (215). For example, the size distribution of Se NPs can be adjusted by controlling the biomass concentration of *Shewanella* sp. HN-41 and

the initial selenite concentration. Within 2 h, 1–20 nm amorphous Se NPs were produced with low initial biomass under anaerobic conditions. Much larger NPs (about 150 nm) were also observed. Se NPs around 123 nm were produced when a larger initial biomass was exposed for 24 h (216). Different bacteria can synthesize Se NPs at different sizes using different mechanisms of Se(VI) reduction. Large, 100–250 nm Se NPs were synthesized by *S. oneidensis* MR-1, and smaller 50–100 nm Se NPs were acquired by *Geobacter sulfurreducens* (ATCC 51573), while the smallest Se NPs (around 50 nm) were synthesized by *Veillonella atypica* (ATCC 14894) (217). Another study showed that the bigger Se NPs (around 100 nm) formed inside the cells, while smaller Se NPs (around 20 nm) formed extracellularly; the biosynthesis of Se NPs is potentially controlled by the EPS (160).

Another metalloid NP biosynthesis by EAB was also reported (63). Tellurite (Te) nanomaterials were formed inside *S. oneidensis* MR-1, and a pathway different from Se reduction was proposed (198). More than 90% of Te(IV) was recovered after incubating *S. oneidensis* MR-1 in 100 μM of sodium Te and 10 mM sodium lactate for 120 h (197). The products are single-crystalline Te nanorods with a length of 100–200 nm. Notably, the presence of Fe(III) will change the synthesis location and the size of the Te nanorods. When Te(IV) and Fe(III) co-exist in the medium, more extracellular Te nanorods accumulated with 240 nm and 25 nm for the length and diameter, respectively. However, when Te(IV) was introduced after Fe(III) was reduced to Fe(II), exclusively extracellular crystalline Te nanorods were formed at a smaller size (*i.e.*, 89 nm and 7.5 nm in the length and diameter, respectively were found) (218). In addition, *Shewanella baltica* was reported as having the ability to reduce Te(IV) and form 8–75 nm Te nanorods (219).

1.3.5 Applications of Biogenic Nanocatalysts

As noted, different bacteria can synthesize various nanomaterials. The resulting nanomaterials offer numerous applications. The applications of catalytic NPs synthesized by *S. oneidensis* MR-1 and other representative bacteria are summarized in Table 1.2. Three kinds of applications (*i.e.*, electrocatalysts, photocatalysts, and biocatalysts) are discussed below.

Table 1.2. Nanocatalysts synthesized by bacteria and their applications

Nanocatalysts	Bacteria	Applications	References
Au	<i>S. oneidensis</i> MR-1	Biocatalysts	(165)
Cu	<i>S. oneidensis</i> MR-1	Biocatalysts	(158)
Pt	<i>S. oneidensis</i> MR-1	Biocatalysts	(220)

Pd	<i>S. oneidensis</i> MR-1	Electrocatalysts	(173, 221)
		Biocatalysts	(157, 165, 220)
Se	<i>Lysinibacillus</i> sp. ZYM-1	Photocatalysts	(168)
Te	<i>Shewanella baltica</i>	Photocatalysts	(219)
Ag ₂ S	<i>S. oneidensis</i> MR-1	Photocatalysts	(205)
		Biocatalysts	(159)
FeS	<i>Shewanella putrefaciens</i> CN32	Biocatalysts	(208)
CdS	<i>Moorella thermoacetica</i>	Biocatalysts	(175)
		<i>S. oneidensis</i> MR-1	Antibacterial agent
ZnS	<i>S. oneidensis</i> MR-1	Photocatalysts	(222)
PdAu	<i>S. oneidensis</i> MR-1	Electrocatalysts	(156)
		Biocatalysts	(165)
PdPt	<i>S. oneidensis</i> MR-1	Biocatalysts	(220)

1.3.5.1 Electrocatalysis

The biosynthesized nanocatalysts not only exhibit some exclusive morphology, but also unique catalytic properties. Pd NPs synthesized by *S. oneidensis* MR-1 show unique selective catalysis to formate electrooxidation, but no electrocatalysis to oxidize other biofuels, such as ethanol, methanol, and acetate, in neutral solution. The selectivity is caused by preferential binding of formate over the other fuels. Moreover, compared to Pd electrodeposited on an electrode, the anodic peak for formate oxidation is more negative by 220 mV (0.10 V vs. a saturated calomel electrode), and exhibit less activation energy (173). The poor conductivity of the cell substrate itself is compensated by the PdNP coating, as inferred clearly from the current-sensing AFM images (Figure 1.23).

EAB can also facilitate nanocatalyst formation not only on the cell surface, but also on electrochemical electrode surfaces. For example, 10–100 nm Pd NPs were coated on a cathode (a piece of carbon cloth) by *S. oneidensis* MR-1 poised at 0.8 V. The size increased to 200–250 nm for abiotic Pd NPs produced using electrochemical method. The smaller size of the NPs and the presence of cells as biocatalysts led to a larger surface area, resulting 90.0 ± 1.4 Coulombs of electron transfer in dihydrogen production with a Pd loading of $40.5 \text{ m}^2 \text{ g}^{-1}$. This is much higher than the 75.0 ± 1.2 Coulombs in the absence of the bacteria. As a result, the dihydrogen production and recovery ($61.8 \pm 2.0 \text{ L-H}_2 \text{ m}^{-3} \text{ day}^{-1}$, hydrogen volume per reactor volume per day, and $65.5 \pm 3.1\%$, respectively) in the

presence of the bacteria were significantly higher than in the absence of bacteria ($38.5 \pm 2.0 \text{ L-H}_2 \text{ m}^{-3} \text{ day}^{-1}$ and $47.3 \pm 3.9\%$, respectively). However, the stability of the biodeposited Pd NPs was not satisfactory and the dihydrogen production decreased by 37% after five cycles. Addition of Nafion as binding agents therefore was needed to improve consistent catalytic performance (221).

The nanocatalysts synthesized by EAB are small and uniform but have poor crystallinity and conductivity, which may prevent electrocatalysis. Other subsequent treatments can be employed to improve the performance. A highly efficient electrocatalyst with a hybrid PdAu alloy covered with graphene oxide has been designed. The hybrid was initially synthesized by *S. oneidensis* MR-1 and underwent subsequent hydrothermal treatment. As shown in Figure 1.24, the hybrid showed a 6.15-fold higher mass electrocatalytic activity for ethanol oxidation in alkaline condition and a 6.58-fold higher activity for formate oxidation in acid condition compared to a commercial Pd/C catalyst with the same Pd loading of $4 \mu\text{g cm}^{-2}$ (156). The hybrid also showed better stability and continued outperforming the commercial Pd/C catalyst after 2000 s. The high catalytic activity was attributed to the three-dimensional porous structure and the carbon support as well as doping elements from *S. oneidensis* MR-1 cells, the nature of PdAu alloy, and the enhanced conductivity of reduced graphene oxide (156).

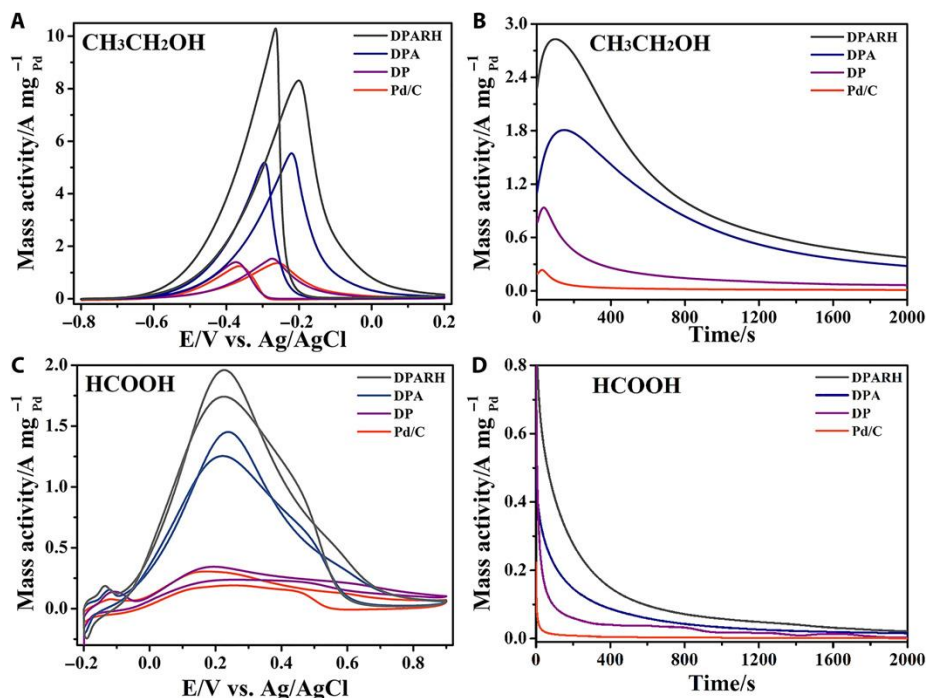


Figure 1.24. Electrocatalytic performances of as-prepared biogenic catalysts. (A) Cyclic voltammetry (CV) of the carbonized hybrids of *S. oneidensis* MR-1 cells, PdAu alloy with reduced graphene oxide

(DPA), carbonized hybrids of *S. oneidensis* MR-1 cells and PdAu alloy (DPA), carbonized hybrids of *S. oneidensis* MR-1 cells and Pd NPs (DP), and commercial Pd/C catalyst-modified electrodes in 1 M KOH + 1 M ethanol. Scan rate 50 mV s⁻¹. Potentials versus Ag/AgCl (saturated KCl). (B) Chronoamperometric curves of the catalyst-modified electrodes in 1 M KOH + 1 M ethanol at -0.3 V for 2000 s. (C) CVs of these catalyst-modified electrodes in 0.5 M H₂SO₄ + 0.5 M HCOOH. Scan rate 50 mV s⁻¹. (D) Chronoamperometric curves of the catalyst-modified electrodes in 0.5 M H₂SO₄ + 0.5 M HCOOH at 0.1 V for 2000 s. The Pd mass amounts of all the catalysts were about 1 μg in each electrode. Reproduced from ref. (156).

1.3.5.2 Photocatalysis

The nanocatalysts formed on the EAB surface possess an ability to degrade pollutants that are resistant to biodegradation. As shown in Figure 1.25A, a hybrid of *S. oneidensis* MR-1 and 50 mg of biosynthesized ZnS NPs with a diameter of 5 nm totally degraded 20 mg L⁻¹ of rhodamine B (RhB) in 3 h under UV irradiation. The 554-nm peak belonging to RhB vanished, and a new, blue-shifted peak (from 550 nm to 500 nm) appeared with the degradation, indicative of de-ethylation of the N,N,N',N'-tetraethylrhodamine structure in RhB (Figure 1.25B). Further investigation concluded that the photogenerated holes generated by the biosynthesized ZnS, not the hydroxyl radicals, contributed to the photocatalysis (222).

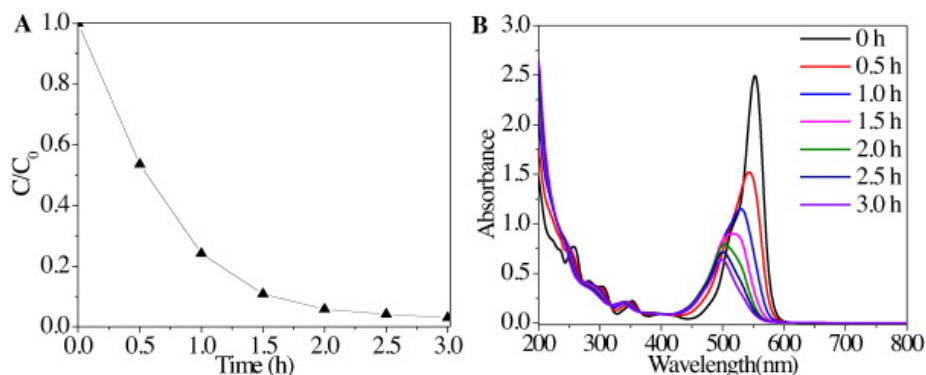


Figure 1.25. (A) Photocatalytic activity of synthesized ZnS nanocrystals for the photodegradation of rhodamine B (RhB) in aqueous solution (20 mg/L) in air. C_0 and C represent the initial concentration and residual concentrations of RhB, respectively. (B) UV-vis absorption changes of an RhB aqueous solution at room temperature in the presence of ZnS NPs under UV irradiation. Reproduced from ref. (222) with permission.

In a recent study, a mixture of chemically synthesized Ag₃PO₄ NPs and *S. oneidensis* MR-1 can degrade RhB with visible light irradiation under anaerobic conditions. After five days of light irradiation, 15 mg/L of RhB had been completely degraded by the Ag₃PO₄ NPs (0.5g/L) and *S. oneidensis* MR-1 cells. In this case, *S. oneidensis* MR-1 cells significantly enhanced the photocatalytic efficiency. As shown in Figure 1.26, the main

role of *S. oneidensis* MR-1 was to provide electrons to the Ag_3PO_4 photocatalyst after Ag_3PO_4 excitation by light to produce photogenerated electrons in stepwise decomposition of RhB to rhodamine (223).

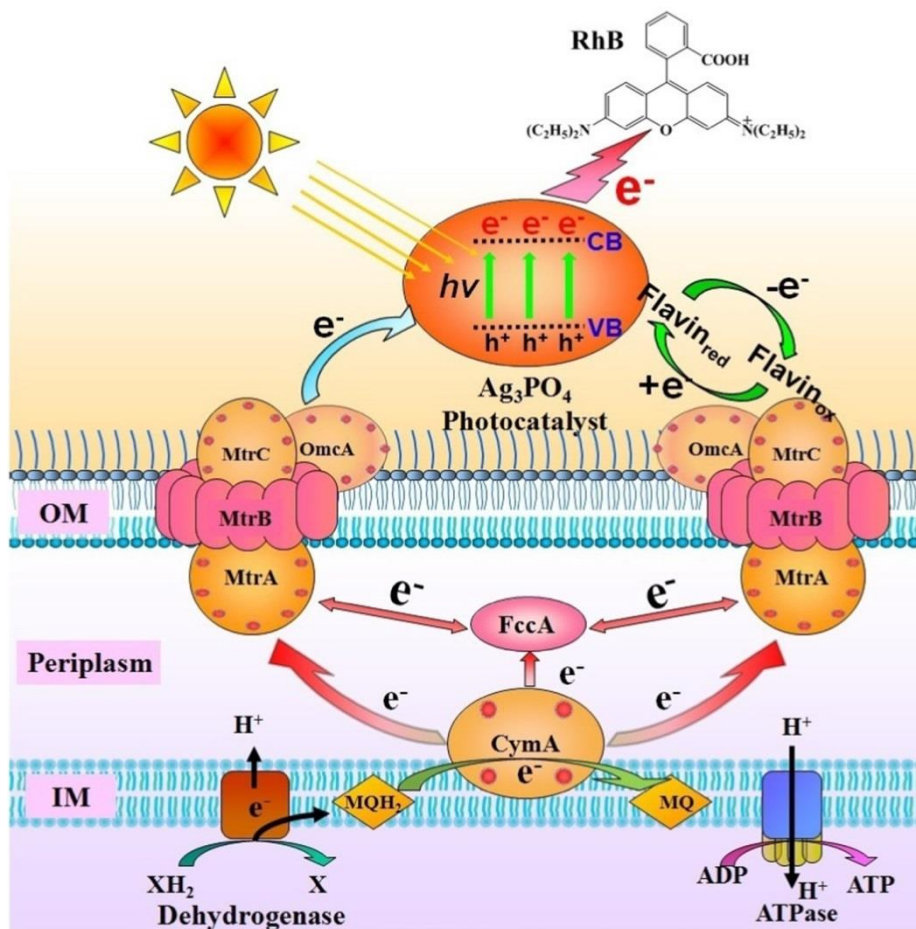


Figure 1.26. Proposed photocatalytic RhB degradation mechanisms in a bio-photoelectric reductive degradation system. Arrows represent the electron flow. OM, outer membrane; IM, inner membrane. Reproduced from ref. (223) with permission.

RhB can also be photodegraded by Se nanocatalysts synthesized by *Lysinibacillus* sp. ZYM-1 under visible light irradiation in combination with H_2O_2 . *Lysinibacillus* sp. ZYM-1 produces Se nanorods, nanocubes, and nanospheres with different initial concentrations of selenite, but only the nanospheres showed photocatalytic performance. Ten milligrams of Se nanospheres photodecomposed RhB (10 mg L^{-1} , 50 mL) in 5 hours with a reaction rate constant of 0.0048 min^{-1} outperforming chemogenic Se nanomaterials. Both chromophore cleavage and N-de-ethylation contributed to the photodegradation (168).

The biogenic Ag₂S nanocatalysts produced by *S. oneidensis* MR-1 were also found to degrade pollutants under visible light irradiation. For example, coated on TiO₂ nanotubes, 20-mg Ag₂S nanocatalysts can photodecompose 4-nitrophenol (0.12 mmol L⁻¹, 50 mL) to 4-aminophenol completely within five hours. The photocatalytic activity increased with increasing molar ratio of Ag/Ti until 1/10, where the excess Ag₂S conglomerates and hinders the activity. One of the key factors is the electron transfer between Ag₂S NPs and TiO₂ nanotubes (206).

The reduction of methylene blue dye under sunlight is relatively slow, and only 20% reduction was detected after four hours. However, 90% reduction with 10 µg/mL Te NPs synthesized by *S. baltica* is achieved within the same period. Compared to the Te NPs obtained from chemical synthesis, the option of recycling is a notable advantage (219).

1.3.5.3 Biocatalysis

Biogenic Pd NPs also act as biocatalysts in other ways, such as in reductive dechlorination of polychlorinated biphenyls both in aqueous solution and in sediment matrices. Using formate as an electron donor, the hybrid of *S. oneidensis* MR-1 cells exposed to 500 mg/L of Pd(II) decomposed the polychlorinated 1 mg L⁻¹ of 2,3,4-chlorobiphenyl to undetectable levels in 1 h at room temperature. The biocatalysis is enhanced when incubated in contaminated sediments. The hybrid from 50 mg/L of Pd(II) achieved dechlorination of seven polychlorinated biphenyls in 48 h, which is comparable to 500 mg/L of commercial Pd(0) powder (157).

Dechlorination of carbon tetrachloride was achieved using FeS biosynthesized by *S. putrefaciens* CN32. The hybrid of *S. putrefaciens* CN32 and biogenic FeS showed eight- and five-fold increases in dechlorination compared to *S. putrefaciens* CN32 and chemogenic FeS NPs, respectively. The efficient catalysis was attributed to the even distribution of FeS nanocatalysts and the larger amount of Fe(II) and disulfide. The addition of Fe(III) can enhance the catalytic efficiency further. The main role of *S. putrefaciens* CN32 is to produce FeS NPs that are well dispersed on the cell surface. The cell contribution is minimal after FeS formation (208).

The conventional method of biosynthesizing nanocatalysts is to retain the nanocatalyst coating on the cell membranes (“metallized” cells such as “palladized” cells) and ignore the non-cell-associated nanocatalysts in the bulk medium. However, one study showed that the extracellular nanocatalysts produced by *S. oneidensis* MR-1 outperformed the palladized cells. The initial rate of reduction of methyl viologen to methyl viologen cations radical of non-cell-associated Ag₂S (0.26 mM/s) is thus three-fold higher than that of cell-associated Ag₂S (0.26 mM/s). Another notable result is that the non-cell-associated Ag₂S from the mutant lacking OmcA and MtrC shows better performance than the wild-type strain (159). The morphology and structure of cell-associated nanocatalysts and non-cell-

associated nanocatalysts may therefore not be identical, and equal attention should be given to these two kinds of nanocatalysts. In contrast to chemogenic nanocatalysts, no additional capping agents or protecting agents are needed during biosynthesis due to the EPS secreted by the bacteria.

Photoautotrophic microorganisms can harvest light and carbon sources to produce food and energy. However, these processes are slow. On the other hand, although solid-state semiconductors can efficiently absorb light, semiconductors still face the challenge of converting photoexcited electrons into chemical bonds. Moreover, chemogenic semiconductors pose a threat to the environment during the synthesis process. A recent study combined the high efficiency of light harvesting by semiconductors with the low cost, self-replication, and self-repairing of the biology process. CdS NPs (<10 nm) were biodeposited on a nonphotosynthetic bacterium (*M. thermoacetica*) by incubating the bacteria in a solution of Cd^{2+} and cysteine. The CdS NPs act as a photocatalyst and collect photons under light irradiation. The excited CdS NPs then deliver electrons to *Moorella thermoacetica*, which act as biocatalysts, producing acetic acid from CO_2 , as shown in Figure 1.27. The CdS NPs have three roles in the overall process: to harvest photons, to provide electrons, and to protect the bacteria from the damage caused by the light irradiation. High production of acetic acid was in fact harvested from this hybrid system over several days with light-dark cycles (175).

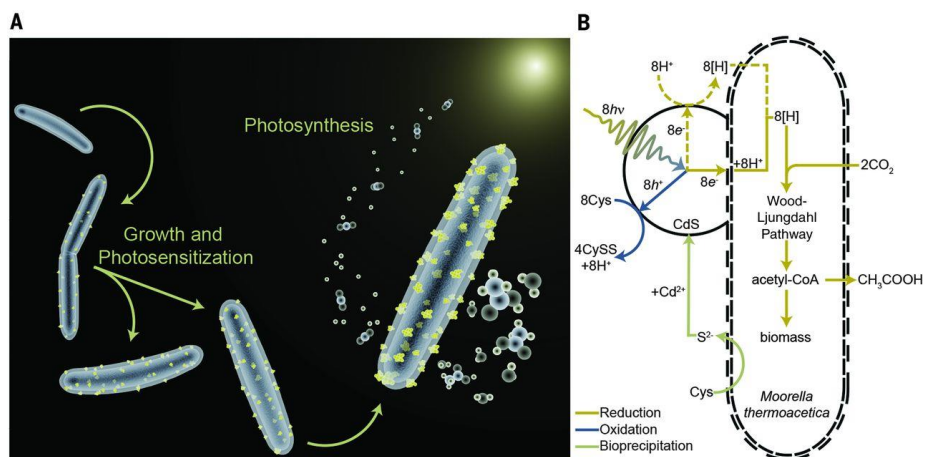


Figure 1.27. *M. thermoacetica*–CdS reaction schematics. (A) Depiction of the *M. thermoacetica*–CdS hybrid system, proceeding from the growth of the cells and bioprecipitation (loading) of the CdS NPs (shown in yellow) through photosynthetic conversion of CO_2 (center right) to acetic acid (right). (B) Pathway diagram for the *M. thermoacetica*–CdS system. Two possible routes to generate reducing equivalents, $[\text{H}]$, exist: generation outside the cell (dashed line) or generation by direct electron transport to the cell (solid line). Reproduced from ref. (175) with permission.

1.3.6 Outlook

In summary, biogenic nanocatalysts are small, well-dispersed, environmentally friendly, biocompatible, narrow-sized, and of low cost. In addition, some morphologies and properties are exclusive to biogenic nanocatalysts. However, there are also limitations on the biosynthesis of nanomaterials including nanocatalysts. Compared to their well-developed chemical synthesis counterparts, current biosynthesis of nanocatalysts are normally trial-and-error efforts, especially regarding morphology and structure control. The challenges of biosynthesis of nanocatalysts come from the complexity of biological processes. Different organisms, for example, bacteria, fungi, yeasts, and even plants are able to achieve biosynthesis, but even for the same microorganisms, the processes proceed differently in different growth phases. The main contributing parts in biosynthesis are proteins, enzymes, polysaccharides, and specific functional groups in the cell membrane (such as carboxylate groups), most of which evolve during the lifetime of microbes. Another challenge is the scaling-up of the biosynthesis. Most biosynthesis is in the millimole scale, as a high concentration of metal ions can harm the microbes or inhibit the biosynthesis. Moreover, the biosynthesis of nanomaterials under mild temperature is time-consuming and unlikely to be accelerated by higher temperature and pressure as in chemical synthesis. The low concentration and relatively long synthesis time are bottlenecks for large-scale synthesis of biogenic nanocatalysts.

Considerable research efforts are needed to further explore the potential of biogenic nanocatalysts, with a focus on several key directions. First, the complete biosynthesis processes need to be mapped in detail, addressing, for example, whether or not metal ions pass through the outer cell membrane and which specific components of the microorganism (organelles, protein complexes, DNA) are key players in the biosynthesis. The answers to these questions offer clues to the synthesis sites of biogenic nanocatalysts, the constituents of the nanocatalysts, and the genes involved in the synthesis processes. Secondly, efforts should also be spent on exploring and designing applications for nanocatalysts. The main advantages of nanocatalyst synthesis and operations are mild experimental conditions, self-replication, and self-rehabilitation, but they are also fraught with low yields and long synthesis durations. A suitable application should make use of the advantages of biogenic nanocatalysts and avoid the disadvantages. Finally, subsequent treatments should be considered to overcome the shortcomings of biogenic nanocatalysts. Biosynthesis is therefore not the end of the synthesis process. Instead, the biogenic nanocatalysts act as precursors, and further processes should be mobilized to optimize the morphologies and structures of the nanocatalysts, aiming at better performance.

1.4 Conclusions

In this chapter, we have introduced the principles of EET and its great impact on the environment, the applications of BESs, and an emerging nanomaterials synthesis method—microbial biosynthesis. The outward EET mechanism come becomes clearer as more investigations carried out, especially in *S. oneidensis* MR-1 and *Geobacter sulfurreducens*. Cytochromes *c* are critical in the EET of *S. oneidensis* MR-1. In fact, all of three EET pathways of *S. oneidensis* MR-1 link with cytochromes *c*. However, only six of 39 cytochromes *c* have been investigated and the others remain unknown. On the other hand, inward EET of EAB, which is another aspect of EET, are inexplicit. More efforts should be taken to illustrate the functions of the unexplored cytochromes *c* and other possible EET forms of EAB, including inward EET. For microbial biosynthesis, different NPs have been obtained with different microbes and different applications using these NPs have been attempted. Most of studies using artificial medium with addition of desired metals or metalloids as well as buffers. To synchronously achieve microbial biosynthesis and environmental remediation, experimental condition close to actual wastewater should be applied.

To broaden the horizons of BESs, we use the model EAB, *S. oneidensis* MR-1, to probe other potential EET forms of EAB. Moreover, to advance achieve microbial biosynthesis and environmental remediation, we aim at achieving these two goals under experimental conditions realistic scenarios.

Chapter 2

Methodology

This chapter provides an overview of the main techniques used in the project. Various electrochemical techniques are the main tools to probe the EET. Microscopic techniques are mainly for the morphology characterization of bacteria and electrodes. The primary purpose of spectroscopic techniques is to quantify elements or bacteria. Fundamental principles of these techniques are presented in this chapter and following discussions in the following chapters.

2.1 Electrochemical techniques

2.1.1 Cyclic voltammetry

A three-electrode system is an extensively used platform for electrochemical experiments. The three-electrode system is made up of a working electrode (WE), a reference electrode (RE), and a counter electrode (CE) which is also termed auxiliary electrode (Figure 2.1A). All three electrodes are immersed in supporting electrolyte. Target reactions occur at the WE surface. The WE is normally made of inert metal (platinum, gold, silver, *etc.*) or carbon materials, such as graphite and glassy carbon. The main role of the RE is to provide reference for the applied WE potential. The RE, therefore, requires a stable and well-known potential. Examples of RE are standard hydrogen electrode (SHE), saturated calomel electrode, Ag/AgCl electrode, mercury-mercurous sulfate electrode, and reversible hydrogen electrode. The CE with a large area is also made of inert and conductive materials, for example, carbon, gold, and platinum. During electrochemical experiments, the current between the WE and CE is measured, and the potential is applied to WE against RE. Coupled with desired reactions on the WE surface, the oxidation or reduction of electrolyte take place at the CE surface to complete a closed circuit. The reactions on the CE surface are of less importance, but in some cases, the isolation of CE is needed to avoid interference with the reactions on WE. The products of the reactions on WE may also interact with CE and the local pH around WE may be affected by the CE reactions if the CE and WE are very close. Moreover, the effective surface area of CE needs to be

much larger than that of WE to ensure low current density and prevent the reactions on CE limiting the current. The current through RE should be minimal to maintain a stable potential. The RE must be close to the WE to minimize the ohmic potential drop (IR drop) and, therefore, guarantee precise potential. The supporting electrolyte is not electrochemically active in the desired potential window. The main functions of the electrolyte are to decrease IR drop, enhance mass transfer of electroactive species, and stabilize pH and ionic strength (224). Common supporting electrolytes are KNO_3 , KCl , phosphate buffer, *etc.*

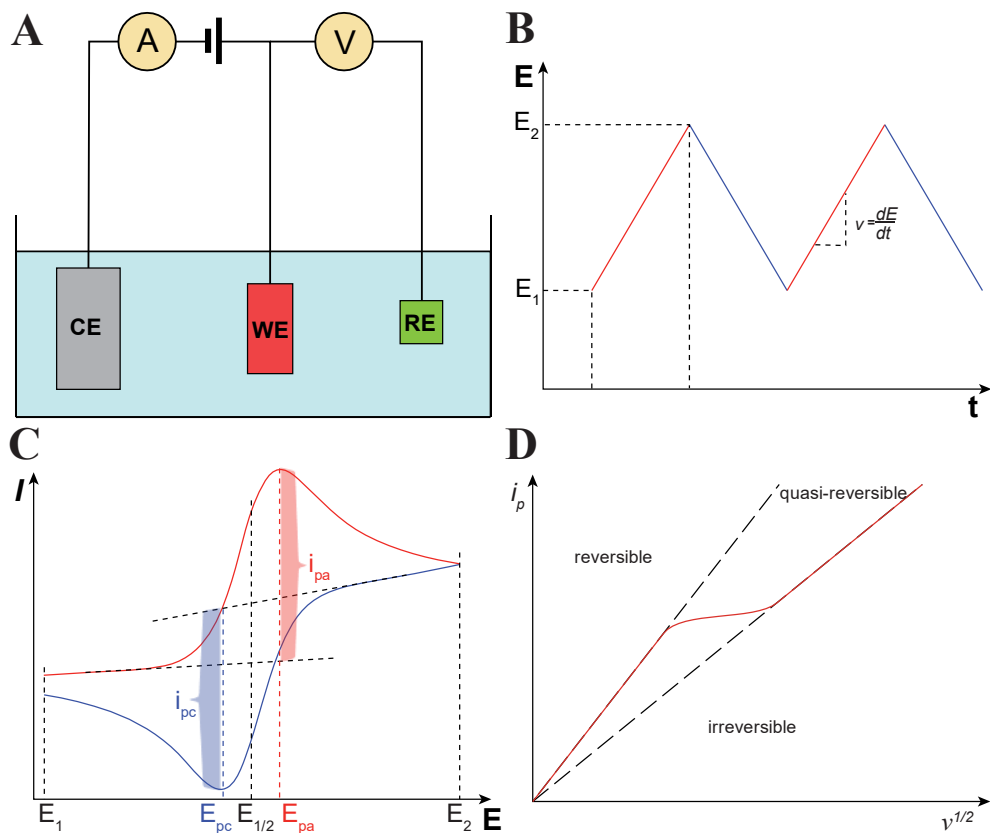


Figure 2.1. Electrochemical platform and cyclic voltammetry. (A) Scheme of three-electrode system. (B) Typical time-potential profile of cyclic voltammetry. (C) Cyclic voltammetry of a reversible electrochemical reaction and related parameters. E_1 and E_2 are identical in (B) and (C). (D) A plot of the dependence of the peak current (i_p) on the square root of the potential sweep rate ($v^{1/2}$).

Cyclic voltammetry (CV) is a versatile electrochemical technique, in which the current is monitored while the potential is swept periodically between low potential (E_1) and high potential (E_2) (Figure 2.1B). The scan rate is reflected by the slope in the time-potential plot (Figure 2.1B). A CV is plotted current (I) or current density (J) against potential (E).

In reversible reactions, diffusion is the slowest step (225), which means the electron exchange rate on the surface of WE is much faster than the rate of mass transport of the analyte, and so Nernstian equilibrium is established throughout the CV scan. A representative CV of a reversible electrochemical reaction with symmetric shape is shown in Figure 2.1C. Anodic current is obtained when the potential is scanned from low potential to high potential (*i.e.*, from E_1 to E_2); the height from highest current to background current is denoted as anodic peak current (i_{pa}), and the corresponding potential as anodic peak potential (E_{pa}). Similarly, when the potential is swept from E_2 to E_1 , these parameters are cathodic current, cathodic peak current (i_{pc}), and cathodic peak potential (E_{pc}). The mean of E_{pa} and E_{pc} is called the midpoint potential ($E_{1/2}$), *i.e.*, $E_{1/2} = (E_{pa} + E_{pc})/2$. The difference between E_{pa} and the E_{pc} is termed peak-to-peak potential separation (ΔE), *i.e.*, $\Delta E = E_{pa} - E_{pc}$. $\Delta E = 59/n$ (mV) for reversible reactions, where n is the number of electrons exchanged in the reaction. $E_{1/2}$ is close to the standard potential (E^0). The peak current (i_p) of electrochemically reversible reactions is proportional to the concentration of analyte and the square root of scan rate and can be expressed by Randles-Sevcik equation (225):

$$i_p = 0.4463nAF C \left(\frac{nFvD}{RT} \right)^{1/2} \quad (2.1)$$

A simpler numerical form is obtained at 25°C:

$$i_p = (2.69 \times 10^5) n^{3/2} A C D^{1/2} v^{1/2} \quad (2.2)$$

A is the geometrical area of the WE (cm^2), F the Faraday's constant ($96,485 \text{ C} \cdot \text{mol}^{-1}$), C the molar concentration of bulk analyte ($\text{mol} \cdot \text{cm}^{-3}$), v the scan rate ($\text{V} \cdot \text{s}^{-1}$), D the diffusion coefficient of the analyte ($\text{cm}^2 \cdot \text{s}^{-1}$), R the gas constant ($8.314 \text{ J} \cdot \text{K}^{-1} \cdot \text{mol}^{-1}$), and T the temperature (K).

If the rate of mass transport is comparable to the rate of electron transfer, the reaction is totally irreversible, and the peak current is expressed as (224):

$$i_p = 0.496 \alpha^{1/2} n A F C \left(\frac{n F v D}{R T} \right)^{1/2} \quad (2.3)$$

A simpler form at 25°C:

$$i_p = (2.99 \times 10^5) \alpha^{1/2} n^{3/2} A C D^{1/2} v^{1/2} \quad (2.4)$$

where α is the transfer coefficient, which represent the ratio between the height change of energy barrier overcome by the electron to the change of electrode potential (226).

Commonly, reversible electrochemical reactions turn to be irreversible at a high scan rate, with the behavior denoted as a quasi-reversible in the intermediate stage, (Figure 2.1D). One evident feature of totally reversible reactions is the complete absence of a reversible peak and

shows an asymmetric shape in CVs. However, the absence of a reversible peak can also be the consequence of a fast subsequent chemical reaction (225).

2.1.2 Differential pulse voltammetry

CV is a powerful and versatile technique to investigate the kinetics and the reversibility of electrochemical reactions. However, CV also suffers from the interference of capacitive background current and it is difficult to interpret weak signals. A more sensitive electrochemical technique is differential pulse voltammetry (DPV), which can achieve a limit of detection about 10^{-7} M (224). The time-potential profile of DPV combines staircase and pulse voltammetry (Figure 2.2A). The current signal is sampled twice, *i.e.*, I_s is sampled before applying a pulse, and I_p is sampled before the end of the pulse. The difference between these current signals ($\Delta I = I_p - I_s$) is plotted versus the staircase potential (Figure 2.2B). The step potential is typically 10 mV or smaller, the pulse amplitude 50 mV, the pulse period 0.5~5 s, and the pulse width 5~100 ms. Normally, the pulse width is at least ten times shorter than the pulse period (224).

The high sensitivity of DPV is due to the compensation of background current. The current in voltammetry consists of Faraday and non-Faraday current. The Faraday current is caused by the reduction or oxidation of electrochemically active species on the WE surface. The non-Faraday current is mainly charging current. When the potential is shifted (*e.g.*, after applying a potential pulse), ions and electrons are rearranged to restructure the electrical double layer and generate charging current. The Faraday current and charging current behave differently. For diffusion-controlled electrochemical reactions, the charging current decreases exponentially with time, while the Faradaic current decays as a function of $1/t^{1/2}$ due to the consumption of electroactive species on the surface of WE, where t is time (Figure 2.2C). Charging current often dies away within one or two milliseconds, which is much faster than that of the Faraday current (224). The undesired charging current should be eliminated as much as possible. The current is therefore sampled right before the pulse ends. This is the basis for all the pulse voltammetry.

Despite the high sensitivity in analytical electrochemical experiments, DPV for mechanistic and kinetic studies is still challenging, the main reason is the delay between the potential pulse and current measurement in the electrochemical workstations.

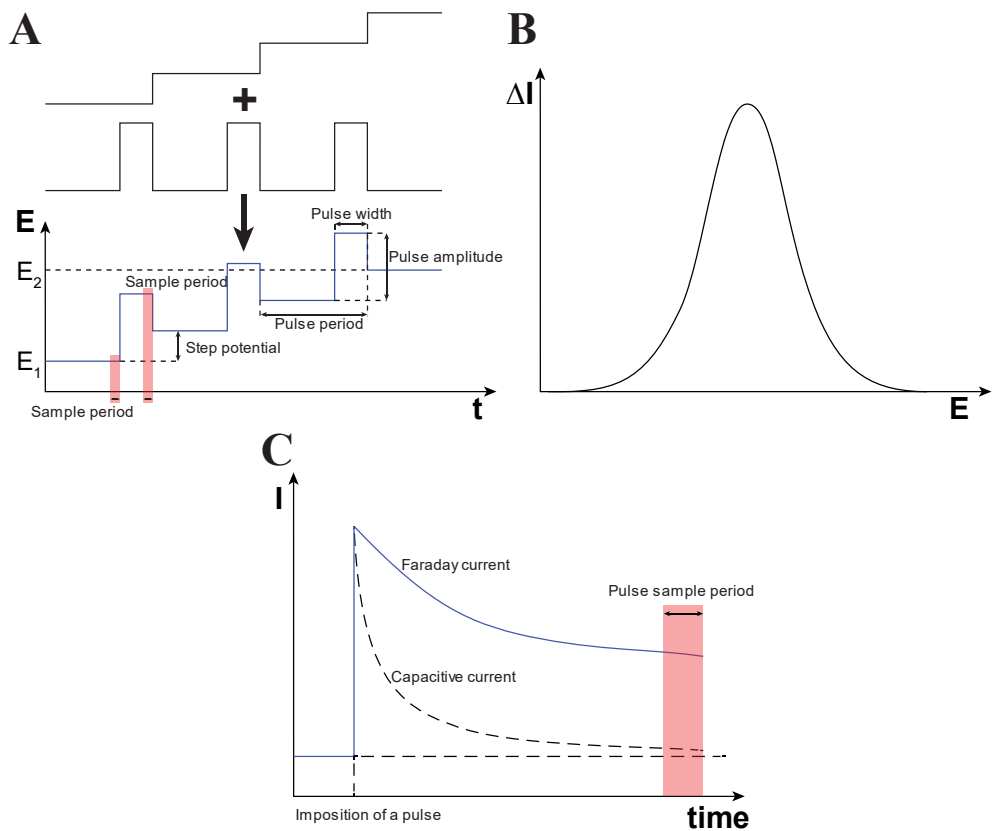


Figure 2.2. Principle of DPV. (A) Schematic pulses waveform superimposed on a staircase. (B) Typical DPV profile. (C) The difference in Faraday current and capacitive current and sample period in potential pulsing in diffusion-controlled electrochemical reactions.

2.1.3 Chronoamperometry

In chronoamperometry, the potential is firstly held on a potential (E_1), for example, the open circuit potential (OCP), where no electrochemical reaction occurs. Then the potential is shifted to a different potential (E_2) and the current response recorded (Figure 2.3A). Different I-t responses appear depending on different analyte added and on the new potential (E_2). If the reaction is diffusion-controlled at E_2 , the current decays as the Cottrell equation indicated and curve a in Figure 2.3B (225):

$$|I| = \frac{nFAD^{1/2}C}{\pi^{1/2}t^{1/2}} \quad (2.5)$$

where t is the time after the shift of potential.

If the standard rate constant of the electrochemical reaction of an analyte is small, or the overpotential from E_2 is low, the I-t response will behave as curve b in Figure 2.3B. In a transitional situation between curve a and b, the curve c is exhibited Figure 2.3B.

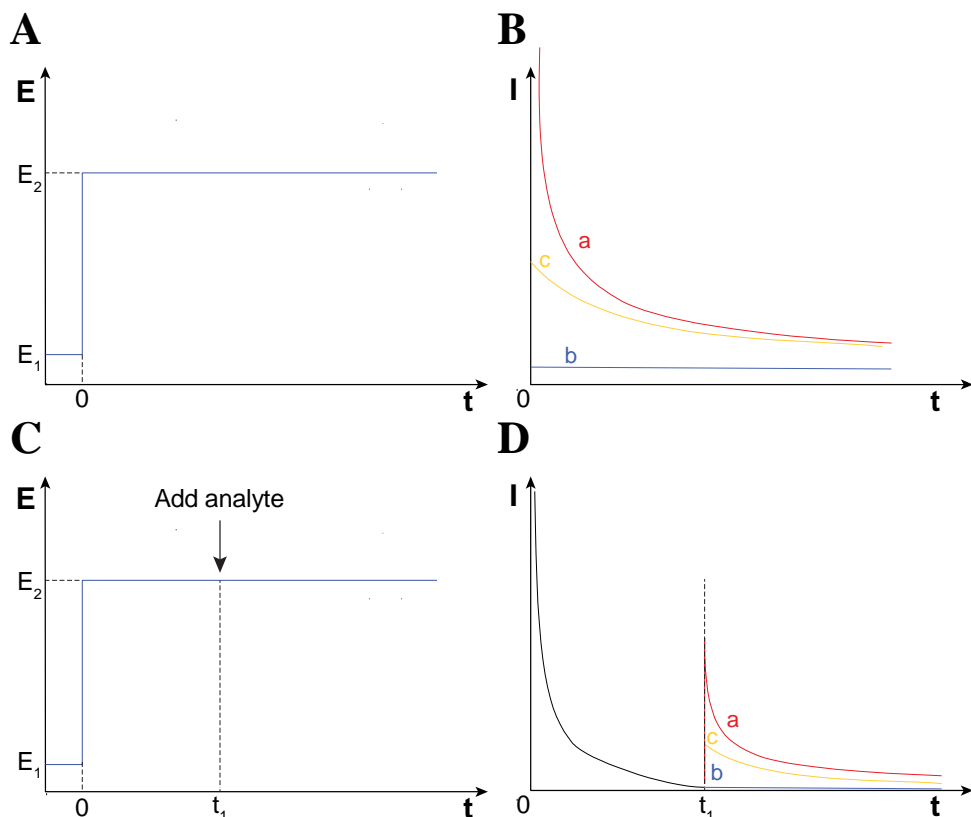


Figure 2.3. Scheme of chronoamperometry. (A) waveform of chronoamperometry. (B) I-t curve of chronoamperometry. In curve a, the reaction is diffusion controlled; in curve b, the reaction is kinetically controlled; in curve c, the reaction is intermediate between a and b, i.e., mixed controlled. (C) One application of chronoamperometry. The WE is immersed in supporting electrolyte and a potential pulse imposed. At t_1 , a certain amount of analyte is added into the electrochemical cell. (D) Different I-t responses after the addition of the analyte.

Different I-t response in chronoamperometry can be interpreted to evaluate the overpotential of different WEs towards a specific analyte. To do this, each WE is immersed in supporting electrolyte and E_2 is applied. After the charging current dies away and the current is stable, a certain amount of specific analyte is added into the supporting electrolyte and the current response is monitored. By comparing different current response (e.g., the maximum current height and the number of electrons transferred), different overpotentials for the WE towards a specific reaction under E_2 can be monitored and a current/overpotential conclusion constructed.

2.2 Microscopic techniques

2.2.1 Scanning electron microscopy

Scanning electron microscopy (SEM) is a powerful microscopy using a focused electron beam to image the surface of a sample. A very wide magnification from 10 to 500,000 can be achieved, and a resolution as high as 0.4 nm is realized by an SEM from Hitachi High-Technologies. The principle of SEM is shown in Figure 2.4. SEM contains three main components: electron gun, vacuum, and column (including lens system, scanning coil, stigmator, sample holder, and detector) (227). The role of the electron gun is to generate a strong, stable, and concentrated current. Two types of electron gun have been widely employed: thermionic emitters and field emission emitters (228). The thermionic emitters generate electrons by heating a filament, which is typically made of tungsten or lanthanum hexaboride. The current generation in field emission emitters is realized by applying a strong electrical potential gradient on a tungsten wire with a sharp tip. The electrons generated from the electron gun, which serves as a cathode, are accelerated by the high voltage drop (0.2 keV ~ 40 keV) between the electron gun and the anode below. The lens system focuses and ejects the electron beam onto the surface of the sample. The diameter and position of the electron beam are controlled by objective lens and scanning coils. The vacuum system guarantees a high vacuum in the column, which is critical to the transmission of the electron beam.

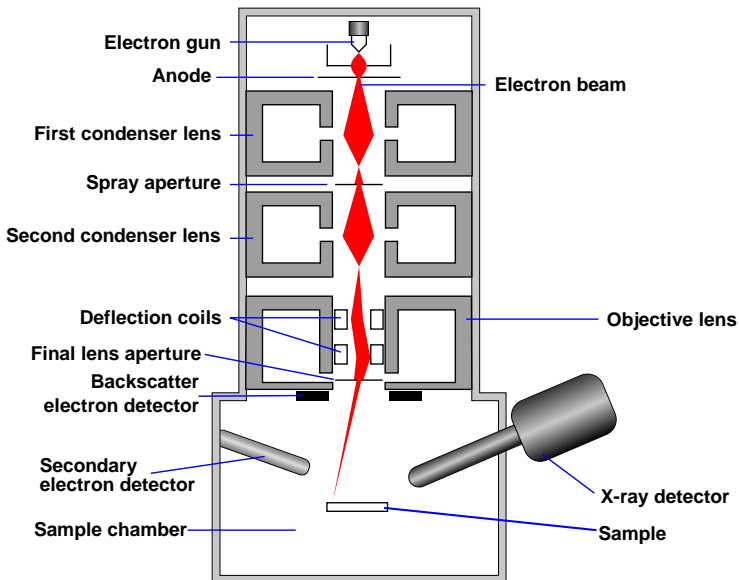


Figure 2.4. Schematic representation of SEM

When the electron beam is cast on the surface of the sample, it interacts with the sample within a teardrop-shaped volume called interaction volume (Figure 2.5) (229). Different electrons and X-rays are emitted from the interaction. The most useful electron in SEM imaging is the secondary electrons and the backscattered electrons. The former are detected by a so-called Everhart-Thornley detector and responsible for the topographic imaging. To get enough secondary electrons, non-conductive samples need to be coated with a conductive layer, for example, gold, platinum, or carbon. The latter is detected by a backscattered electron detector and provides atomic number contrast. Moreover, the characteristic X-ray is the base for energy-dispersive X-ray spectroscopy and provides elemental composition and mapping of the sample.

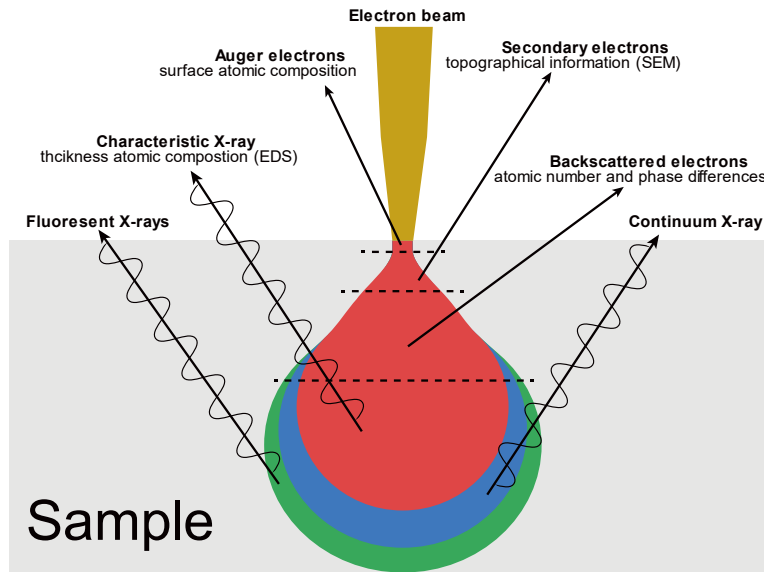


Figure 2.5. Interaction volumes of the sample in electron microscopy.

2.2.2 Transmission electron microscopy

Another highly useful electron microscopy is transmission electron microscopy (TEM) which uses a parallel beam of electrons with high energy to transmit through thin samples to generate images (Figure 2.6). TEM is crucial to the study of morphological, structural, chemical, and electrical properties at an atomic scale and widely used in materials science (especially in nanoscience and nanotechnology), and in environmental, biological, and medical science. The main components of TEM are electron gun, electron lens system, vacuum system, and apertures. The electron gun emits an electron beam and can be categorized into two types just like the electron gun in SEM: thermionic emission guns and field emission guns. The primary function of the electron lens system is to focus the electron beam at certain focus distance which is similar to optical lens. The vacuum

system creates a high vacuum, conventionally of an order of 10^{-4} Pa and can be as high as $10^{-7} \sim 10^{-9}$ Pa at high-voltage operation. A high vacuum is important to prevent the generation of an electrical arc, contamination and distortion of the electron beam, and to keep samples clean. Apertures are thick metallic disks with holes through which electrons flow and the electrons further than a certain distance to the optical axis are stopped. The apertures can help users to choose desired electrons and prevent the contamination to samples (230).

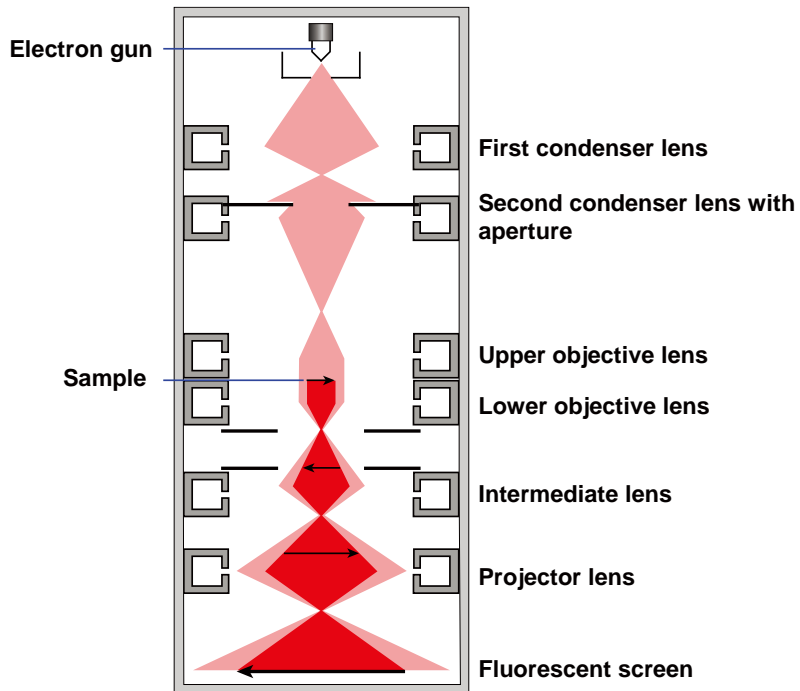


Figure 2.6. Schematic representation of TEM.

Different from SEM, TEM collects transmitted electrons for imaging (Figure 2.7). The sample thickness is therefore normally less than 100 nm, which is unnecessary for SEM samples. On the other hand, the conductivity is not required in TEM and, therefore, coating with a conductive layer on non-conductive samples is not needed. TEM can obtain a much higher resolution than SEM and a single column of atoms can be observed in TEM images. The contrast of TEM originates from mass-thickness contrast, diffraction contrast, phase contrast, and Z contrast (230).

The initial application of TEM is imaging. With the development of the technology, various other applications have emerged (Figure 2.7). Another mode of TEM is selected area electron diffraction (SAED) with which diffraction patterns of desired positions on samples can be observed. With aberration correctors, high-resolution transmission electron microscopy (HREM or HRTEM) can achieved a resolution of 0.05 nm (231). TEM, 50

HRTEM, and SAED collect elastic signals, but inelastic signals are also used nowadays. Scanning transmission electron microscopy (STEM) utilizes a focused electron beam as a probe to scan samples and the contrast only depends on the atomic number. STEM is very useful for energy-dispersive spectroscopy (EDS). Energy-filtered transmission electron microscopy (EFTEM) and electron energy loss spectroscopy (EELS) utilize the difference in energy of electron beam after interacting with samples.

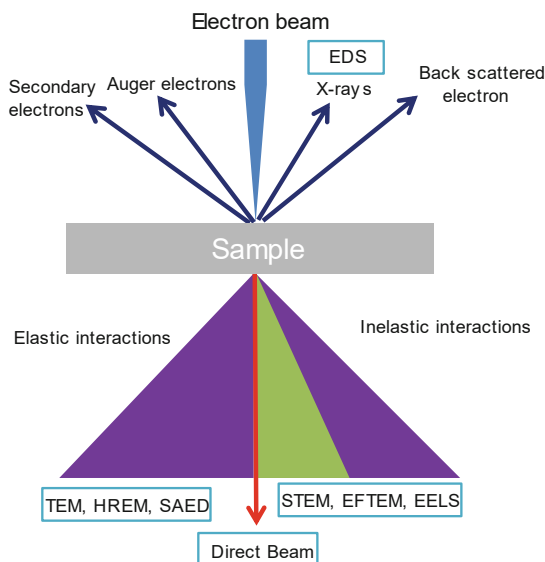


Figure 2.7. Overview of different electron interactions with sample and corresponding techniques in TEM using specific interaction. EDS, energy-dispersive X-ray spectroscopy; HREM, high-resolution transmission electron microscopy; SAED, selected area electron diffraction; STEM, scanning transmission electron microscopy; EFTEM, energy-filtered transmission electron microscopy; EELS, electron energy loss spectroscopy. Reproduced from ref. (230) with permission.

2.2.3 Atomic force microscopy

Atomic force microscopy (AFM) is a type of scanning probe microscopy based on the change of various forces between the tip and samples. A scheme of AFM is presented in Figure 2.8. The main components of AFM are laser, piezo, cantilever, tip, and photo detector. During measurement, a sharp tip (typically the radius of curvature is several nanometers) fixed on the free end of the cantilever is placed very close to the surface of samples. The cantilever together with the tip are then accurately moved in x, y, and z direction by the piezoelectric element. A laser beam is cast on the cantilever and the reflected laser beam recorded by the photo detector. The cantilever bends due to the interaction between the tip and the surface of the sample and results in the shift of the laser. AFM can provide atomic resolution and three-dimensional information of samples. The coating of samples and high vacuum is not needed to AFM, and biological samples

can be well-preserved during measurement. Moreover, AFM can be operated in ambient conditions and even liquid environment.

Three main functions of AFM are widely exploited: imaging, force measurement, and manipulating. AFM imaging is achieved by moving the tip around the surface of the target samples and recording the height at atomic resolution. In force measurement, a force-distance curve is generated by moving the tip towards and away from the sample surface. A force change in the nano newton scale can be detected. The manipulation by AFM is an emerging field and can position a single molecule or even a single atom at room temperature (232).

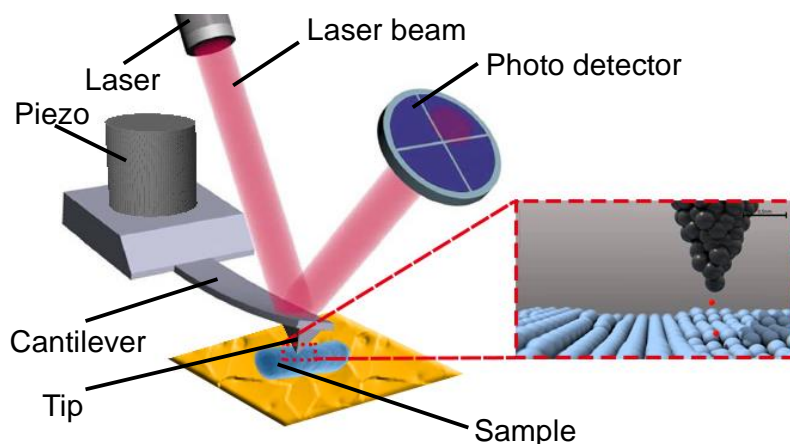


Figure 2.8. Schematic representation of AFM

2.3 Spectroscopic techniques

2.3.1 Ultraviolet-visible spectroscopy

Ultraviolet-visible spectroscopy (UV-Vis) is a quantitative technique that records the absorption or reflectance of the light in visible and near-ultraviolet regions. A brief scheme is shown in Figure 2.9. When light travels through materials (*e.g.*, solution, transparent solid, and gas), the absorption of light by the materials reflect the properties of the materials which can be expressed by Beer-Lambert law (233):

$$A = \varepsilon cL = \lg\left(\frac{I_0}{I}\right) \quad (2.6)$$

where A is absorbance (arbitrary unit, a.u.), ε molar absorptivity ($\text{L}\cdot\text{mol}^{-1}\cdot\text{cm}^{-1}$), c the concentration of analyte ($\text{mol}\cdot\text{L}^{-1}$), L the light path length (cm), and I_0 and I the intensity of incident and transmitted light respectively. For a specific measurement, ε and L are constant, and hence c proportional to A . A and c can be therefore interpreted by measuring I_0 and I .

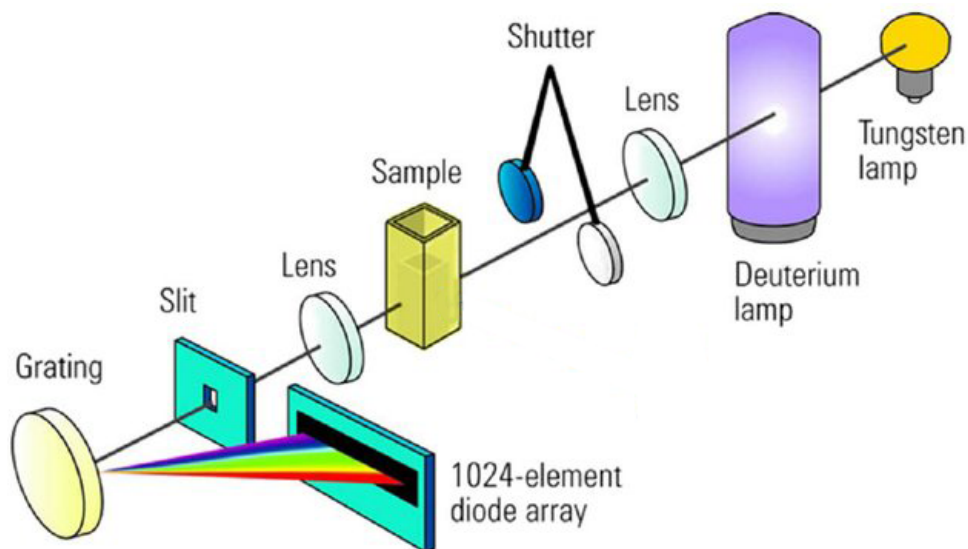


Figure 2.9. Schematic representation of UV-Vis. Reproduced from ref. (234).

Similar to the ions in solution, bacteria in media also scatter light. The change in cell number can therefore be recorded with UV-Vis (1). UV-Vis is very fast and non-invasive. Different wavelengths have been reported to evaluate biomass, for example, 420, 590, 600, 600 nm, *etc* (235). Note that during the measurement of biomass by UV-Vis, the values do not necessarily match the specific amount of cells. The primary goal is to track the growth phase of bacteria, which is very important since bacteria behave differently in different growth phases.

2.3.2 Energy-dispersive X-ray spectroscopy

Energy-dispersive X-ray spectroscopy (EDS or EDX) is an analytical technique that emits charged particles with high energy to hit samples and collect characteristic X-rays and obtain the elemental composition. The main compounds of EDS are an excitation source, an X-ray detector, a pulse processor, and an analyzer. The charged particles can be electrons, protons, or X-rays. When charged particles from the excitation source bombard a sample, the electrons in an inner shell of the atoms of the sample can be kicked out and create holes. An electron in an outer shell can then jump and fill the hole (Figure 2.10). The transmission of the electron in the outer shell (high energy) to the inner shell (low energy) creates an energy difference and can generate X-rays. The two shells and atomic structure are unique to elements and, hence, the X-rays are characteristic. The characteristic X-rays are recorded and transferred to electric signals by the X-ray detector. The electric signals are then measured by the pulse processor and passed to the analyzer for recording, analysis, and display.

EDS can be seamlessly integrated into other techniques, such as SEM and TEM/STEM and record elemental mapping at nanoscale (Figure 2.7). When interacted with SEM, qualitative and quantitative chemical information of the surface of samples is accessible (229). The chemical information of bulk samples can be obtained when EDS is integrated with TEM/STEM, or by X-ray fluorescence spectrometry.

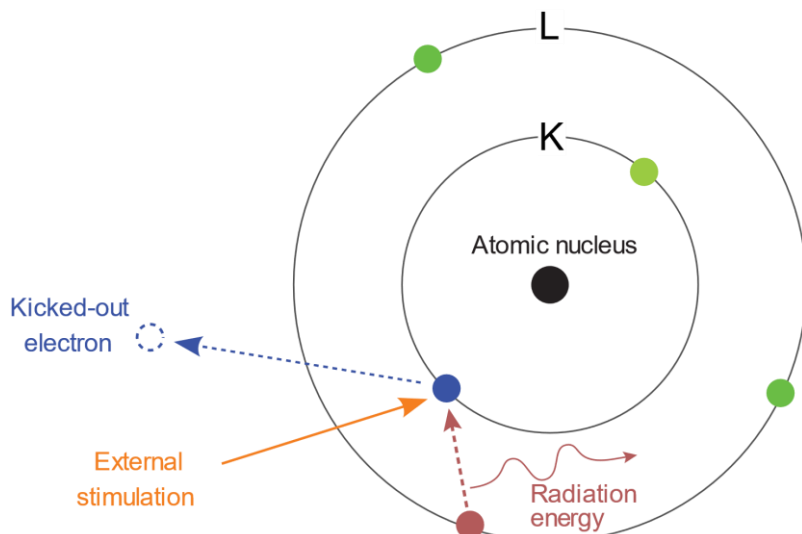


Figure 2.10. A brief principle of EDS.

2.3.3 Inductively coupled plasma optical emission spectroscopy

Inductively coupled plasma optical emission spectroscopy (ICP-OES) is also called inductively coupled plasma atomic emission spectroscopy (ICP-AES). ICP-OES is an analytical technique that uses plasma to stimulate atoms and ions and quantify these elements by measuring the electromagnetic radiation from excited atoms and ions. ICP-OES contains two main parts: the ICP part and the optical spectrometer. Differently from EDS, ICP-OES uses an intense electromagnetic field to create a stable plasma with high temperature (around 7000 K) containing argon and electrons (Figure 2.11). The nebulized sample is next introduced into the core of the plasma. The sample is broken into corresponding atoms and the atoms undergo a cycle between the ground and excited states and emits radiation with characteristic wavelengths. The radiation is finally recorded by the optical spectrometer.

ICP-OES applies to a high dynamic concentration range (236), from $0.5 \text{ ng}\cdot\text{L}^{-1}$ to hundreds of $\text{mg}\cdot\text{L}^{-1}$ depending on elements. Up to 70 elements can be measured simultaneously in one sample analysis. However, ICP-OES is unable to determine some elements such as hydrogen, nitrogen, oxygen, etc. ICP-OES is also a “wet” sampling method, and so solid samples must be digested or dissolved into solution to be determined.

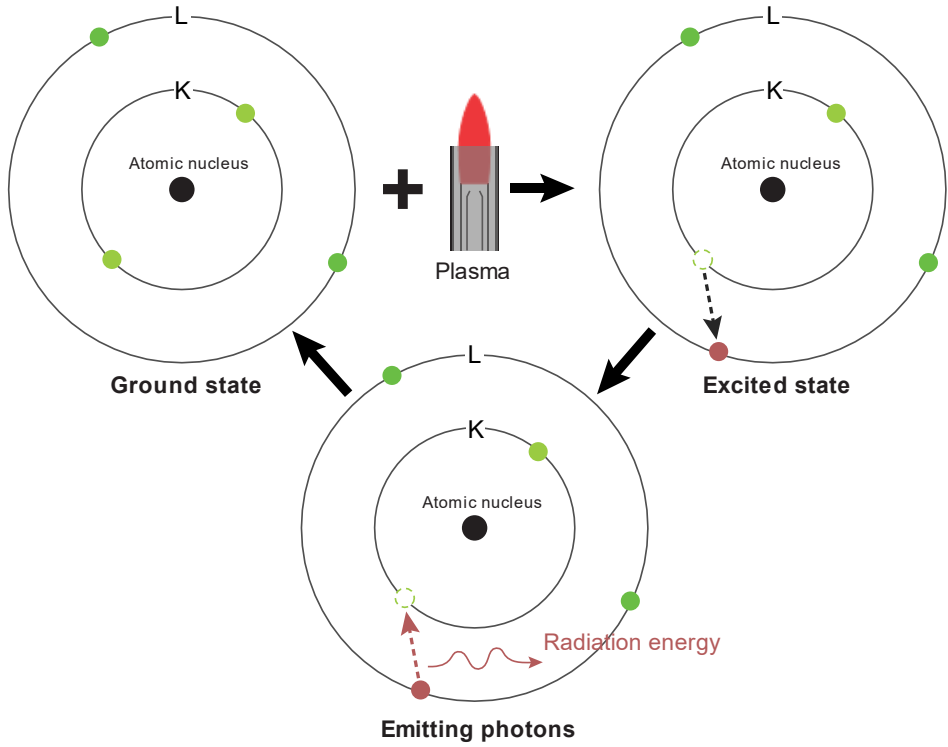


Figure 2.11. A brief principle of ICP-OES

Chapter 3

Selective electrooxidation catalyzed by

S. oneidensis MR-1

This chapter describes an unconventional phenomenon—a oxidation of redox molecules by a metal-reducing bacterium *S. oneidensis* MR-1. The efficiency, selectivity, scan rate and concentration dependence are detailed. The function of riboflavin, EPS, and *in vitro* cytochrome *c* are discussed. The mechanism of the electrocatalytic oxidation will be discussed in Chapter 4.

3.1 Introduction

Extracellular electron transfer (EET) has been widely investigated due to the application of bioelectrochemical systems (BESs) in biosensors (76, 237) and energy harvest (199, 238, 239). A deep understanding of the mechanism of BESs is a pre-requisite of optimized performance of the applications. In EET, electrochemically active bacteria (EAB) exchange electrons with external redox compounds, electrodes or even other microorganisms *via* short-range direct electron transfer (ET) through redox proteins on the cell membrane, long-range ET through conductive nanowires, and indirect ET through mediators (11, 80, 125, 240, 241).

In addition to outward EET, *e.g.* the reduction of insoluble Fe(III)/Mn(IV) (hydr)oxides by EAB (such as MR-1 and *Geobacter sulfurreducens*) (242-244), inward EET, in which microbes take electrons from electron donors in the environment and transport the electrons into the cells, has also been reported. An iron-oxidizing photoautotroph *Rhodospseudomonas palustris* TIE-1, for example, is able to accept electrons from an electrode poised at +100 mV vs. standard hydrogen electrode (SHE), coupling with the reduction of carbon dioxide (98). Moreover, an outer membrane-bound cytochrome *c* C_{yc2} is regarded as the first electron acceptor in the iron respiratory chain of the acidophilic bacterium *Acidithiobacillus ferrooxidans*, with a redox potential of as high as 560 mV vs.

SHE (245). The outward EET of MR-1 can be reversed in OmcA–MtrCAB pathway, *i.e.*, this pathway can transport electrons from electrodes into the cells (119). In addition, *Shewanella* strain 4t3-1-2LB with an ability to use metallic iron as the sole electron donor was discovered (246), but it is not clear whether MR-1 is able to directly take electrons from inorganic/organic compounds.

As a model EAB, the metal-reducing bacterium *Shewanella oneidensis* MR-1 (MR-1) transport electrons from the cells to extracellular electron acceptors, such as Cu(II) ions (158), thiosulfate (247), fumarate (248), nitrate (249), Mn(IV) oxides (250), and Fe(III) (hydro)oxides (89). Several cytochromes *c* in the cell membrane are involved in the EET of MR-1 by OmcA–MtrCAB respiratory pathway (251–253). First, CymA (an inner membrane cytochrome *c*) obtain electrons by oxidizing quinol, and the electrons are switched to MtrA (an inner membrane decaheme cytochrome *c*) *via* the periplasmic fumarate reductase FccA and a small tetraheme cytochrome. Secondly, the electrons are further delivered through a trans-outer membrane protein complex formed by MtrA, MtrB (a transmembrane protein), and MtrC to the surface of MR-1. Third, a complex of MtrC and OmcA (decaheme cytochromes *c* on the outer cell membrane) transfer the electrons to extracellular electron acceptors on the cellular surface (85, 101). Recently, MtrA is reported to fully extend through MtrB (254), so MtrA is possibly exposed to the environment when MtrC and OmcA are knocked out.

In this chapter, we find that MR-1 can take electrons from $[\text{Fe}(\text{CN})_6]^{4-}$ and catalytically electrooxidize $[\text{Fe}(\text{CN})_6]^{4-}$ to $[\text{Fe}(\text{CN})_6]^{3-}$. No such electrocatalysis is found in reference bacteria, for example, *Escherichia coli* K-12 and *Streptococcus mutans*. Interestingly, we notice that MR-1 electrocatalyzes only negatively charged redox molecules with a high midpoint potential, such as $[\text{Fe}(\text{CN})_6]^{4-}$ and $[\text{Ru}(\text{CN})_6]^{4-}$, among 12 redox molecules that include mediators (*e.g.*, riboflavin, $[\text{Ru}(\text{NH}_3)_6]\text{Cl}_3$, and resorufin). Crucial compounds (riboflavin, EPS, and cytochrome *c*) in the outward EET of MR-1 are also explored.

3.2 Experimental Section

3.2.1 Chemicals

Luria-Bertani broth (LB, 10 g L⁻¹ tryptone, 5 g L⁻¹ yeast extract, 5 g L⁻¹ NaCl), Na₂HPO₄·12H₂O (99~101%), Nafion DE 1021 (10%), KCl (≥ 99.0%), 6-Mercaptocaproic acid (90%), cytochrome *c* (from equine heart, > 95%), KH₂PO₄ (98~100.5%), NH₄Cl (≥ 99.5%), CaCl₂·2H₂O (99%), hydroxymethylferrocene (97%), and sodium DL-lactate (60%) were obtained from Sigma-Aldrich, Germany. Ferrocenecarboxylic acid (≥ 97.0% (Fe)) was from Sigma-Aldrich, China. Riboflavin (≥ 98%) and aminoferrocene (≥ 98.0%) were from Sigma-Aldrich, Japan. Hexaammineruthenium(III) chloride (98%), resorufin (Dye content 95 %), 1,9-Dimethyl-methylene blue zinc chloride double salt (Dye content 80%),

glucose ($\geq 99\%$), and potassium hexachloroiridate (technical grade) were from by Sigma-Aldrich, USA. Potassium hexacyanoferrate(II) trihydrate (99.0~102.0%) was from Merck, Germany. $\text{NaH}_2\text{PO}_4 \cdot 2\text{H}_2\text{O}$ ($\geq 99.0\%$), NaCl ($\geq 99.5\%$), and 2,2'-Azino-bis(3-ethylbenzothiazoline-6-sulfonic acid) diammonium salt ($\geq 98.0\%$) were supplied by Fluka, Germany. $\text{MgSO}_4 \cdot 7\text{H}_2\text{O}$ (99.8%) and potassium hexacyanoferrate(III) ($\geq 99.5\%$) were from Riedel-de-Haën, France. 1,1'-Ferrocenedicarboxylic acid ($> 97.0\%$) was obtained from Fluka, Switzerland. Potassium hexacyanoruthenate(II) hydrate (Ru 23.0% min) was from Alfa Aesar, USA. All chemicals were used as received. Aqueous solutions were prepared with MilliQ water (18.2 M Ω cm, arium® pro VF system, Sartorius AG, Germany).

3.2.2 Culture and collection of *S. oneidensis* MR-1

S. oneidensis MR-1 wild type (MR-1) and *S. oneidensis* MR-1 $\Delta\text{omcA}/\text{mtrC}$ mutant (MR-1 mutant) were original from Prof. K. H. Neelson at the University of Southern California (255) and further developed in Prof. Feng Zhao's lab at Institute of Urban Environment (IUE), CAS (164). These strains were introduced to Department of Chemistry, Technical University of Denmark in 2014. Briefly, strain medium (1.0 mL) was taken from 4°C refrigerator and added to Luria-Bertani broth (100 mL). The medium was incubated in a shaker controller at 30°C (for MR-1 and MR-1 mutant) or 37°C (for *E. coli* K-12) with a speed of 100 rpm for about 22 h. The bacteria were collected by centrifuging at 4000 rpm for 5 min. The bacteria were re-suspended in 50 mM phosphate buffered saline [PBS, pH 7.0; $\text{NaH}_2\text{PO}_4 \cdot 2\text{H}_2\text{O}$ (3.04 g L⁻¹), $\text{Na}_2\text{HPO}_4 \cdot 12\text{H}_2\text{O}$ (10.92 g L⁻¹)] following centrifugation. The resuspension and centrifugation were repeated three times to remove the excreta on the surface of the bacteria. Bacterial precipitate (5.0 μL) was mixed and cast on electrode surfaces (\O 4.0 mm), and dried in a fume cupboard at room temperature. Nafion solution (5.0 μL , 1%) was added to the bacterial precipitate before cast on the electrode surface for chronoamperometry.

3.2.3 Electrochemical measurements

Cyclic voltammetry (CV) was recorded using a potentiostat (Autolab PGSTAT12, Eco Chemie, Utrecht, The Netherlands) in a three-electrode mode. Glassy carbon electrodes (GCE) or gold electrodes (Au) and platinum grid were used as working electrode and counter electrode respectively. Before electrochemical experiment, working electrodes were polished with 1.0, 0.3, 0.05 μm Al_2O_3 slurries sequentially, and sonicated in MilliQ water for 1 min, and dried at room temperature. The reference electrode was an Ag/AgCl electrode with saturated KCl (0.197 V vs. Standard hydrogen electrode, SHE). The electrolyte was PBS (50 mM, pH 7.0). Oxygen in the electrolyte was removed by bubbling argon (High Purity 5N) for 30 min prior to measurement. CVs were recorded with a scan rate of 10 mV s⁻¹ (unless stated otherwise) and steps of 2 mV, starting from the open circuit potential unless otherwise specified. For differential pulse voltammetry (DPV), the

potential window was -0.6 V to 0.4 V vs. Ag/AgCl with a scan rate of 10 mV s⁻¹, 5 mV pulse increments, 25 mV pulse amplitude, and 50 ms pulse width. The electrochemical analysis was repeated in at least triplicate and typical results are presented.

3.2.4 Extraction of extracellular polymeric substances

The bacterial cells were cultured and harvested by centrifugation (4000 rpm, 10 min, 4°C) and washed twice with 0.9% NaCl (w/v) solution. Washed cell pellets were re-suspended in 0.9% NaCl solution and heated in a water bath at 38°C for 30 min. Cell suspensions were centrifuged again (4000 rpm, 10 min, 4°C) and cell pellets collected for electrochemical analysis. (80)

3.2.5 Coating of cytochrome *c* on gold electrodes

A freshly polished gold electrode (Au) was immersed in 1 mM 6-Mercaptocaproic acid ethanol solution overnight, followed by rinsing with MilliQ water. The resulting electrode was termed Au/6C-HS. The Au/6C-HS was transferred to cytochrome *c* (from equine heart) solution (40 μM in 50 mM PBS, pH 7.0) for adsorption overnight, obtaining Au/6C-HS/cyt-*C*. (256)

3.2.6 Coating of riboflavin on GCE

A mixture of 5 μL 30 mM dispersion of riboflavin and 5 μL 1% Nafion solution were mixed and cast on a freshly polished GCE. The modified GCE was dried in a fume cupboard at room temperature.

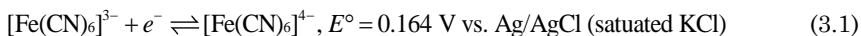
3.2.7 AFM mapping of the cells

Atomic force microscopy (AFM) was performed using an Agilent 5500 instrument (Agilent Technologies, Chandler, AZ, USA) equipped with a silicon nitride tip (DNP-S10, Bruker, USA) in contact mode in air under ambient conditions. One drop (4 ~ 10 μL) of sample dispersion was placed on a cleaned platinum sheet surface and dried in air at ambient temperature for at least four hours (80).

3.3 Results and discussion

3.3.1 Electrooxidation of [Fe(CN)₆]⁴⁻ catalyzed by MR-1 is highly selective and efficient

[Fe(CN)₆]^{4-/3-} is a redox couple with typical standard redox potential at 0.164 V vs. Ag/AgCl (all electrode potentials are measured against Ag/AgCl unless stated otherwise), according to the one-electron transfer reaction below:



Either $[\text{Fe}(\text{CN})_6]^{3-}$ or $[\text{Fe}(\text{CN})_6]^{4-}$ can exchange electrons with a bare electrode such as a glassy carbon electrode (GCE) or a gold electrode (Au) with fast and reversible oxidation of $[\text{Fe}(\text{CN})_6]^{4-}$ or reduction of $[\text{Fe}(\text{CN})_6]^{3-}$, presenting symmetric voltammetry (Figure 3.1 left). In fact, $[\text{Fe}(\text{CN})_6]^{3-}$ is extensively utilized as an electron acceptor added to cathodic chambers in bioelectrochemical systems (BESs) (20, 21, 257, 258). The reversibility and rate of electron transfer can be measured by peak-peak potential separation in cyclic voltammetry (CV) at a given scan rate (259). When an electrode surface is covered by an insulator or a less conductive layer, the interfacial electron transfer rate is reduced, with low current and broad peak-peak potential separation, or both redox peaks vanish. Electron transfer decreases exponentially with the increase of the layer thickness (260). As an example, the thickness of 6-Mercaptohexanoic acid is only about 1 nm, but the electrochemical signal from the cycling between $[\text{Fe}(\text{CN})_6]^{4-}$ and $[\text{Fe}(\text{CN})_6]^{3-}$ has been completely blocked (Figure 3.1 middle).

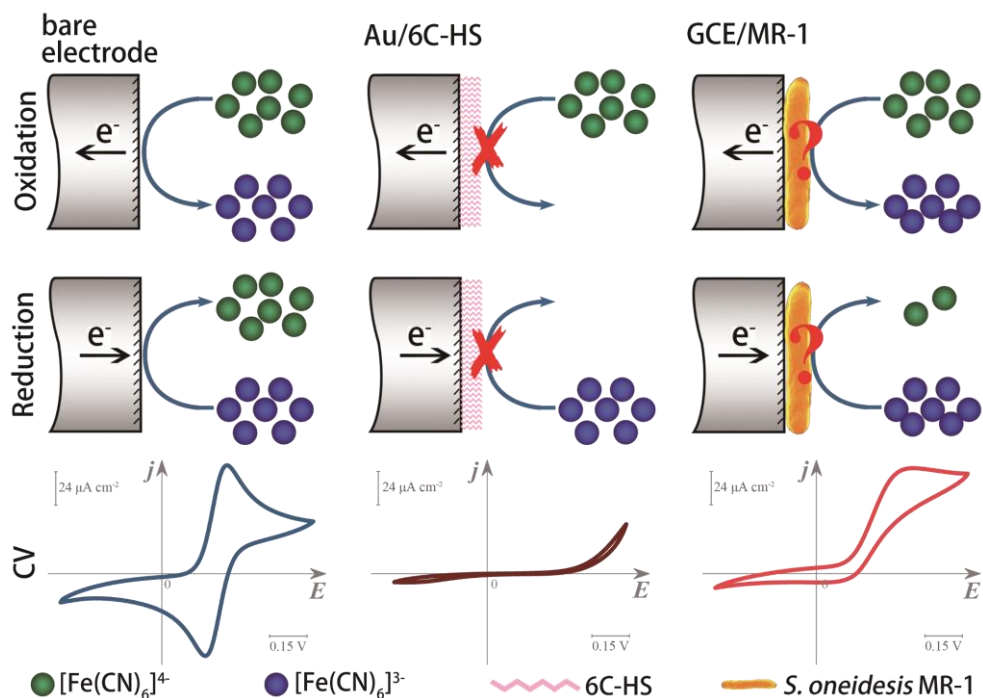


Figure 3.1. Conversion of $[\text{Fe}(\text{CN})_6]^{4-/3-}$ on different electrodes. Reversible conversion of $[\text{Fe}(\text{CN})_6]^{4-}$ to $[\text{Fe}(\text{CN})_6]^{3-}$ on a bare electrode (left), nonreversible conversion of $[\text{Fe}(\text{CN})_6]^{4-/3-}$ on a 6-Mercaptohexanoic acid modified gold electrode (Au/6C-HS, middle), and electrocatalytic oxidation of $[\text{Fe}(\text{CN})_6]^{4-}$ to $[\text{Fe}(\text{CN})_6]^{3-}$ on a MR-1 coated on GCE (GCE/MR-1, right). Scan rate 10 mV s^{-1} . Electrolyte $50 \text{ mM PBS (pH 7.0)}$.

Notably, a strong anodic voltammetric peak appears similar to that on bare electrode when MR-1 cells coat a GCE, but the cathodic peak almost vanishes (Figure 3.1 right). MR-1 is a model dissimilatory metal-reducing bacterium with a rod shape, as the cluster of MR-1 cells shows in atomic force microscopy (AFM) (Figure 3.2A). The length and diameter of MR-1 are in a range of 2~5 μm and 0.4~0.7 μm respectively, in agreement with the SEM and TEM analysis. Pili were sometimes found around the cells. Being physically attached on a GCE, the thickness of the MR-1 layer is at least the same as the monolayer of MR-1 cells, *i.e.*, 400 times larger than 1 nm. Moreover, after GCE was coated with Nafion, both anodic and cathodic peak current decrease to the same degree (Figure 3.3). The possible reason is that Nafion can prevent the anion ($[\text{Fe}(\text{CN})_6]^{4-}$) from reaching the electrode surface and slow the electrochemical reaction. The MR-1 cells efficiently relay the electrons from $[\text{Fe}(\text{CN})_6]^{4-}$ to the electrode compared to 6-Mercaptohexanoic acid. The enhanced electron transfer rate is responsible for the augmented anodic peak current (Figure 3.1 right). The asymmetric voltammetry pattern therefore suggests the electrocatalytic oxidation of $[\text{Fe}(\text{CN})_6]^{4-}$ by MR-1.

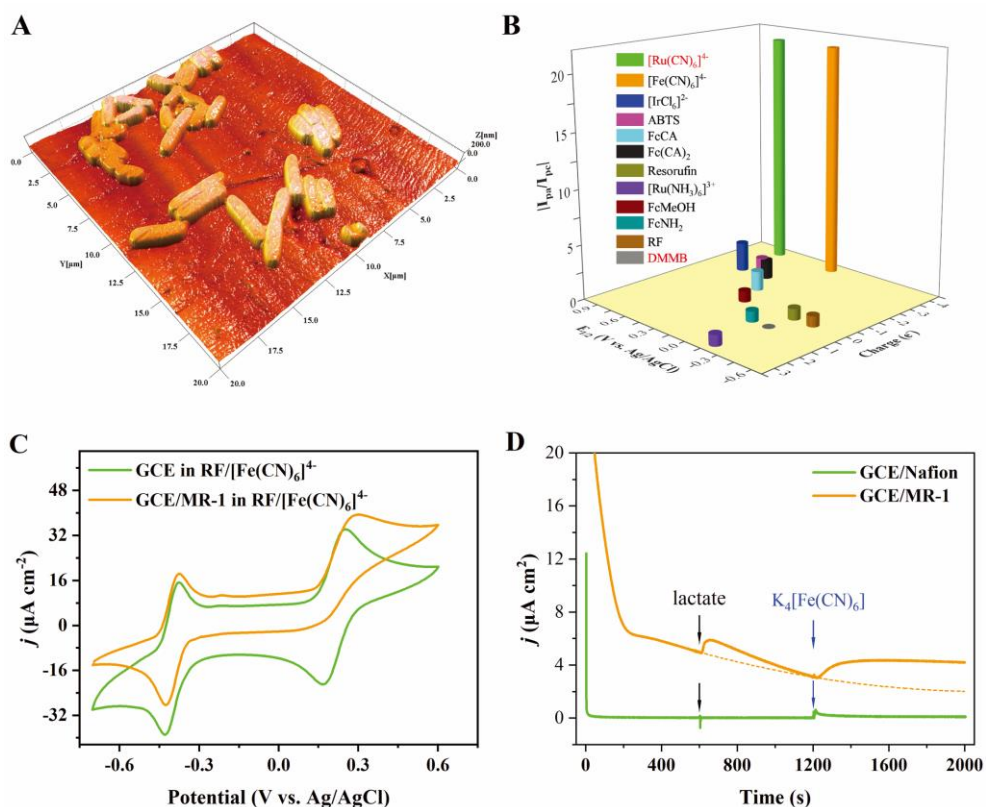


Figure 3.2. AFM mapping and electrochemical investigation of MR-1. (A) 3D AFM image of MR-1 cluster on a platinum sheet, with sub-monolayer to visualize individual cells. (B) Effects of midpoint

potential ($E_{1/2}$) and overall charge(s) of redox molecules on the ratio of anodic peak current to cathodic peak current on GCE/MR-1 ($|I_{pa}/I_{ca}|$). ABTS, azino-di-[3-ethylbenzthiazoline sulfonate (6)]; FcCA, ferrocenecarboxylic acid; Fc(CA)₂, 1,1'-ferrocenedicarboxylic acid; RF, riboflavin; FcMeOH, hydroxymethylferrocene; FcNH₂, aminoferrocene; DMMB, 1,9-Dimethyl-methylene blue zinc chloride double salt. No cathodic peak was observed on GCE/MR-1 in $[Ru(CN)_6]^{4-}$, so the ratio was set as that of $[Fe(CN)_6]^{4-}$. Both anodic and cathodic peak disappeared on GCE/MR-1 in DMMB. Voltammetry curves are detailed in Figure 3.6. (C) CVs of GCE and GCE/MR-1 in a mixture of 0.25 mM RF and 0.50 mM $[Fe(CN)_6]^{4-}$ (RF/ $[Fe(CN)_6]^{4-}$). Scan rate 10 mV s⁻¹, 50 mM PBS (pH 7.0). (D) Chronoamperometric curve of lactate and $[Fe(CN)_6]^{4-}$ on MR-1 at a potential of 0.33 V. Lactate (1.07 mmol) and $[Fe(CN)_6]^{4-}$ (10⁻⁴ mmol), respectively, were added to 10 mL PBS (50 mM, pH 7.0). The orange dot line is a fitting baseline.

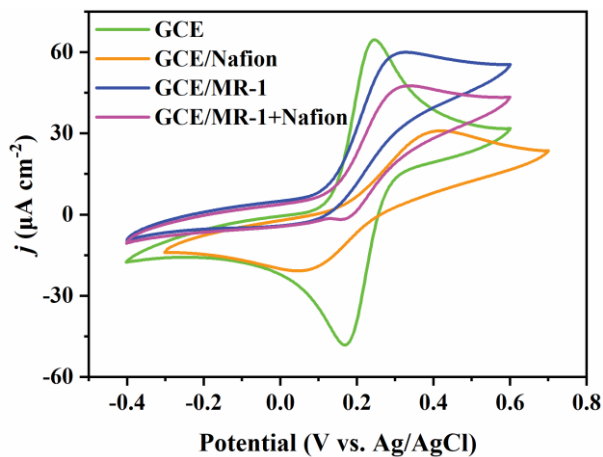


Figure 3.3. The effect of Nafion on the conversion of $K_4[Fe(CN)_6]$. Cyclic voltammetry (CV) on glassy carbon electrode (GCE), GCE coated with Nafion (GCE/Nafion), MR-1 coated on GCE (GCE/MR-1), and the mixture of MR-1 and Nafion coated on GCE (GCE/MR-1 + Nafion). 50 mM PBS (pH 7.0), scan rate 10 mV s⁻¹.

The voltammetric pattern was further detailed. When MR-1 cells were coated on a GCE, the anodic peak for $[Fe(CN)_6]^{4-}$ oxidation to $[Fe(CN)_6]^{3-}$ almost sustained at the same level as on a bare GCE, the cathodic peak significantly shrunk for the reduction of $[Fe(CN)_6]^{3-}$ to $[Fe(CN)_6]^{4-}$ (Figure 3.4). Peak-peak potential separation broadened (ideally 59 mV for GCE, but 168 mV for GCE coated with MR-1) due to the electrochemical polarization caused by the MR-1 layer. A CV of redox inactive *Escherichia coli* K-12 coated on a GCE was also conducted as a control. Both anodic and cathodic peak currents decreased uniformly, and the peak-peak potential separation increased (Figure 3.4, blue line). Similar symmetric CV shape was reported for *Streptococcus mutans* (261), Figure 3.5.

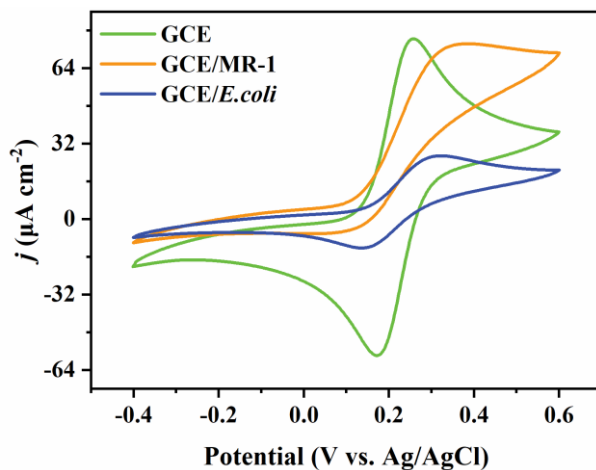


Figure 3.4. The conversion of $[Fe(CN)_6]^{4-}$ by different bacteria. The cyclic voltammetry (CV) on glassy carbon electrode (GCE), MR-1 coated on GCE (GCE/MR-1), and *E. coli* K-12 coated on GCE (GCE/*E.coli*) in 1 mM $[Fe(CN)_6]^{4-}$, 50 mM PBS (pH 7.0), scan rate 10 mV s⁻¹.

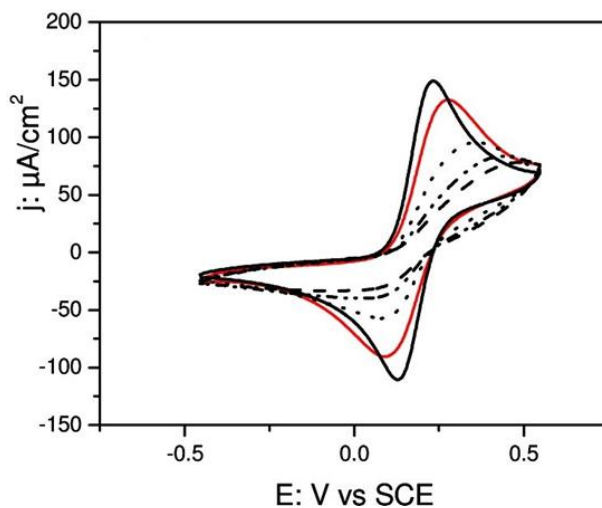


Figure 3.5. Symmetric voltammograms observed for *Streptococcus mutans* in $[Fe(CN)_6]^{4-/3-}$ used as a redox mediator. Black solid line, black dotted line, black dotted-dashed line, and black dashed line are *Streptococcus mutans* on Au(111) at second, 20th, 40th, and 60th cycle, respectively; red solid line, bare Au (111). Reproduced from ref. (261) with permission.

A systematic investigation was conducted on other 11 redox molecules with different midpoint potential and overall charge(s) (Figure 3.2B and Figure 3.6). Apparently, among these molecules asymmetric CV patterns were only observed on the redox molecules with high midpoint potentials and negative charge(s).

Among the 12 redox molecules, riboflavin is special because it is a redox mediator secreted by MR-1. We therefore further compared the different voltammetric responses between $[\text{Fe}(\text{CN})_6]^{4-}$ and riboflavin. CVs in an electrolyte containing 0.50 mM $[\text{Fe}(\text{CN})_6]^{4-}$ and 0.25 mM riboflavin were recorded. As expected, CV on a bare GCE showed two pairs of highly symmetric peaks in the mixed electrolyte (Figure 3.2C). One pair of peaks belongs to $[\text{Fe}(\text{CN})_6]^{4-}$ (0.253 and 0.173 V) and the other one is attributed to the two-electron transfer of riboflavin (-0.380 and -0.426 V, Figure 3.8), which agrees with the reported results (89, 133, 262, 263). In contrast, a pair of asymmetric peaks (0.294 and 0.174 V) and a pair of symmetric peaks (-0.377 and -0.423 V) are found on a GCE/MR-1 (Figure 3.2C) for $[\text{Fe}(\text{CN})_6]^{4-}$ and riboflavin, respectively. Moreover, the shifts in peak potential are very slight for riboflavin after GCE was coated with MR-1: with a maximum of 3 mV positive shift, while a 39 mV positive shift was observed on the anodic peak for $[\text{Fe}(\text{CN})_6]^{4-}$ (Figure 3.2C). These results further support the selectivity of the electrocatalysis of $[\text{Fe}(\text{CN})_6]^{4-}$ by MR-1. The highly selective electrocatalytic oxidation of $[\text{Fe}(\text{CN})_6]^{4-}$ by MR-1 is therefore related to the high midpoint potential and negative charges.

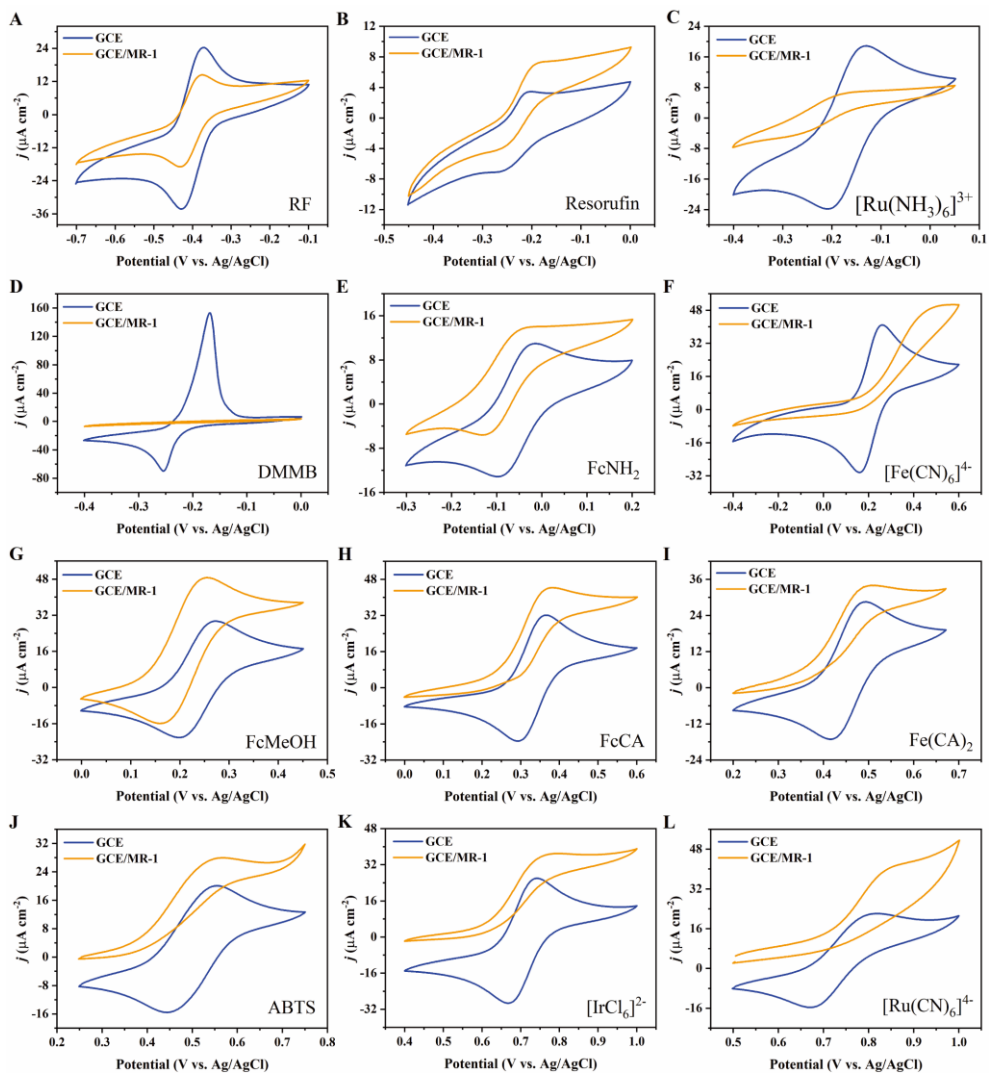


Figure 3.6. The electrochemical conversion of different redox molecules by MR-1. The cyclic voltammetry of (A) 0.25 mM riboflavin (RF), (B) 0.50 mM resorufin, (C) 0.50 mM $[\text{Ru}(\text{NH}_3)_6]^{3+}$, (D) 0.50 mM 1,9-Dimethyl-methylene blue zinc chloride double salt (DMMB), (E) 0.20 mM aminoferrocene (FcNH_2), (F) 0.50 mM $[\text{Fe}(\text{CN})_6]^{4-}$, (G) 0.50 mM hydroxymethylferrocene (FcMeOH), (H) 0.50 mM ferrocenecarboxylic acid (FcCA), (I) 0.50 mM 1,1'-ferrocenedicarboxylic acid ($\text{Fc}(\text{CA})_2$), (J) 0.50 mM azino-di-[3-ethylbenzthiazoline sulfonate (6)] (ABTS), (K) 0.50 mM $[\text{IrCl}_6]^{2-}$, (L) 0.50 mM $[\text{Ru}(\text{CN})_6]^{4-}$ on GCE, and GCE/MR-1. The inconsistent concentrations of riboflavin and aminoferrocene are due to poor water solubilities. The electrolyte 50 mM PBS (pH 7.0), scan rate 10 mV s^{-1} .

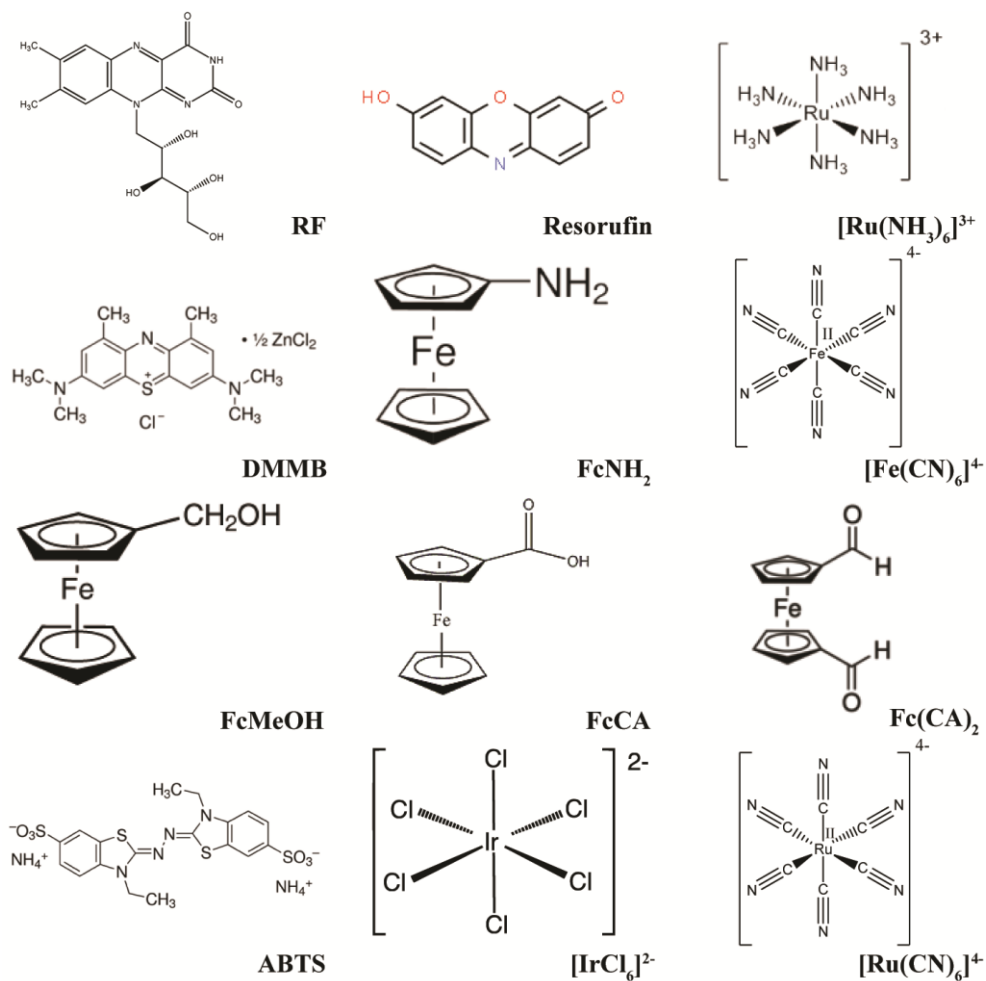


Figure 3.7. The structure of the 12 redox molecules investigated. The names of the structures are denoted lower right

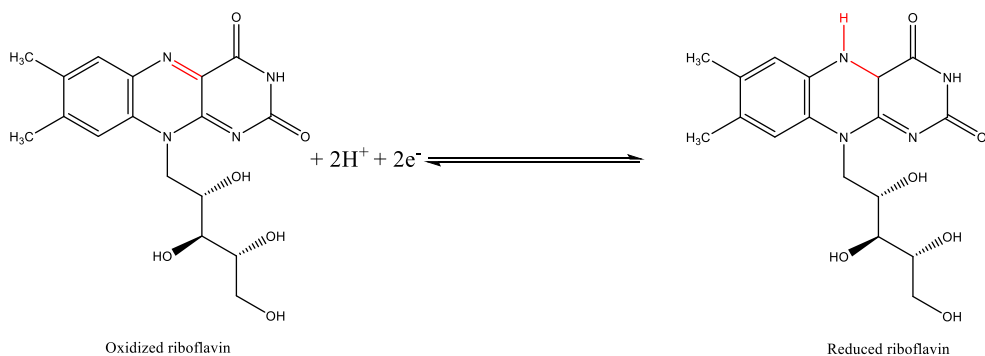


Figure 3.8. The riboflavin redox system

Electrocatalysis promotes an oxidation or a reduction process electrochemically by increasing current or reducing overpotential, giving asymmetric voltammetry (264), Figure 3.9. Catalytic responses of EAB from substrate (*e.g.*, acetate) in BESs were widely studied in BES (265-267). In the current case, the electrocatalysis of $[\text{Fe}(\text{CN})_6]^{4-}$ oxidation is manifested by a strong anodic peak with a weak cathodic peak, compared to other microbes and molecules (Figure 3.1middle and Figure 3.4). This process includes both interfacial electron transfer and diffusion of the redox molecule toward the electrode surface. MR-1 can utilize lactate as an electron donor (138, 156, 268, 269). The corresponding oxidation is reflected by a current increase in chronoamperometry (Figure 3.2D). To ensure that the MR-1 cells maintain immobilized on the electrode surface, Nafion was added to the cell layer, which would slightly decrease the catalytic current (Figure 3.3). After adding lactate, the current through GCE/MR-1 increase, but not GCE coated with Nafion, suggesting an oxidization of lactate by MR-1 as expected. Furthermore, a much higher current growth was detected through GCE/MR-1 following the addition of $[\text{Fe}(\text{CN})_6]^{4-}$, while there was a transient dramatically rise and a rapid drop in the current at bare GCE (Figure 3.2D). Notably, 10^{-4} mmol $[\text{Fe}(\text{CN})_6]^{4-}$ resulted in $1.84 \mu\text{A cm}^{-2}$ current increase, visibly higher than $1.10 \mu\text{A cm}^{-2}$ caused by 1.07 mmol lactate. Compared to a four-electron transfer for lactate oxidation (89), $[\text{Fe}(\text{CN})_6]^{4-}$ oxidation is a one-electron transfer. These differences indicate that the presence of $[\text{Fe}(\text{CN})_6]^{4-}$ significantly enhances the oxidation of $[\text{Fe}(\text{CN})_6]^{4-}$ or lactate, or both.

In summary, MR-1 catalytically electrooxidized the redox molecules with highly efficient and selectivity, exhibiting asymmetric voltammetry patterns. These redox molecules have high midpoint potentials and negative charge(s). Reference bacteria did not show the electrocatalysis. As a representative of these molecules, $[\text{Fe}(\text{CN})_6]^{4-}$ is chosen for further investigations.

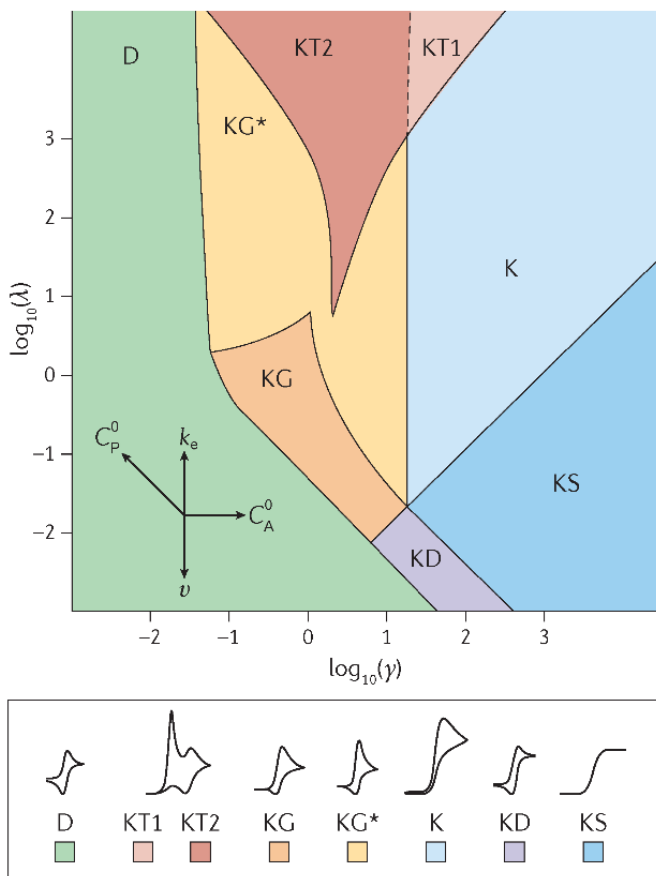


Figure 3.9. The voltammetric responses for electrocatalysis in K, KG, and KG* zone is asymmetric. In the reaction: $P + n'e^- \rightleftharpoons Q$; $Q + A \xrightarrow{k_e} P + B$, the kinetic parameter $\lambda = \left(\frac{RT}{F}\right) \left(\frac{k_e C_P^0}{v}\right)$, the excess factor $\gamma = \frac{C_A^0}{C_P^0}$ where k_e is the rate constant, C_P^0 and C_A^0 the concentrations of product P and substrate A, respectively. Reproduced from ref (264) with permission.

3.3.2 The key factors in MR-1 for $[\text{Fe}(\text{CN})_6]^{4-}$ electrocatalysis

A number of redox-active compounds have been confirmed to promote the EET of MR-1 (80, 85, 89). To identify the components in MR-1 that cause the electrocatalysis, extracellular polymeric substances (EPS), cytochrome c, and riboflavin, which are common redox compounds of MR-1, were investigated. In the absence and presence of EPS, MR-1 shows similar electrocatalysis patterns, with an anodic peak slightly enhanced in the absence of EPS (Figure 3.10A), implying that EPS does not play a crucial role in the electrocatalytic oxidation of $[\text{Fe}(\text{CN})_6]^{4-}$. Small enhancement of the anodic peak could be due to the improved mass transfer caused by the removal of EPS. No redox peak

is found on the CV in 1 mM $[\text{Fe}(\text{CN})_6]^{4-}$ for the gold electrode modified with 6-Mercaptohexanoic acid (6C-HS), (Figure 3.10B). A broad and weak $[\text{Fe}(\text{CN})_6]^{4-}$ reduction peak appeared after the formation of a cytochrome *c* layer (from equine heart) on 6C-HS (Figure 3.10B). However, the CV of Au/MR-1 shows a similar pattern as GCE/MR-1 in 1 mM $[\text{Fe}(\text{CN})_6]^{4-}$ (Figure 3.10B), meaning that MR-1 cells on the gold electrode contribute to the electrocatalysis of $[\text{Fe}(\text{CN})_6]^{4-}$ oxidation. Additionally, GCE coated with riboflavin does not change the electrochemical behavior of GCE in $[\text{Fe}(\text{CN})_6]^{4-}$ solution, as inferred from the reversible voltammetric peaks belonging to riboflavin and $[\text{Fe}(\text{CN})_6]^{4-}$ (Figure 3.10C). The symmetric peaks imply that riboflavin does not affect the electrocatalytic oxidation of $[\text{Fe}(\text{CN})_6]^{4-}$. The oxidation of $[\text{Fe}(\text{CN})_6]^{4-}$ by MR-1 therefore differs totally from the reduction of Fe(III) compounds by dissimilatory metal reduction bacteria, since the reduction is enhanced by redox shuttles such as riboflavin (89, 101).

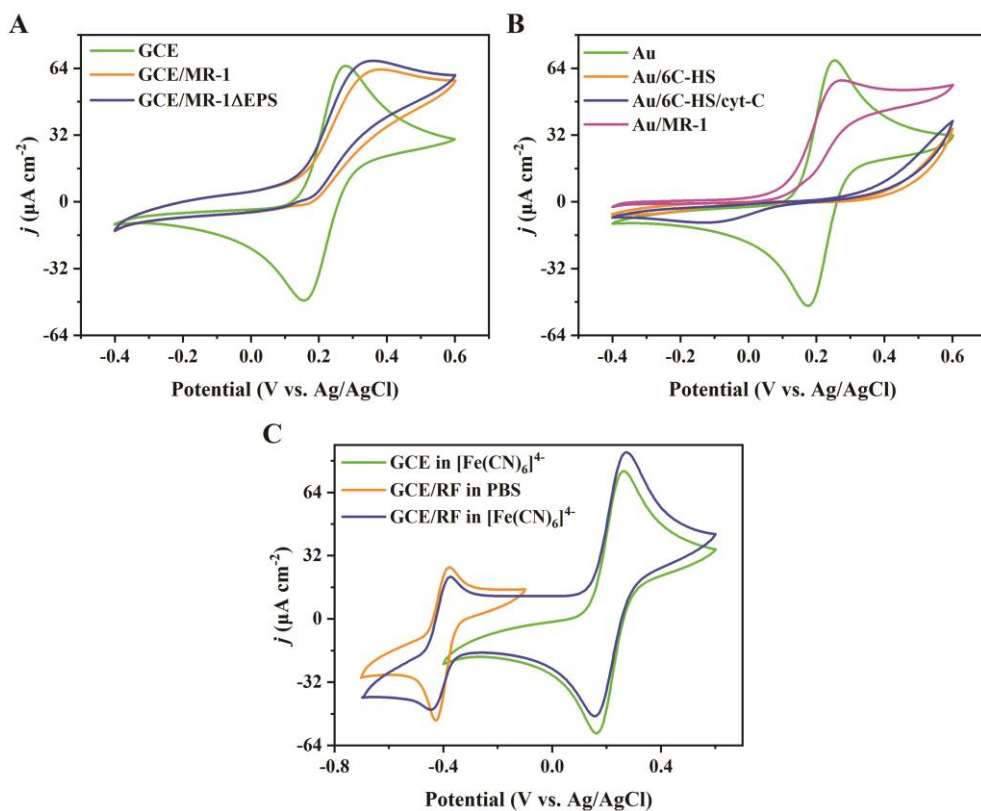


Figure 3.10. Identification of the composition of MR-1 for the electrocatalysis of $[\text{Fe}(\text{CN})_6]^{4-}$. (A) Cyclic voltammetry (CV) on GCE, GCE/MR-1, GCE coated with MR-1 without EPS (GCE/MR-1 Δ EPS) in 1.0 mM $[\text{Fe}(\text{CN})_6]^{4-}$. (B) CV on a gold electrode (Au), gold electrode modified with 6-Mercaptohexanoic acid (Au/6C-HS), gold electrode modified with 6-Mercaptohexanoic acid linking cytochrome *c* from equine heart (Au/6C-HS/cyt-C), and gold electrode modified with MR-1 (Au/MR-1)

in 1.0 mM $[\text{Fe}(\text{CN})_6]^{4-}$. (C) CV on GCE in 1.0 mM $[\text{Fe}(\text{CN})_6]^{4-}$, GCE coated with riboflavin (GCE/RF) in PBS and 1.0 mM $[\text{Fe}(\text{CN})_6]^{4-}$. The electrolyte for CVs is 50 mM PBS (pH 7.0) and the scan rate 10 mV s⁻¹.

Hence, EPS, cytochrome *c*, and riboflavin, as important components in the outward EET of MR-1, were investigated in the electrocatalysis of $[\text{Fe}(\text{CN})_6]^{4-}$ by MR-1. No apparent contribution is observed.

3.3.3 The dependence of electrocatalysis on CV scan rate

Electrocatalysis of $[\text{Fe}(\text{CN})_6]^{4-}$ oxidation by MR-1 displays an asymmetric voltammetry shape. The shape of CV depends on the scan rate at given $[\text{Fe}(\text{CN})_6]^{4-}$ concentration. To investigate the effect of scan rate on electrocatalytic oxidation, a series of CVs with scan rate from 0.01 to 3.0 V/s were conducted, Figure 3.11A. CV is asymmetric at low scan rates. When the scan rate increases, such asymmetry becomes weaker for GCE/MR-1 (Figure 3.11B). In contrast, the CVs at all scan rates are symmetric in the same $[\text{Fe}(\text{CN})_6]^{4-}$ solution for bare GCE (Figure 3.11C). The ratio of anodic to cathodic peak current (I_{pa}/I_{pc}) dropped from 7.17 to 1.50 when the scan rate increased from 0.01 to 3.0 V s⁻¹ for GCE/MR-1 (Figure 3.11D). At high scan rate, the electron transfer rate of $[\text{Fe}(\text{CN})_6]^{4-}$ oxidation is limited by mass transfer, rather than interfacial electron transfer, where the electrocatalysis occurs. The ability of MR-1 to electrocatalyze $[\text{Fe}(\text{CN})_6]^{4-}$ oxidation is limited by the amount of MR-1. The current through GCE/MR-1 is dominated by the electrocatalysis by MR-1 at low scan rates. At high scan rates, the current is controlled by the $[\text{Fe}(\text{CN})_6]^{4-}$ and $[\text{Fe}(\text{CN})_6]^{3-}$ diffusion toward the surface of GCE/MR-1. This is supported by Figure 3.11E and F, which show an linear peak current increased with the square root of scan rate with a larger slope for slow scan rates (270).

3.3.4 The dependence of electrocatalysis on $[\text{Fe}(\text{CN})_6]^{4-}$ concentration

The influence of the $[\text{Fe}(\text{CN})_6]^{4-}$ concentration on the electrocatalysis was further studied. Different CVs in 0.10 to 20 mM $[\text{Fe}(\text{CN})_6]^{4-}$ were recorded. Clear electrocatalysis is seen at low $[\text{Fe}(\text{CN})_6]^{4-}$ concentration (Figure 3.12A), but becomes obscure at high concentration (Figure 3.12B) for GCE/MR-1, while the CVs are symmetric at all $[\text{Fe}(\text{CN})_6]^{4-}$ concentration (Figure 3.12C) for bare GCE. The I_{pa}/I_{pc} decreased from 21 to 1.43 when the concentration increased from 0.50 to 20 mM (Figure 3.12D). It is noteworthy that the cathodic peak is barely detected in 0.1 mM $[\text{Fe}(\text{CN})_6]^{4-}$ (Figure 3.12A). This also confirms the limitation of $[\text{Fe}(\text{CN})_6]^{4-}$ catalysis by MR-1. In high concentration of $[\text{Fe}(\text{CN})_6]^{4-}$, the fraction of the anodic current of electrocatalysis by MR-1 is relatively small and overlapped by the strong signal of $[\text{Fe}(\text{CN})_6]^{4-/3-}$ conversion. The slopes of both anodic and cathodic peak current density vs. $[\text{Fe}(\text{CN})_6]^{4-}$ concentration for GCE/MR-1 are completely different at low and high $[\text{Fe}(\text{CN})_6]^{4-}$ concentration. In contrast, slopes are

almost the same within experimental uncertainty for GCE (Figure 3.12E and Figure 3.12F).

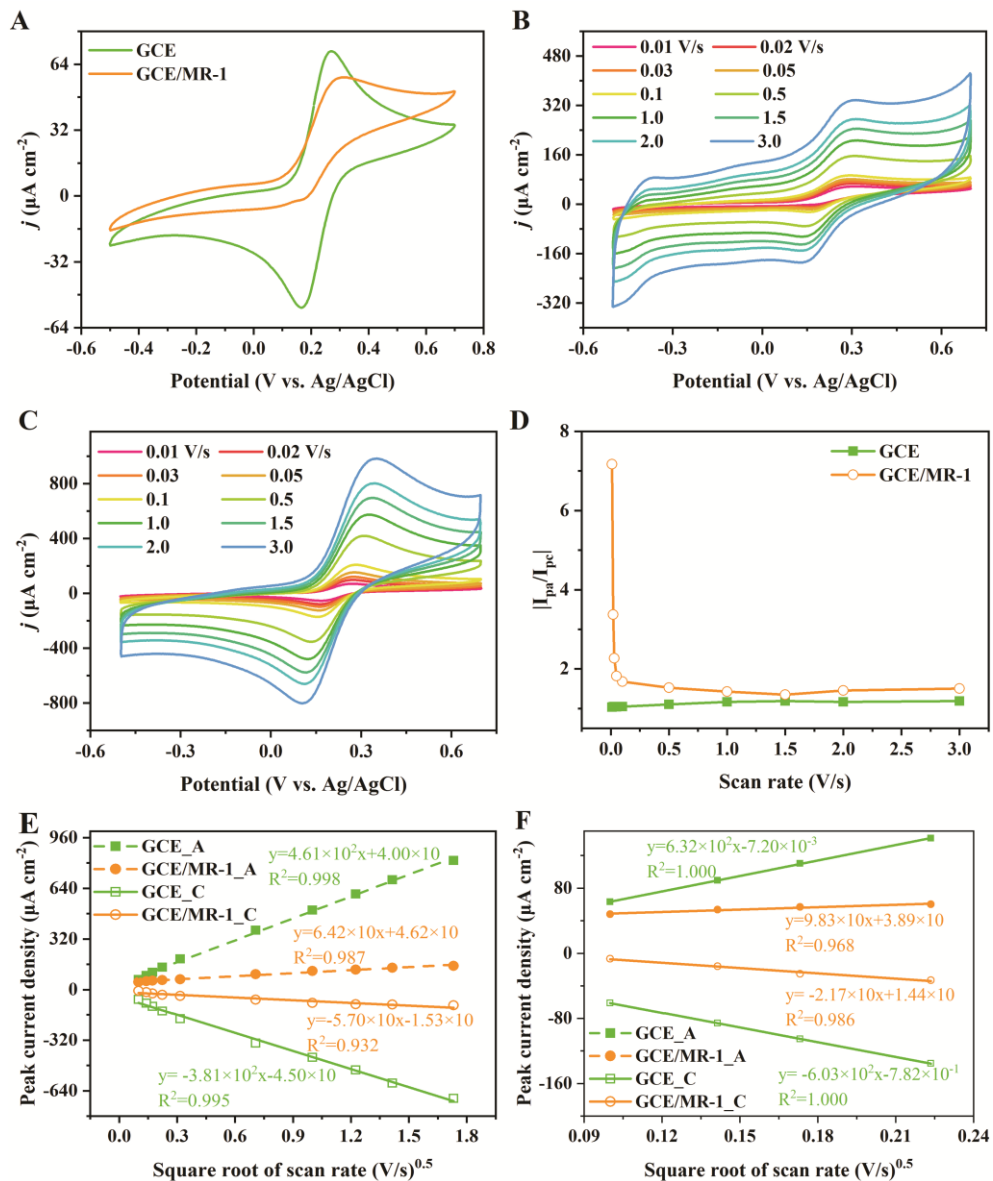


Figure 3.11. Scan rate-dependent conversion of $[Fe(CN)_6]^{4-}$ by MR-1. (A) Cyclic voltammety on MR-1 coated on GCE (GCE/MR-1) in 1.0 mM $[Fe(CN)_6]^{4-}$ at 0.01 V s⁻¹. The cyclic voltammety on (B) MR-1 coated on GCE (GCE/MR-1), and on (C) bare GCE in 1.0 mM $[Fe(CN)_6]^{4-}$ at different scan rates. (D) The ratio of anodic (I_{pa}) to cathodic peak current (I_{ca}) in (b). (E) Plots of peak current density vs. the square root of scan rate in the range 0.01~ 3.0 V s⁻¹. (F) Plots of peak current density vs. the square

root of scan rate in the range 0.01~ 0.05 V s⁻¹. The electrolyte 50 mM PBS (pH 7.0).

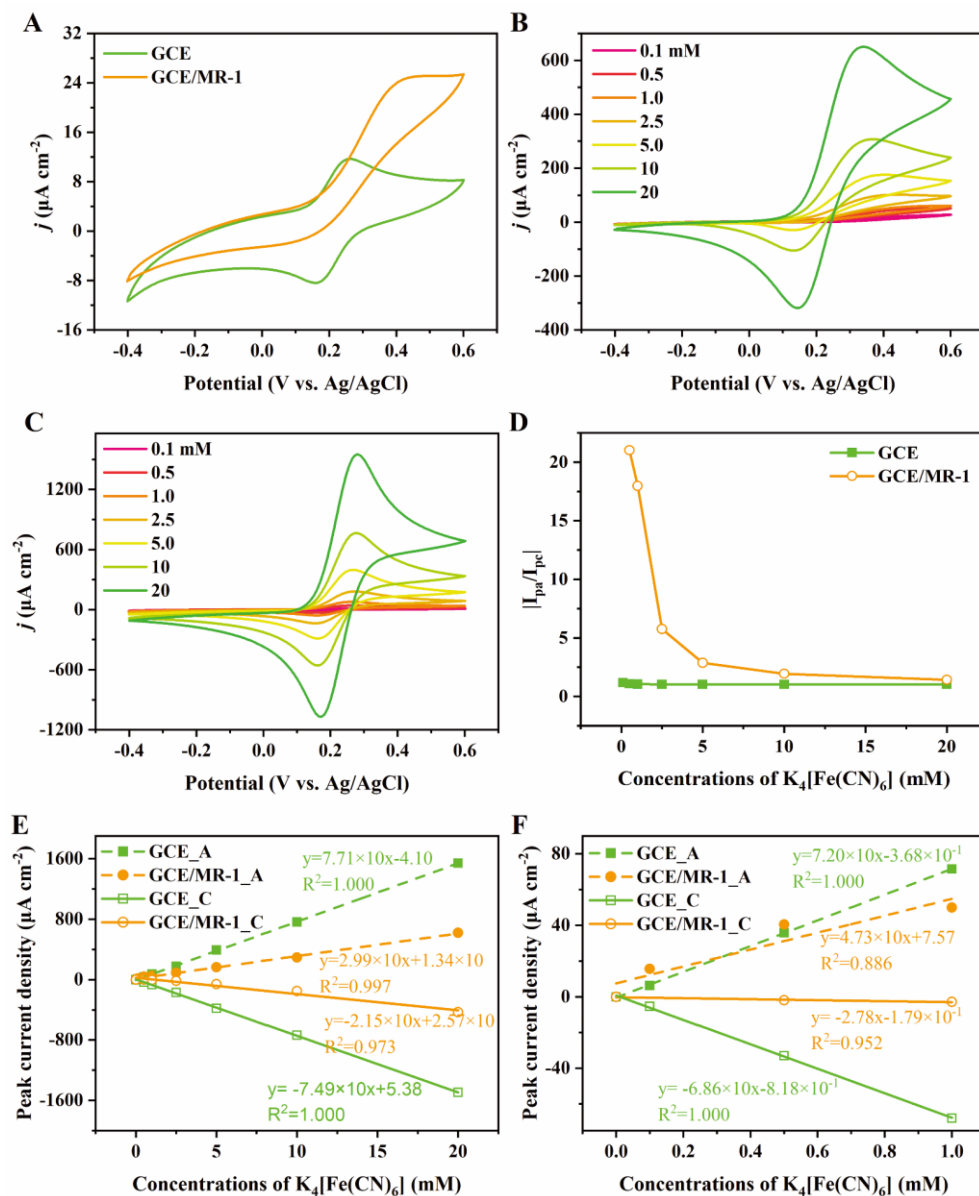


Figure 3.12. Conversion of $[Fe(CN)_6]^{4-}$ by MR-1 in different $[Fe(CN)_6]^{4-}$ concentrations. (A) Cyclic voltammetry on MR-1 coated on GCE (GCE/MR-1) in 0.1 mM $[Fe(CN)_6]^{4-}$. Cyclic voltammetry on (B) MR-1 coated on GCE (GCE/MR-1), and on (C) bare GCE at different $[Fe(CN)_6]^{4-}$ concentrations. (D) The ratio of anodic (I_{pa}) to cathodic peak current (I_{ca}) in (B). (E) Plots of peak current density vs. the $[Fe(CN)_6]^{4-}$ concentration from 0.1~20 mM. (F) The plots of peak current density vs. the concentration of $[Fe(CN)_6]^{4-}$ from 0.1~1.0 mM. The electrolyte is 50 mM PBS (pH 7.0), scan rate 10 mV/s.

The clearly different dependence of voltammetric shape on $[\text{Fe}(\text{CN})_6]^{4-}$ concentration and scan rate on bare GCE and MR-1 coated GCE implies different mechanisms, which will be detailed in the Chapter 5.

3.4 Conclusions

MR-1 electrocatalyzes $[\text{Fe}(\text{CN})_6]^{4-}$ oxidation with high efficiency and selectivity. The selectivity is most likely connected with the midpoint potential and overall charge(s) since only the investigated redox molecules with high redox midpoint potential and negative charges show clear catalytic electro-oxidation. The electrocatalysis of oxidation is clear at slow scan rate and low $[\text{Fe}(\text{CN})_6]^{4-}$ concentration, presenting a notable asymmetric voltammetry patterns, which further justifies electrocatalytic processes. As a representative of the 12 redox molecules investigated, $\text{K}_4[\text{Fe}(\text{CN})_6]$ was chosen for further investigation. $[\text{Fe}(\text{CN})_6]^{4-}$ oxidation is an inward EET process, in which $[\text{Fe}(\text{CN})_6]^{4-}$ donate electrons to MR-1. This oxidation is entirely distinct from the reduction of Fe(III) oxides and Mn(IV) oxides by MR-1 and not affected by riboflavin, EPS, and *in vitro* cytochrome *c*. In spite of the clear demonstration of the phenomenon of catalytic electrooxidation of $[\text{Fe}(\text{CN})_6]^{4-}$, the more detailed mechanism beyond, *i.e.*, the exact EET process, is not clear yet, and will be addressed in the following chapter.

Chapter 4

Electrons uptake by *S. oneidensis* MR-1

This chapter further explores the electrocatalytic phenomenon described in Chapter 3 and a model for the inward EET of *S. oneidensis* MR-1 has been proposed. The model implies the collaboration effect of the $[\text{Fe}(\text{CN})_6]^{4-}$ electrooxidation and the mediating process by $[\text{Fe}(\text{CN})_6]^{4-/3-}$.

4.1 Introduction

There is general consensus that cytochromes *c*, especially Mtr proteins are crucial to the outward EET of MR-1. Interestingly, Mtr homologues are also discovered in Fe(II)-oxidizing bacteria. The operon of phototrophic iron oxidation in *Rhodopseudomonas palustris* TIE-1 consists of *pioA*, *pioB*, and *pioC*. The *pioA* and *pioB* are homologues of MtrA and MtrB of MR-1, respectively (271). More Mtr homologues have been found in other Fe(II)-oxidizing bacteria, such as *Dechloromonas aromatica* RCB, *Gallionella capsiferiformans* ES-2, and *Sideroxydans lithotrophicus* ES-1 (272, 273). It seems that Mtr proteins are not only involved with outward, but also with inward EETs.

The outward EET of MR-1 can be reversed in the OmcA–MtrCAB pathway, *i.e.*, this pathway can transport electrons from electrodes into the cells (119). Additionally, the *Shewanella* strain 4t3-1-2LB with an ability to use metallic iron as the sole electron donor was discovered (246). Notably, some metal-reducing bacteria have been discovered to oxidize Mn(II). *Shewanella* sp. was found to be a Mn(II)-oxidizer in a seamount (274). Moreover, other *Shewanella* strains have been reported to play a role in metal oxidation, including manganese (275-277) and Fe-oxidation (278). According to a detailed study, five *Shewanella* strains (*Shewanella oneidensis* MR-1, *Shewanella putrefaciens* CN-32, *Shewanella putrefaciens* 200, *Shewanella loihica* PV-4, and *Shewanella denitrificans* OS217) oxidize Mn(II) and produce manganese oxide NPs under aerobic conditions. The manganese oxide NPs were reduced by the same bacteria when lactate was added, and oxygen was degassed (279). Multicopper oxidase enzymes are involved in the oxidations, including Mn(II) oxidation (280). Additionally, laccases, a member of multicopper oxidase enzymes, have been discovered in *Shewanella* species (281, 282). It is reasonable to

assume that laccases contribute to the Mn(II) oxidation since the redox potential of some laccases can be higher than 0.7 V vs SHE (283, 284) or even 0.8 V vs SHE (285). Some laccases produced by fungi actually oxidize Mn(II) (286). Furthermore, peroxidases from fungi are also involved in Mn(II) oxidation (287). However, it is not clear whether MR-1 is able to directly take electrons extracellularly from iron compounds. There are more than 39 genes relevant to cytochromes *c* in the genome of MR-1 (114), but only six of cytochromes *c* (MtrA, MtrC, OmcA, CymA, small tetraheme cytochrome, and FccA) have been discovered in the outward EET. The rest of the cytochromes *c* and potential laccases may offer other function to MR-1 in EET. More effort is thus needed to explore the possibility of other EET forms to disclose the role and function of MR-1 in the environment.

In this chapter, we further probe the electrocatalytic oxidation—an inward EET process of MR-1. The electrooxidation decays after Pd NPs are formed on the surface of MR-1. On the other hand, the electrooxidation remains for inactive MR-1 and MR-1 free of MtrC and OmcA. Based on these results, a model with the combination of the electrocatalytic oxidation of $[\text{Fe}(\text{CN})_6]^{4-}$ by MR-1 and the mediating process of $[\text{Fe}(\text{CN})_6]^{4-/3-}$ is proposed.

4.2 Experimental section

4.2.1 Chemicals

Luria-Bertani broth (LB, 10 g L⁻¹ tryptone, 5 g L⁻¹ yeast extract, 5 g L⁻¹ NaCl), Na₂HPO₄·12H₂O (99~101%), Nafion DE 1021 (10%), KCl (≥ 99.0%), 6-Mercaptocaproic acid (90%), cytochrome *c* (from equine heart, > 95%), KH₂PO₄ (98~100.5%), NH₄Cl (≥ 99.5%), CaCl₂·2H₂O (99%), hydroxymethylferrocene (97%), sodium DL-lactate (60%), Na₂[PdCl₄] (98%), and glutaraldehyde (25%) were obtained from Sigma-Aldrich, Germany. Ferrocenecarboxylic acid (≥ 97.0% (Fe)) was from Sigma-Aldrich, China. Riboflavin (≥ 98%) and aminoferrocene (≥ 98.0%) were purchased from Sigma-Aldrich, Japan. Hexaammineruthenium(III) chloride (98%), resorufin (Dye content 95 %), 1,9-Dimethyl-methylene blue zinc chloride double salt (Dye content 80%), glucose (≥ 99%), and potassium hexachloroiridate (technical grade) were from by Sigma-Aldrich, USA. Potassium hexacyanoferrate(II) trihydrate (99.0~102.0%) was from Merck, Germany. NaH₂PO₄·2H₂O (≥ 99.0%), NaCl (≥ 99.5%), and 2,2'-Azino-bis(3-ethylbenzothiazoline-6-sulfonic acid) diammonium salt (≥ 98.0%) were from by Fluka, Germany. MgSO₄·7H₂O (99.8%) and potassium hexacyanoferrate(III) (≥ 99.5%) were from Riedel-de-Haën, France. 1,1'-Ferrocenedicarboxylic acid (> 97.0%) was from Fluka, Switzerland. Potassium hexacyanoruthenate(II) hydrate (Ru 23.0% min) was from by Alfa Aesar, USA. Absolute ethanol (100%) was produced by VWR Chemicals, France. All chemicals were used as received without further purification. Aqueous solutions were prepared with MilliQ water (18.2 MΩ cm, arium® pro VF system, Sartorius AG, Germany).

4.2.2 Culture and collection of *S. oneidensis* MR-1

The culture and collection are the same as described in section [3.2.2 Culture and collection of *S. oneidensis* MR-1](#)

4.2.3 Electrochemical measurements.

The conditions and parameters of the electrochemical measurements are the same as in the section [3.2.3 Electrochemical measurements](#).

4.2.4 Formation of Pd NPs on MR-1

MR-1 cells were incubated and washed as noted. The washed cells were resuspended in 20 mL sterilized M9 buffer [pH 7.0; KH_2PO_4 (3.00 g L⁻¹), $\text{Na}_2\text{HPO}_4 \cdot 12\text{H}_2\text{O}$ (15.14 g L⁻¹), NH_4Cl (1.00 g L⁻¹), NaCl (0.50 g L⁻¹), $\text{CaCl}_2 \cdot 2\text{H}_2\text{O}$ (0.015 g L⁻¹), $\text{MgSO}_4 \cdot 7\text{H}_2\text{O}$ (0.025 g L⁻¹) (156) and deoxygenated with argon. A 1.0 mL cell suspension was injected into 24.0 mL sterilized and deoxygenated M9 buffer containing 18 mM sodium DL-lactate and different concentrations of $\text{Na}_2[\text{PdCl}_4]$ (0.08 mM, 0.40 mM, and 0.80 mM). The cells were cultured for 1 h at 30°C at 100 rpm. The cells were then washed and collected for further investigation.

4.2.5 Formation of Pd NPs on GCE

Pd NPs were deposited electrochemically on GCE from 1.0 mM $\text{Na}_2[\text{PdCl}_4]$ in 50 mM PBS (pH 7.0) by applying a potential of -1.00 V vs. Ag/AgCl for 5 min (GCE/Pd_5), 15 min (GCE/Pd_15), 30 min (GCE/Pd_30), and 50 min (GCE/Pd_50). The Pd NPs modified GCE was rinsed with MilliQ water and placed in the electrochemical cell containing 50 mM PBS (pH 7.0) to verify the presence of Pd NPs by CV with a scan rate of 100 mV s⁻¹.

4.2.6 Preparation of inactive MR-1

MR-1 cells were incubated in LB medium at 30°C by shaking at 100 rpm overnight. The cells were then washed twice with 0.9% NaCl, resuspended with 50 mM PBS (pH 7.0) and packed into a test tube sealed with a blue butyl rubber stopper. The stopper was penetrated with a syringe needle connecting with a sterilized filter (0.22 μm) to avoid the pressure change during the freezing process. The test tube was immersed into liquid nitrogen to freeze the cells, until the medium became solid. Afterwards, the test tube was taken out and put into water (room temperature) to melt. The freezing and melting process was repeated 20 times to kill the cells while retaining the activity of the proteins in the cell membrane.

4.2.7 Morphology characterization

All bacteria for morphology characterization were washed twice with 0.9% NaCl unless otherwise stated. Bacteria for scanning electron microscopy (SEM) were resuspended in 2.5% glutaraldehyde and stored at 4°C for 48 h. The cells were then washed twice with 50 mM PBS (pH 7.0) and further subjected to dehydration in a gradient ethanol series (50, 70, 80, 95%) for 15 min each. The cells were dehydrated again with absolute ethanol, with 3 changes within 15 minutes. The cells were then loaded onto a silicon wafer and dried at room temperature overnight. The Pd NPs on GCE were dried at room temperature overnight before SEM observation. Both bacteria and Pd NPs were coated with 1 nm gold film for SEM observation (Quanta FEG 200 ESEM, FEI, USA). The elemental composition of bacteria and Pd NPs were characterized by energy-dispersive X-ray spectroscopy (EDS) analysis.

Transmission electron microscopy (TEM) samples were cast on lacey carbon-coated copper grids (Ted Pella Inc., Redding CA, USA) by placing one drop of sample dispersion onto the grids. The samples were then observed with a Tecnai G2 T20 instrument (FEI Company, Hillsboro, USA).

4.2.8 Cell growth monitoring.

The growth kinetics of MR-1 and inactive MR-1 was observed by suspending the cells in LB medium to an OD600 of about 0.02 and the cells incubated at 30°C with shaking of 100 rpm. Aliquots were sampled at fixed times for optical density measurements using an Agilent 8453 UV-vis spectrophotometer (Santa Clara, USA) with a 1 cm light path quartz cuvette. All samples were conducted in triplicates.

4.3 Results and discussion

4.3.1 The formation of palladium NPs on MR-1 block the $[\text{Fe}(\text{CN})_6]^{4-}$ electrocatalytic oxidation

As a dissimilatory metal reduction bacterium, MR-1 is able to reduce various metals, for example, Au(III) ions (164), Pd(II) ions (157, 173), and Ag(I) ions (180), forming corresponding NPs on the surface of the MR-1 cells. Some noble metal NPs (for example, Au and Pd NPs) assist EET and oxidize catalytically fuel molecules (164, 173, 201). Surprisingly, the presence of Pd NPs on MR-1 weakened the anodic peak of $[\text{Fe}(\text{CN})_6]^{4-}$ systematically (Figure 4.1). Such an effect is much clearer on MR-1 cultured in a medium containing a higher concentration of $[\text{PdCl}_4]^{2-}$. Obviously, Pd NPs on MR-1 weaken the oxidation of $[\text{Fe}(\text{CN})_6]^{4-}$. The viability of MR-1 maintained in the presence of $[\text{PdCl}_4]^{2-}$ in the experimental concentration, confirmed by a previous report (201). More Pd NPs were

formed on the surface of MR-1 with a higher concentration of $[\text{PdCl}_4]^{2-}$ (Figure 4.2, Figure 4.3, and Figure 4.4). Pd NPs formation on cells can have three consequences: (a) blocking the mass transfer between specific sites on MR-1 cell membrane and $[\text{Fe}(\text{CN})_6]^{4-}$ in extracellular environment; (b) introducing the inherent properties of Pd NPs, including boosting electroconductivity, exhibiting catalysis behavior of the MR-1 coated with Pd NPs to specific substances (*156, 173, 201, etc.*); (c) increasing the specific surface area of MR-1 coated with Pd NPs.

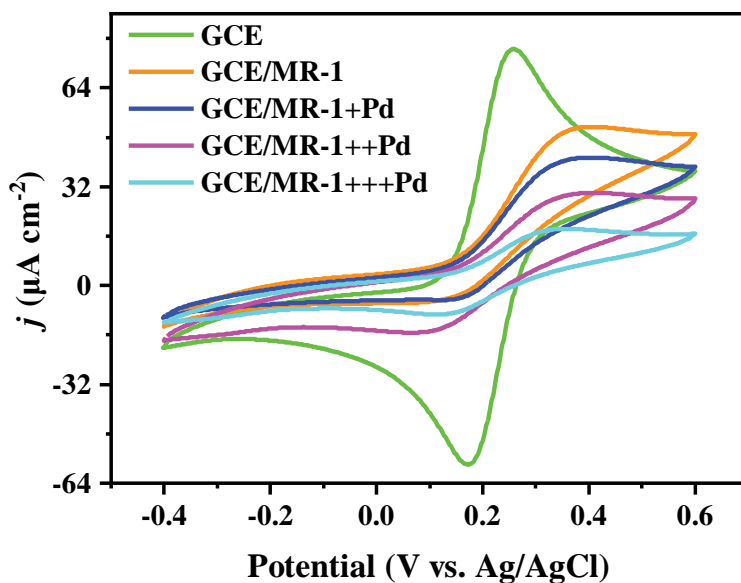


Figure 4.1. The effect of the formation of Pd NPs on the electrooxidation of $[\text{Fe}(\text{CN})_6]^{4-}$ by MR-1. CV of 1.0 mM $[\text{Fe}(\text{CN})_6]^{4-}$ on GCE, GCE/MR-1, GCE coated with MR-1 cultured in M9 medium with $[\text{PdCl}_4]^{2-}$: 0.08 mM (MR-1+Pd), 0.40 mM (MR-1++Pd), and 0.80 mM (MR-1+++Pd) $[\text{PdCl}_4]^{2-}$ were used. 50 mM PBS (pH 7.0). Scan rate 10 mV s^{-1} .

To investigate the effect of inherent properties and the change of specific surface area of Pd NPs on the catalysis of $[\text{Fe}(\text{CN})_6]^{4-}$ oxidation, Pd NPs were electrodeposited on a GCE and corresponding voltammetry experiments conducted (Figure 4.5A). The increasing amount of Pd NPs is reflected by enhanced anodic and cathodic peaks on GCE modified with Pd NPs in 50 mM PBS (pH 7.0) (Figure 4.5A), caused by the adsorption and corresponding desorption of hydrogen and oxygen (*259*). As shown in SEM and EDS, different sizes and amounts of Pd NPs on GCE, with consequently varied electrode specific surface area, were further confirmed (Figure 4.6). However, both the anodic and cathodic peak of $[\text{Fe}(\text{CN})_6]^{4-}$ slightly decreased to an almost same extent for all Pd NPs modified GCE (Figure 4.5B). These results exclude the influence of inherent Pd NPs properties and the change of specific surface area. Clearly, the presence of Pd NPs on MR-1 is likely to block the electrocatalytic sites on MR-1.

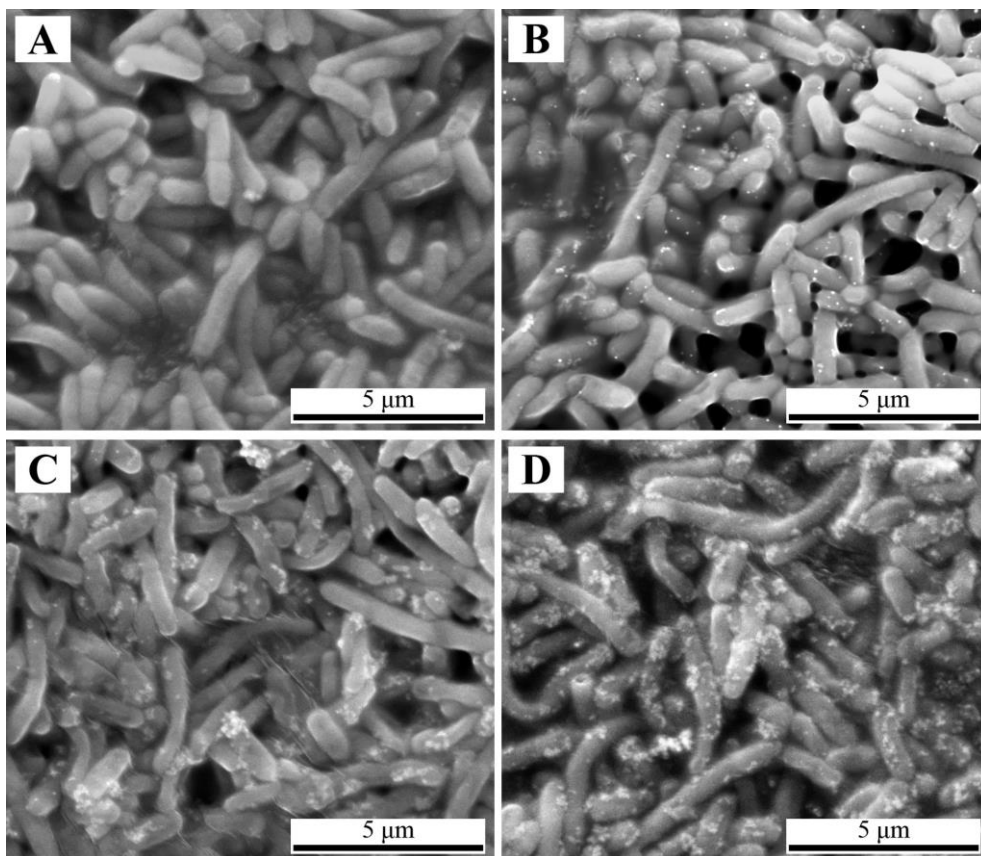


Figure 4.2. SEM images of MR-1 and MR-1 coated with Pd NPs. MR-1 cultured in M9 medium (A) without $[\text{PdCl}_4]^{2-}$, (B) with 0.08 mM $[\text{PdCl}_4]^{2-}$ (MR-1+Pd), (C) with 0.40 mM $[\text{PdCl}_4]^{2-}$ (MR-1++Pd), (D) with 0.80 mM $[\text{PdCl}_4]^{2-}$ (MR-1+++Pd). The white dots are Pd NPs.

Briefly, Pd NPs on cellular surface systematically blocked the electrocatalysis of $[\text{Fe}(\text{CN})_6]^{4-}$ by MR-1. The role of abiotic Pd NPs on GCE in the electrocatalysis was studied to exclude the intrinsic properties of Pd NPs. The results imply that the Pd NPs are mostly likely to physically block the pathway of $[\text{Fe}(\text{CN})_6]^{4-}$ oxidation.

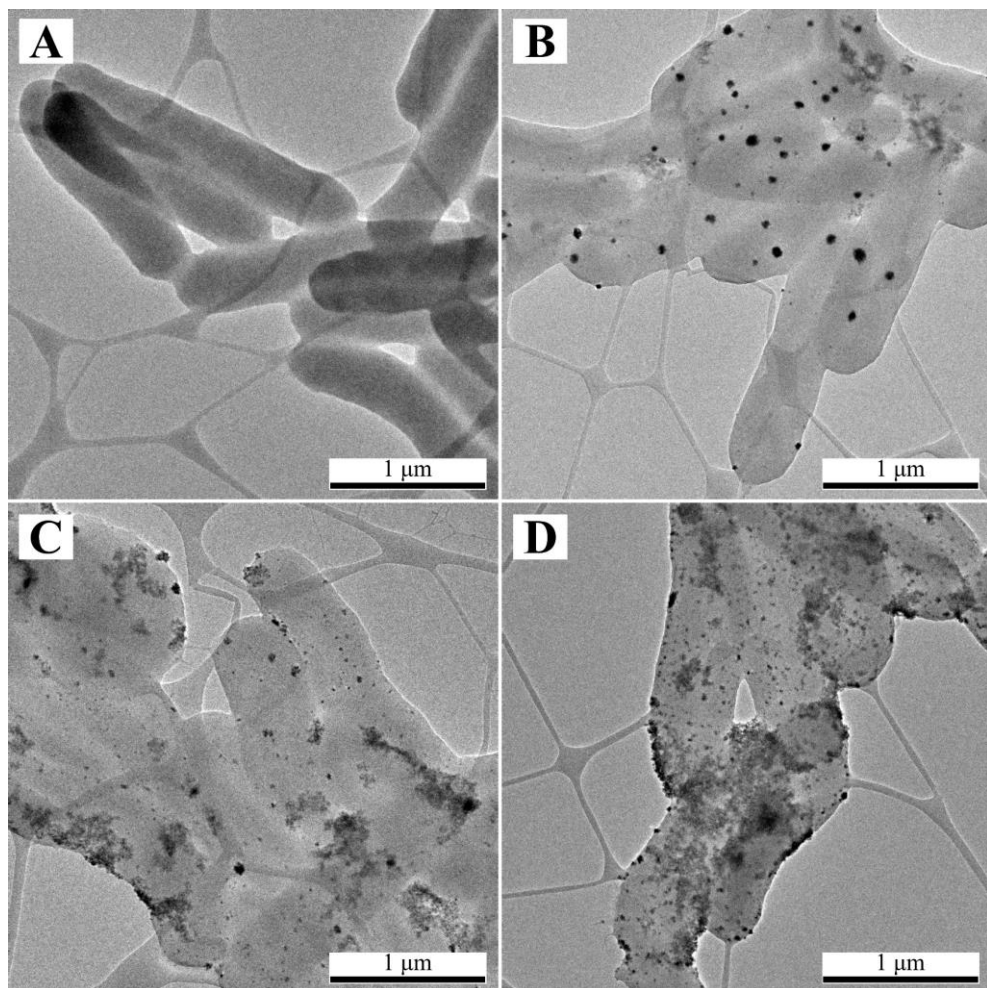


Figure 4.3. TEM images of MR-1 and Pd NPs on MR-1. (A) MR-1 cultured in M9 medium without $[PdCl_4]^{2-}$. (B) MR-1 cultured in M9 medium with 0.08 mM $[PdCl_4]^{2-}$ (MR-1+Pd). (C) MR-1 cultured in M9 medium with 0.40 mM $[PdCl_4]^{2-}$ (MR-1++Pd). (D) MR-1 cultured in M9 medium with 0.80 mM $[PdCl_4]^{2-}$ (MR-1+++Pd). The black dots are Pd NPs.

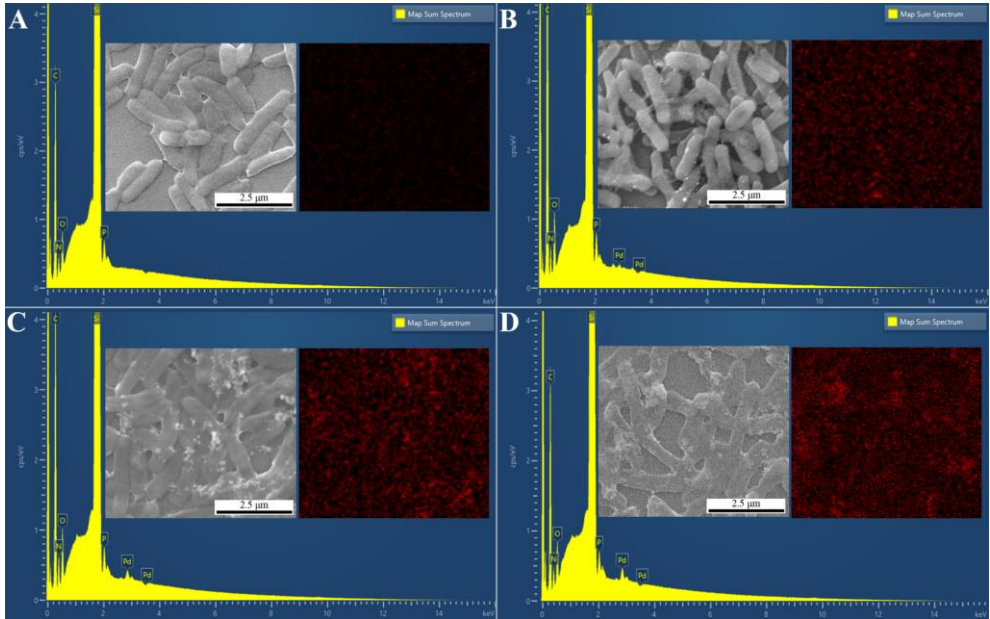


Figure 4.4. EDS spectrum, SEM and corresponding EDS mapping patterns (insert) of MR-1 with Pd NPs in different concentration. (A) MR-1 cultured in M9 medium without $[\text{PdCl}_4]^{2-}$. (B) MR-1 cultured in M9 medium with 0.08 mM $[\text{PdCl}_4]^{2-}$ (MR-1+Pd). (C) MR-1 cultured in M9 medium with 0.4 mM $[\text{PdCl}_4]^{2-}$ (MR-1++Pd). (D) MR-1 cultured in M9 medium with 0.8 mM $[\text{PdCl}_4]^{2-}$ (MR-1+++Pd).

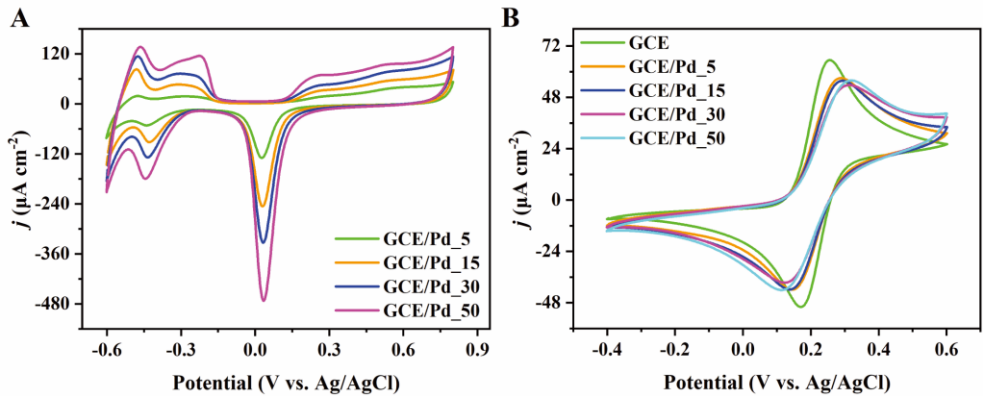


Figure 4.5. Conversion of $[\text{Fe}(\text{CN})_6]^{4-}$ by Pd NPs. (A) CV of Pd NPs coated on GCE for 5 min (GCE/Pd_5), 15 min (GCE/Pd_15), 30 min (GCE/Pd_30) and 50 min (GCE/Pd_50) in 0.1 mM $[\text{PdCl}_4]^{2-}$. Scan rate: 100 mV s^{-1} . 50 mM PBS (pH 7.0). (B) CVs of 1 mM $[\text{Fe}(\text{CN})_6]^{4-}$ on the electrodes in (a). Scan rate 10 mV s^{-1} . 50 mM PBS (pH 7.0).

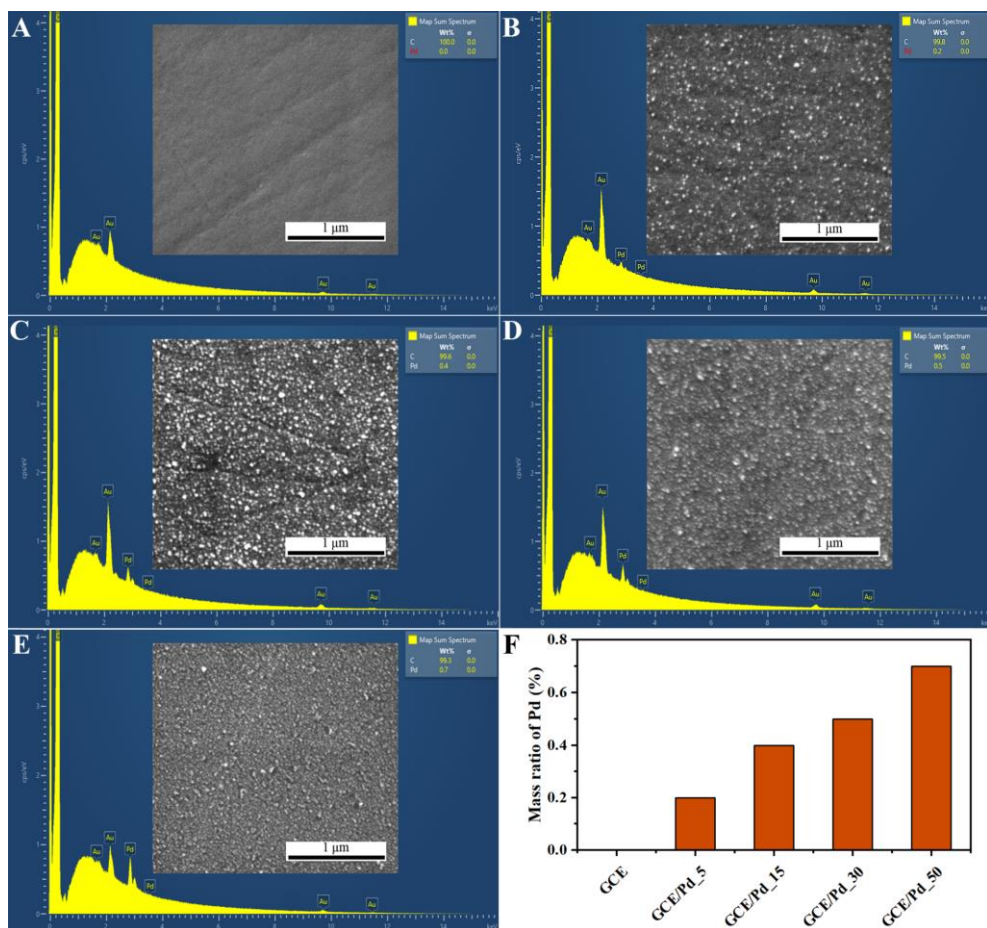


Figure 4.6. EDS spectrum and SEM (insert) of different amounts of Pd NPs on GCE. (A) clean GCE surface. (B) Pd NPs coated on GCE for 5 min (GCE/Pd_5). (C) Pd NPs coated on GCE for 15 min (GCE/Pd_15). (D) Pd NPs coated on GCE for 30 min (GCE/Pd_30). (E) Pd NPs coated on GCE for 50 min (GCE/Pd_50). (F) The summary of mass ratio of Pd on the different samples in A~E. The mass ratio of Pd is the Pd ratio to the sum of Pd and carbon in atomic mass. Note the peaks belonging to Au were caused by Au coating during SEM preparation, Au is therefore excluded in the map sum spectrum table

4.3.2 The effect of MtrC, OmcA, cellular respiration

The cytochromes *c* play an important role in EET, and they are also possibly responsible for the biological formation of Pd NPs (157). The cytochromes *c* MtrC and OmcA on MR-1 cells membrane are implicated in the EET process (85, 164) and the outward EET process is severely inhibited after MtrC and OmcA were knocked out (288), as shown in Figure 4.7. To explore the role of MtrC and OmcA, a *Shewanella oneidensis* MR-1

$\Delta omcA/mtrC$ mutant (MR-1 mutant) was studied under the same experimental conditions. A similar electrocatalysis phenomenon is observed for the MR-1 mutant with the same irreversible CV pattern (Figure 4.8A), implying only minor effects of MtrC and OmcA, which is contrast to Fe(III) reduction by this mutant (288). Other active sites can therefore possibly contribute to the electrocatalysis. To study the role of the metabolism of MR-1 in the electrocatalysis, inactive MR-1 cells were prepared by repeatedly freezing with liquid nitrogen, maintaining most of the proteins. As shown in the growth curves, the inactive MR-1 cell culture were unable to grow up to 96 h (Figure 4.9), demonstrating a total inhibition of metabolic activities. The main cell membrane of inactive MR-1 was, however, retained regardless of some deformation (Figure 4.10). Notably, the inactive MR-1 caused an asymmetric voltammetric pair of peaks in $[\text{Fe}(\text{CN})_6]^{4-}$ solution (Figure 4.8B) with a strong anodic peak, indicating the maintaining of the electrocatalysis to $[\text{Fe}(\text{CN})_6]^{4-}$.

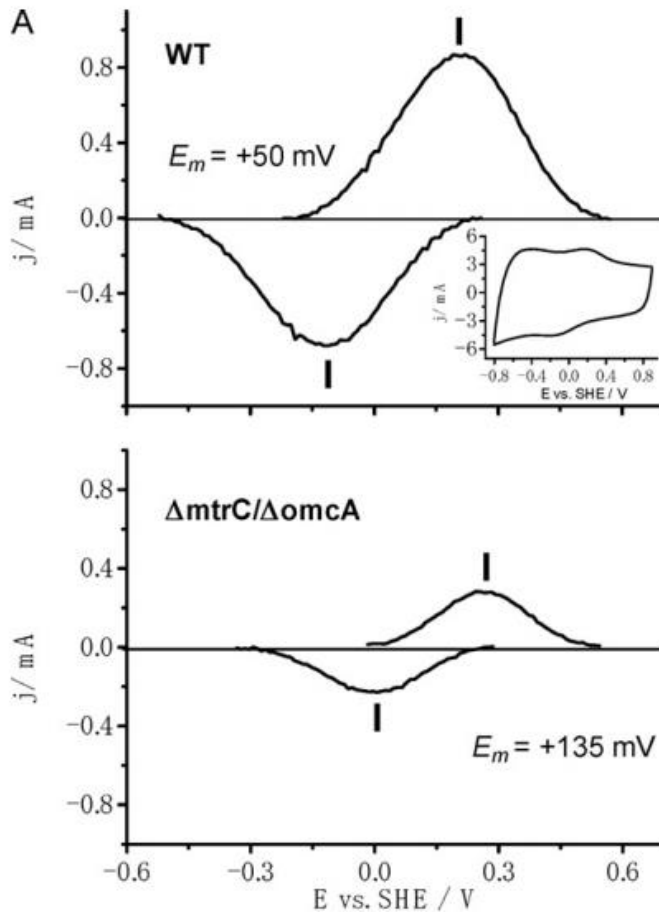


Figure 4.7. Baseline-subtracted cyclic voltammogram of a monolayer biofilm of wild type (WT) and

ΔomcA/ΔmtrC obtained after electrochemical cultivation. The inset shows the raw data for WT cells. Reproduced from ref (288) with permission.

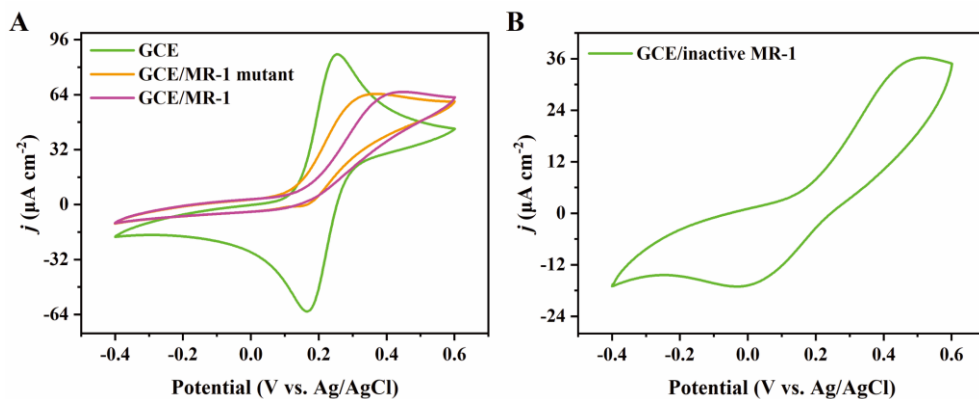


Figure 4.8. The effect of *OmcA*, *MtrC*, and the metabolism of MR-1 on $[Fe(CN)_6]^{4-}$ oxidation. CV on (A) MR-1 $\Delta omcA/mtrC$ mutant (MR-1 mutant) and (B) repeatedly frozen MR-1 (inactive MR-1) in 1.0 mM $[Fe(CN)_6]^{4-}$. 50 mM PBS (pH 7.0). Scan rate 10 mV s^{-1} .

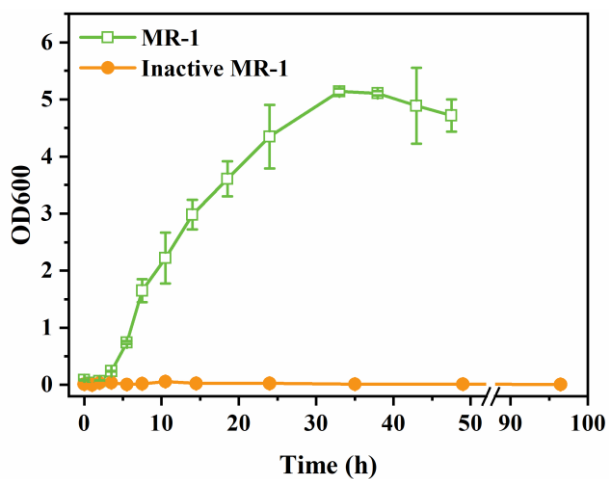


Figure 4.9. Growth curves of MR-1 and repeatedly frozen MR-1 (inactive MR-1) in LB medium.

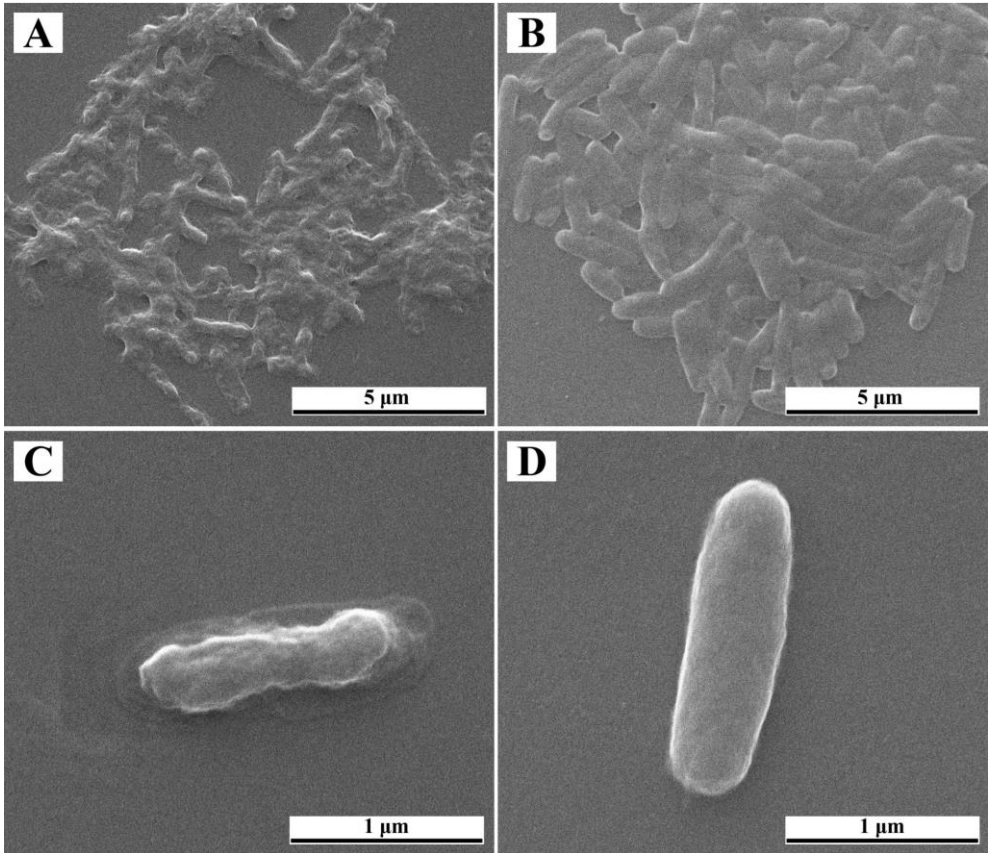


Figure 4.10. SEM of MR-1 before and after freezing. SEM of (A and C) repeatedly frozen MR-1 (inactive MR-1) and (B and D) MR-1 before freezing.

In brief, MtrC, OmcA, and cellular respiration are not critical in the inward EET process of MR-1, which infer different pathways of the inward EET compared to the outward EET.

4.3.3 The mediating effect of $[\text{Fe}(\text{CN})_6]^{4-/3-}$ without extracellular electron donors is limited

$[\text{Fe}(\text{CN})_6]^{4-/3-}$ can act as a redox mediator in some bioelectrochemical process due to high reversibility (140, 289), like an endogenous redox mediator riboflavin secreted by *Shewanella* (89). However, the mediating effect of $[\text{Fe}(\text{CN})_6]^{4-/3-}$ alone in non-turnover (without external electron donors) conditions is hard to explain the electrocatalysis.

In the mediating model, $[\text{Fe}(\text{CN})_6]^{4-/3-}$ shuttle between the electrode surface and the surface of EAB. The model seems applicable to the current experiments since the MR-1 layer is not impenetrable and a limited amount of $[\text{Fe}(\text{CN})_6]^{4-}$ may penetrate the cell layers and reach the confined electrode surface not occupied by MR-1 cells. Note that the

occupation by microbes will decrease the current (290), Figure 4.11. When limited amounts of $[\text{Fe}(\text{CN})_6]^{4-/3-}$ are confined to the small space between the cell layer and the electrode, $[\text{Fe}(\text{CN})_6]^{3-}$ is reduced to $[\text{Fe}(\text{CN})_6]^{4-}$ on the interface between the electrolyte and the EAB after taking electrons from the EAB. $[\text{Fe}(\text{CN})_6]^{4-}$ is re-oxidized to $[\text{Fe}(\text{CN})_6]^{3-}$ on the interface between the electrolyte and the electrode after releasing electrons to the electrode (Figure 4.12A). In this case, $[\text{Fe}(\text{CN})_6]^{4-}$ tends to accumulate, and an asymmetric CV with a strong anodic peak and a weak cathodic peak appear on condition that the ET from $[\text{Fe}(\text{CN})_6]^{3-}$ reduction by the EAB continuously outperforms that from $[\text{Fe}(\text{CN})_6]^{4-}$ oxidation by the electrode during the whole scan (e.g., in a CV with low scan rate). Furthermore, the electrons relayed by $[\text{Fe}(\text{CN})_6]^{4-/3-}$ are ultimately from the metabolism of EAB, for example, the oxidation of acetate or lactate.

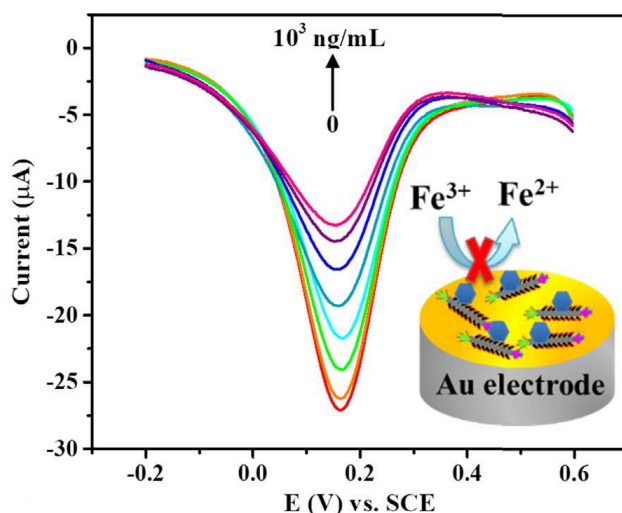


Figure 4.11. DPV responses of fabricated immunosensors after immunological recognition with different concentrations of total prostate-specific antigen (*t*-PSA) ($0, 10^{-2}, 10^{-1}, 1, 10, 10^2$ and 10^3 ng mL^{-1}). Inset, the schematic illustration of the phage-based immunosensor for *t*-PSA detection. The Fe^{2+} and Fe^{3+} indicate $[\text{Fe}(\text{CN})_6]^{4-}$ and $[\text{Fe}(\text{CN})_6]^{3-}$, respectively. Reproduced from ref. (290) with permission.

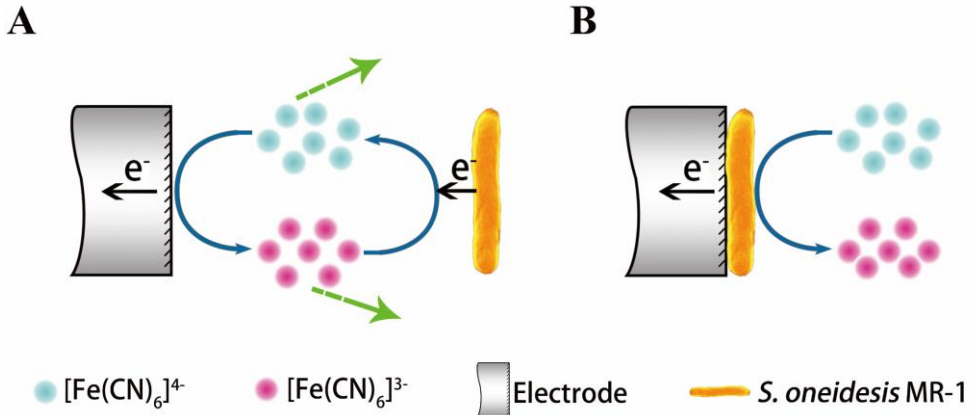


Figure 4.12. Two different models of $[\text{Fe}(\text{CN})_6]^{4-/3-}$ in the interaction with MR-1. (A) Mediating model, in which $[\text{Fe}(\text{CN})_6]^{4-/3-}$ act as a redox mediator between MR-1 and electrode. $[\text{Fe}(\text{CN})_6]^{4-/3-}$ can diffuse into the bulk electrolyte if the space between the MR-1 layer and the electrode is wide or not isolated (green dotted arrows). (B) Electrocatalysis model, in which $[\text{Fe}(\text{CN})_6]^{4-/3-}$ acts as the reactant/product of the electrocatalysis by MR-1

On the other hand, different CVs will be observed if $[\text{Fe}(\text{CN})_6]^{4-/3-}$ can diffuse to the bulk electrolyte freely, or the distance between the electrode surface and EAB layer is long, or the voltammetric scan is fast. The $[\text{Fe}(\text{CN})_6]^{4-}$ reduced by MR-1 can diffuse to bulk electrolyte and unlikely to get back to the electrode and be re-oxidized. Similarly, the $[\text{Fe}(\text{CN})_6]^{3-}$ oxidized by the electrode can spread into the electrolyte solution and MR-1 is difficult to capture and reduce the $[\text{Fe}(\text{CN})_6]^{3-}$. Moreover, the $[\text{Fe}(\text{CN})_6]^{3-}$ from bulk electrolyte can further dilute the mediating effect of $[\text{Fe}(\text{CN})_6]^{4-/3-}$. Symmetric CV shape would be therefore presented in this situation. For example, when a polyviologen modified glassy carbon electrode (PV-GCE) was used to separate microbes from the electrode surface (140), as shown in Figure 4.13, microbes including EAB colonizing on the PV layer need to employ mediators $[\text{Fe}(\text{CN})_6]^{3-}$ to communicate with the electrode (Figure 4.12A). However, the mediating $[\text{Fe}(\text{CN})_6]^{4-/3-}$ can freely diffuse to the bulk electrolyte, one symmetric CV was therefore observed (140). A similar voltammetric experiment was conducted in 1 mM $[\text{Fe}(\text{CN})_6]^{3-}$ and 9 mM glucose at 50 mV s⁻¹, but $[\text{Fe}(\text{CN})_6]^{4-/3-}$ was trapped in the narrow space between the MR-1 layer and the electrode surface. Although MR-1 is unable to use glucose as an electron donor (291), the addition of glucose aims to obtain a full comparison. In contrast, the CV became asymmetrical when MR-1 cells were attached on an electrode in solution containing 1 mM $[\text{Fe}(\text{CN})_6]^{3-}$ and 9 mM glucose at 50 mV s⁻¹ (Figure 4.14). The different CV shapes in mediating models may originate from the varied freedom to diffuse and the size of confinement of $[\text{Fe}(\text{CN})_6]^{4-/3-}$. In another study, diaphorase molecules, which catalyze the oxidation of nicotinamide adenine dinucleotide (NADH), were absorbed on a PV layer on GCE. The PV layer can accumulate or “trap” $[\text{Fe}(\text{CN})_6]^{4-/3-}$. An asymmetric CV, similar to the ones in the current experiment,

appeared when the PV-GCE was immersed in a mixed electrolyte containing $[\text{Fe}(\text{CN})_6]^{4-}$, diaphorase, and NADH (292). Electrons were captured from NADH by diaphorase, from which the electrons were shuttled by $[\text{Fe}(\text{CN})_6]^{4-/3-}$ to the electrode. Consequently, a strong anodic peak and a weak cathodic peak appeared, and the anodic peak from NADH oxidation vanished because $[\text{Fe}(\text{CN})_6]^{4-/3-}$, rather than NADH, interacted with the electrode. Additionally, sufficient electron donor NADH (1 mM) ensured a steady catalytic CV curve.

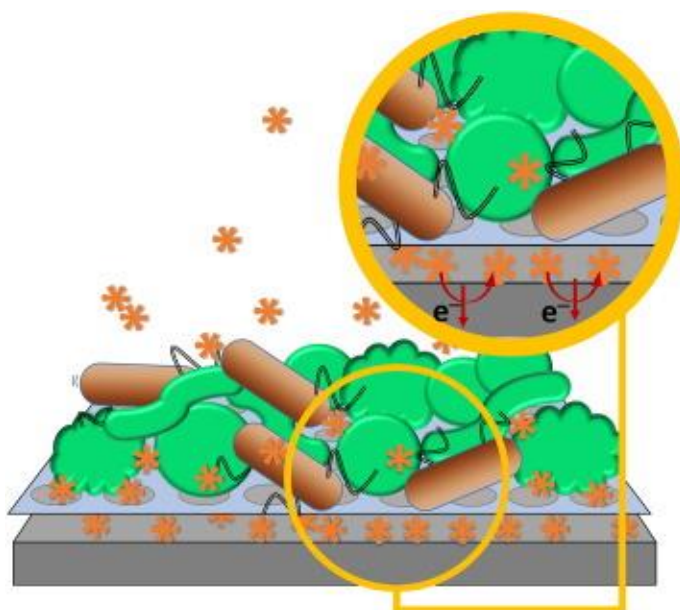


Figure 4.13. Schematic diagram of environmental microbes colonizing on the PV-GCE and exploiting soluble $[\text{Fe}(\text{CN})_6]^{3-}$ for current generation, Reproduced from reference (140).

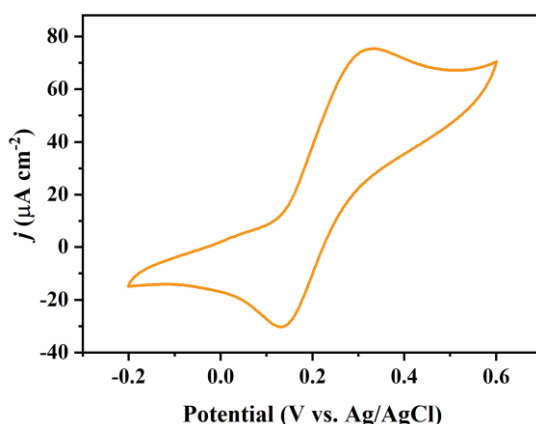


Figure 4.14. The conversion of $\text{K}_3[\text{Fe}(\text{CN})_6]$ on MR-1. The CV of GCE/MR-1 in 1 mM $\text{K}_3[\text{Fe}(\text{CN})_6]$ and 9 mM glucose at 50 mV s^{-1} . The electrolyte 50 mM PBS (pH 7.0)

In brief, in the mediating model, asymmetric CVs emerge provided that limited amounts of $[\text{Fe}(\text{CN})_6]^{3-}$ are confined in a small space between the EAB layer and the electrode surface, abundant substrates (*e.g.*, lactate for MR-1) are provided, and the CV scan rate is relatively low. In contrast, CV is symmetric if $[\text{Fe}(\text{CN})_6]^{4-/3-}$ can spread into bulk electrolyte freely, or the confined space is large, or the scan rate is high. This model explained the dependence of $[\text{Fe}(\text{CN})_6]^{4-}$ concentration and scan rate in **Figure 3.11** (page 71) and Figure 3.12 (page 72). In the current experiment, the asymmetric CV pattern is unchanged from the second to the sixth CV scan (Figure 4.15). The anodic peak current in the first scan was lower than the rest of scans due to partial oxidation of $[\text{Fe}(\text{CN})_6]^{4-}$ by oxygen in the air during preparation. The CVs were conducted under non-turnover conditions, *i.e.*, without substrates. The anodic current from substrates oxidation would therefore shrink with the gradual consumption of stored substrates (if there is any) in the cells, which is in contrast to the current experimental results (Figure 3.4 in page 63, Figure 3.10A in page 68, and Figure 4.15).

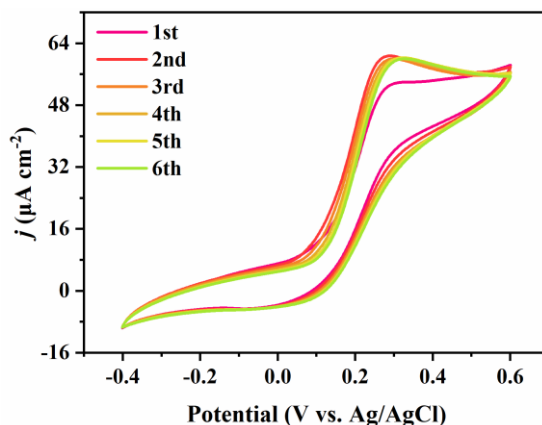


Figure 4.15. The first to the sixth scan of cyclic voltammetry (CV) of the conversion of $[\text{Fe}(\text{CN})_6]^{4-}$ by MR-1. The CV on MR-1 coated glassy carbon electrode (GCE/MR-1) in 1 mM $[\text{Fe}(\text{CN})_6]^{4-}$. 50 mM PBS (pH 7.0). Scan rate 10 mV s^{-1} .

Pd NPs can participate in the EET process of *Desulfovibrio desulfuricans* (201), and a similar function of Au NPs was also found in MR-1 $\Delta omcA/mtrC$ mutant (164). An anodic current increase, or at least not a decrease, would therefore be expected when MR-1 is modified by Pd NPs, which is different from the observation that the anodic current decreases with the increasing loading of Pd NPs (Figure 4.1). In addition, since RF is an endogenous redox mediator utilized by MR-1, an asymmetric CV would be obtained for RF if the mediating model can lead to electrocatalysis. This does not, however, match the result shown in Figure 3.2C in page 61. Furthermore, the electrocatalysis remained after the MR-1 cells were deactivated. The metabolic activity of the cells is the premise of the mediating effect. However, MR-1 cells exhibit electrocatalysis, even when they are unable to multiply (Figure 4.8B).

4.3.4 The direct EET between MR-1 and the electrode is feeble

An electrocatalysis model was considered, in which MR-1 could oxidize $[\text{Fe}(\text{CN})_6]^{4-}$ and capture electrons at the interface between the electrolyte and the cell surface. The electrons are transported to the electrode through the interface between cell surface and the electrode coupled with the oxidation of some redox molecules (e.g., cytochromes *c*) on the cell membrane (Figure 4.12B). This model is justified by the fact that considerable MR-1 cells are attached on the electrode surface. The electrochemical signals of redox proteins in the outer membrane of MR-1 were detected in DPV (Figure 4.16). A redox pair with the peak potentials -0.435 V (anodic) and -0.415 V (cathodic) are attributed to flavins (80, 89, 293), while the pairs at -0.137 as well as 0.065 V (anodic) and -0.124 as well as 0.113 V (cathodic) are attributed to outer membrane cytochromes *c* (80, 293, 294). Similar electrochemical signals were obtained from previous reports when MR-1 are physically attached *via* this method (80, 133, 138, 164, 177, 201). These results strongly support that sufficient MR-1 cells are directly contacting the electrode surface instead of being far away from the surface of the electrode. In the electrocatalysis model, the electrons are from the oxidation of abundant $[\text{Fe}(\text{CN})_6]^{4-}$ instead of MR-1 cells. The anodic current therefore remained at a comparable level with bare electrodes.

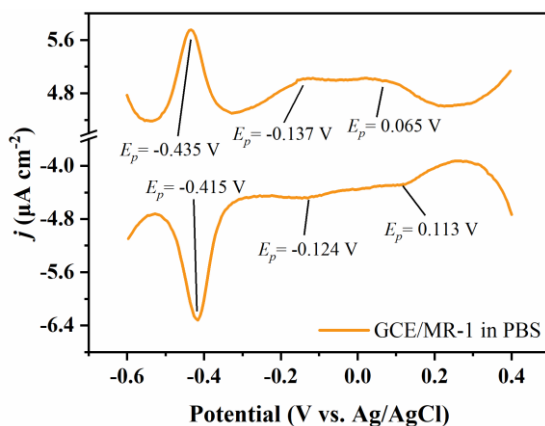


Figure 4.16. Differential pulse voltammetry (DPV) of MR-1 cells coated on a GCE

However, the electrocatalysis model hardly rationalize the midpoint potential shifts when different redox molecules were used (Figure 3.6, page 65). During the forward CV scan (from low potential to high potential), the electrode directly oxidizes the redox molecules on the cell membrane regardless of which reactant in electrolyte. The midpoint potential in CVs is thus related to the redox molecules on the cell membrane, not the reactant in the electrolyte. For example, the peaks of cytochromes *c* on *Geobacter sulfurreducens*, instead of the peak of acetate, were enhanced when *Geobacter sulfurreducens* catalyzed the oxidation of acetate (295). By contrast, the peak belonging to cytochromes *c* around -0.1 V disappeared when $[\text{Fe}(\text{CN})_6]^{4-}$ was introduced (Figure 4.17). The peak of

cytochromes *c* should be enhanced if electrons were transported directly from cytochromes *c* to the electrode.

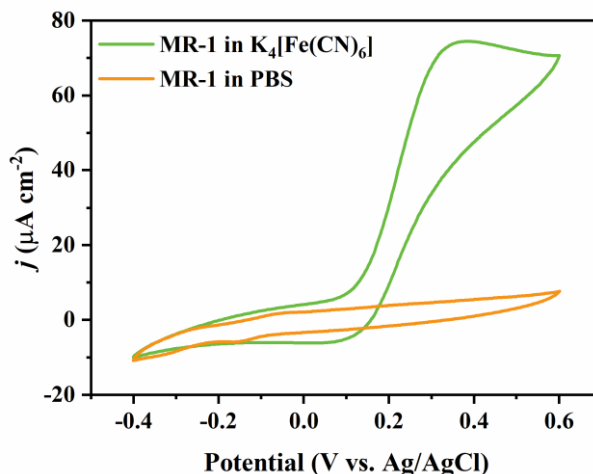


Figure 4.17. Comparison of electrochemical signal of GCE/MR-1 in PBS and PBS containing 1 mM $[\text{Fe}(\text{CN})_6]^{4-}$. Scan rate 10 mV s^{-1} .

The direct EET between MR-1 and the electrode is therefore weak, and the strong ET signal in the forward scan (*i.e.*, anodic current) must be accomplished through another EET pathway. A plausible model combining electrocatalysis and mediating model is proposed and will be discussed in the section 4.3.5.

4.3.5 Electron uptake mechanism by MR-1

We here have found the intake of electrons from $[\text{Fe}(\text{CN})_6]^{4-}$ by MR-1, presenting an irreversible voltammetry pattern. The discovery of the ability for MR-1 to take electrons from $[\text{Fe}(\text{CN})_6]^{4-}$ broadens our knowledge about the role of dissimilatory metal reduction bacteria in BESs. MR-1 promotes only anodic current and blocks cathodic current during $[\text{Fe}(\text{CN})_6]^{4-/3-}$ cycling. This electrocatalysis is in contrast to *E. coli* K-12 and *Streptococcus mutans* (261), in which both cathodic and anodic CV peaks shrunk equally. So far, we only find that MR-1 electrocatalyzes the oxidation of negatively charged redox molecules with high midpoint potentials. Hence, other bacteria do not catalyze the oxidation of $[\text{Fe}(\text{CN})_6]^{4-}$ to $[\text{Fe}(\text{CN})_6]^{3-}$, but increase the barrier for interfacial ET. These results also exclude the effect of the negative charges on electrode surfaces causing “electrochemical rectification” with an asymmetric voltammetric shape for a redox couple (296), because MR-1, *E. coli* K-12, and *Streptococcus mutans* are all negatively charged in a neutral medium (297). The occurrence of irreversible voltammetry on other negatively charged redox molecules with high midpoint potentials implies clear connection between the electrocatalysis and redox potential as well as overall charge(s).

As an inward EET, $[\text{Fe}(\text{CN})_6]^{4-}$ oxidation is different from the reduction of insoluble Fe(III) or Mn(IV) hydr(oxides). In spite of the fact that there is porin protein on the cell membrane, e.g., GspD, Figure 4.18, but they are not open until protein secretion occurs (298). Small molecules such as $\text{S}_2\text{O}_3^{2-}$, SO_4^{2-} and NO_3^- (Figure 4.19) can be taken up by MR-1, but these molecules are small, about 0.24, 0.22, and 0.20 nm, respectively in diameter based on the bond type and bond length, Figure 4.19, Table 4.1, and Table 4.2. The diameter of hydrated $[\text{Fe}(\text{CN})_6]^{4-}$ is at least 1.2 nm (299), and $[\text{Fe}(\text{CN})_6]^{4-}$ can hardly penetrate the lipid bilayer of the cell membrane (300). However, the $[\text{Fe}(\text{CN})_6]^{4-}$ can effectively diffuse to the outer membrane due to its high solubility. The presence or absence of EPS on MR-1 make no difference in $[\text{Fe}(\text{CN})_6]^{4-}$ oxidation, while EPS plays a crucial role in the outward EET of MR-1 (80).

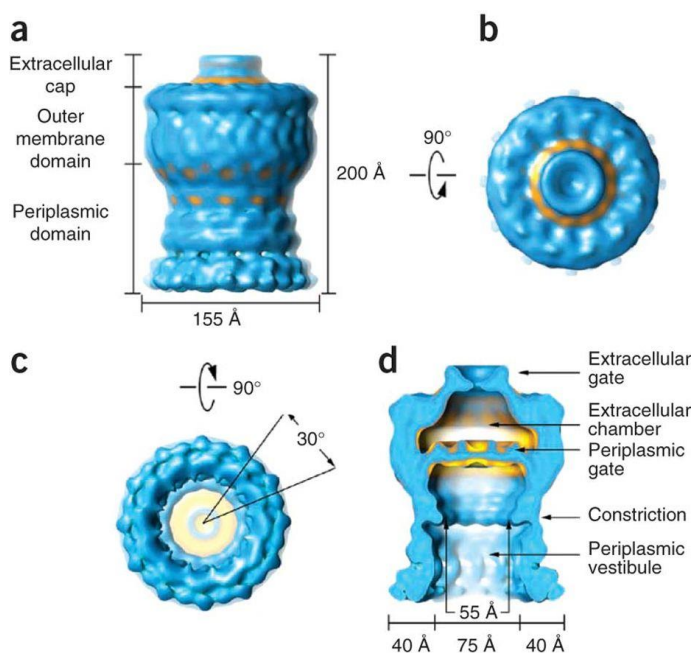


Figure 4.18. Three-dimensional electron cryo-EM reconstruction of GspD. Reproduced from ref. (298) with permission.

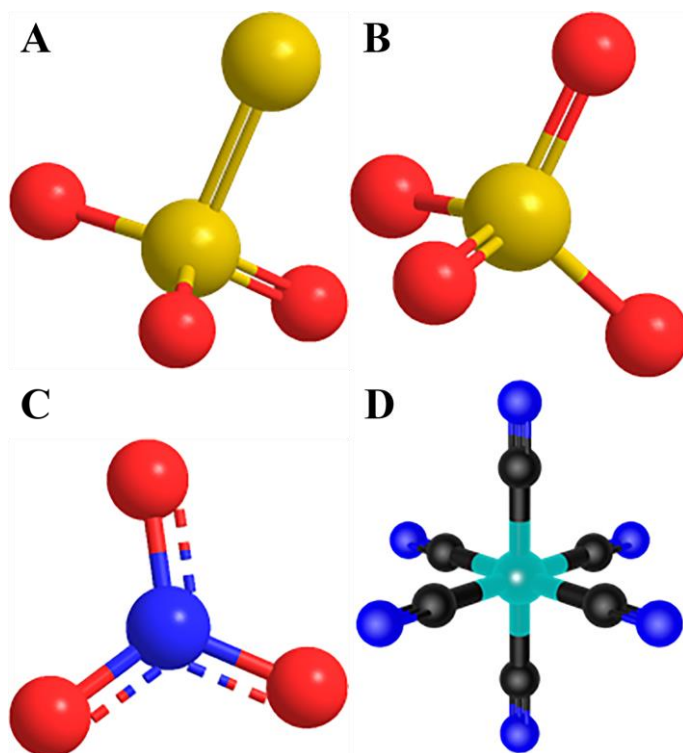
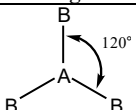
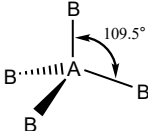
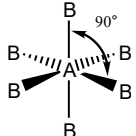


Figure 4.19. Structure of (A) $S_2O_3^{2-}$, (B) SO_4^{2-} , (C) NO_3^- and (D) $[Fe(CN)_6]^{4-}$. The S, O, N, Fe, and C is yellow, red, blue, green, and black respectively.

Table 4.1. Average bond lengths

Bond type	Bond length (pm)
C≡N	116
C–Fe	194
N=O	131
S–O	166
S=O	145
S=S	175

Table 4.2. Geometry of molecules

Geometry type	Molecular geometry	Examples
Trigon planar		NO_3^-
Tetrahedral		$\text{S}_2\text{O}_3^{2-}$, SO_4^{2-}
Octahedral		$[\text{Fe}(\text{CN})_6]^{4-}$

Very notably, Pd NPs on MR-1 are found to block $[\text{Fe}(\text{CN})_6]^{4-}$ oxidation catalyzed by the cells. The production of Pd NPs involves cytochrome *c* (157). Hence it is possible that certain cytochromes *c* affect or participate in the electrocatalytic oxidation. On the other hand, cytochromes *c* MtrC and OmcA do not catalyze $[\text{Fe}(\text{CN})_6]^{4-}$ oxidation, which are crucial to the reduction of various insoluble electron acceptors (85, 164). Considering the unique electrocatalysis of $[\text{Fe}(\text{CN})_6]^{4-}$ oxidation, we believe that other active sites on MR-1 are responsible for the catalysis. We have not identified the composition of these active sites, but we hypothesize that they could be, macromolecules even proteins, such as high-redox potential cytochromes *c*, laccases, or peroxidase, adjacent to active sites of $[\text{PdCl}_4]^{2-}$ reduction and contribute to the electrocatalysis of $[\text{Fe}(\text{CN})_6]^{4-}$ oxidation. These active sites may also be responsible for the Mn(II) oxidation as mentioned in the introduction part of this chapter. There are two possible pathways for iron respiratory, *i.e.*, downhill pathway and uphill pathway. The downhill pathway produces energy, in which the electrons from iron oxidizing are terminally transferred to oxygen reduction. The uphill pathway is related to protonmotive forces, in which electrons are transported against the unfavorable redox potential and finally reach NAD(P)^+ (245, 301), as show in Figure 4.20. The cytochromes *c* thus cannot be excluded completely. Furthermore, MR-1 is capable of oxidizing $[\text{Fe}(\text{CN})_6]^{4-}$ after repeated freezing. In this case, the respiration of MR-1 is negligible. Instead of the respiration of MR-1, the inherent properties of the active sites therefore dominate the catalysis of $[\text{Fe}(\text{CN})_6]^{4-}$, which further differs from the reduction of insoluble Fe(III)/Mn(IV) oxides.

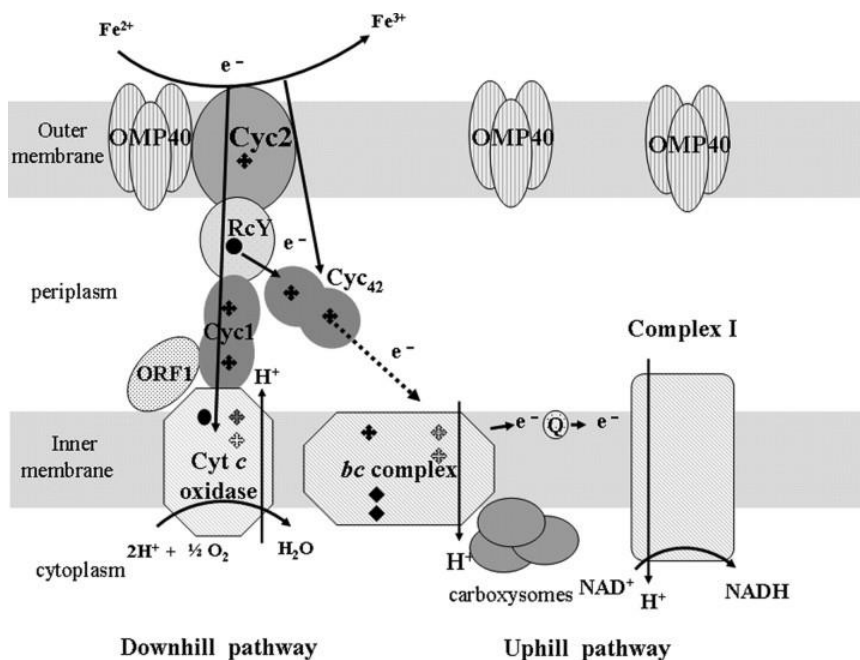


Figure 4.20. Two pathways of iron respiration. Reproduced from ref. (245) with permission.

A plausible model with inward EET and outward EET is proposed for $[\text{Fe}(\text{CN})_6]^{4-}$ oxidation electrocatalyzed by MR-1 (Figure 4.21). $[\text{Fe}(\text{CN})_6]^{4-}$ can diffuse into the space between the MR-1 layer and the electrode or adsorb on the surface of the MR-1 cells, as well as stay in the bulk electrolyte. In fact, $[\text{Fe}(\text{CN})_6]^{4-}$ plays two roles in the model. Firstly, electrons from $[\text{Fe}(\text{CN})_6]^{4-}$ are transferred into the MR-1 cells where the active sites on the cell membrane oxidize $[\text{Fe}(\text{CN})_6]^{4-}$ to $[\text{Fe}(\text{CN})_6]^{3-}$. This is an inward EET process (Figure 4.21B). Secondly, the electrons obtained can be transferred to the electrode by two forms of outward EET. It has been reported that mediated EET is the main outward EET strategy of MR-1, contributing more than 70% current of outward EET (89). The majority of electrons would therefore be transferred by the indirect EET mediated by $[\text{Fe}(\text{CN})_6]^{4-/3-}$. A small fraction of electrons may be transferred to the electrode via the direct EET form. The mediating effect of $[\text{Fe}(\text{CN})_6]^{4-/3-}$ are valid both in the complete MtrCAB pathway and the incomplete MtrCAB pathway. In the complete MtrCAB pathway, the electrons are delivered from CymA to MtrA, where MtrA and MtrB relay the electrons to MtrC and OmcA, and electrons are finally received by $[\text{Fe}(\text{CN})_6]^{3-}$. In the incomplete MtrCAB pathway, MtrC and OmcA are removed. Nonetheless, MtrA fully inserts into MtrB (254), and $[\text{Fe}(\text{CN})_6]^{3-}$ may therefore execute outward EET by directly accepting electrons from the MtrA (Figure 4.21C). The exact route for the ET from the active sites on the cell membrane (red dotted circle in Figure 4.21) to the sites where $[\text{Fe}(\text{CN})_6]^{4-/3-}$ mediate EET (blue dotted circle in Figure 4.21) is not clear yet and needs further investigation.

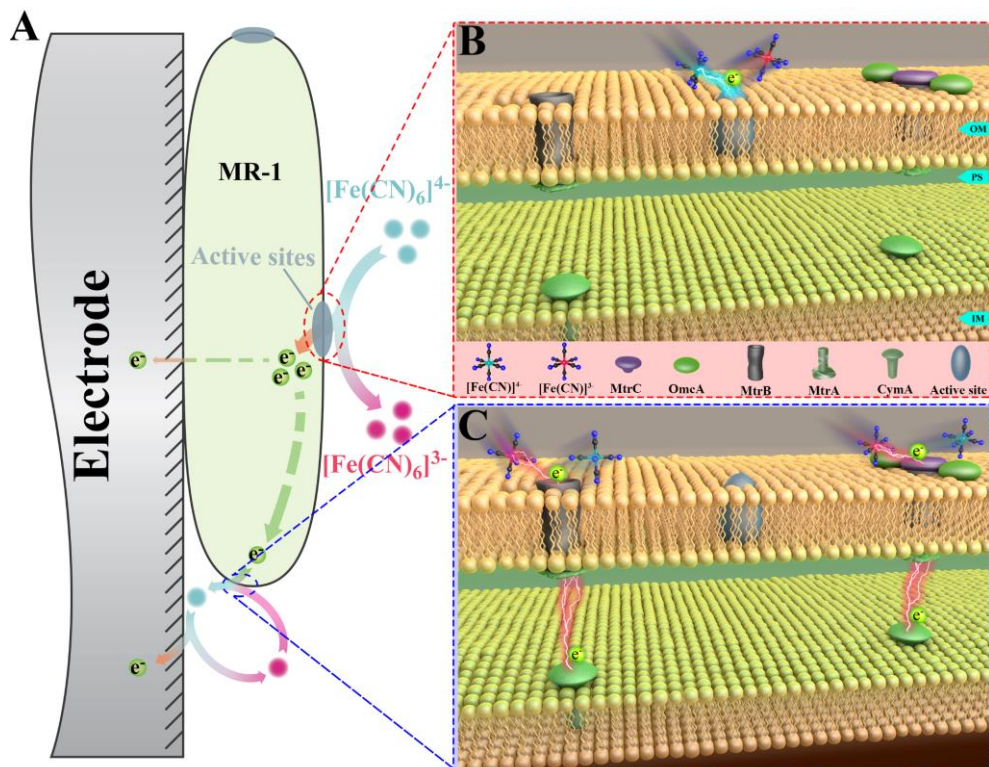


Figure 4.21. Illustration of electron uptake by MR-1 from $[\text{Fe}(\text{CN})_6]^{4-}$. (A) The overall process of the inward and outward EET of $[\text{Fe}(\text{CN})_6]^{4-}$ from MR-1 to the electrode. $[\text{Fe}(\text{CN})_6]^{4-}$ is oxidized (red dotted circle) and the electrons obtained are mainly transported by the indirect EET through the mediator $[\text{Fe}(\text{CN})_6]^{4-/3-}$ (blue dotted circle). The rest of electrons may be transferred via short-range direct EET by redox molecules on the membrane. The processes indicated by green dotted arrows are not clear yet. Only one MR-1 cell is presented for clarity. (B) Inward EET. In this process, bulk $[\text{Fe}(\text{CN})_6]^{4-}$ in the electrolyte is oxidized by the active sites on MR-1 and electrons are captured. (C) Outward EET. In this process, a small portion of $[\text{Fe}(\text{CN})_6]^{4-}$ diffuse into the narrow confinement between the MR-1 layer and the electrode surface and shuttle the EET process between the cell and the electrode. This mediating process can proceed with or without MtrC and OmcA. Only relevant parts are presented, and the quinone and quinol pool in the cytoplasmic membrane are not shown for simplicity. OM: outer membrane; PS: periplasm; IM: inner membrane. The scale is not proportional.

Chemical compositions of the relevant active sites on MR-1 contributing to such unique electrocatalysis is not clear yet. However, the function of these active sites is somehow similar to metalloproteins such as high-potential cytochromes *c*, laccases, or peroxidase. Moreover, we notice that, instead of the respiration of MR-1, the intrinsic catalytic activities of the active sites contribute to the electrocatalytic oxidation of $[\text{Fe}(\text{CN})_6]^{4-}$. We cannot exclude the possibility of other compounds as the origin of the active sites on MR-1. Although MR-1 was reported to be able to oxidize Mn(II) (279), the ability of MR-1 to

oxidize iron compounds has not been discovered before. More effort should be spent to study the composition and function of the active sites in future studies.

4.4 Conclusions

Pd NPs on the cells can block the active sites and undermine the electrocatalysis of $[\text{Fe}(\text{CN})_6]^{4-}$ oxidation by MR-1. The Pd NPs *per se* do not impair the electrooxidation of $[\text{Fe}(\text{CN})_6]^{4-}$, as confirmed by CV of abiotic Pd NPs. Moreover, the electrocatalysis is mainly attributed to the inherent catalytic properties of the active sites rather than the respiration of MR-1. A model with the combination of electrocatalysis of $[\text{Fe}(\text{CN})_6]^{4-}$ and the mediating effect of $[\text{Fe}(\text{CN})_6]^{4-/3-}$ is therefore proposed. The electrocatalysis of $[\text{Fe}(\text{CN})_6]^{4-}$ involves unidentified active sites. Furthermore, the mediating role of $[\text{Fe}(\text{CN})_6]^{4-/3-}$ can be executed either with or without MtrC and OmcA. Our experiments indicate strongly that the active sites are most likely located in cell membrane with biomolecule properties. The properties of the active sites are different from those of the widely studied substances related with MR-1 (*e.g.*, RF, MtrC, and OmcA). To identify the origin and chemical composition of these active sites on MR-1 is crucial, and such investigations require comprehensive efforts in electrochemistry, microbiology, and nanochemistry. The discovery of unique electrocatalysis of MR-1 towards the oxidation of $[\text{Fe}(\text{CN})_6]^{4-}$ provides a better understanding of the role of dissimilatory metal reduction bacteria in BESs and the detection of redox molecules with high midpoint potential and negative charge(s).

Chapter 5

Co-recycling of metals by *S. oneidensis*

MR-1

This chapter describes the effect of Cu(II) and various media to the recycling of Pd(II) from solution. The removal efficiency of Cu and Pd, as well as the morphologies and elemental compositions of the biotic Pd, Cu, CuPd NPs is discussed.

5.1 Introduction

With the development of human technological activities and the human population, the emissions of metals into the environment have been increasing and caused serious environmental pollution, which threatens the sustainable development of human society. Different techniques have been developed to tackle the problem, and biotechnological methods are drawing attention as an emerging clean alternative. Among biotechnological methods, bioremediation and biorecovery using microbes to remove and recover metals from wastewater have plenty of merits, such as rapid growth of biomass, mild operational conditions, and high sensitivity (can reclaim metals as low as $\text{mg}\cdot\text{L}^{-1}$) (302).

Biorecovery and bioremediation (bio-remediation/recovery) are achieved by the biosorption and redox reactions of metals on the surface and inside of microbes. According to existing studies, the reduction and oxidation of metals by microbes are frequently primary actors for bio-remediation/recovery (302, 303). Fundamental investigations of how microbes reduce or oxidize metals are therefore of importance. Numerous studies have been conducted to illustrate the ability of different microbes and optimize experimental conditions to improve the performance of bio-remediation/recovery. *Shewanella putrefaciens* CN32 bacterium was able to reclaim fast Au(III), Co(II), and Fe(II) with high absorption capacities up to 1346, 335, and 302 mg metals/g biomass from solution (203). Amorphous Ru, Rh, Co, Ni, and Li NPs, and crystalline Ag, Fe, Pd, and Pt

NPs were synthesized by *Pseudomonas aeruginosa* SM1 separately. NPs in cells (Co and Li) and out of cells (Ag, Pd, Fe, Rh, Ni, Ru, and Pt) were both observed (304).

In spite of extensive investigations relating to bio-remediation/recovery, gaps exist between common experimental conditions in labs and practical applications. One of the gaps is the difference in the composition between synthetic wastewater and real wastewater. Different metals are individually researched in labs while actual wastewater, in most cases, is a cocktail of various metals. The presence of given metal ions in aqueous solution can significantly influence the formation of other metal NPs. Hydrogenases are involved in a number of metal reductions, such as the reduction of Au(III) and Pd(II) by *Escherichia coli* (302, 303), and Pd(II) by MR-1 (161). However, Cu(II), which is very common in practical wastewater, is a hydrogenase inhibitor. Cu(II) can selectively inhibit the activities of hydrogenases in the periplasm, and spare the ones in the cytoplasm (305, 306). The presence of Cu(II) in solution would therefore impair the bio-remediation/recovery of other metals (303, 305, 306). MR-1 was recently reported to reduce Cu(II) to Cu(0) either intracellularly and extracellularly (158), but the effect of Cu(II) on the bio-remediation/recovery of MR-1 remains to be explored. On the other hand, the presence of some metal ions can enhance the formation of other metal NPs. Fe(III) promotes the reduction of Te(IV) to Te(0) and produces crystalline Te(0) nanorods extracellularly by MR-1, while fewer Te(0) nanorods were formed intracellularly in the absence of Fe(II) (218). Outer membrane-bound cytochromes *c* are also responsible for the formation of diverse metal and metalloid NPs (Figure 1.20, page 26). The formation of solid NPs can have dual influences. The formation of solid NPs can apparently block the mass transfer and prevent the transport of metal ions into the periplasm and cytoplasm. The NPs formation from the metal ions that have to be reduced intracellularly would therefore decrease, but the formation of certain NPs can enhance EET (164, 201). The reduction of metal ions on the outer membrane would then be elevated and as a result, the biosynthesis of corresponding NPs boosted. As a model EAB, MR-1 exerts versatile roles in bio-remediation/recovery, but the inhibition of Cu(II) to the metal reduction by MR-1 is not clear yet.

Another gap is the difference in the media. To keep the viability of microbes, buffer agents (HEPES, MOPS, *etc.*) are often added to the solution to maintain neutral pH. However, this is impractical in treating actual wastewater, because it is either cost-effective nor environmentally-friendly. Moreover, the addition of some buffer agents will precipitate some metal ions, which actually achieves remediation but the subsequent biorecovery is unlikely to proceed. Some buffer agents also possess redox properties and potentially promote redox reactions that could be credited to the effect of microbes. Some buffers also evoke the formation of complexes with metals and the generation of radicals (307, 308), which further challenge bio-remediation/recovery in practical applications.

In this chapter, we explore the bio-remediation/recovery of Cu(II) by MR-1, and the simultaneous bio-remediation/recovery of Cu(II) and Pd(II) by MR-1. The effect of Cu(II) on the biorecovery of Pd(II) as well as the influence different media on bio-remediation/recovery of Cu(II) and Pd(II) by MR-1 is practically addressed.

5.2 Experimental section

5.2.1 Chemicals

$\text{CuCl}_2 \cdot 2\text{H}_2\text{O}$ (Analytical Reagent) was from Riedel-de Haën, France and HNO_3 (75%) from the Fisher chemical, UK. HCl (37%) was supplied by Sigma-Aldrich, Germany. The rest of the chemicals are the same as described in [3.2.1 Chemicals](#) (page 57) and [4.2.1 Chemicals](#) (page 75).

5.2.2 Removal of Pd and Cu by MR-1

The synthesis of Pd NPs by MR-1 in the M9 medium is similar as described in [4.2.5 Formation of Pd NPs on GCE](#) (page 76), except that the final concentration of $\text{Na}_2[\text{PdCl}_4]$ was 0.08 mM, the culture time for the formation of Pd NPs was 48 h, and the medium 0.9% NaCl solution. OD_{600} of the final MR-1 cell suspension is about 0.6. The MR-1 cultured in Pd(II) was indicated as S/Pd (“S” for *Shewanella*). Correspondingly, the MR-1 cultured in Cu(II) was indicated as S/Cu when 0.08 mM $\text{Na}_2[\text{PdCl}_4]$ was replaced with 0.08 mM $\text{CuCl}_2 \cdot \text{H}_2\text{O}$. S/CuPd was obtained when 0.08 mM $\text{CuCl}_2 \cdot \text{H}_2\text{O}$ and 0.08 mM $\text{Na}_2[\text{PdCl}_4]$ were added into the medium at $t = 0$ and $t = 24$ respectively. Experiments were conducted in triplicate.

5.2.3 Measurement of reduced Cu and Pd

The residual Cu and Pd in the medium were measured by ICP-OES (Thermo scientific; iCAP 7000 series) before being filtered by 0.22 μm filters and diluted with 3% HNO_3 solution. Standards of 0~ 2.0 $\text{mg} \cdot \text{L}^{-1}$ Pd and Cu were also prepared with 3% HNO_3 .

5.2.4 Preparation of Cu, Pd, and CuPd NPs by MR-1

The synthesis of Cu, Pd, and CuPd NPs by MR-1 in the M9 medium are similar to the one described in [4.2.5 Formation of Pd NPs on GCE](#) (page 76) with some modifications. For S/Pd-M9, $\text{Na}_2[\text{PdCl}_4]$ with a concentration of 0.20 mM was added at $t = 0$ and then cultured for 48 h. For S/CuPd-M9, 0.10 $\text{CuCl}_2 \cdot \text{H}_2\text{O}$ and 0.20 mM $\text{Na}_2[\text{PdCl}_4]$ were added to the M9 medium at $t = 0$ and $t = 24$ respectively. To study the effect of medium, M9 medium was replaced by 0.9% NaCl solution to obtain S/Pd-NaCl and S/CuPd-NaCl were. The pellets of S/Pd-M9, S/CuPd-M9, S/Pd-NaCl, and S/CuPd-NaCl were separately resuspended in 15 mL MilliQ water and subjected to the microwave process (200°C, 2 h). OD_{600} of the

final MR-1 cell suspension is about 0.6. The resulted products were indicated as S/Pd-M9_C, S/CuPd-M9_C, S/Pd-NaCl_C, and S/CuPd-NaCl_C, respectively. Note that the names of biotic NPs (e.g., *CuPd*) here do not necessarily match their chemical states.

5.2.5 Characterizations of biosynthesized NPs

The SEM and TEM operations are the same as noted in section [4.2.7 Morphology characterization](#) (page 77).

5.3 Results and discussion

5.3.1 Co-removal of Cu and Pd

The Cu and Pd standard curves of ICP-OES show excellent linearity, Figure 5.1. The linearity confirms the feasibility of the determination of Cu and Pd within this concentration range. The concentration of aliquots of samples was therefore diluted into this concentration range.

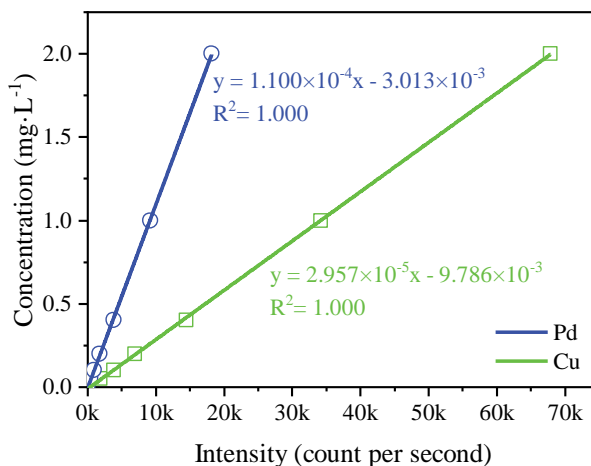


Figure 5.1. Cu and Pd standard curves of ICP-OES

With lactate as an electron donor, Cu(II) in solution was removed by 48.8% by MR-1 in the first 24 h and by 72.8% in whole 48 h if Cu(II) is the sole electron acceptor (Figure 5.2A). The decreased removal rate of Cu(II) may due to the gradual saturation of active Cu(II) binding and reduction sites in MR-1 cells. With the presence of Pd(II) added at $t = 24$ h, the removal of Cu(II) decreased to 60.1%. The decreased Cu(II) removal in the presence of Pd(II) suggests a competition for an electron acceptor between Cu(II) reduction and Pd(II) reduction, a competition for active sites, or potential blocking effect of Pd(0) NP formation.

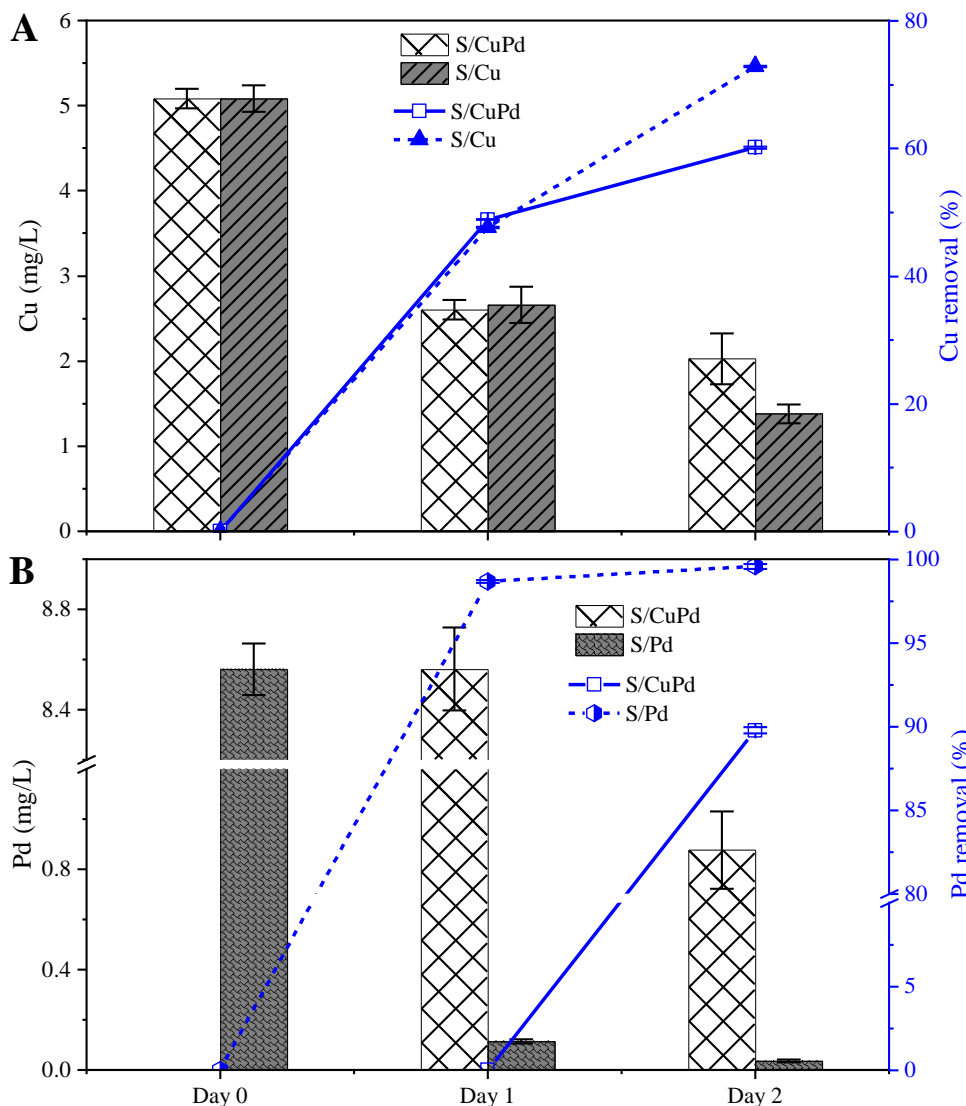


Figure 5.2. Co-removal of (A) Cu and (B) Pd by MR-1. Residual metals in the medium and corresponding removal efficiency are shown. The error bar indicates the standard deviation from triplicate ($n = 3$).

The reclaim of Pd(II) from solution by MR-1 is rapid and 98.7% of Pd(II) removal was achieved in the first 24 h (Figure 5.2B). Another 24 h incubation further increases Pd(II) removal to 99.6%. The Pd(II) reduction is a very fast process and black precipitates are visible after 10 min after the addition of Pd(II) (305). The Pd(II) removal rate decreased after 1 h and tended to be equilibrated at 2 h under aerobic condition (309). The presence

of Cu(II) compromised the removal of Pd(II), but removal efficiency as high as 89.8% was still obtained 24 h after the addition of Pd(II).

The presence of Cu(II) has minor effect on the bioremediation of Pd(II), which is surprising. Cu(II) can attack and break the bacterial cell membrane and cause denaturation of proteins and eventually lead to the death of the cell (310, 311). Ag(I) ions also show well-known antibacterial activity (310-312). Cu(II) can also cause conformational changes in proteins and as little as 0.05 mM Cu(II) can significantly decrease the ATPase activity of *Enterococcus hirae* (313). However, MR-1 can resist a certain concentration of Cu(II) and Ag(I), and even synthesize corresponding NPs (158, 205, 312). At 0.01 mM and 0.10 mM Cu(II) in 30 mM MOPS buffer, growth of MR-1 cells (initial OD₆₀₀: 0.02) was 100% and 20% compared to the control free of Cu(II) (158). The ability of MR-1 to withstand Cu(II) and Ag(I) may owe to the EET of MR-1 which can be a defense mechanism. The concentration of Cu(II) in the current experiment is 0.08 mM free of buffer (0.9% NaCl solution), and the initial OD₆₀₀ about 0.8. The number of MR-1 cells after 24 h incubation should therefore be similar to that of initial MR-1 inoculation.

Cu(II) is an inhibitor of periplasmic hydrogenases widely reported to be responsible for metal reduction (303). The exposure of microbes to Cu(II) solution for 30 min can eliminate 50% and 70% of the ability of microbes to reduce Au(III) by *E. coli* and *Desulfovibrio desulfuricans* respectively (303). Similarly, no Pd(0) NPs formed when *Desulfovibrio desulfuricans* was challenged with Pd(II) after being exposed to Cu(II) for 10 min (305). This is because the ability of *E. coli* to reduce Pd(II) originates from its periplasmic hydrogenase(s). The slightly decreased Cu(II) removal rate of S/CuPd in the first 24 h after the addition of Pd(II) (Day 1 to Day 2) compared to that of S/Pd (Day 0 to Day 1) indicates the maintenance of the ability to reduce Pd(II). This is in dramatic contrast to the 50% and even 70% elimination of the ability of noble metal reduction just noted.

Based on the antibacterial properties of Cu(II), the presence of Cu(II) in the medium is apparently undesired in bio-remediation/recovery. However, in reality, Cu(II) is very common in metal cleaning and plating baths, wood-pulp wastewater, mining activities, tire manufacturing, and fertilizer industries (314). Hence, it is essential to study the effect of Cu(II) on the biotechnological remediation of other metal.

The Pd(II) reduction by MR-1 was mainly attributed to the [NiFe]-hydrogenase HyaB in the periplasm, not the MtrC/OmcA or CymA on the outer membrane of MR-1 according to a study (161). It should be noted that about half of Pd(II) reducing ability remained, even when HyaB was knocked out from MR-1 (161). Only part of Pd(II) reduction may originate from HyaB, and other pathways differing from the MtrCAB-OmcA pathway remain to be explored.

The Cu(II) reduction by MR-1 was attributed to NDH-2 which is type II NADH: a quinone oxidoreductase or alternative NADH dehydrogenase in the cytoplasm of MR-1. The deletion MtrC, MtrF (a homolog of MtrC), OmcA, MtrABCDEF, DmsE (a periplasmic decaheme cytochrome *c*), CctA (a periplasmic tetraheme cytochrome *c*), and gene SO_4360 (coding for Periplasmic decaheme cytochrome *c* MtrA family, Figure 1.15 in page 17) have less effect on the reduction by MR-1 (158).

In summary, both Cu(II) reduction and Pd(II) reduction by MR-1 are reported to be intracellular processes and independent on the MtrCAB-OmcA pathway. Cu(II) is proposed to be reduced in the cytoplasm and periplasm, and Pd(II) believed to be reduced in the periplasm. The incubation of MR-1 cells in Cu(II) for 24 h did not significantly weaken the ability to reduce Pd(II), which implies no major the overlap of active sites for Cu(II) reduction and Pd(II) reduction and that the antibacterial activities from Cu(II) have only feeble effects on Pd(II) reduction.

5.3.2 Effect of Cu(II) and the medium on the biorecovery of Pd(II)

To study the effect of Cu(II) and different media on the biorecovery of Pd(II), the biorecovery of Pd(II) by MR-1 in two different media (M9 medium and 0.9% aqueous NaCl solution) containing Cu(II) was studied. M9 medium and 0.9% NaCl solution without Cu(II) were used as controls. M9 medium contains phosphate which is common in wastewater and possibly precipitates Cu(II), hence a low concentration of Cu(II) (0.10 mM) was applied. The reason for using 0.9% NaCl solution instead of pure water is that pure water cannot provide osmotic pressure which is critical to maintaining the viability of bacterial cells.

The biogenic NPs associated with MR-1 cells were subjected to a microwave process after synthesis. The microwave process served two purposes: to terminate the biosynthesis process and stabilize the NPs, and to carbonize cells and enhance their conductivity for specific applications, for example, electrochemical catalysis. The complexes obtained here are termed “hybrids”. Conventional methods include hydrothermal reactions and high-temperature carbonization (156, 315-317). Hydrothermal reactions are preferred for biosynthesized NPs with cells compared to high-temperature carbonization because the aggregation of NPs as well as the biomass is prevented (156, 315). Microwave heating is similar to hydrothermal heating and both of them introduce high temperature and high pressure. However, microwave heating is more efficient than hydrothermal heating because microwave heating is homogeneous throughout the sample, while hydrothermal is relatively heterogeneous (318). Microwave heating is also more controllable than hydrothermal heating due to the delicate control of the microwave by computer programs.

The carbonized hybrids synthesized by *S. oneidensis* MR-1 in M9 medium containing Cu(II) and Pd(II) are denoted as S/CuPd-M9_C. Correspondingly, there are S/Pd-M9_C,

S/CuPd-NaCl_C, S/Pd-NaCl_C. The morphology of the resulting hybrids was characterized by SEM, TEM, and SAED, and the elemental compositions evaluated using EDS (Figure 5.3~Figure 5.22).

5.3.2.1 The effect of Cu(II) on the biorecovery of Pd(II)

The morphology of S/CuPd-M9_C is presented in Figure 5.3. Apparently, the microwave process in the current experiment did not damage the integrity of the MR-1 cells, since no debris is observed in SEM. Compared to the MR-1 cells cultured in Pd(II) for 1 h (Figure 4.2B~D, page 79), the cells are slightly shorter, and cell longer than 2 μm not observed. This implies growth inhibition of MR-1 by the presence of Cu(II). It is surprising to find that numerous NPs are spread out extracellularly (Figure 5.3A and B), which is different from the Pd NPs in the absence of Cu(II), which are associated with the outer membrane of MR-1 cells (Figure 4.2B~D, page 79). In contrast, the surface of MR-1 cells is smooth in SEM as the pristine cells cultured in M9 without Pd(II) (Figure 4.2A, page 79). However, the Pd signal is observed in the MR-1 cells according to the Pd mapping (Figure 5.4H). Meanwhile, the Cu signal is visibly weaker than the Pd signal in EDS (Figure 5.4G). To facilitate comparison, the element abundance associated with cells, *i.e.*, C, N, O, P, and S, and element(s) originating from NPs, *i.e.*, Pd (and Cu for S/CuPd) are calculated. The element P is also possibly from the M9 medium if phosphate precipitates. The ratio of initial molar concentration of Cu(II) (0.10 mM) and Pd(II) (0.20 mM) is 1: 2, which is close to the ratio of Cu: Pd (2.04: 0.81) in the EDS spectrum (Figure 5.7) from the investigated area of Figure 5.4 containing the cells and extracellular NPs in comparable amount. However, a closer observation of the cells and extracellular NPs further details their compositions. The EDS results of three cells and a pile of extracellular NPs reveals that the main composition of the extracellular NPs is C, N, O, P, Cu, and Pd (Figure 5.5). The signals of O, P, and Cu from extracellular NPs in EDS mapping are slightly stronger than that from the cells (Figure 5.5D, E, and G). These NPs are therefore unlikely to be pure Cu(0) NPs or Pd(0) NPs, but probably complexes consisting of Cu NPs and Pd NPs associated with EPS. A higher molar ratio of Cu: Pd (0.76: 1.05) compared with Figure 5.4A (0.81: 2.04) indicates that Cu tends to accumulate in the extracellular NPs while Pd accumulates in the cells.

Some large flower-like structures up to 10 μm are observed among the S/CuPd-M9_C hybrids (Figure 5.3D). EDS mapping shows that the main elemental composition is C, N, O, P, and Cu (Figure 5.6). The Pd signal possibly comes from MR-1 cells attached on the flower-like structure (Figure 5.6H). The molar ratio of Cu: Pd is as high as 3.91: 0.63 and the content of O and P considerably higher than the counterparts in Figure 5.4 and Figure 5.5. Hence, the flower-like structures are very likely the products of precipitation of phosphate and Cu(II). C and N signals in EDS are likely due to the sorption of leachates of MR-1 cells during the microwave process. Large and extracellular copper agglomerates

(above 200 nm) were also observed when MR-1 was cultured in MOPS and Cu(II) (158). The authors did not explain the generation of these large copper agglomerates, but it could be due to the precipitation of Cu(II) at neutral pH, e.g., *Cu(II) (hydro)oxides*.

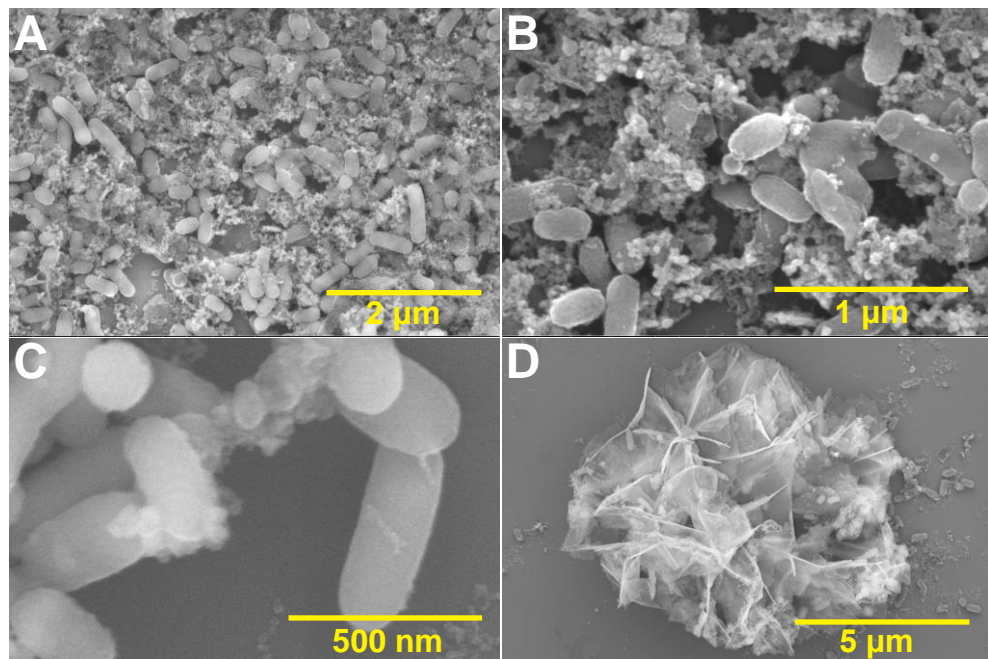


Figure 5.3. SEM observation of *S/CuPd-M9_C*. (A) – (C) SEM images at different magnifications. (D) SEM of flower-like structure.

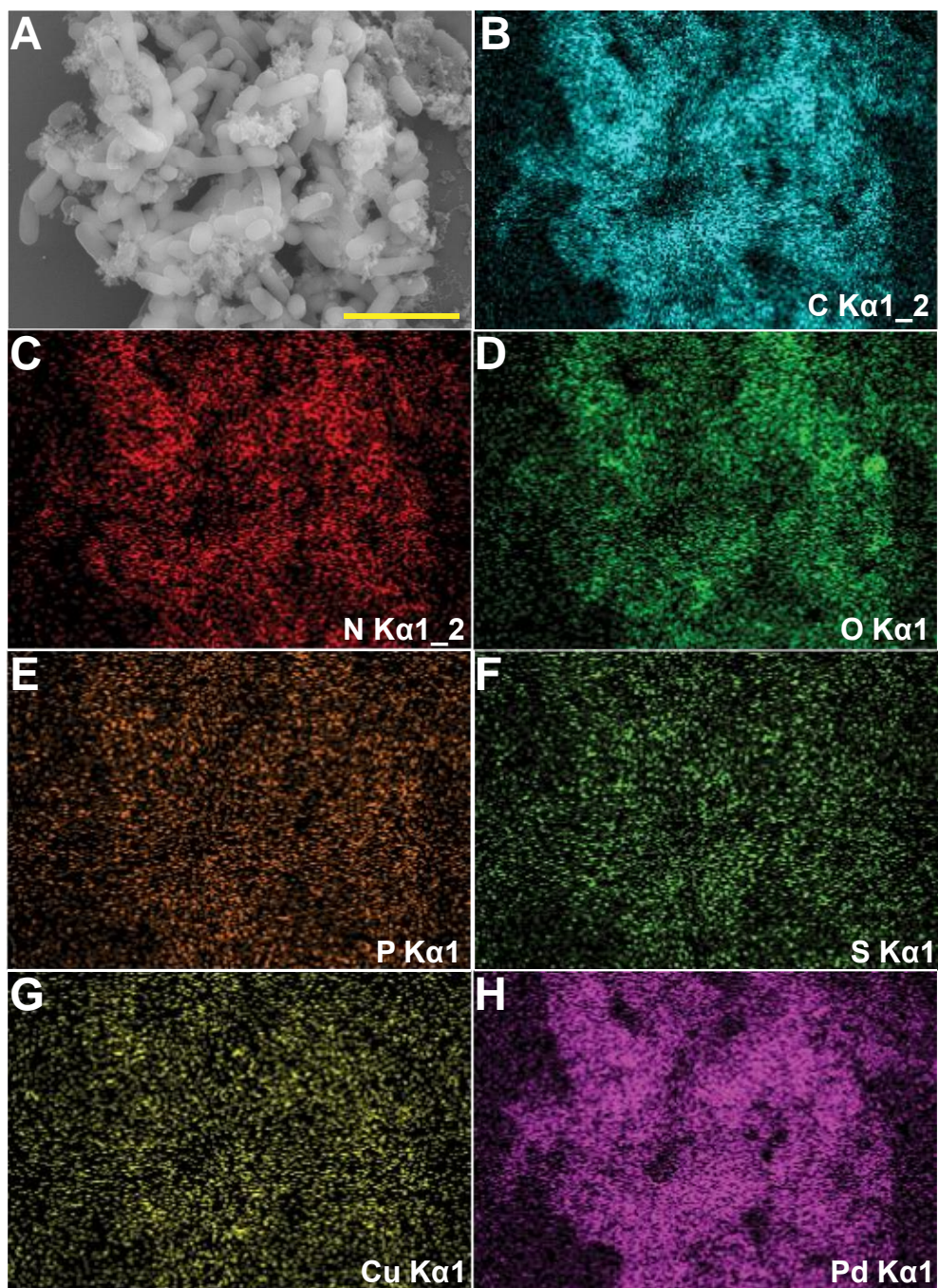


Figure 5.4. EDS of *S/CuPd-M9_C*. (A) SEM image; (B) – (H) Corresponding element mapping. Scan bar: 1 μm .

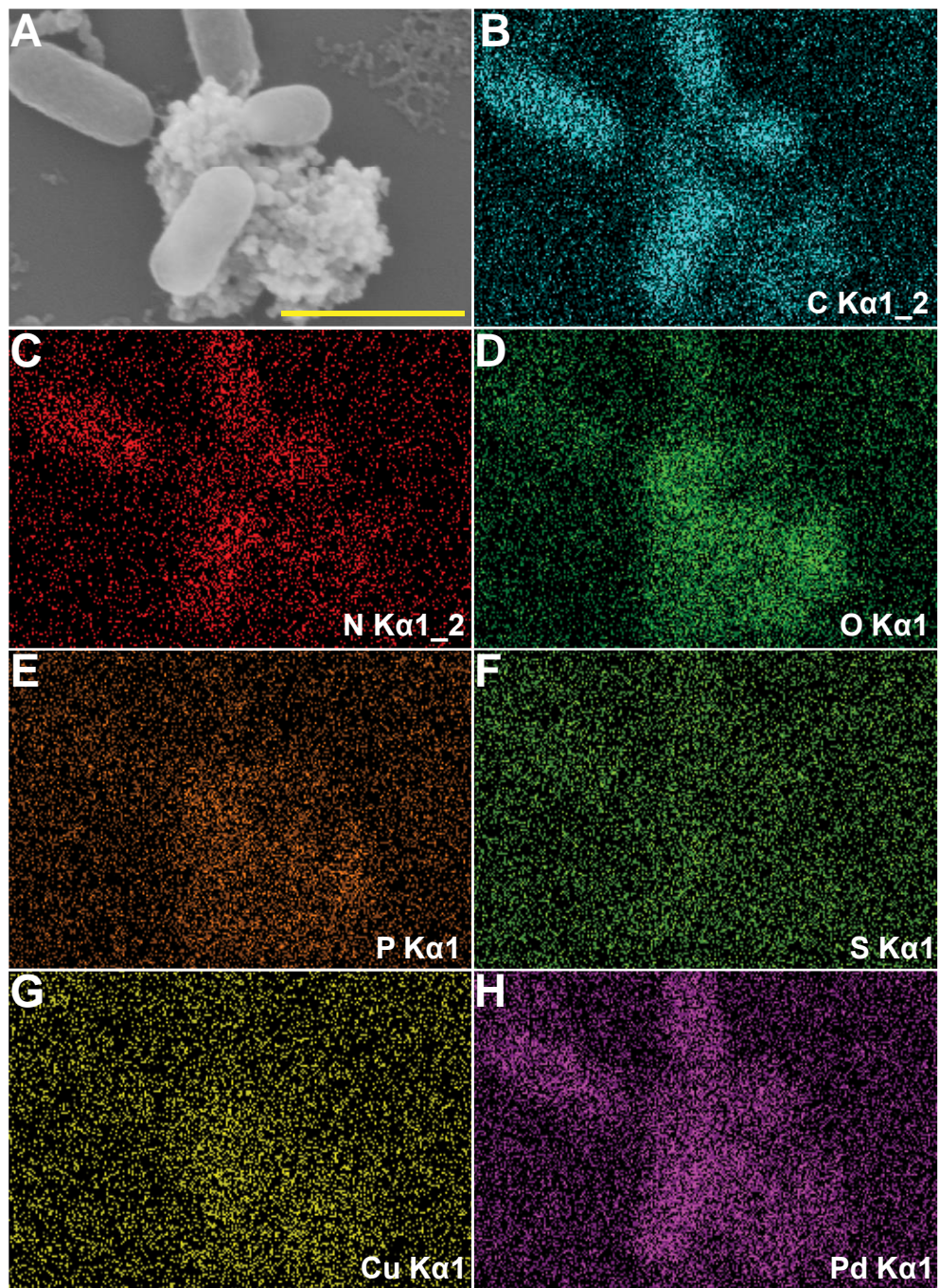


Figure 5.5. EDS of S/CuPd-M9_C. (A) SEM image; (B) – (H) Corresponding element mapping. Scan bar: 500 nm.

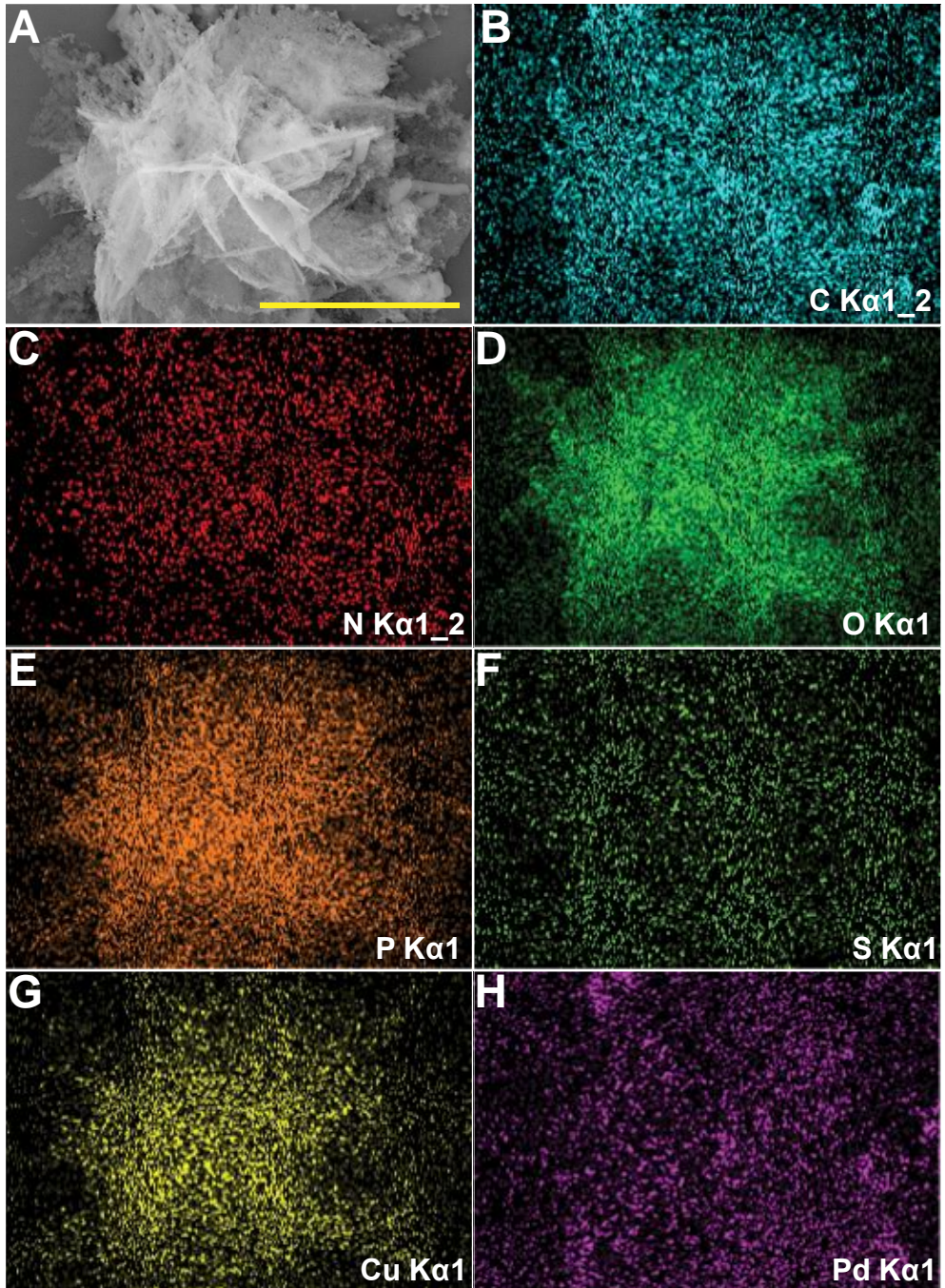


Figure 5.6. EDS of flower-like structure in S/CuPd-M9_C. (A) SEM image; (B) – (H) Corresponding element mapping. Scan bar: 2.5 μm .

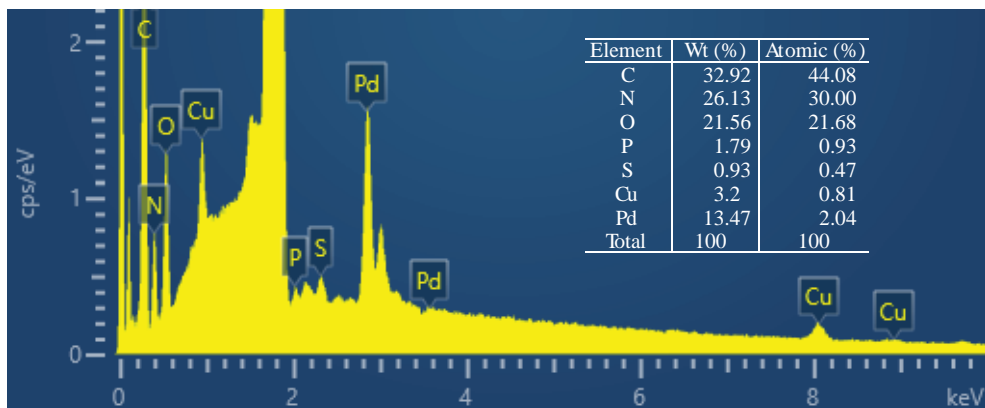


Figure 5.7. Summary of EDS spectra of S/CuPd-M9_C corresponding to Figure 5.4

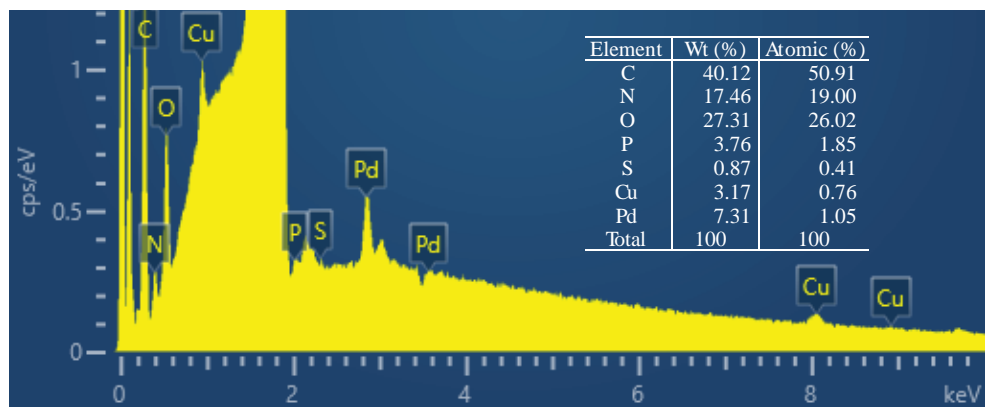


Figure 5.8. Summary of EDS spectra of S/CuPd-M9_C corresponding to Figure 5.5.

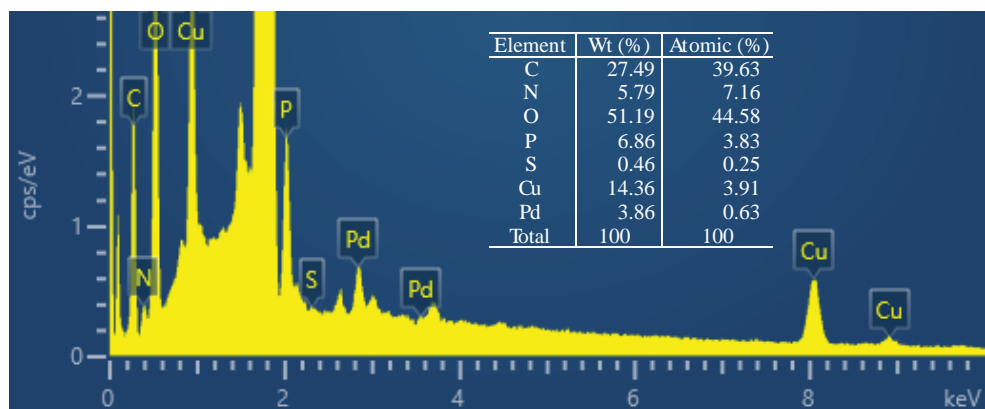


Figure 5.9. Summary of the EDS spectra of the flower-like structure in S/CuPd-M9_C corresponding to Figure 5.6.

The NPs were further investigated using TEM and SAED. The NPs are not uniform, and the size ranges from 3 nm to 15 nm. Some of the small NPs are sparsely spread onto the supporting film of the TEM grid, and some small NPs are enveloped in the polymer structures (possibly EPS). Other small NPs are encapsulated in MR-1 cells (Figure 5.10A and B). Further observations at high magnification show clear lattices, indicating that the NPs are crystalline (Figure 5.10C and D). Four main patterns are observed in SAED of the NPs (Figure 5.10E and F). The interplanar distance (d) of these NPs are calculated according to the equation (319):

$$d = \frac{2}{D} \quad (5.1)$$

where d is the interplanar distance (nm), and D the diameter of the ring (or the distance between two symmetric spots) in SAED (1/nm). The resulting lattice distance of 0.27, 0.22, 0.19, 0.15 nm are assigned to PdO (002), Pd(111), Pd(200), and Cu₂O respectively (158, 320-322). A similar SEAD pattern of Cu₂O(220) in Figure 5.10F was observed in the Cu₂O NPs synthesized by MR-1 when Cu(II) was the sole electron acceptor (158). It seems that a relatively large portion of Pd(II) was not completely reduced due to the inhibition of bacterial activity by Cu(II). The presence of Cu₂O implies that the Cu(0) NPs may be oxidized to Cu(I) when exposed to the air, or Cu(II) was reduced to Cu(I) without further reduction.

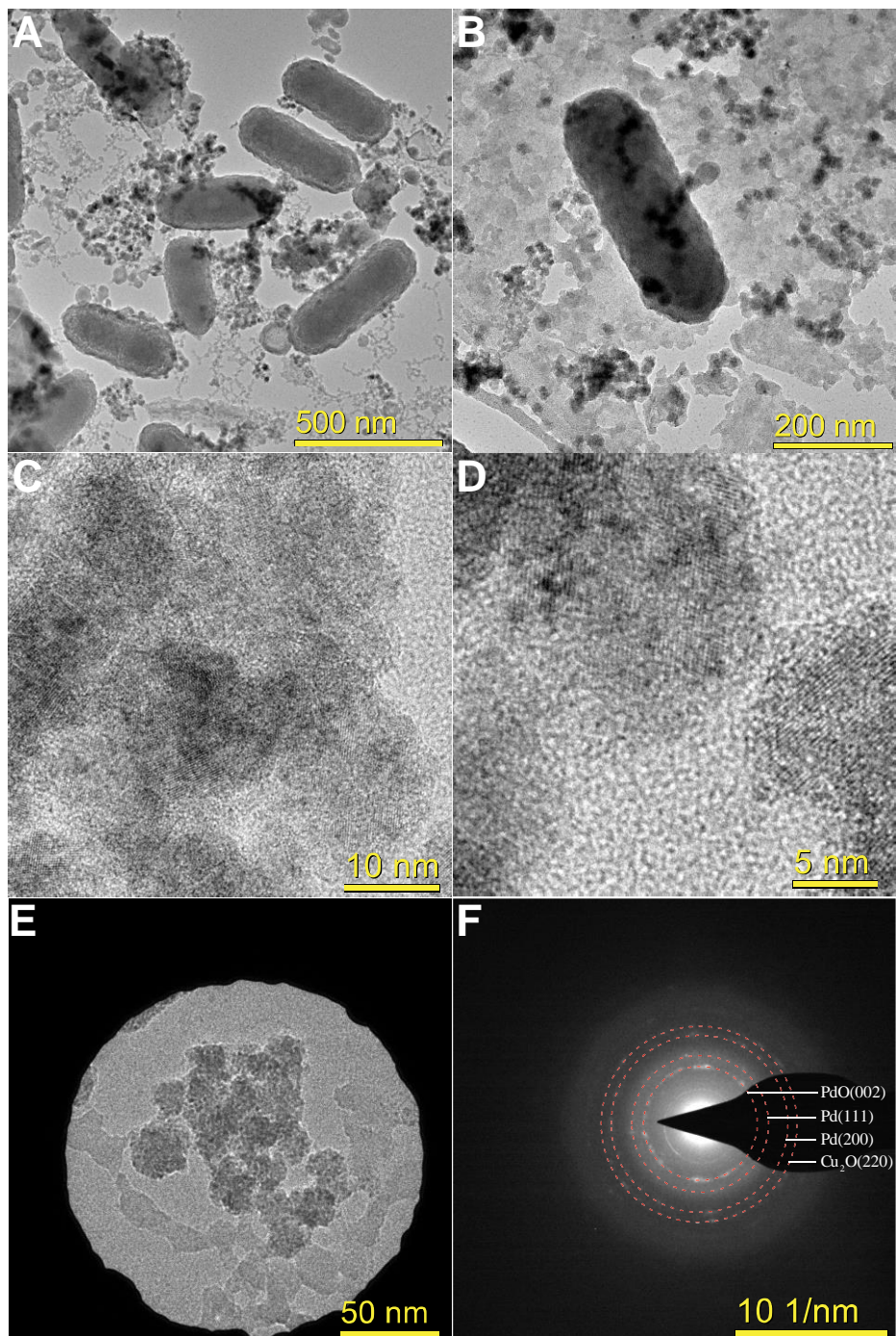


Figure 5.10. TEM of S/CuPd-M9_C. (A) – (D) TEM images of S/CuPd-M9_C at different magnifications. (E) – (F) SAED area and corresponding diffraction pattern.

The morphology of S/Pd-M9_C is presented in Figure 5.11. Most of the cells are completely enveloped with Pd NPs which form a dense and rugged coating. However, the MR-1 cells cultured in Pd(II) for 1 h are only sparsely coated with NPs, even at as high as 0.80 mM Pd(II) (Figure 4.2B~D, page 79). The formation of Pd NPs is therefore a fast process as noted, but one hour is not enough to recover all the Pd(II). Besides, cells without Pd NPs coating are also observed (as indicated by the red arrow in Figure 5.11D). These cells probably multiplied after available Pd(II) was depleted. The presence of palingenetic cells also justifies the maintenance of bacterial viability in the M9 medium containing Pd(II). Different from the NPs spreading out in S/CuPd-M9_C, most of the NPs in S/Pd-M9_C were attached to the bacterial surface. EDS mapping shows that the signal of Pd, along with that of C, N, O, P, S, are all observed in the MR-1 cells (Figure 5.12). The NPs clothing cells therefore contain Pd. The EDS spectrum of S/Pd-M9_C shows a high content of Pd (Figure 5.13), *i.e.*, an atomic ratio of 5.55% (a mass ratio of 31.37%), which is at least three times higher than that of S/CuPd-M9_C (Figure 5.7~ Figure 5.9).

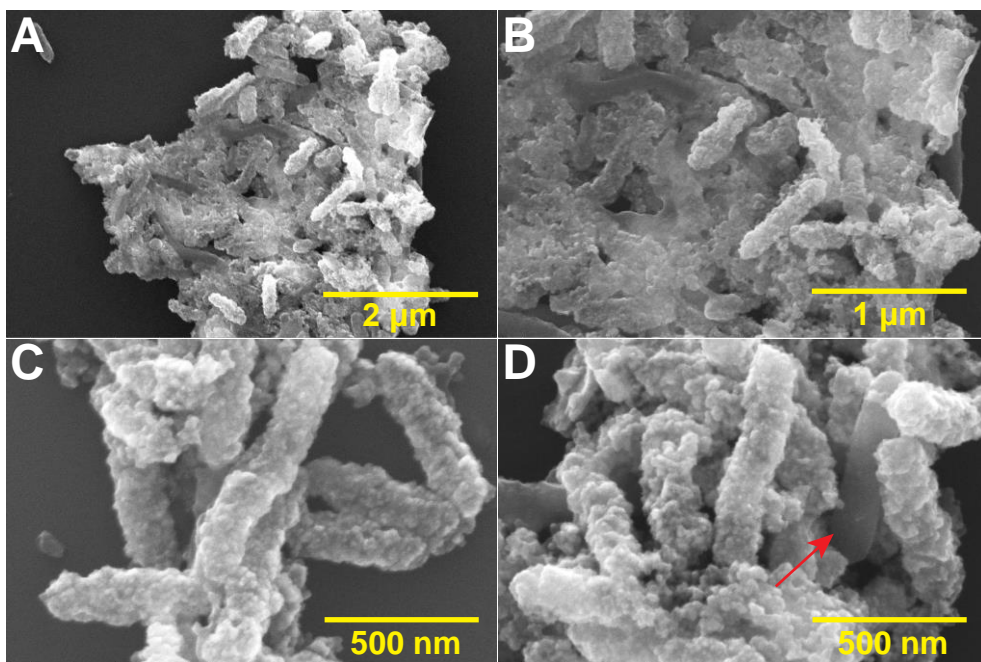


Figure 5.11. SEM observation of S/Pd-M9_C. (A) – (D) SEM images at different magnifications. Red arrow indicates a cell without Pd NPs covering.

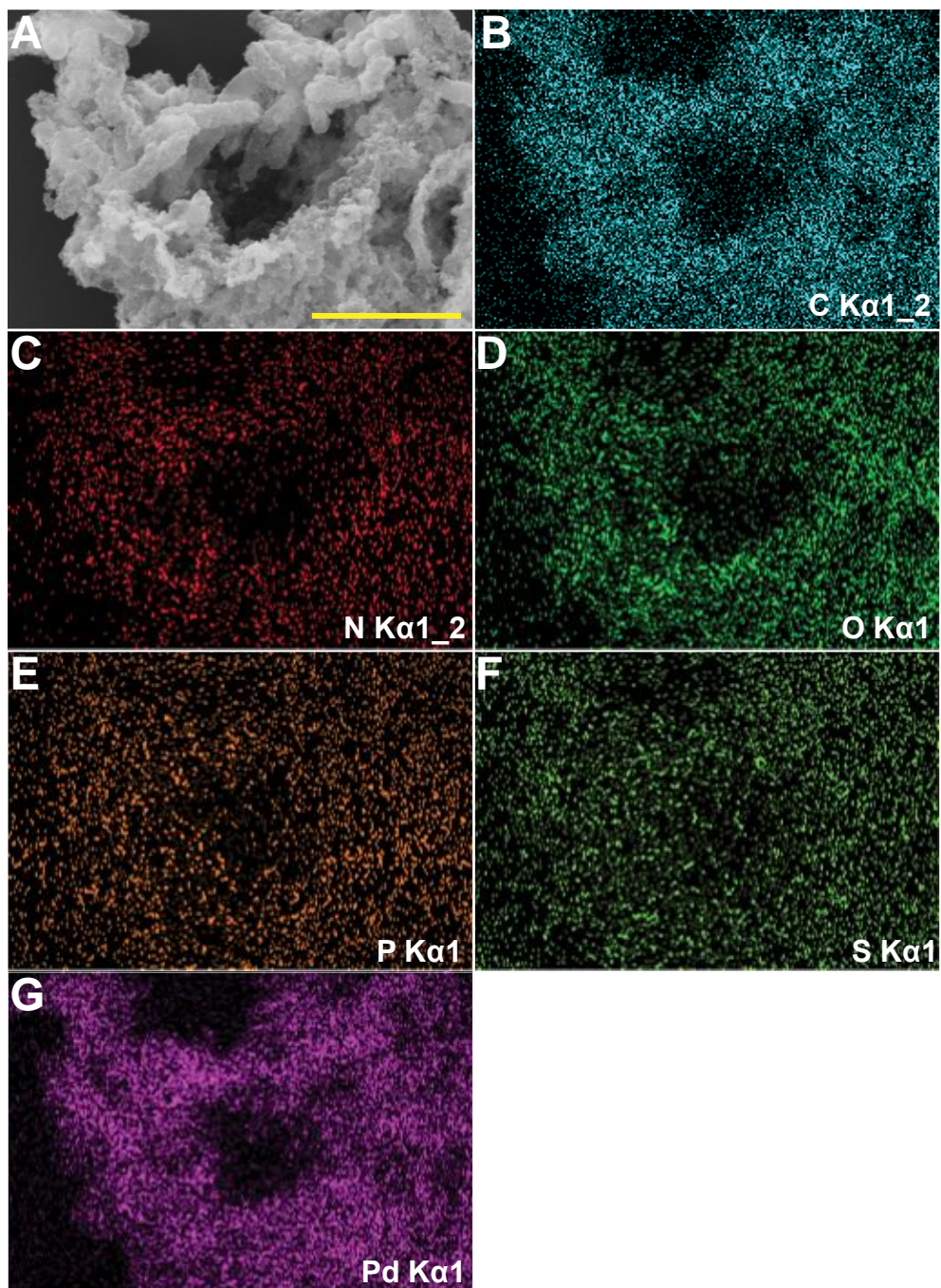


Figure 5.12. EDS of S/Pd-M9_C. (A) SEM image; (B) – (G) Corresponding element mapping. Scan bar: 1 μm .

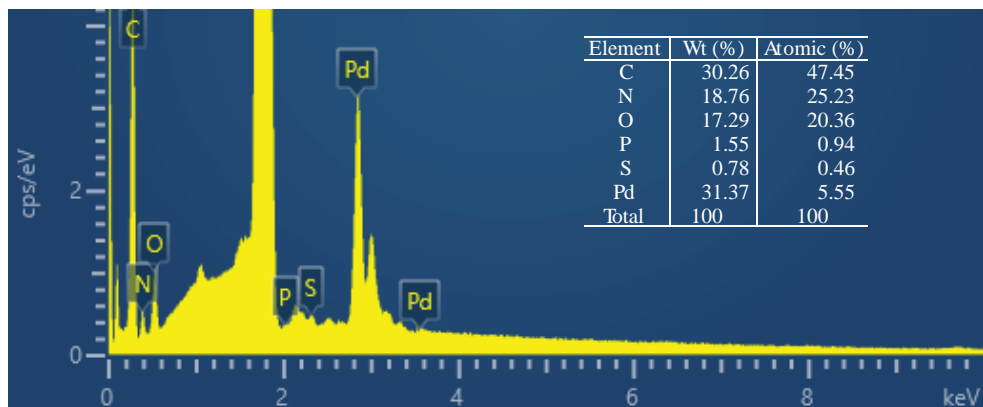


Figure 5.13. Summary of EDS spectra of S/Pd-M9_C corresponding to Figure 5.12.

The Pd NPs in S/Pd-M9_C were further investigated *via* TEM and SAED (Figure 5.14). Some polymer structures possibly EPS coated with Pd NPs are present in the TEM images (Figure 5.14A). The distribution of Pd NPs on the cell surface is pretty dense and the sizes of the NPs about 5~ 10 nm (Figure 5.14B and C). It is difficult to tell whether or not the NPs were formed in the periplasm of MR-1, as many studies suggested (161, 309), but NPs clearly adhere to the outer membrane. Individual Pd NPs on supporting film are not observed in TEM. Lattices can be observed at higher magnifications (Figure 5.14D), but not as clear as that of S/CuPd-M9_C (Figure 5.10C and D) since the TEM electron beam is difficult to penetrate the cells. Similar to S/CuPd-M9_C, Pd(111) and Pd(200) are observed. Additionally, lattice distances of 0.14, 0.12, and 0.09 nm are allocated to Pd(220), Pd(311), and Pd(331), respectively (Figure 5.14E and F). Pd(II) was therefore completely reduced and corresponding crystalline Pd(0) NPs formed on the surface of cells or within the periplasm.

In summary, the cellular surface is covered with Pd NPs in the absence of Cu(II), but is smooth in the presence of Cu(II) because Pd NPs tend to accumulate in the periplasm. However, the phosphate seems precipitate Cu(II), medium without phosphate is therefore needed for further studies, which is detailed in the following section.

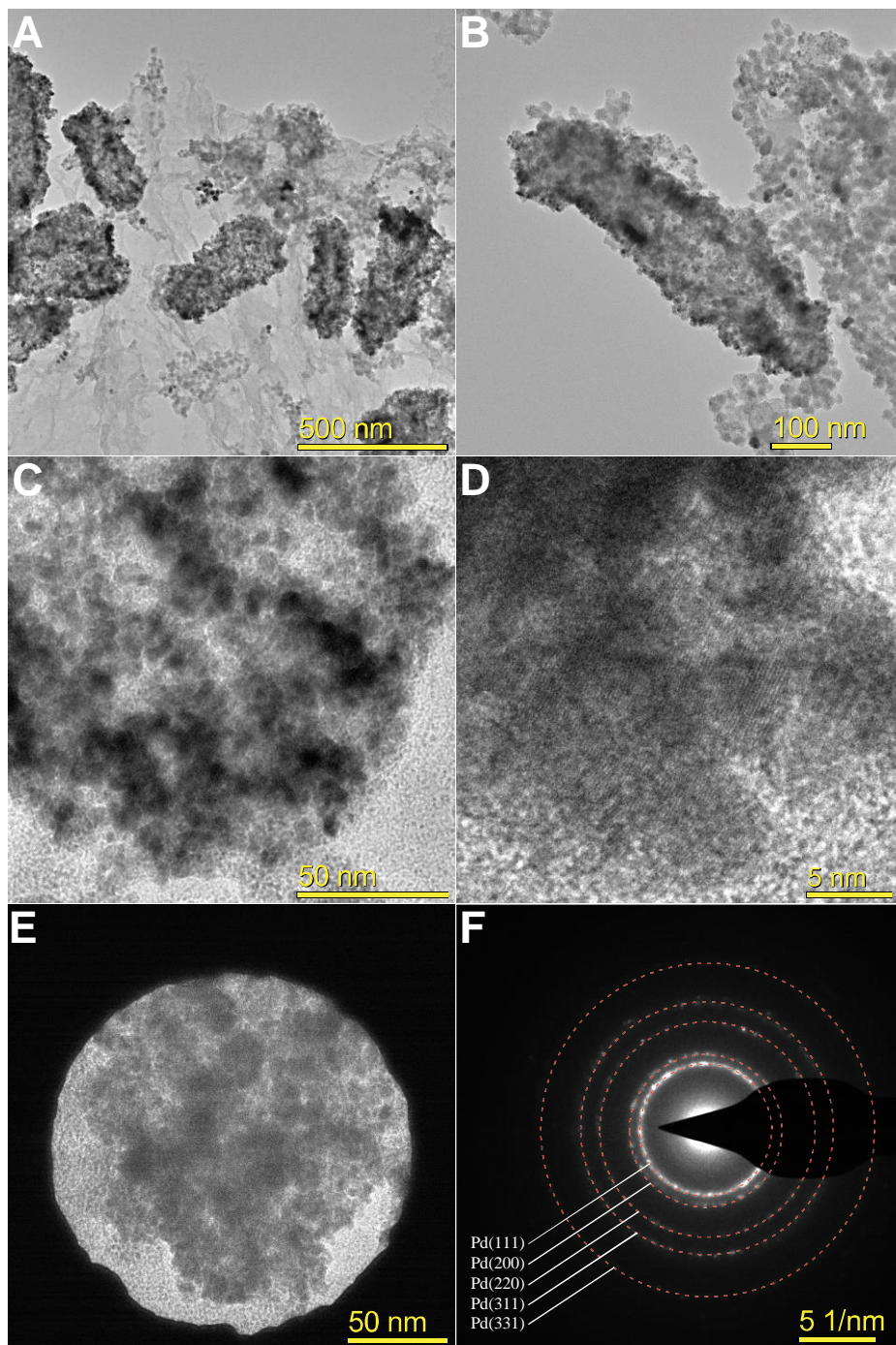


Figure 5.14. TEM of S/Pd-M9_C. (A) – (D) TEM images of S/Pd-M9_C at different magnifications. (E) – (F) SAED area and corresponding diffraction pattern.

5.3.2.2 The effect of medium composition on the biorecovery of Pd(II)

S/CuPd and S/Pd synthesized in 0.9% NaCl solution, *i.e.*, S/CuPd-NaCl_C and S/Pd-NaCl_C, were also studied. Although both media (M9 and 0.9% NaCl solution) contain Cu(II) and Pd(II) for S/CuPd-NaCl_C and S/CuPd-M9_C, their morphologies are quite different (Figure 5.3 and Figure 5.15). The surface of the cells in S/CuPd-NaCl_C are smooth like the cells in S/CuPd-M9_C, except that several large particles are attached to each cell, and the spreading of NPs are absent in S/CuPd-NaCl_C according to the SEM results. The white dots in the SEM images (Figure 5.15) are similar to but larger than the white dots in the MR-1 cells cultured in 0.08 mM Pd(II) for 1 h (Figure 4.2B, page 79). Note that the Pd(II) concentration in the biosynthesis of S/CuPd-NaCl_C is 0.20 mM, and the culture time 24 h. The presence of Cu(II) thus altered the MR-1 metabolism. The big NPs may be formed on certain active sites free of Cu(II) inhibition. EDS mapping shows considerable and homogeneous Pd signals from MR-1 cells (Figure 5.16), implying that Pd is in or on the cells although the outer membrane is smooth. The molar Cu: Pd ratio is 0.08: 2.24 (Figure 5.17) which is much lower than that from S/CuPd-NaCl_C (Figure 5.7 to Figure 5.9). This is probably due to no copper precipitation because Cu(II) is quite stable in 0.9% NaCl solution. However, the Pd content is comparable to S/CuPd-NaCl_C (Figure 5.7). Based on the quantitative investigation, Pd(II) and Cu(II) have been removed from the medium with high efficiency (Figure 5.2). Copper must be therefore within the cells where the EDS signals are undetectable, or copper is lost during the microwave process.

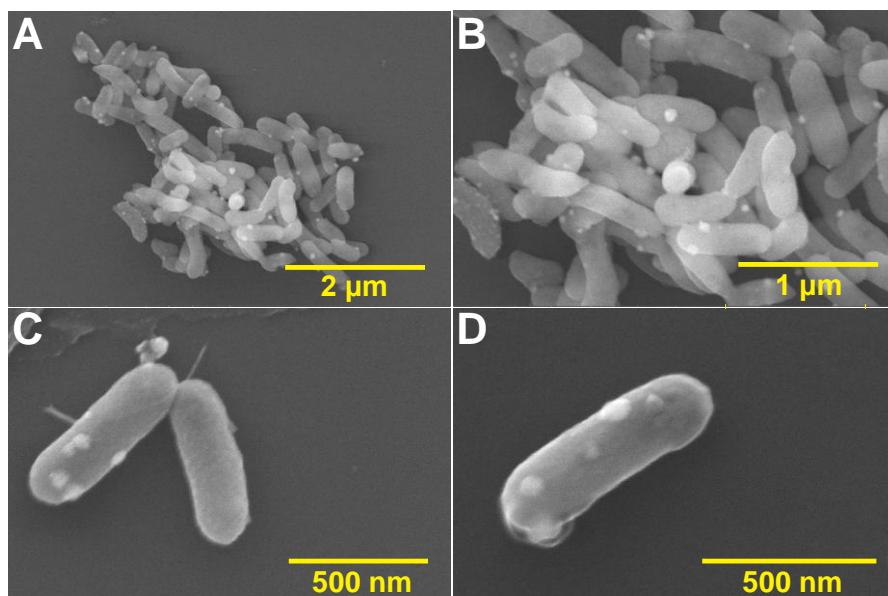


Figure 5.15. SEM observation of S/CuPd-NaCl_C. (A) – (D) SEM images at different magnifications. Note the white spots are NPs.

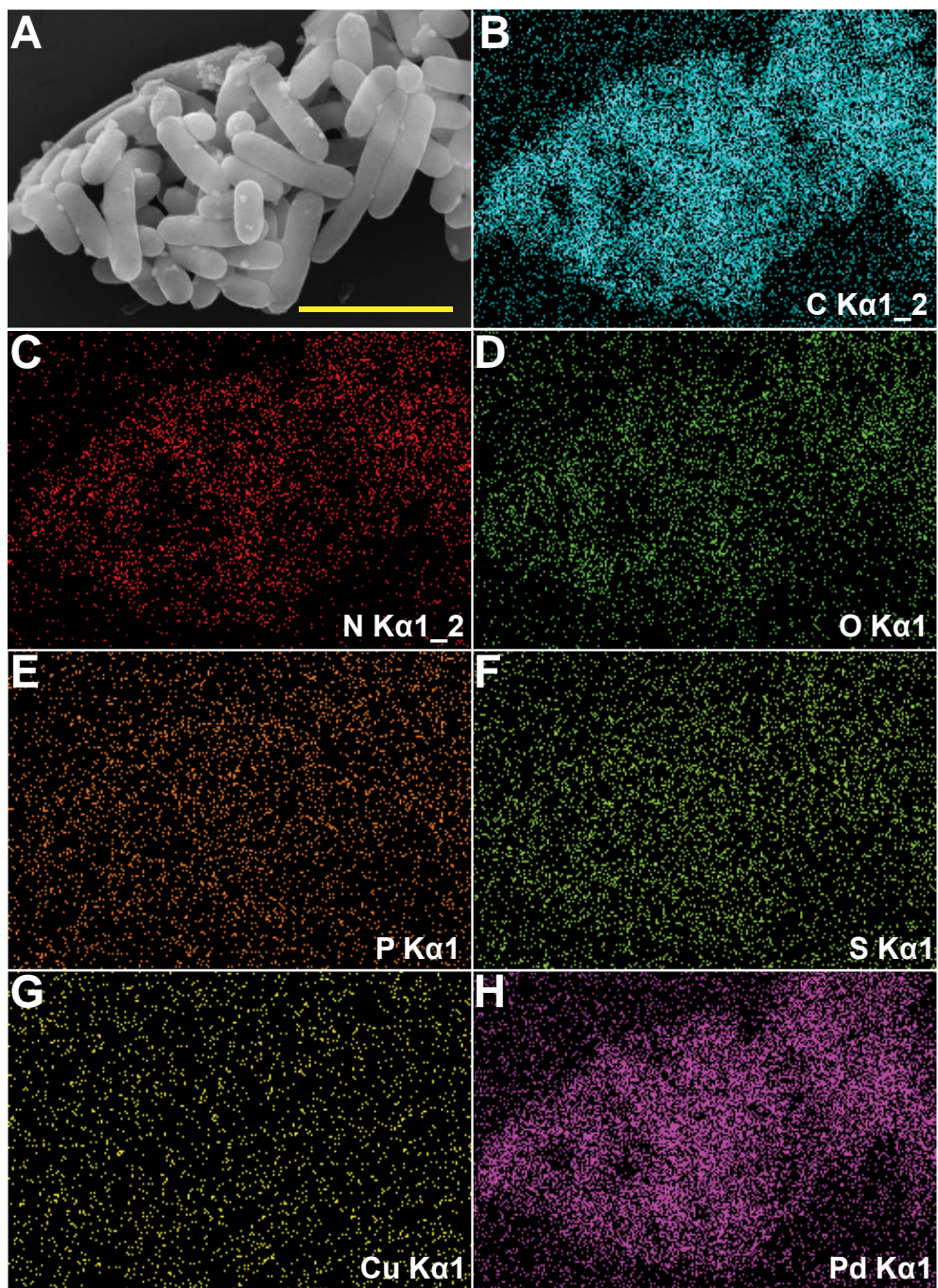


Figure 5.16. EDS of S/CuPd-NaCl_C. (A) SEM image; (B) – (H) Corresponding element mapping. Scan bar: 1 μm .

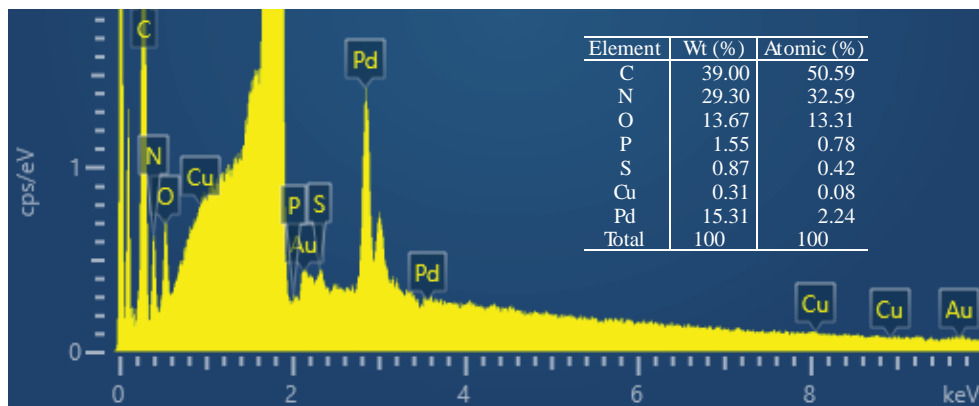


Figure 5.17. Summary of EDS spectra of *S/CuPd-NaCl_C* corresponding to Figure 5.16.

The surface of the cells of *S/CuPd-NaCl_C* was further investigated using TEM and SAED. The large NPs attached to the outer membrane are 40~ 70 nm (Figure 5.18A and B). Smaller NPs are evenly dispersed on the cells, and TEM images at higher magnifications show that the size of the small NPs are about 4 nm (Figure 5.18C and D). However, lattices are not observed in these TEM images because these small NPs are inside the periplasm. SAED results reveal that the NPs are crystalline and the Pd(111), Pd(220), and Pd(311) patterns. The hazy halo ring around Pd(111) caused by the small size of Pd(0) NPs (Figure 5.18E and F). No signal of copper crystals is detected, which is probably due to the low content of copper or the amorphous property of copper products.

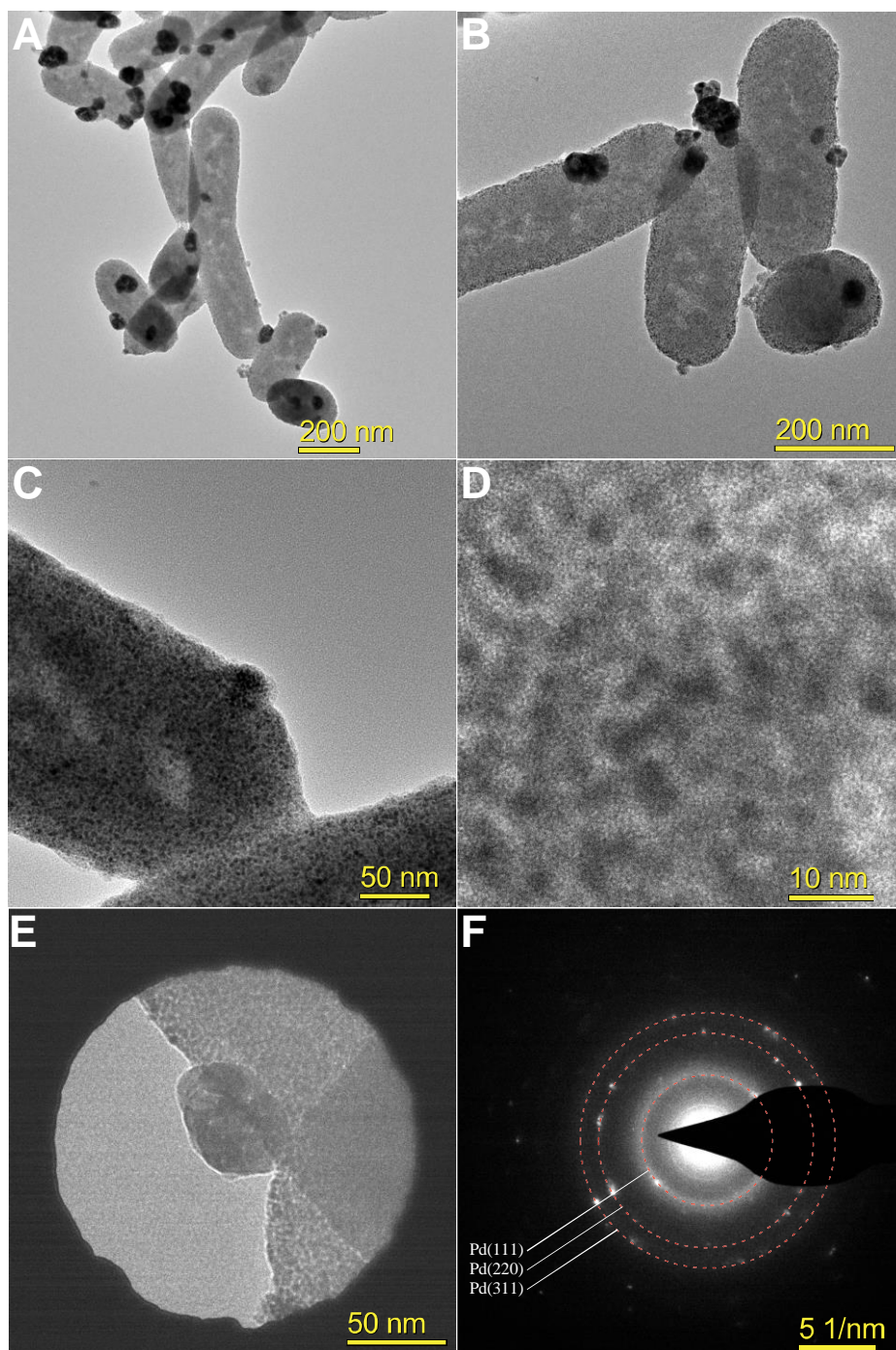


Figure 5.18. TEM of S/CuPd-NaCl_C. (A) – (D) TEM images of S/CuPd-NaCl_C at different magnifications. (E) – (F) SAED area and corresponding diffraction pattern.

In the absence of Cu(II), the surface of cells (S/Pd-NaCl_C) is back to coarse, but not as rough as S/Pd-M9_C. Fewer and smaller NPs coated the outer membrane of the cells compared to the cells in S/Pd-M9_C (Figure 5.19). The different morphology of S/Pd-NaCl_C compared to S/Pd-M9_C is attributed to the absence of buffer agents. Similar to S/Pd-M9_C, the cells in S/Pd-NaCl_C emit significant Pd signal in EDS mapping (Figure 5.20G). Hence, the NPs on the surface of cells are biotic Pd NPs. The Pd content in S/Pd-NaCl_C, which is 4.17% in the atomic ratio or 25.55% in the mass ratio (Figure 5.21), is mildly smaller than in its S/Pd-M9_C analog.

Further TEM imaging shows that some extracellular Pd NPs are gathered and connected with cells (Figure 5.22A and B). Accumulation of Pd NPs in the periplasm is clear as the red arrow indicates (Figure 5.22B). Closer observations show that the size of the most NPs is about 5 nm (Figure 5.22C and D). Lattices are observed but are not very clear (Figure 5.22D). SAED results uncover analogous patterns as S/Pd-M9_C except for the absence of Pd(200). A similar hazy halo ring around Pd(111) is also shown, indicating that the nanostructures in S/Pd-NaCl_C are also crystalline Pd(0) NPs.

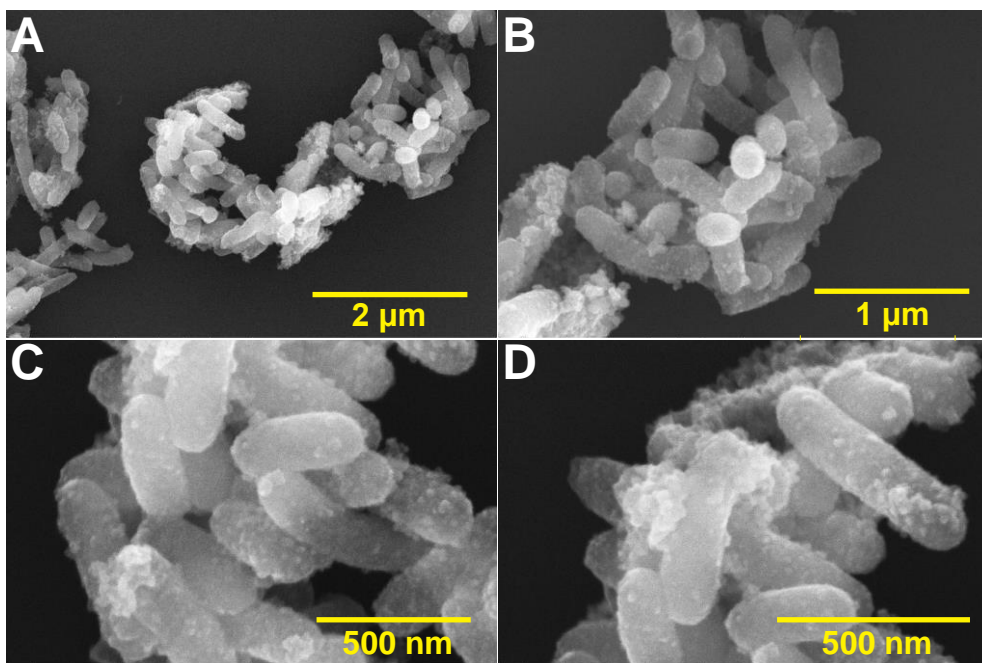


Figure 5.19. SEM of S/Pd-NaCl_C. (A) – (D) SEM images at different magnifications.

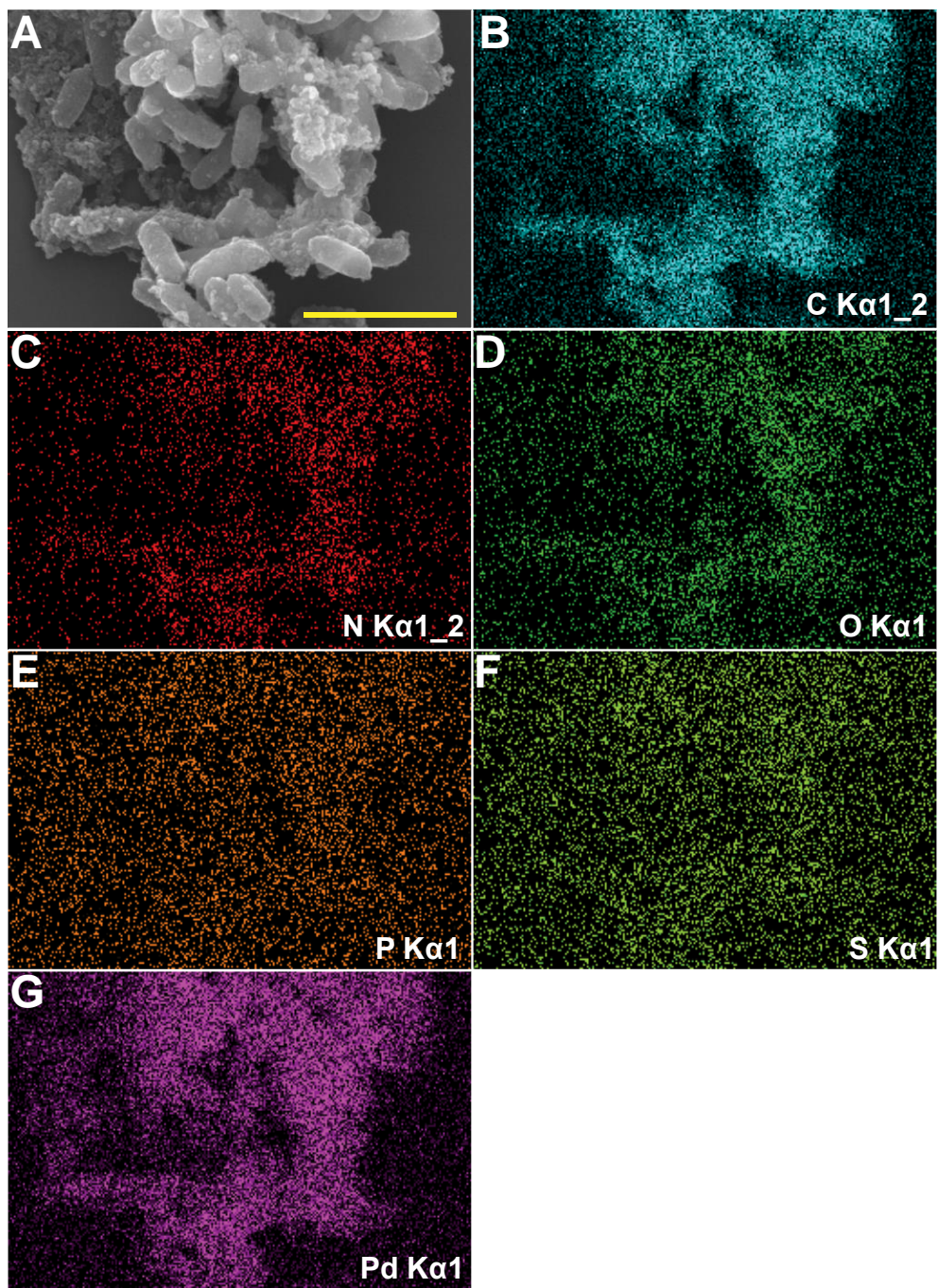


Figure 5.20. EDS of S/Pd-NaCl_C. (A) SEM image; (B) – (G) Corresponding element mapping. Scan bar: 1 μm .

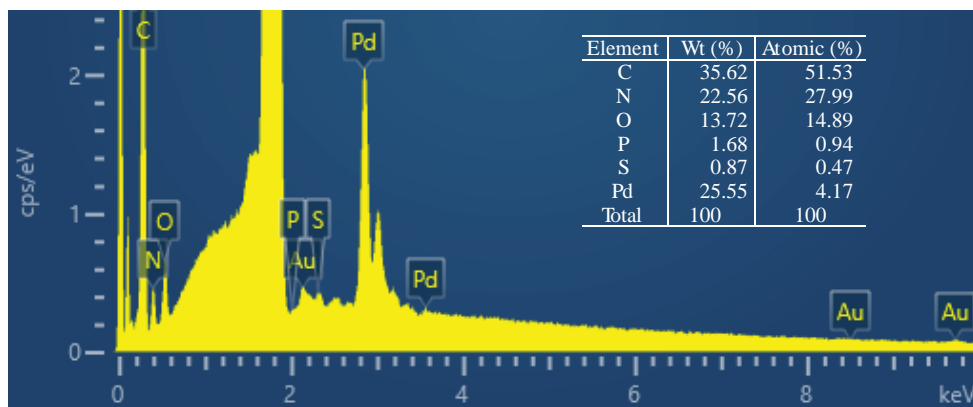


Figure 5.21. Summary of EDS spectra of S/Pd-NaCl_C to corresponding Figure 5.20.

The results detailed in this chapter illustrate the influence of Cu(II) and different media on the bio-recovery of Pd(II) are illustrated.

When the medium is neutral or contains phosphate, after the addition of Cu(II), part of Cu(II) ions precipitate (*e.g.*, copper phosphate and copper hydroxide). MR-1 then reduce these precipitates to Cu(I) or Cu(0), and corresponding NPs are formed as the extracellular NPs in S/CuPd-M9_C. The rest of the Cu(II) ions interact with MR-1. The interactions between Cu(II) ions and MR-1 cells include biosorption, reduction, and inhibition. Cu(II) can be absorbed by MR-1 as other metal ions do, then the Cu(II) ions can be reduced in the cells, for example, in the cytoplasm and the periplasm. Cu(II) mainly inhibits the transport of Pd(0) from the periplasm to the extracellular surface of the outer membrane. As a result, Pd(0) NPs accumulate inside the cells other than on the outer membrane, and smooth cell surfaces are observed when the medium contains Cu(II) (Figure 5.3 and Figure 5.15). The inhibition of Pd(II) sorption by MR-1 is only slight, but the inhibition of the reduction of Pd(II) to Pd(0) by MR-1 as well the growth of Pd NPs are observed. As a consequence, a few Pd(II) ions were transformed into PdO, and Pd NPs are smaller compared to Pd NPs formed in media without Cu(II) (Figure 5.10~ Figure 5.22).

Compared to 0.9% NaCl medium, the M9 medium can increase the bio-recovery to a small extent according to the Pd content shown in Figure 5.13 and Figure 5.21. The addition of buffer agents in the medium may therefore be profitable but is not critical under the current experimental conditions.

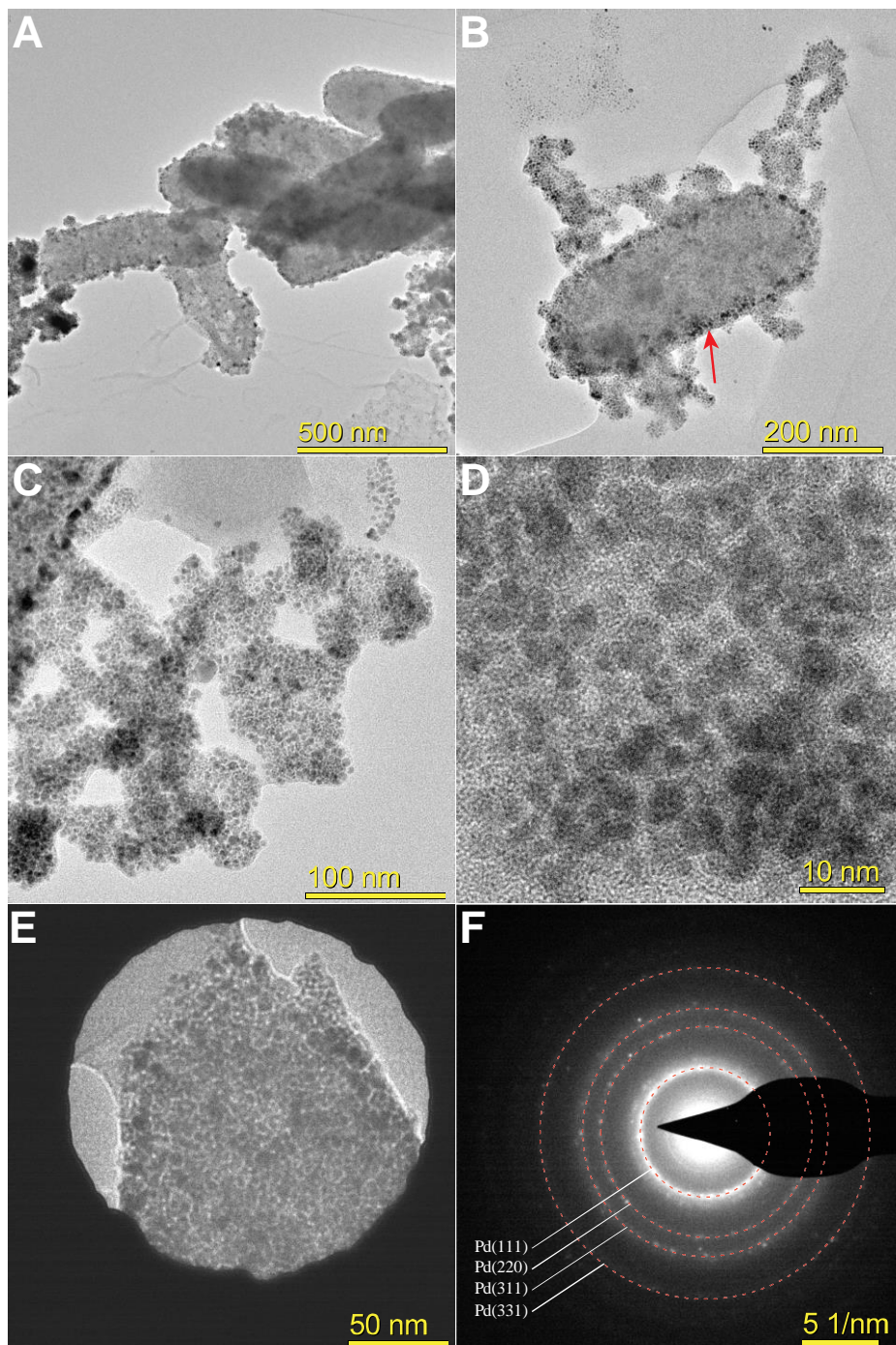


Figure 5.22. TEM of S/Pd-NaCl_C. (A) – (D) TEM images of S/Pd-NaCl_C at different magnifications. Red arrow indicates NPs in the periplasm. (E) – (F) SAED area and corresponding diffraction pattern.

5.4 Conclusions

The inhibition of Cu(II) to Pd(II) reduction by MR-1 is different from that of other microbes, such as *E. coli*. Inhibition of Cu(II) to the bio-remediation of Pd(II) was observed but only to a mild degree. MR-1 incubated in Cu(II) for 24 h still exhibited a significant reducing ability to Pd(II) and a removal efficiency as high as 89.8% was achieved. In comparison, a removal efficiency of 98.7% was obtained without Cu(II) culturing. Competition between Cu(II) removal and Pd(II) removal was observed, and the addition of Pd(II) slowed the Cu(II) removal. In the bio-recovery of Pd(II), apparent differences in morphologies of hybrid NPs presented with and without Cu(II) in the medium were observed. With Cu(II), Pd NPs tend to accumulate in the periplasm, and no NPs were evenly distributed on the outer membrane. In addition, the NPs are small, and part of Pd(II) may not be completely reduced to Pd(0). Without Cu(II), MR-1 cells were fully covered with relatively larger Pd(0) NPs.

Phosphate buffer is not critical to the bio-recovery of Pd(II). The presence of phosphate in the medium slightly increased the content of Pd(II) in the hybrids, but also precipitates Cu(II) in the medium. The precipitation of metal is undesired for the biorecovery. More compatible media such as 0.9% NaCl solution are probably a better alternative.

Inhibition of Cu(II) to the Pd(II) transportation from the periplasm across the outer membrane is thus proposed. Further investigations are needed to detail the effect of Cu(II) to the bio-remediation/recovery of metals by MR-1, such as the effect of Cu(II) concentration and the inhibition of Cu(II) in other metal reduction.

Chapter 6

Conclusions and perspectives

As a model dissimilatory metal-reducing bacterium, the ability of *S. oneidensis* MR-1 (MR-1) to transfer electrons from the inside of cells to extracellular redox partners (outward EET) is widely studied. Cytochromes *c* are crucial roles in this process, but detailed studies uncovered the existence of unexplored active sites, probably cytochromes *c* with high redox potentials or multicopper oxidase which potentially enable other MR-1 EET pathways than those learned hitherto.

In this Ph.D. project, the inward EET process of MR-1 was investigated in great detail. MR-1 can transmit intracellular electrons to external redox molecules with high redox potentials and negative charge(s) and achieve an inward EET process and electrocatalysis. The catalytic electrooxidation manifest asymmetric voltammetric shape with an enhanced anodic peak and a decreased cathodic peak. The inward EET is high effective and selective. Only the redox molecules with high midpoint potential and negative charge(s) showed electrocatalysis among the 12 redox molecules investigated. Reference bacteria, such as *E. coli* and *Streptococcus mutans* are unable to execute electrocatalysis. The selectivity of both redox molecules and bacteria is therefore confirmed, which means only specific bacteria show the electrocatalysis to specific redox molecules. Notably, the addition of 10^{-4} mmol $[\text{Fe}(\text{CN})_6]^{4-}$ caused a higher current increase than that of 1.07 mmol lactate. EPS, *in vitro* cytochrome *c*, and riboflavin, which exert important roles in the outward EET, make no difference in the inward EET. Hence, the inward EET of MR-1 is possibly independent on the outward EET. The electrocatalysis showed a dependence on the scan rate of CVs and the concentration of $[\text{Fe}(\text{CN})_6]^{4-}$. Electrocatalysis is clear at low scan rates and low $[\text{Fe}(\text{CN})_6]^{4-}$ concentrations, indicating a different mechanism other than simple transformation between $[\text{Fe}(\text{CN})_6]^{4-/3-}$ on electrode surface.

The inward EET of MR-1 is fairly independent on the cellular respiration and the presence of MtrC and OmcA. Inactive cells and a mutant without MtrC and OmcA still show significant electrocatalysis. Notably, the presence of Pd NPs in cells, especially with large amounts, weakened the electrocatalysis. The Pd NPs is likely to physically block the active sites which are not MtrC and OmcA. The CV peaks were associated with the redox molecules,

and not with the cytochromes *c* on the outer membrane. Together, these results suggest a model incorporating the oxidation of $[\text{Fe}(\text{CN})_6]^{4-}$ and a mediating EET process of $[\text{Fe}(\text{CN})_6]^{4-/\text{3-}}$. The former is an inward EET, in which MR-1 captures electrons from $[\text{Fe}(\text{CN})_6]^{4-}$ via unidentified active site(s). The electrons are then relocated around the outer membrane close to the electrode, from where the electrons are shuttled to the electrode by $[\text{Fe}(\text{CN})_6]^{4-/\text{3-}}$. Electron transfer from the cell to the electrode is therefore an outward EET process. This outward EET mediated by $[\text{Fe}(\text{CN})_6]^{4-/\text{3-}}$ differs from the conventional outward EET of insoluble redox partners, and proceed both with and without MtrC and OmcA.

The combination of two different role of $[\text{Fe}(\text{CN})_6]^{4-}$ is quite interesting. The asymmetric voltammetric pattern implies that the MR-1 cells take electrons from $[\text{Fe}(\text{CN})_6]^{4-}$ and give to $[\text{Fe}(\text{CN})_6]^{3-}$ effectively, but cannot transfer electrons in the opposite direction. The exact mechanism on molecule level is not clear, but this discovery indicates complicated roles of bacteria in the environment. The connection between the electrocatalysis and redox potential seems implies the role of driving forces caused by potential difference, and “electrochemical stress” in CV cycling. Redox molecules with high redox potential possess a stronger ability to take electrons than those with lower redox molecules. Large local accumulation of oxidized redox molecule with high redox potential close to a cell could lead to considerable electron drain from the cell, which is possibly compensated by triggering the oxidation of the reduced redox molecules around other parts of the cell. The discover of the electrocatalysis broaden our view of EET including Mn(II) oxidation by *Shewanella* spp. noted in the introduction of Chapter 5, and can also provide information to the sensing of specific redox molecules.

The influence of Cu(II) and different media on the bio-remediation/recovery by MR-1 have been studied. The pre-culture of MR-1 for 24 h showed a Pd(II) removal efficiency of 89.8% in 24 h after the addition of Pd(II). Co-existence of Pd(II) and Cu(II) decreased the removal efficiency, implying a competition between Cu(II) reduction and Pd(II) reduction. Additionally, the pre-incubation with Cu(II) distinctly changed the morphology of obtained hybrids of NPs on MR-1 surface. Cu(II) possible impairs the transport of Pd(0) NPs, which are reduced from Pd(II) by MR-1 in the periplasm, through the outer membrane. Consequently, the surface of cells culturing in media containing both Cu(II) and Pd(II) is smooth. In comparison, the cells are enveloped with numerous NPs when no Cu(II) was presented in the medium. Cu(II) can inhibit the reduction of Pd(II) and lead to small Pd(0) NPs and the formation of PdO. The inclusion of phosphate in medium precipitates of Cu(II) and cause a higher content of Pd in the hybrids, however, the increase is small.

The study of the effect of Cu(II) and medium on the bio-remediation/recovery can bridge the considerable laboratory research with practical implications. As a general inhibitor to microbes, Cu(II) is quite common in the environment and challenge the bio-

remediation/recovery in real wastewater. Previous investigations showed that Cu(II) can significantly decrease the bio-remediation/recovery of different metals such as Pd(II) and Au(III) by several bacteria, for example, *E. coli*. However, the main actor in bio-remediation/recovery should be EAB since the major reactions are redox reactions, and the studies of the influence of Cu(II) are therefore very important. Notably, the behavior of EAB is different from non-EAB, for example, EAB can survive in media containing high metal concentration. A different effect of Cu(II) on the bio-remediation/recovery by MR-1 is therefore expected, which is informative to the practical operations. The influence of medium to the bio-remediation/recovery is also needed since it is often neglected in related studies. Real wastewater is often a mixture of different metal ions or even organic compounds. The potential process such as redox reactions, precipitation, and complexation caused by the medium should be considered in bio-remediation/recovery.

Bibliography

1. Madigan, M. T.; Bender, K. S.; Buckley, D. H.; Sattley, W. M.; Stahl, D. A., *Brock biology of microorganisms*. 15th ed.; Pearson Education: MA, USA, 2018.
2. Tortora, G. J.; Funke, B. R.; Case, C. L., *Microbiology: an introduction*. 13 ed.; Pearson Education: MA, USA, 2018.
3. Finsterbusch, T.; Mankertz, A., Porcine circoviruses—Small but powerful. *Virus Res.* **2009**, *143* (2), 177-183.
4. Schulz, H. N.; Brinkhoff, T.; Ferdelman, T. G.; Mariné, M. H.; Teske, A.; Jørgensen, B. B., Dense populations of a giant sulfur bacterium in namibian shelf sediments. *Science* **1999**, *284* (5413), 493.
5. Crowther, T. W.; van den Hoogen, J.; Wan, J.; Mayes, M. A.; Keiser, A. D.; Mo, L.; Averill, C.; Maynard, D. S., The global soil community and its influence on biogeochemistry. *Science* **2019**, *365* (6455), eaav0550.
6. Fenchel, T.; King, G. M.; Blackburn, T. H., *Bacterial biogeochemistry: the ecophysiology of mineral cycling*. 3rd ed.; Academic press: 2012.
7. Kirchman, D. L.; Suzuki, Y.; Garside, C.; Ducklow, H. W., High turnover rates of dissolved organic carbon during a spring phytoplankton bloom. *Nature* **1991**, *352* (6336), 612-614.
8. Canfield, D. E., Palaeoecology: A breath of fresh air. *Nature* **1999**, *400* (6744), 503-505.
9. Calhoun, A.; King, G. M., Characterization of root-associated methanotrophs from three freshwater macrophytes: *Pontederia cordata*, *Sparganium eurycarpum*, and *Sagittaria latifolia*. *Appl. Environ. Microbiol.* **1998**, *64* (3), 1099-1105.
10. Ettwig, K. F.; Butler, M. K.; Le Paslier, D.; Pelletier, E.; Mangenot, S.; Kuypers, M. M. M.; Schreiber, F.; Dutilh, B. E.; Zedelius, J.; de Beer, D.; Gloerich, J.; Wessels, H. J. C. T.; van Alen, T.; Luesken, F.; Wu, M. L.; van de Pas-Schoonen, K. T.; Op den Camp, H. J. M.; Janssen-Megens, E. M.; Francoijs, K.-J.; Stunnenberg, H.; Weissenbach, J.; Jetten, M. S. M.; Strous, M., Nitrite-driven anaerobic methane oxidation by oxygenic bacteria. *Nature* **2010**, *464* (7288), 543-548.
11. Zheng, Z.; Zheng, Y.; Tian, X.; Yang, Z.; Jiang, Y.; Zhao, F., Interactions between iron mineral-humic complexes and hexavalent chromium and the corresponding bio-effects. *Environ. Pollut.* **2018**, *241*, 265-271.
12. Canfield, D. E.; Glazer, A. N.; Falkowski, P. G., The evolution and future of earth's nitrogen cycle. *Science* **2010**, *330* (6001), 192.
13. Poole, R. K., *Advances in bacterial electron transport systems and their regulation*. Elsevier Science: 2016.
14. Rabaey, K.; Angenent, L.; Schröder, U.; Keller, J., *Bioelectrochemical systems: From extracellular electron transfer to biotechnological application*. 2009; Vol. 8.
15. Riser, S. C.; Johnson, K. S., Net production of oxygen in the subtropical ocean. *Nature* **2008**, *451* (7176), 323-325.
16. Pant, D.; Singh, A.; Van Bogaert, G.; Irving Olsen, S.; Singh Nigam, P.; Diels, L.; Vanbroekhoven, K., Bioelectrochemical systems (BES) for sustainable energy production and product recovery from organic wastes and industrial wastewaters. *RSC Adv.* **2012**, *2* (4), 1248-1263.
17. Bajracharya, S.; Sharma, M.; Mohanakrishna, G.; Dominguez Benneton, X.; Strik, D. P. B. T. B.; Sarma, P. M.; Pant, D., An overview on emerging bioelectrochemical

-
- systems (BESs): Technology for sustainable electricity, waste remediation, resource recovery, chemical production and beyond. *Renewable Energy* **2016**, *98*, 153-170.
18. Sleutels, T. H. J. A.; Ter Heijne, A.; Buisman, C. J. N.; Hamelers, H. V. M., Bioelectrochemical systems: An outlook for practical applications. *ChemSusChem* **2012**, *5* (6), 1012-1019.
 19. Hamelers, H. V. M.; Ter Heijne, A.; Sleutels, T. H. J. A.; Jeremiasse, A. W.; Strik, D. P. B. T. B.; Buisman, C. J. N., New applications and performance of bioelectrochemical systems. *Appl. Microbiol. Biotechnol.* **2010**, *85* (6), 1673-1685.
 20. Xiao, Y.; Wu, S.; Zhang, F.; Wu, Y.; Yang, Z.; Zhao, F., Promoting electrogenic ability of microbes with negative pressure. *J. Power Sources* **2013**, *229* (0), 79-83.
 21. Wang, Z.; Zheng, Y.; Xiao, Y.; Wu, S.; Wu, Y.; Yang, Z.; Zhao, F., Analysis of oxygen reduction and microbial community of air-diffusion biocathode in microbial fuel cells. *Bioresour. Technol.* **2013**, *144* (Supplement C), 74-79.
 22. Wang, Z.; Wu, Y.; Wang, L.; Zhao, F., Polarization behavior of microbial fuel cells under stack operation. *Chin. Sci. Bull.* **2014**, *59* (18), 2214-2220.
 23. Liu, Q.; Chen, S.; Zhou, Y.; Zheng, S.; Hou, H.; Zhao, F., Phosphorus-doped carbon derived from cellulose phosphate as efficient catalyst for air-cathode in microbial fuel cells. *J. Power Sources* **2014**, *261*, 245-248.
 24. Clauwaert, P.; Verstraete, W., Methanogenesis in membraneless microbial electrolysis cells. *Appl. Microbiol. Biotechnol.* **2009**, *82* (5), 829-836.
 25. Liu, H.; Grot, S.; Logan, B. E., Electrochemically assisted microbial production of hydrogen from acetate. *Environ. Sci. Technol.* **2005**, *39* (11), 4317-4320.
 26. Reimers, C. E.; Stecher, H. A.; Westall, J. C.; Alleau, Y.; Howell, K. A.; Soule, L.; White, H. K.; Girguis, P. R., Substrate degradation kinetics, microbial diversity, and current efficiency of microbial fuel cells supplied with marine plankton. *Appl. Environ. Microbiol.* **2007**, *73* (21), 7029.
 27. Schampelaire, L. D.; Bossche, L. V. d.; Dang, H. S.; Höfte, M.; Boon, N.; Rabaey, K.; Verstraete, W., Microbial fuel cells generating electricity from rhizodeposits of rice plants. *Environ. Sci. Technol.* **2008**, *42* (8), 3053-3058.
 28. Cao, X.; Huang, X.; Liang, P.; Xiao, K.; Zhou, Y.; Zhang, X.; Logan, B. E., A new method for water desalination using microbial desalination cells. *Environ. Sci. Technol.* **2009**, *43* (18), 7148-7152.
 29. Davis, J. B.; Yarbrough, H. F., Preliminary experiments on a microbial fuel cell. *Science* **1962**, *137* (3530), 615.
 30. Logan, B. E., Exoelectrogenic bacteria that power microbial fuel cells. *Nat. Rev. Microbiol.* **2009**, *7* (5), 375-381.
 31. Kiely, P. D.; Regan, J. M.; Logan, B. E., The electric picnic: synergistic requirements for exoelectrogenic microbial communities. *Curr. Opin. Biotechnol.* **2011**, *22* (3), 378-385.
 32. Zhou, M.; Chi, M.; Luo, J.; He, H.; Jin, T., An overview of electrode materials in microbial fuel cells. *J. Power Sources* **2011**, *196* (10), 4427-4435.
 33. Liu, H.; Cheng, S.; Huang, L.; Logan, B. E., Scale-up of membrane-free single-chamber microbial fuel cells. *J. Power Sources* **2008**, *179* (1), 274-279.
 34. Logan, B.; Cheng, S.; Watson, V.; Estadt, G., Graphite fiber brush anodes for increased power production in air-cathode microbial fuel cells. *Environ. Sci. Technol.* **2007**, *41* (9), 3341-3346.
 35. Wang, X.; Cheng, S.; Feng, Y.; Merrill, M. D.; Saito, T.; Logan, B. E., Use of carbon mesh anodes and the effect of different pretreatment methods on power production in microbial fuel cells. *Environ. Sci. Technol.* **2009**, *43* (17), 6870-6874.

36. Logan, B. E.; Murano, C.; Scott, K.; Gray, N. D.; Head, I. M., Electricity generation from cysteine in a microbial fuel cell. *Water Res.* **2005**, *39* (5), 942-952.
37. Zhang, L.; Zhou, S.; Zhuang, L.; Li, W.; Zhang, J.; Lu, N.; Deng, L., Microbial fuel cell based on *Klebsiella pneumoniae* biofilm. *Electrochem. Commun.* **2008**, *10* (10), 1641-1643.
38. Qiao, Y.; Li, C. M.; Bao, S.-J.; Bao, Q.-L., Carbon nanotube/polyaniline composite as anode material for microbial fuel cells. *J. Power Sources* **2007**, *170* (1), 79-84.
39. Guo, K.; Donose, B. C.; Soeriyadi, A. H.; PrévotEAU, A.; Patil, S. A.; Freguia, S.; Gooding, J. J.; Rabaey, K., Flame oxidation of stainless steel felt enhances anodic biofilm formation and current output in bioelectrochemical systems. *Environ. Sci. Technol.* **2014**, *48* (12), 7151-6.
40. Alatraktchi, F. A. a.; Zhang, Y.; Angelidaki, I., Nanomodification of the electrodes in microbial fuel cell: Impact of nanoparticle density on electricity production and microbial community. *Appl. Energy* **2014**, *116*, 216-222.
41. Morris, J. M.; Jin, S.; Wang, J.; Zhu, C.; Urynowicz, M. A., Lead dioxide as an alternative catalyst to platinum in microbial fuel cells. *Electrochem. Commun.* **2007**, *9* (7), 1730-1734.
42. Zhang, L.; Liu, C.; Zhuang, L.; Li, W.; Zhou, S.; Zhang, J., Manganese dioxide as an alternative cathodic catalyst to platinum in microbial fuel cells. *Biosens. Bioelectron.* **2009**, *24* (9), 2825-2829.
43. Cheng, S.; Liu, H.; Logan, B. E., Power densities using different cathode catalysts (Pt and CoTMPP) and polymer binders (Nafion and PTFE) in single chamber microbial fuel cells. *Environ. Sci. Technol.* **2006**, *40* (1), 364-369.
44. Zhao, F.; Harnisch, F.; Schroder, U.; Scholz, F.; Bogdanoff, P.; Herrmann, I., Application of pyrolysed iron(II) phthalocyanine and CoTMPP based oxygen reduction catalysts as cathode materials in microbial fuel cells. *Electrochem. Commun.* **2005**, *7* (12), 1405-1410.
45. HaoYu, E.; Cheng, S.; Scott, K.; Logan, B., Microbial fuel cell performance with non-Pt cathode catalysts. *J. Power Sources* **2007**, *171* (2), 275-281.
46. Min, B.; Cheng, S.; Logan, B. E., Electricity generation using membrane and salt bridge microbial fuel cells. *Water Res.* **2005**, *39* (9), 1675-1686.
47. Rabaey, K.; Boon, N.; Höfte, M.; Verstraete, W., Microbial phenazine production enhances electron transfer in biofuel cells. *Environ. Sci. Technol.* **2005**, *39* (9), 3401-3408.
48. Rabaey, K.; Ossieur, W.; Verhaege, M.; Verstraete, W., Continuous microbial fuel cells convert carbohydratesto electricity. *Water Sci. Technol.* **2005**, *52* (1-2), 515-523.
49. Rosenbaum, M.; Schröder, U.; Scholz, F., In situ electrooxidation of photobiological hydrogen in a photobioelectrochemical fuel cell based on *Rhodobacter sphaeroides*. *Environ. Sci. Technol.* **2005**, *39* (16), 6328-6333.
50. Liu, H.; Logan, B. E., Electricity generation using an air-cathode single chamber microbial fuel cell in the presence and absence of a proton exchange membrane. *Environ. Sci. Technol.* **2004**, *38* (14), 4040-4046.
51. Logan, B. E.; Hamelers, B.; Rozendal, R.; Schröder, U.; Keller, J.; Freguia, S.; Aelterman, P.; Verstraete, W.; Rabaey, K., Microbial fuel cells: methodology and technology. *Environ. Sci. Technol.* **2006**, *40* (17), 5181-5192.
52. Janicek, A.; Fan, Y.; Liu, H., Design of microbial fuel cells for practical application: A review and analysis of scale-up studies. *Biofuels* **2014**, *5* (1), 79-92.
53. Wang, H.; Park, J.-D.; Ren, Z. J., Practical energy harvesting for microbial fuel cells: A review. *Environ. Sci. Technol.* **2015**, *49* (6), 3267-3277.

-
54. Aelterman, P.; Rabaey, K.; Pham, H. T.; Boon, N.; Verstraete, W., Continuous electricity generation at high voltages and currents using stacked microbial fuel cells. *Environ. Sci. Technol.* **2006**, *40* (10), 3388-3394.
55. Oh, S. E.; Logan, B. E., Voltage reversal during microbial fuel cell stack operation. *J. Power Sources* **2007**, *167* (1), 11-17.
56. Li, W.; Zhang, S.; Chen, G.; Hua, Y., Simultaneous electricity generation and pollutant removal in microbial fuel cell with denitrifying biocathode over nitrite. *Appl. Energy* **2014**, *126*, 136-141.
57. Huang, L.; Regan, J. M.; Quan, X., Electron transfer mechanisms, new applications, and performance of biocathode microbial fuel cells. *Bioresour. Technol.* **2011**, *102* (1), 316-323.
58. Zhao, F.; Zheng, Z.; Chen, L.; Wu, R. Large creatures cathode microbial fuel cell stack device. CN105355950B, 2015-10-26, 2015. <https://patents.google.com/patent/CN105355950A/en>
59. Zhang, Y.; Angelidaki, I., Microbial electrolysis cells turning to be versatile technology: Recent advances and future challenges. *Water Res.* **2014**, *56*, 11-25.
60. Logan, B. E.; Call, D.; Cheng, S.; Hamelers, H. V.; Sleutels, T. H.; Jeremiasse, A. W.; Rozendal, R. A., Microbial electrolysis cells for high yield hydrogen gas production from organic matter. *Environ. Sci. Technol.* **2008**, *42* (23), 8630-8640.
61. Cheng, S.; Xing, D.; Call, D. F.; Logan, B. E., Direct biological conversion of electrical current into methane by electromethanogenesis. *Environ. Sci. Technol.* **2009**, *43* (10), 3953-3958.
62. Beese-Vasbender, P. F.; Grote, J.-P.; Garrelfs, J.; Stratmann, M.; Mayrhofer, K. J. J., Selective microbial electrosynthesis of methane by a pure culture of a marine lithoautotrophic archaeon. *Bioelectrochemistry* **2015**, *102*, 50-55.
63. Steinbusch, K. J. J.; Hamelers, H. V. M.; Schaap, J. D.; Kampman, C.; Buisman, C. J. N., Bioelectrochemical ethanol production through mediated acetate reduction by mixed cultures. *Environ. Sci. Technol.* **2010**, *44* (1), 513-517.
64. Zhao, H.-Z.; Zhang, Y.; Chang, Y.-Y.; Li, Z.-S., Conversion of a substrate carbon source to formic acid for carbon dioxide emission reduction utilizing series-stacked microbial fuel cells. *J. Power Sources* **2012**, *217*, 59-64.
65. Wang, Q.; Dong, H.; Yu, H.; Yu, H.; Liu, M., Enhanced electrochemical reduction of carbon dioxide to formic acid using a two-layer gas diffusion electrode in a microbial electrolysis cell. *RSC Adv.* **2015**, *5* (14), 10346-10351.
66. Nevin, K. P.; Woodard, T. L.; Franks, A. E.; Summers, Z. M.; Lovley, D. R., Microbial electrosynthesis: Feeding microbes electricity to convert carbon dioxide and water to multicarbon extracellular organic compounds. *mBio* **2010**, *1* (2), e00103-10.
67. Zhang, Y.; Angelidaki, I., Submersible microbial desalination cell for simultaneous ammonia recovery and electricity production from anaerobic reactors containing high levels of ammonia. *Bioresour. Technol.* **2015**, *177*, 233-239.
68. Pan, K.; Zhou, P., A hermetic self-sustained microbial solar cell based on *Chlorella vulgaris* and a versatile charge transfer chain. *J. Power Sources* **2015**, *293*, 467-474.
69. Zheng, Y.; Wang, C.; Zheng, Z.; Che, J.; Xiao, Y.; Yang, Z.; Zhao, F., Ameliorating acidic soil using bioelectrochemistry systems. *RSC Adv.* **2014**, *4* (107), 62544-62549.
70. Sun, H.; Zhang, Y.; Wu, S.; Dong, R.; Angelidaki, I., Innovative operation of microbial fuel cell-based biosensor for selective monitoring of acetate during anaerobic digestion. *Sci. Total Environ.* **2019**, *655*, 1439-1447.
71. Zhou, S.; Huang, S.; Li, Y.; Zhao, N.; Li, H.; Angelidaki, I.; Zhang, Y., Microbial fuel cell-based biosensor for toxic carbon monoxide monitoring. *Talanta* **2018**, *186*, 368-371.

72. Zhao, N.; Li, X.; Jin, X.; Angelidaki, I.; Zhang, Y., Integrated electrochemical-biological process as an alternative mean for ammonia monitoring during anaerobic digestion of organic wastes. *Chemosphere* **2018**, *195*, 735-741.
73. Zhao, N.; Angelidaki, I.; Zhang, Y., Current as an indicator of ammonia concentration during wastewater treatment in an integrated microbial electrolysis cell - Nitrification system. *Electrochim. Acta* **2018**, *281*, 266-273.
74. Jin, X.; Li, X.; Zhao, N.; Angelidaki, I.; Zhang, Y., Bio-electrolytic sensor for rapid monitoring of volatile fatty acids in anaerobic digestion process. *Water Res.* **2017**, *111*, 74-80.
75. Jin, X.; Angelidaki, I.; Zhang, Y., Microbial electrochemical monitoring of volatile fatty acids during anaerobic digestion. *Environ. Sci. Technol.* **2016**, *50* (8), 4422-4429.
76. Zhang, Y.; Angelidaki, I., A simple and rapid method for monitoring dissolved oxygen in water with a submersible microbial fuel cell (SBMFC). *Biosens. Bioelectron.* **2012**, *38* (1), 189-194.
77. Kumar, R.; Singh, L.; Wahid, Z. A.; Din, M. F. M., Exoelectrogens in microbial fuel cells toward bioelectricity generation: a review. *Int. J. Energy Res.* **2015**, *39* (8), 1048-1067.
78. Zheng, Z.; Xiao, Y.; Wu, R.; Mølager Christensen, H. E.; Zhao, F.; Zhang, J., Electrons selective uptake of a metal-reducing bacterium *Shewanella oneidensis* MR-1 from ferrocyanide. *Biosens. Bioelectron.* **2019**, *142*, 111571.
79. Shi, L.; Dong, H.; Reguera, G.; Beyenal, H.; Lu, A.; Liu, J.; Yu, H.-Q.; Fredrickson, J. K., Extracellular electron transfer mechanisms between microorganisms and minerals. *Nat. Rev. Microbiol.* **2016**, *14* (10), 651-662.
80. Xiao, Y.; Zhang, E.; Zhang, J.; Dai, Y.; Yang, Z.; Christensen, H. E. M.; Ulstrup, J.; Zhao, F., Extracellular polymeric substances are transient media for microbial extracellular electron transfer. *Sci. Adv.* **2017**, *3* (7), e1700623.
81. Myers, C. R.; Nealsen, K. H., Bacterial manganese reduction and growth with manganese oxide as the sole electron acceptor. *Science* **1988**, *240* (4857), 1319-1321.
82. Chaudhuri, S. K.; Lovley, D. R., Electricity generation by direct oxidation of glucose in mediatorless microbial fuel cells. *Nat. Biotechnol.* **2003**, *21* (10), 1229-1232.
83. Kim, H. J.; Park, H. S.; Hyun, M. S.; Chang, I. S.; Kim, M.; Kim, B. H., A mediatorless microbial fuel cell using a metal reducing bacterium, *Shewanella putrefaciens*. *Enzyme Microb. Technol.* **2002**, *30* (2), 145-152.
84. Reguera, G.; McCarthy, K. D.; Mehta, T.; Nicoll, J. S.; Tuominen, M. T.; Lovley, D. R., Extracellular electron transfer via microbial nanowires. *Nature* **2005**, *435* (7045), 1098-1101.
85. Shi, L.; Squier, T. C.; Zachara, J. M.; Fredrickson, J. K., Respiration of metal (hydr)oxides by *Shewanella* and *Geobacter*: a key role for multihaem c-type cytochromes. *Mol. Microbiol.* **2007**, *65* (1), 12-20.
86. Yang, Y.; Xu, M.; Guo, J.; Sun, G., Bacterial extracellular electron transfer in bioelectrochemical systems. *Process Biochem.* **2012**, *47* (12), 1707-1714.
87. Gorby, Y. A.; Yanina, S.; McLean, J. S.; Rosso, K. M.; Moyles, D.; Dohnalkova, A.; Beveridge, T. J.; Chang, I. S.; Kim, B. H.; Kim, K. S.; Culley, D. E.; Reed, S. B.; Romine, M. F.; Saffarini, D. A.; Hill, E. A.; Shi, L.; Elias, D. A.; Kennedy, D. W.; Pinchuk, G.; Watanabe, K.; Ishii, S. i.; Logan, B.; Nealsen, K. H.; Fredrickson, J. K., Electrically conductive bacterial nanowires produced by *Shewanella oneidensis* strain MR-1 and other microorganisms. *Proc. Natl. Acad. Sci. U. S. A.* **2006**, *103* (30), 11358-11363.
88. Tender, L. M.; Gray, S. A.; Groveman, E.; Lowy, D. A.; Kauffman, P.; Melhado, J.; Tyce, R. C.; Flynn, D.; Petrecca, R.; Dobarro, J., The first demonstration of a microbial

-
- fuel cell as a viable power supply: Powering a meteorological buoy. *J. Power Sources* **2008**, *179* (2), 571-575.
89. Marsili, E.; Baron, D. B.; Shikhare, I. D.; Coursolle, D.; Gralnick, J. A.; Bond, D. R., *Shewanella* secretes flavins that mediate extracellular electron transfer. *Proc. Natl. Acad. Sci. U. S. A.* **2008**, *105* (10), 3968-3973.
90. Pirbadian, S.; El-Naggar, M. Y., Multistep hopping and extracellular charge transfer in microbial redox chains. *Phys. Chem. Chem. Phys.* **2012**, *14* (40), 13802-13808.
91. Malvankar, N. S.; Lovley, D. R., Microbial nanowires: A new paradigm for biological electron transfer and bioelectronics. *ChemSusChem* **2012**, *5* (6), 1039-1046.
92. Gross, B. J.; El-Naggar, M. Y., A combined electrochemical and optical trapping platform for measuring single cell respiration rates at electrode interfaces. *Rev. Sci. Instrum.* **2015**, *86* (6), 064301.
93. Jiang, X.; Hu, J.; Petersen, E. R.; Fitzgerald, L. A.; Jackan, C. S.; Lieber, A. M.; Ringeisen, B. R.; Lieber, C. M.; Biffinger, J. C., Probing single- to multi-cell level charge transport in *Geobacter sulfurreducens* DL-1. *Nat. Commun.* **2013**, *4*, 2751.
94. Gregory, K. B.; Bond, D. R.; Lovley, D. R., Graphite electrodes as electron donors for anaerobic respiration. *Environ. Microbiol.* **2004**, *6* (6), 596-604.
95. Gregory, K. B.; Lovley, D. R., Remediation and recovery of uranium from contaminated subsurface environments with electrodes. *Environ. Sci. Technol.* **2005**, *39* (22), 8943-8947.
96. Strycharz, S. M.; Glaven, R. H.; Coppi, M. V.; Gannon, S. M.; Perpetua, L. A.; Liu, A.; Nevin, K. P.; Lovley, D. R., Gene expression and deletion analysis of mechanisms for electron transfer from electrodes to *Geobacter sulfurreducens*. *Bioelectrochemistry* **2011**, *80* (2), 142-150.
97. Ueki, T.; Nevin, K. P.; Woodard, T. L.; Lovley, D. R., Converting carbon dioxide to butyrate with an engineered strain of *Clostridium ljungdahlii*. *mBio* **2014**, *5* (5), e01636-14.
98. Bose, A.; Gardel, E. J.; Vidoudez, C.; Parra, E. A.; Girguis, P. R., Electron uptake by iron-oxidizing phototrophic bacteria. *Nat. Commun.* **2014**, *5*, 3391.
99. Deutzmann, J. S.; Sahin, M.; Spormann, A. M., Extracellular enzymes facilitate electron uptake in biocorrosion and bioelectrosynthesis. *mBio* **2015**, *6* (2), e00496-15.
100. Yates, M. D.; Eddie, B. J.; Kotloski, N. J.; Lebedev, N.; Malanoski, A. P.; Lin, B.; Strycharz-Glaven, S. M.; Tender, L. M., Toward understanding long-distance extracellular electron transport in an electroautotrophic microbial community. *Energy Environ. Sci.* **2016**, *9* (11), 3544-3558.
101. Kumar, A.; Hsu, L. H.-H.; Kavanagh, P.; Barrière, F.; Lens, P. N. L.; Lapinonnière, L.; Lienhard V, J. H.; Schröder, U.; Jiang, X.; Leech, D., The ins and outs of microorganism–electrode electron transfer reactions. *Nat. Rev. Chem.* **2017**, *1* (3), 0024.
102. Liu, X.; Zhuo, S.; Rensing, C.; Zhou, S., Syntrophic growth with direct interspecies electron transfer between pili-free *Geobacter* species. *ISME J.* **2018**, *12* (9), 2142-2151.
103. Ueki, T.; Nevin, K. P.; Rotaru, A.-E.; Wang, L.-Y.; Ward, J. E.; Woodard, T. L.; Lovley, D. R., *Geobacter* strains expressing poorly conductive pili reveal constraints on direct interspecies electron transfer mechanisms. *mBio* **2018**, *9* (4), e01273-18.
104. Ha, P. T.; Lindemann, S. R.; Shi, L.; Dohnalkova, A. C.; Fredrickson, J. K.; Madigan, M. T.; Beyenal, H., Syntrophic anaerobic photosynthesis via direct interspecies electron transfer. *Nat. Commun.* **2017**, *8*, 13924.

105. Chen, S.; Rotaru, A.-E.; Liu, F.; Philips, J.; Woodard, T. L.; Nevin, K. P.; Lovley, D. R., Carbon cloth stimulates direct interspecies electron transfer in syntrophic co-cultures. *Bioresour. Technol.* **2014**, *173*, 82-86.
106. Kang, H.-J.; Lee, S.-H.; Lim, T.-G.; Park, H.-D., Effect of inoculum concentration on methanogenesis by direct interspecies electron transfer: Performance and microbial community composition. *Bioresour. Technol.* **2019**, *291*, 121881.
107. Liu, F.; Rotaru, A.-E.; Shrestha, P. M.; Malvankar, N. S.; Nevin, K. P.; Lovley, D. R., Promoting direct interspecies electron transfer with activated carbon. *Energy Environ. Sci.* **2012**, *5* (10), 8982-8989.
108. Summers, Z. M.; Fogarty, H. E.; Leang, C.; Franks, A. E.; Malvankar, N. S.; Lovley, D. R., Direct exchange of electrons within aggregates of an evolved syntrophic coculture of anaerobic bacteria. *Science* **2010**, *330* (6009), 1413.
109. Logan, B. E.; Rossi, R.; Ragab, A. a.; Saikaly, P. E., Electroactive microorganisms in bioelectrochemical systems. *Nat. Rev. Microbiol.* **2019**, *17* (5), 307-319.
110. Beyenal, H.; Babauta, J., *Biofilms in bioelectrochemical systems: From laboratory practice to data interpretation*. Wiley: 2015; p 1-412.
111. Marsili, E.; Rollefson, J. B.; Baron, D. B.; Hozalski, R. M.; Bond, D. R., Microbial biofilm voltammetry: Direct electrochemical characterization of catalytic electrode-attached biofilms. *Appl. Environ. Microbiol.* **2008**, *74* (23), 7329.
112. Picioreanu, C.; Head, I. M.; Katuri, K. P.; van Loosdrecht, M. C. M.; Scott, K., A computational model for biofilm-based microbial fuel cells. *Water Res.* **2007**, *41* (13), 2921-2940.
113. Nevin, K. P.; Lovley, D. R., Lack of production of electron-shuttling compounds or solubilization of Fe(III) during reduction of insoluble Fe(III) oxide by *Geobacter metallireducens*. *Appl. Environ. Microbiol.* **2000**, *66* (5), 2248.
114. Heidelberg, J. F.; Paulsen, I. T.; Nelson, K. E.; Gaidos, E. J.; Nelson, W. C.; Read, T. D.; Eisen, J. A.; Seshadri, R.; Ward, N.; Methe, B.; Clayton, R. A.; Meyer, T.; Tsapin, A.; Scott, J.; Beanan, M.; Brinkac, L.; Daugherty, S.; DeBoy, R. T.; Dodson, R. J.; Durkin, A. S.; Haft, D. H.; Kolonay, J. F.; Madupu, R.; Peterson, J. D.; Umayam, L. A.; White, O.; Wolf, A. M.; Vamathevan, J.; Weidman, J.; Impraim, M.; Lee, K.; Berry, K.; Lee, C.; Mueller, J.; Khouri, H.; Gill, J.; Utterback, T. R.; McDonald, L. A.; Feldblyum, T. V.; Smith, H. O.; Venter, J. C.; Nealson, K. H.; Fraser, C. M., Genome sequence of the dissimilatory metal ion-reducing bacterium *Shewanella oneidensis*. *Nat. Biotechnol.* **2002**, *20* (11), 1118-1123.
115. Derby, H.; Hammer, B., Bacteriology of butter IV. Bacteriological studies on surface taint butter. *Research Bulletin (Iowa Agriculture and Home Economics Experiment Station)* **1931**, *11* (145), 1.
116. MacDonell, M. T.; Colwell, R. R., Phylogeny of the vibronaceae, and recommendation for two new genera, *Listonella* and *Shewanella*. *Syst. Appl. Microbiol.* **1985**, *6* (2), 171-182.
117. Venkateswaran, K.; Moser, D. P.; Dollhopf, M. E.; Lies, D. P.; Saffarini, D. A.; MacGregor, B. J.; Ringelberg, D. B.; White, D. C.; Nishijima, M.; Sano, H.; Burghardt, J.; Stackebrandt, E.; Nealson, K. H., Polyphasic taxonomy of the genus *Shewanella* and description of *Shewanella oneidensis* sp. nov. *Int. J. Syst. Evol. Microbiol.* **1999**, *49* (2), 705-724.
118. Coursolle, D.; Gralnick, J. A., Modularity of the Mtr respiratory pathway of *Shewanella oneidensis* strain MR-1. *Mol. Microbiol.* **2010**, *77* (4), 995-1008.
119. Ross, D. E.; Flynn, J. M.; Baron, D. B.; Gralnick, J. A.; Bond, D. R., Towards electrosynthesis in *Shewanella*: Energetics of reversing the mtr pathway for reductive metabolism. *PLoS ONE* **2011**, *6* (2), e16649.

-
120. Coursolle, D.; Baron, D. B.; Bond, D. R.; Gralnick, J. A., The Mtr respiratory pathway is essential for reducing flavins and electrodes in *Shewanella oneidensis*. *J. Bacteriol.* **2010**, *192* (2), 467-474.
121. Breuer, M.; Rosso, K. M.; Blumberger, J., Electron flow in multiheme bacterial cytochromes is a balancing act between heme electronic interaction and redox potentials. *Proc. Natl. Acad. Sci. U. S. A.* **2014**, *111* (2), 611.
122. Clarke, T. A.; Edwards, M. J.; Gates, A. J.; Hall, A.; White, G. F.; Bradley, J.; Reardon, C. L.; Shi, L.; Beliaev, A. S.; Marshall, M. J.; Wang, Z.; Watmough, N. J.; Fredrickson, J. K.; Zachara, J. M.; Butt, J. N.; Richardson, D. J., Structure of a bacterial cell surface decaheme electron conduit. *Proc. Natl. Acad. Sci. U. S. A.* **2011**, *108* (23), 9384.
123. Strycharz-Glaven, S. M.; Snider, R. M.; Guiseppi-Elie, A.; Tender, L. M., On the electrical conductivity of microbial nanowires and biofilms. *Energy Environ. Sci.* **2011**, *4* (11), 4366-4379.
124. Pirbadian, S.; Barchinger, S. E.; Leung, K. M.; Byun, H. S.; Jangir, Y.; Bouhenni, R. A.; Reed, S. B.; Romine, M. F.; Saffarini, D. A.; Shi, L.; Gorby, Y. A.; Golbeck, J. H.; El-Naggar, M. Y., *Shewanella oneidensis* MR-1 nanowires are outer membrane and periplasmic extensions of the extracellular electron transport components. *Proc. Natl. Acad. Sci. U. S. A.* **2014**, *111* (35), 12883-12888.
125. El-Naggar, M. Y.; Wanger, G.; Leung, K. M.; Yuzvinsky, T. D.; Southam, G.; Yang, J.; Lau, W. M.; Nealsen, K. H.; Gorby, Y. A., Electrical transport along bacterial nanowires from *Shewanella oneidensis* MR-1. *Proc. Natl. Acad. Sci. U. S. A.* **2010**, *107* (42), 18127-18131.
126. Venkata Mohan, S.; Velvizhi, G.; Annie Modestra, J.; Srikanth, S., Microbial fuel cell: Critical factors regulating bio-catalyzed electrochemical process and recent advancements. *Renewable Sustainable Energy Rev.* **2014**, *40*, 779-797.
127. Pankratova, G.; Hederstedt, L.; Gorton, L., Extracellular electron transfer features of Gram-positive bacteria. *Anal. Chim. Acta* **2019**, *1076*, 32-47.
128. Hernandez, M. E.; Kappler, A.; Newman, D. K., Phenazines and other redox-active antibiotics promote microbial mineral reduction. *Appl. Environ. Microbiol.* **2004**, *70* (2), 921.
129. Freguia, S.; Masuda, M.; Tsujimura, S.; Kano, K., *Lactococcus lactis* catalyses electricity generation at microbial fuel cell anodes via excretion of a soluble quinone. *Bioelectrochemistry* **2009**, *76* (1), 14-18.
130. Qiao, Y.; Li, C. M.; Bao, S.-J.; Lu, Z.; Hong, Y., Direct electrochemistry and electrocatalytic mechanism of evolved *Escherichia coli* cells in microbial fuel cells. *Chem. Commun. (Camb.)* **2008**, (11), 1290-1292.
131. von Canstein, H.; Ogawa, J.; Shimizu, S.; Lloyd, J. R., Secretion of flavins by *Shewanella* species and their role in extracellular electron transfer. *Appl. Environ. Microbiol.* **2008**, *74* (3), 615-623.
132. Xu, S.; Jangir, Y.; El-Naggar, M. Y., Disentangling the roles of free and cytochrome-bound flavins in extracellular electron transport from *Shewanella oneidensis* MR-1. *Electrochim. Acta* **2016**, *198*, 49-55.
133. Wu, S.; Xiao, Y.; Wang, L.; Zheng, Y.; Chang, K.; Zheng, Z.; Yang, Z.; Varcoe, J. R.; Zhao, F., Extracellular electron transfer mediated by flavins in Gram-positive *Bacillus* sp. WS-XY1 and yeast *Pichia stipitis*. *Electrochim. Acta* **2014**, *146*, 564-567.
134. Park, D. H.; Laivenieks, M.; Guettler, M. V.; Jain, M. K.; Zeikus, J. G., Microbial utilization of electrically reduced neutral red as the sole electron donor for growth and metabolite production. *Appl. Environ. Microbiol.* **1999**, *65* (7), 2912-2917.

135. Lovley, D. R.; Coates, J. D.; Blunt-Harris, E. L.; Phillips, E. J. P.; Woodward, J. C., Humic substances as electron acceptors for microbial respiration. *Nature* **1996**, *382* (6590), 445-448.
136. Lovley, D. R.; Fraga, J. L.; Blunt-Harris, E. L.; Hayes, L. A.; Phillips, E. J. P.; Coates, J. D., Humic substances as a mediator for microbially catalyzed metal reduction. *Acta Hydrochim. Hydrobiol.* **1998**, *26* (3), 152-157.
137. Hernandez, M. E.; Newman, D. K., Extracellular electron transfer. *Cell. Mol. Life Sci.* **2001**, *58* (11), 1562-1571.
138. Tian, X.; Zhao, F.; You, L.; Wu, X.; Zheng, Z.; Wu, R.; Jiang, Y.; Sun, S., Interaction between *in vivo* bioluminescence and extracellular electron transfer in *Shewanella woodyi* via charge and discharge. *Phys. Chem. Chem. Phys.* **2017**, *19* (3), 1746-1750.
139. Covington, E. D.; Gelbmann, C. B.; Kotloski, N. J.; Gralnick, J. A., An essential role for UshA in processing of extracellular flavin carbon shuttles by *Shewanella oneidensis*. *Mol. Microbiol.* **2010**, *78* (2), 519-532.
140. Li, S.-L.; Bai, M.-D.; Hsiao, C.-J.; Cheng, S.-S.; Nealson, K. H., A metabolic-activity-detecting approach to life detection: Restoring a chemostat from stop-feeding using a rapid bioactivity assay. *Bioelectrochemistry* **2017**, *118*, 147-153.
141. ISO, 2015. International Organization for Standardization. Nanotechnologies—vocabulary—part 1: Core Terms. ISO/TS 80004-1:2015
142. Fu, Y.; Liang, F.; Tian, H.; Hu, J., Nonenzymatic glucose sensor based on ITO electrode modified with gold nanoparticles by ion implantation. *Electrochim. Acta* **2014**, *120*, 314-318.
143. Jukk, K.; Kozlova, J.; Ritslaid, P.; Sammelselg, V.; Alexeyeva, N.; Tammeveski, K., Sputter-deposited Pt nanoparticle/multi-walled carbon nanotube composite catalyst for oxygen reduction reaction. *J. Electroanal. Chem.* **2013**, *708*, 31-38.
144. Patel, N.; Fernandes, R.; Guella, G.; Kale, A.; Miotello, A.; Patton, B.; Zanchetta, C., Structured and nanoparticle assembled Co-B thin films prepared by pulsed laser deposition: A very efficient catalyst for hydrogen production. *J. Phys. Chem. C* **2008**, *112* (17), 6968-6976.
145. Ariga, K.; Mori, T.; Hill, J. P., Mechanical control of nanomaterials and nanosystems. *Adv. Mater.* **2012**, *24* (2), 158-176.
146. Xu, J.; Sun, J.; Wang, Y.; Sheng, J.; Wang, F.; Sun, M., Application of iron magnetic nanoparticles in protein immobilization. *Molecules* **2014**, *19* (8), 11465-11486.
147. Gupta, S.; Kershaw, S. V.; Rogach, A. L., 25th Anniversary article: Ion exchange in colloidal nanocrystals. *Adv. Mater.* **2013**, *25* (48), 6923-6944.
148. Schwamborn, S.; Etienne, M.; Schuhmann, W., Local electrocatalytic induction of sol-gel deposition at Pt nanoparticles. *Electrochem. Commun.* **2011**, *13* (8), 759-762.
149. Cao, H.; Wang, X.; Gu, H.; Liu, J.; Luan, L.; Liu, W.; Wang, Y.; Guo, Z., Carbon coated manganese monoxide octahedron negative-electrode for lithium-ion batteries with enhanced performance. *RSC Adv.* **2015**, *5* (44), 34566-34571.
150. Cao, H.; Wu, N.; Liu, Y.; Wang, S.; Du, W.; Liu, J., Facile synthesis of rod-like manganese molybdate crystallines with two-dimensional nanoflakes for supercapacitor application. *Electrochim. Acta* **2017**, *225*, 605-613.
151. Engelbrekt, C.; Sørensen, K. H.; Lübcke, T.; Zhang, J.; Li, Q.; Pan, C.; Bjerrum, N. J.; Ulstrup, J., 1.7 nm platinum nanoparticles: Synthesis with glucose starch, characterization and catalysis. *ChemPhysChem* **2010**, *11* (13), 2844-2853.
152. Engelbrekt, C.; Sorensen, K. H.; Zhang, J.; Welinder, A. C.; Jensen, P. S.; Ulstrup, J., Green synthesis of gold nanoparticles with starch-glucose and application in bioelectrochemistry. *J. Mater. Chem.* **2009**, *19* (42), 7839-7847.

-
153. Hulkoti, N. I.; Taranath, T. C., Biosynthesis of nanoparticles using microbes—A review. *Colloids Surf., B* **2014**, *121*, 474-483.
154. Mohanpuria, P.; Rana, N. K.; Yadav, S. K., Biosynthesis of nanoparticles: technological concepts and future applications. *J. Nanopart. Res.* **2008**, *10* (3), 507-517.
155. Roy, K.; Mao, H.-Q.; Huang, S. K.; Leong, K. W., Oral gene delivery with chitosan-DNA nanoparticles generates immunologic protection in a murine model of peanut allergy. *Nat. Med.* **1999**, *5* (4), 387-391.
156. Liu, J.; Zheng, Y.; Hong, Z.; Cai, K.; Zhao, F.; Han, H., Microbial synthesis of highly dispersed PdAu alloy for enhanced electrocatalysis. *Sci. Adv.* **2016**, *2* (9), e1600858.
157. Windt, W. D.; Aelterman, P.; Verstraete, W., Bioreductive deposition of palladium (0) nanoparticles on *Shewanella oneidensis* with catalytic activity towards reductive dechlorination of polychlorinated biphenyls. *Environ. Microbiol.* **2005**, *7* (3), 314-325.
158. Kimber, R. L.; Lewis, E. A.; Parmeggiani, F.; Smith, K.; Bagshaw, H.; Starborg, T.; Joshi, N.; Figueroa, A. I.; van der Laan, G.; Cibin, G.; Gianolio, D.; Haigh, S. J.; Pattrick, R. A. D.; Turner, N. J.; Lloyd, J. R., Biosynthesis and characterization of copper nanoparticles using *Shewanella oneidensis*: Application for click chemistry. *Small* **2018**, *14* (10), 1703145.
159. Ng, C. K.; Sivakumar, K.; Liu, X.; Madhaiyan, M.; Ji, L.; Yang, L.; Tang, C.; Song, H.; Kjelleberg, S.; Cao, B., Influence of outer membrane *c*-type cytochromes on particle size and activity of extracellular nanoparticles produced by *Shewanella oneidensis*. *Biotechnol. Bioeng.* **2013**, *110* (7), 1831-1837.
160. Li, D.-B.; Cheng, Y.-Y.; Wu, C.; Li, W.-W.; Li, N.; Yang, Z.-C.; Tong, Z.-H.; Yu, H.-Q., Selenite reduction by *Shewanella oneidensis* MR-1 is mediated by fumarate reductase in periplasm. *Sci. Rep.* **2014**, *4*, 3735.
161. Ng, C. K.; Cai Tan, T. K.; Song, H.; Cao, B., Reductive formation of palladium nanoparticles by *Shewanella oneidensis*: role of outer membrane cytochromes and hydrogenases. *RSC Adv.* **2013**, *3* (44), 22498-22503.
162. Zhou, N.-Q.; Tian, L.-J.; Wang, Y.-C.; Li, D.-B.; Li, P.-P.; Zhang, X.; Yu, H.-Q., Extracellular biosynthesis of copper sulfide nanoparticles by *Shewanella oneidensis* MR-1 as a photothermal agent. *Enzyme Microb. Technol.* **2016**, *95*, 230-235.
163. Xiao, X.; Liu, Q.-Y.; Lu, X.-R.; Li, T.-T.; Feng, X.-L.; Li, Q.; Liu, Z.-Y.; Feng, Y.-J., Self-assembly of complex hollow CuS nano/micro shell by an electrochemically active bacterium *Shewanella oneidensis* MR-1. *Int. Biodeterior. Biodegrad.* **2017**, *116*, 10-16.
164. Wu, R.; Cui, L.; Chen, L.; Wang, C.; Cao, C.; Sheng, G.; Yu, H.; Zhao, F., Effects of bio-Au nanoparticles on electrochemical activity of *Shewanella oneidensis* wild type and $\Delta omCA/mtrC$ mutant. *Sci. Rep.* **2013**, *3*, 3307.
165. Tuo, Y.; Liu, G.; Dong, B.; Zhou, J.; Wang, A.; Wang, J.; Jin, R.; Lv, H.; Dou, Z.; Huang, W., Microbial synthesis of Pd/Fe₃O₄, Au/Fe₃O₄ and PdAu/Fe₃O₄ nanocomposites for catalytic reduction of nitroaromatic compounds. *Sci. Rep.* **2015**, *5*, 13515.
166. Miller, A.; Singh, L.; Wang, L.; Liu, H., Linking internal resistance with design and operation decisions in microbial electrolysis cells. *Environ. Int.* **2019**, *126*, 611-618.
167. Huang, B. C.; Yi, Y.-C.; Chang, J.-S.; Ng, I. S., Mechanism study of photo-induced gold nanoparticles formation by *Shewanella oneidensis* MR-1. *Sci. Rep.* **2019**, *9* (1), 7589.
168. Che, L.; Dong, Y.; Wu, M.; Zhao, Y.; Liu, L.; Zhou, H., Characterization of selenite reduction by *Lysinibacillus* sp. ZYM-1 and photocatalytic performance of biogenic selenium nanospheres. *ACS Sustainable Chem. Eng.* **2017**, *5* (3), 2535-2543.

169. Søbjerg, L. S.; Gauthier, D.; Lindhardt, A. T.; Bunge, M.; Finster, K.; Meyer, R. L.; Skrydstrup, T., Bio-supported palladium nanoparticles as a catalyst for Suzuki–Miyaura and Mizoroki–Heck reactions. *Green Chem.* **2009**, *11* (12), 2041-2046.
170. Gauthier, D.; Søbjerg, L. S.; Jensen, K. M.; Lindhardt, A. T.; Bunge, M.; Finster, K.; Meyer, R. L.; Skrydstrup, T., Environmentally benign recovery and reactivation of palladium from industrial waste by using gram-negative bacteria. *ChemSusChem* **2010**, *3* (9), 1036-1039.
171. Bunge, M.; Søbjerg, L. S.; Rotaru, A.-E.; Gauthier, D.; Lindhardt, A. T.; Hause, G.; Finster, K.; Kingshott, P.; Skrydstrup, T.; Meyer, R. L., Formation of palladium(0) nanoparticles at microbial surfaces. *Biotechnol. Bioeng.* **2010**, *107* (2), 206-215.
172. Kowshik, M.; Vogel, W.; Urban, J.; Kulkarni, S. K.; Paknikar, K. M., Microbial synthesis of semiconductor PbS nanocrystallites. *Adv. Mater.* **2002**, *14* (11), 815-818.
173. Wu, R.; Tian, X.; Xiao, Y.; Ulstrup, J.; Molager Christensen, H. E.; Zhao, F.; Zhang, J., Selective electrocatalysis of biofuel molecular oxidation using palladium nanoparticles generated on *Shewanella oneidensis* MR-1. *J. Mater. Chem. A* **2018**, *6* (23), 10655-10662.
174. Wang, T.; Yang, L.; Zhang, B.; Liu, J., Extracellular biosynthesis and transformation of selenium nanoparticles and application in H₂O₂ biosensor. *Colloids Surf., B* **2010**, *80* (1), 94-102.
175. Sakimoto, K. K.; Wong, A. B.; Yang, P., Self-photosensitization of nonphotosynthetic bacteria for solar-to-chemical production. *Science* **2016**, *351* (6268), 74.
176. Zhang, H.; Liu, H.; Tian, Z.; Lu, D.; Yu, Y.; Cestellos-Blanco, S.; Sakimoto, K. K.; Yang, P., Bacteria photosensitized by intracellular gold nanoclusters for solar fuel production. *Nat. Nanotechnol.* **2018**, *13* (10), 900-905.
177. Wu, R.; Wang, C.; Shen, J.; Zhao, F., A role for biosynthetic CdS quantum dots in extracellular electron transfer of *Saccharomyces cerevisiae*. *Process Biochem.* **2015**, *50* (12), 2061-2065.
178. Beveridge, T. J.; Murray, R. G., Sites of metal deposition in the cell wall of *Bacillus subtilis*. *J. Bacteriol.* **1980**, *141* (2), 876-887.
179. Sweeney, R. Y.; Mao, C.; Gao, X.; Burt, J. L.; Belcher, A. M.; Georgiou, G.; Iverson, B. L., Bacterial biosynthesis of cadmium sulfide nanocrystals. *Chem. Biol.* **2004**, *11* (11), 1553-1559.
180. Suresh, A. K.; Pelletier, D. A.; Wang, W.; Moon, J.-W.; Gu, B.; Mortensen, N. P.; Allison, D. P.; Joy, D. C.; Phelps, T. J.; Doktycz, M. J., Silver nanocrystallites: Biofabrication using *Shewanella oneidensis*, and an evaluation of their comparative toxicity on gram-negative and gram-positive bacteria. *Environ. Sci. Technol.* **2010**, *44* (13), 5210-5215.
181. Mal, J.; Nancharaiah, Y. V.; van Hullebusch, E. D.; Lens, P. N. L., Metal chalcogenide quantum dots: biotechnological synthesis and applications. *RSC Adv.* **2016**, *6* (47), 41477-41495.
182. Park, T. J.; Lee, K. G.; Lee, S. Y., Advances in microbial biosynthesis of metal nanoparticles. *Appl. Microbiol. Biotechnol.* **2016**, *100* (2), 521-534.
183. Ghosh, S., Copper and palladium nanostructures: a bacteriogenic approach. *Appl. Microbiol. Biotechnol.* **2018**, *102* (18), 7693-7701.
184. Khatami, M.; Alijani, H. Q.; Sharifi, I., Biosynthesis of bimetallic and core–shell nanoparticles: their biomedical applications – a review. *IET Nanobiotechnol.* **2018**, *12* (7), 879-887.
185. Kim, T.-Y.; Kim, M. G.; Lee, J.-H.; Hur, H.-G., Biosynthesis of nanomaterials by *Shewanella* species for application in lithium ion batteries. *Front. Microbiol.* **2018**, *9*, 2817.

-
186. Vaseghi, Z.; Nematollahzadeh, A.; Tavakoli, O., Green methods for the synthesis of metal nanoparticles using biogenic reducing agents: a review. *Rev. Chem. Eng.* **2018**, *34* (4), 529.
187. Gahlawat, G.; Choudhury, A. R., A review on the biosynthesis of metal and metal salt nanoparticles by microbes. *RSC Adv.* **2019**, *9* (23), 12944-12967.
188. Salunke, B. K.; Sawant, S. S.; Lee, S.-I.; Kim, B. S., Microorganisms as efficient biosystem for the synthesis of metal nanoparticles: current scenario and future possibilities. *World J. Microbiol. Biotechnol.* **2016**, *32* (5), 88.
189. van der Wal, A.; Minor, M.; Norde, W.; Zehnder, A. J. B.; Lyklema, J., Electrokinetic potential of bacterial cells. *Langmuir* **1997**, *13* (2), 165-171.
190. Li, X.; Xu, H.; Chen, Z.-S.; Chen, G., Biosynthesis of nanoparticles by microorganisms and their applications. *J. Nanomater.* **2011**, *2011*, 16.
191. Narayanan, K. B.; Sakthivel, N., Biological synthesis of metal nanoparticles by microbes. *Adv. Colloid Interface Sci.* **2010**, *156* (1), 1-13.
192. Beveridge, T. J., Role of cellular design in bacterial metal accumulation and mineralization. *Annu. Rev. Microbiol.* **1989**, *43* (1), 147-171.
193. Kumar, R.; Singh, L.; Zularisam, A. W., Exoelectrogens: Recent advances in molecular drivers involved in extracellular electron transfer and strategies used to improve it for microbial fuel cell applications. *Renewable Sustainable Energy Rev.* **2016**, *56*, 1322-1336.
194. Belchik, S. M.; Kennedy, D. W.; Dohnalkova, A. C.; Wang, Y.; Sevinc, P. C.; Wu, H.; Lin, Y.; Lu, H. P.; Fredrickson, J. K.; Shi, L., Extracellular reduction of hexavalent chromium by cytochromes MtrC and OmcA of *Shewanella oneidensis* MR-1. *Appl. Environ. Microbiol.* **2011**, *77* (12), 4035.
195. Marshall, M. J.; Beliaev, A. S.; Dohnalkova, A. C.; Kennedy, D. W.; Shi, L.; Wang, Z.; Boyanov, M. I.; Lai, B.; Kemner, K. M.; McLean, J. S.; Reed, S. B.; Culley, D. E.; Bailey, V. L.; Simonson, C. J.; Saffarini, D. A.; Romine, M. F.; Zachara, J. M.; Fredrickson, J. K., c-Type cytochrome-dependent formation of U(IV) nanoparticles by *Shewanella oneidensis*. *PLoS Biol.* **2006**, *4* (8), 1324-1333.
196. Meshulam-Simon, G.; Behrens, S.; Choo, A. D.; Spormann, A. M., Hydrogen metabolism in *Shewanella oneidensis* MR-1. *Appl. Environ. Microbiol.* **2007**, *73* (4), 1153-1165.
197. Kim, D.-H.; Kanaly, R. A.; Hur, H.-G., Biological accumulation of tellurium nanorod structures via reduction of tellurite by *Shewanella oneidensis* MR-1. *Bioresour. Technol.* **2012**, *125*, 127-131.
198. Klonowska, A.; Heulin, T.; Vermeglio, A., Selenite and tellurite reduction by *Shewanella oneidensis*. *Appl. Environ. Microbiol.* **2005**, *71* (9), 5607.
199. Wang, Z.; Zheng, Z.; Zheng, S.; Chen, S.; Zhao, F., Carbonized textile with free-standing threads as an efficient anode material for bioelectrochemical systems. *J. Power Sources* **2015**, *287*, 269-275.
200. Perez-Gonzalez, T.; Jimenez-Lopez, C.; Neal, A. L.; Rull-Perez, F.; Rodriguez-Navarro, A.; Fernandez-Vivas, A.; Iañez-Pareja, E., Magnetite biomineralization induced by *Shewanella oneidensis*. *Geochim. Cosmochim. Acta* **2010**, *74* (3), 967-979.
201. Wu, X.; Zhao, F.; Rahunen, N.; Varcoe, J. R.; Avignone-Rossa, C.; Thumser, A. E.; Slade, R. C. T., A role for microbial palladium nanoparticles in extracellular electron transfer. *Angew. Chem. Int. Ed.* **2010**, *50* (2), 427-430.
202. Konishi, Y.; Ohno, K.; Saitoh, N.; Nomura, T.; Nagamine, S.; Hishida, H.; Takahashi, Y.; Uruga, T., Bioreductive deposition of platinum nanoparticles on the bacterium *Shewanella algae*. *J. Biotechnol.* **2007**, *128* (3), 648-653.

203. Varia, J.; Zegeye, A.; Roy, S.; Yahaya, S.; Bull, S., *Shewanella putrefaciens* for the remediation of Au³⁺, Co²⁺ and Fe³⁺ metal ions from aqueous systems. *Biochem. Eng. J.* **2014**, *85*, 101-109.
204. Burns, J. L.; DiChristina, T. J., Anaerobic respiration of elemental sulfur and thiosulfate by *Shewanella oneidensis* MR-1 requires *psrA*, a homolog of the *phsA* gene of *Salmonella enterica* serovar Typhimurium LT2. *Appl. Environ. Microbiol.* **2009**, *75* (16), 5209-5217.
205. Voeikova, T. A.; Shebanova, A. S.; Ivanov, Y. D.; Kaysheva, A. L.; Novikova, L. M.; Zhuravliova, O. A.; Shumyantseva, V. V.; Shaitan, K. V.; Kirpichnikov, M. P.; Debabov, V. G., The role of proteins of the outer membrane of *Shewanella oneidensis* MR-1 in the formation and stabilization of silver sulfide nanoparticles. *Appl. Biochem. Microbiol.* **2016**, *52* (8), 769-775.
206. Yang, M.; Shi, X., Biosynthesis of Ag₂S/TiO₂ nanotubes nanocomposites by *Shewanella oneidensis* MR-1 for the catalytic degradation of 4-nitrophenol. *Environ. Sci. Pollut. Res.* **2019**, *26* (12), 12237-12246.
207. Butler, E. C.; Hayes, K. F., Effects of solution composition and pH on the reductive dechlorination of hexachloroethane by iron sulfide. *Environ. Sci. Technol.* **1998**, *32* (9), 1276-1284.
208. Huo, Y.-C.; Li, W.-W.; Chen, C.-B.; Li, C.-X.; Zeng, R.; Lau, T.-C.; Huang, T.-Y., Biogenic FeS accelerates reductive dechlorination of carbon tetrachloride by *Shewanella putrefaciens* CN32. *Enzyme Microb. Technol.* **2016**, *95*, 236-241.
209. Wang, L.; Chen, S.; Ding, Y.; Zhu, Q.; Zhang, N.; Yu, S., Biofabrication of morphology improved cadmium sulfide nanoparticles using *Shewanella oneidensis* bacterial cells and ionic liquid: For toxicity against brain cancer cell lines. *J. Photochem. Photobiol., B* **2018**, *178*, 424-427.
210. Lee, J.-H.; Kim, M.-G.; Yoo, B.; Myung, N. V.; Maeng, J.; Lee, T.; Dohnalkova, A. C.; Fredrickson, J. K.; Sadowsky, M. J.; Hur, H.-G., Biogenic formation of photoactive arsenic-sulfide nanotubes by *Shewanella* sp. strain HN-41. *Proc. Natl. Acad. Sci. U. S. A.* **2007**, *104* (51), 20410-20415.
211. Labrenz, M.; Druschel, G. K.; Thomsen-Ebert, T.; Gilbert, B.; Welch, S. A.; Kemner, K. M.; Logan, G. A.; Summons, R. E.; Stasio, G. D.; Bond, P. L.; Lai, B.; Kelly, S. D.; Banfield, J. F., Formation of sphalerite (ZnS) deposits in natural biofilms of sulfate-reducing bacteria. *Science* **2000**, *290* (5497), 1744-1747.
212. Lee, J.-H.; Kennedy, D. W.; Dohnalkova, A.; Moore, D. A.; Nachimuthu, P.; Reed, S. B.; Fredrickson, J. K., Manganese sulfide formation via concomitant microbial manganese oxide and thiosulfate reduction. *Environ. Microbiol.* **2011**, *13* (12), 3275-3288.
213. Lee, J.-H.; Roh, Y.; Hur, H.-G., Microbial production and characterization of superparamagnetic magnetite nanoparticles by *Shewanella* sp. HN-41. *J. Microbiol. Biotechnol.* **2008**, *18* (9), 1572-1577.
214. Jiang, S.; Kim, M.-G.; Kim, I. Y.; Hwang, S.-J.; Hur, H.-G., Biological synthesis of free-standing uniformed goethite nanowires by *Shewanella* sp. HN-41. *J. Mater. Chem. A* **2013**, *1* (5), 1646-1650.
215. Zannoni, D.; Borsetti, F.; Harrison, J. J.; Turner, R. J., The Bacterial Response to the Chalcogen Metalloids Se and Te. *Adv. Microb. Physiol.* **2007**, *53*, 1-312.
216. Tam, K.; Ho, C. T.; Lee, J.-H.; Lai, M.; Chang, C. H.; Rheem, Y.; Chen, W.; Hur, H.-G.; Myung, N. V., Growth mechanism of amorphous selenium nanoparticles synthesized by *Shewanella* sp. HN-41. *Biosci. Biotechnol. Biochem.* **2010**, *74* (4), 696-700.

-
217. Pearce, C. I.; Pattrick, R. A. D.; Law, N.; Charnock, J. M.; Coker, V. S.; Fellowes, J. W.; Oremland, R. S.; Lloyd, J. R., Investigating different mechanisms for biogenic selenite transformations: *Geobacter sulfurreducens*, *Shewanella oneidensis* and *Veillonella atypica*. *Environ. Technol.* **2009**, *30* (12), 1313-1326.
218. Kim, D.-H.; Kim, M.-G.; Jiang, S.; Lee, J.-H.; Hur, H.-G., Promoted reduction of tellurite and formation of extracellular tellurium nanorods by concerted reaction between iron and *Shewanella oneidensis* MR-1. *Environ. Sci. Technol.* **2013**, *47* (15), 8709-8715.
219. Vaigankar, D. C.; Dubey, S. K.; Mujawar, S. Y.; D'Costa, A.; S.K, S., Tellurite biotransformation and detoxification by *Shewanella baltica* with simultaneous synthesis of tellurium nanorods exhibiting photo-catalytic and anti-biofilm activity. *Ecotoxicol. Environ. Saf.* **2018**, *165*, 516-526.
220. Tuo, Y.; Liu, G.; Dong, B.; Yu, H.; Zhou, J.; Wang, J.; Jin, R., Microbial synthesis of bimetallic PdPt nanoparticles for catalytic reduction of 4-nitrophenol. *Environ. Sci. Pollut. Res.* **2017**, *24* (6), 5249-5258.
221. Wang, W.; Zhang, B.; He, Z., Bioelectrochemical deposition of palladium nanoparticles as catalysts by *Shewanella oneidensis* MR-1 towards enhanced hydrogen production in microbial electrolysis cells. *Electrochim. Acta* **2019**, *318*, 794-800.
222. Xiao, X.; Ma, X.-B.; Yuan, H.; Liu, P.-C.; Lei, Y.-B.; Xu, H.; Du, D.-L.; Sun, J.-F.; Feng, Y.-J., Photocatalytic properties of zinc sulfide nanocrystals biofabricated by metal-reducing bacterium *Shewanella oneidensis* MR-1. *J. Hazard. Mater.* **2015**, *288*, 134-139.
223. Xiao, X.; Ma, X.-L.; Liu, Z.-Y.; Li, W.-W.; Yuan, H.; Ma, X.-B.; Li, L.-X.; Yu, H.-Q., Degradation of rhodamine B in a novel bio-photoelectric reductive system composed of *Shewanella oneidensis* MR-1 and Ag_3PO_4 . *Environ. Int.* **2019**, *126*, 560-567.
224. Compton, R. G.; Banks, C. E., *Understanding voltammetry*. World Scientific (Europe): 2018; p 456.
225. Pletcher, D.; Greff, R.; Peat, R.; Peter, L.; Robinson, J., *Instrumental methods in electrochemistry*. Elsevier: 2001.
226. Scholz, F.; Inzelt, G., *Electrochemical dictionary : with 20 tables*. Springer: 2012.
227. Akhtar, K.; Khan, S. A.; Khan, S. B.; Asiri, A. M., Scanning electron microscopy: Principle and applications in nanomaterials characterization. In *Handbook of Materials Characterization*, Sharma, S. K., Ed. Springer International Publishing: Cham, 2018; pp 113-145.
228. Lloyd, G. E., Atomic number and crystallographic contrast images with the SEM: a review of backscattered electron techniques. *Mineral. Mag.* **1987**, *51* (359), 3-19.
229. Ul-Hamid, A., *A beginners' guide to scanning electron microscopy*. Springer: 2018.
230. Javed, Y.; Ali, K.; Akhtar, K.; Jawaria; Hussain, M. I.; Ahmad, G.; Arif, T., TEM for atomic-scale study: Fundamental, instrumentation, and applications in nanotechnology. In *Handbook of Materials Characterization*, Sharma, S. K., Ed. Springer International Publishing: Cham, 2018; pp 147-216.
231. Kisielowski, C.; Freitag, B.; Bischoff, M.; van Lin, H.; Lazar, S.; Knippels, G.; Tiemeijer, P.; van der Stam, M.; von Harrach, S.; Stekelenburg, M.; Haider, M.; Uhlemann, S.; Müller, H.; Hartel, P.; Kabius, B.; Miller, D.; Petrov, I.; Olson, E. A.; Donchev, T.; Kenik, E. A.; Lupini, A. R.; Bentley, J.; Pennycook, S. J.; Anderson, I. M.; Minor, A. M.; Schmid, A. K.; Duden, T.; Radmilovic, V.; Ramasse, Q. M.; Watanabe, M.; Erni, R.; Stach, E. A.; Denes, P.; Dahmen, U., Detection of single atoms and buried defects in three dimensions by aberration-corrected electron microscope with 0.5-Å information limit. *Microsc. Microanal.* **2008**, *14* (5), 469-477.

232. Custance, O.; Perez, R.; Morita, S., Atomic force microscopy as a tool for atom manipulation. *Nat. Nanotechnol.* **2009**, *4* (12), 803-810.
233. Worsfold, P. J.; Zagatto, E. A. G., Spectrophotometry | Overview. In *Encyclopedia of Analytical Science*, 3rd ed.; Worsfold, P.; Poole, C.; Townshend, A.; Miró, M., Eds. Academic Press: Oxford, 2019; pp 244-248.
234. Ghosh, T.; Slanina, T.; König, B., Visible light photocatalytic reduction of aldehydes by Rh(III)-H: a detailed mechanistic study. *Chemical Science* **2015**, *6* (3), 2027-2034.
235. Myers, J. A.; Curtis, B. S.; Curtis, W. R., Improving accuracy of cell and chromophore concentration measurements using optical density. *BMC biophysics* **2013**, *6* (1), 4-4.
236. Fassel, V. A.; Kniseley, R. N., Inductively coupled plasma-optical emission spectroscopy. *Anal. Chem.* **1974**, *46* (13), 1110A-1120a.
237. PrévotEAU, A.; Clauwaert, P.; Kerckhof, F.-M.; Rabaey, K., Oxygen-reducing microbial cathodes monitoring toxic shocks in tap water. *Biosens. Bioelectron.* **2019**, *132*, 115-121.
238. Zhang, Y.; Angelidaki, I., Self-stacked submersible microbial fuel cell (SSMFC) for improved remote power generation from lake sediments. *Biosens. Bioelectron.* **2012**, *35* (1), 265-270.
239. Sun, D.-Z.; Yu, Y.-Y.; Xie, R.-R.; Zhang, C.-L.; Yang, Y.; Zhai, D.-D.; Yang, G.; Liu, L.; Yong, Y.-C., In-situ growth of graphene/polyaniline for synergistic improvement of extracellular electron transfer in bioelectrochemical systems. *Biosens. Bioelectron.* **2017**, *87*, 195-202.
240. Schröder, U.; Harnisch, F., Life electric—Nature as a blueprint for the development of microbial electrochemical technologies. *Joule* **2017**, *1* (2), 244-252.
241. Kumar, A.; Katuri, K.; Lens, P.; Leech, D., Does bioelectrochemical cell configuration and anode potential affect biofilm response? *Biochem. Soc. Trans.* **2012**, *40* (6), 1308-1314.
242. Coker, V. S.; Bennett, J. A.; Telling, N. D.; Henkel, T.; Charnock, J. M.; van der Laan, G.; Patrick, R. A. D.; Pearce, C. I.; Cutting, R. S.; Shannon, I. J.; Wood, J.; Arenholz, E.; Lyon, I. C.; Lloyd, J. R., Microbial engineering of nanoheterostructures: Biological synthesis of a magnetically recoverable palladium nanocatalyst. *ACS Nano* **2010**, *4* (5), 2577-2584.
243. Wang, Q.; Jones, A. A. D.; Gralnick, J. A.; Lin, L.; Buie, C. R., Microfluidic dielectrophoresis illuminates the relationship between microbial cell envelope polarizability and electrochemical activity. *Sci. Adv.* **2019**, *5* (1), eaat5664.
244. Tan, Y.; Adhikari, R. Y.; Malvankar, N. S.; Pi, S.; Ward, J. E.; Woodard, T. L.; Nevin, K. P.; Xia, Q.; Tuominen, M. T.; Lovley, D. R., Synthetic biological protein nanowires with high conductivity. *Small* **2016**, *12* (33), 4481-4485.
245. Castelle, C.; Guiral, M.; Malarte, G.; Ledgham, F.; Leroy, G.; Brugna, M.; Giudici-Ortoni, M.-T., A new iron-oxidizing/O₂-reducing supercomplex spanning both inner and outer membranes, isolated from the extreme acidophile *Acidithiobacillus ferrooxidans*. *J. Biol. Chem.* **2008**, *283* (38), 25803-25811.
246. Philips, J.; Van den Driessche, N.; De Paepe, K.; PrévotEAU, A.; Gralnick, J. A.; Arends, J. B. A.; Rabaey, K., A novel *Shewanella* isolate enhances corrosion by using metallic iron as the electron donor with fumarate as the electron acceptor. *Appl. Environ. Microbiol.* **2018**, *84* (20), e01154-18.
247. Sheetal, S.; Samantha, R.; Margie, R.; Daad, S., The octahaem SirA catalyses dissimilatory sulfite reduction in *Shewanella oneidensis* MR-1. *Environ. Microbiol.* **2011**, *13* (1), 108-115.
248. Pinchuk, G. E.; Geydebekht, O. V.; Hill, E. A.; Reed, J. L.; Konopka, A. E.; Beliaev, A. S.; Fredrickson, J. K., Pyruvate and lactate metabolism by *Shewanella oneidensis*

-
- MR-1 under fermentation, oxygen limitation, and fumarate respiration conditions. *Appl. Environ. Microbiol.* **2011**, *77* (23), 8234-8240.
249. Cruz-García, C.; Murray, A. E.; Klappenbach, J. A.; Stewart, V.; Tiedje, J. M., Respiratory nitrate ammonification by *Shewanella oneidensis* MR-1. *J. Bacteriol.* **2007**, *189* (2), 656-662.
250. J.M., M.; C.R., M., Overlapping role of the outer membrane cytochromes of *Shewanella oneidensis* MR-1 in the reduction of manganese(IV) oxide. *Letts. Appl. Microbiol.* **2003**, *37* (1), 21-25.
251. Lovley, D. R., Electromicrobiology. *Annu. Rev. Microbiol.* **2012**, *66* (1), 391-409.
252. Hartshorne, R. S.; Reardon, C. L.; Ross, D.; Nuester, J.; Clarke, T. A.; Gates, A. J.; Mills, P. C.; Fredrickson, J. K.; Zachara, J. M.; Shi, L.; Beliaev, A. S.; Marshall, M. J.; Tien, M.; Brantley, S.; Butt, J. N.; Richardson, D. J., Characterization of an electron conduit between bacteria and the extracellular environment. *Proc. Natl. Acad. Sci. U. S. A.* **2009**, *106* (52), 22169-22174.
253. Vellingiri, A.; Song, Y. E.; Munussami, G.; Kim, C.; Park, C.; Jeon, B.-H.; Lee, S.-G.; Kim, J. R., Overexpression of *c*-type cytochrome, *CymA* in *Shewanella oneidensis* MR-1 for enhanced bioelectricity generation and cell growth in a microbial fuel cell. *J. Chem. Technol. Biotechnol.* **2018**, *94* (7), 2115-2122.
254. Edwards, M. J.; White, G. F.; Lockwood, C. W.; Lawes, M. C.; Martel, A.; Harris, G.; Scott, D. J.; Richardson, D. J.; Butt, J. N.; Clarke, T. A., Structural modeling of an outer membrane electron conduit from a metal-reducing bacterium suggests electron transfer via periplasmic redox partners. *J. Biol. Chem.* **2018**, *293* (21), 8103-8112.
255. Bretschger, O.; Obraztsova, A.; Sturm, C. A.; Chang, I. S.; Gorby, Y. A.; Reed, S. B.; Culley, D. E.; Reardon, C. L.; Barua, S.; Romine, M. F.; Zhou, J.; Beliaev, A. S.; Bouhenni, R.; Saffarini, D.; Mansfeld, F.; Kim, B.-H.; Fredrickson, J. K.; Nealson, K. H., Current production and metal oxide reduction by *Shewanella oneidensis* MR-1 wild type and mutants. *Appl. Environ. Microbiol.* **2007**, *73* (21), 7003-7012.
256. Chi, Q.; Zhang, J.; Arslan, T.; Borg, L.; Pedersen, G. W.; Christensen, H. E. M.; Nazmudtinov, R. R.; Ulstrup, J., Approach to interfacial and intramolecular electron transfer of the diheme protein cytochrome *c₄* assembled on Au(111) surfaces. *J. Phys. Chem. B* **2010**, *114* (16), 5617-5624.
257. Yu, Y.; Chen, H.; Yong, Y.; Kim, D.; Song, H., Conductive artificial biofilm dramatically enhances bioelectricity production in *Shewanella*-inoculated microbial fuel cells. *Chem. Commun. (Camb.)* **2011**, *47* (48), 12825-12827.
258. Yang, Y.-C.; Chen, C.-C.; Huang, C.-S.; Wang, C.-T.; Ong, H.-C., Developments of metallic anodes with various compositions and surfaces for the microbial fuel cells. *Int. J. Hydrogen Energy* **2017**, *42* (34), 22235-22242.
259. Allen, J. B.; Larry, R. F., *Electrochemical methods: fundamentals and applications*. 2nd ed.; John Wiley & Sons, Inc: 2001; p 156-176.
260. Chi, Q.; Zhang, J.; Andersen, J. E. T.; Ulstrup, J., Ordered assembly and controlled electron transfer of the blue copper protein azurin at gold (111) single-crystal substrates. *J. Phys. Chem. B* **2001**, *105* (20), 4669-4679.
261. Hu, Y.; Zhang, J.; Ulstrup, J., Interfacial electrochemical electron transfer processes in bacterial biofilm environments on Au(111). *Langmuir* **2010**, *26* (11), 9094-9103.
262. Peng, L.; You, S.; Wang, J., Electrode potential regulates cytochrome accumulation on *Shewanella oneidensis* cell surface and the consequence to bioelectrocatalytic current generation. *Biosens. Bioelectron.* **2010**, *25* (11), 2530-2533.
263. Cornejo, J. A.; Lopez, C.; Babanova, S.; Santoro, C.; Artyushkova, K.; Ista, L.; Schuler, A. J.; Atanassov, P., Surface modification for enhanced biofilm formation and electron transport in *Shewanella* anodes. *J. Electrochem. Soc.* **2015**, *162* (9), H597-H603.

264. Lee, K. J.; Elgrishi, N.; Kandemir, B.; Dempsey, J. L., Electrochemical and spectroscopic methods for evaluating molecular electrocatalysts. *Nat. Rev. Chem.* **2017**, *1* (5), 0039.
265. Kumar, A.; Siggins, A.; Katuri, K.; Mahony, T.; O'Flaherty, V.; Lens, P.; Leech, D., Catalytic response of microbial biofilms grown under fixed anode potentials depends on electrochemical cell configuration. *Chem. Eng. J.* **2013**, *230*, 532-536.
266. Jana, P. S.; Katuri, K.; Kavanagh, P.; Kumar, A.; Leech, D., Charge transport in films of *Geobacter sulfurreducens* on graphite electrodes as a function of film thickness. *Phys. Chem. Chem. Phys.* **2014**, *16* (19), 9039-9046.
267. Kumar, A.; Conghaile, P. Ó.; Katuri, K.; Lens, P.; Leech, D., Arylamine functionalization of carbon anodes for improved microbial electrocatalysis. *RSC Adv.* **2013**, *3* (41), 18759-18761.
268. Pinchuk, G. E.; Rodionov, D. A.; Yang, C.; Li, X.; Osterman, A. L.; Dervyn, E.; Geydebrekht, O. V.; Reed, S. B.; Romine, M. F.; Collart, F. R.; Scott, J. H.; Fredrickson, J. K.; Beliaev, A. S., Genomic reconstruction of *Shewanella oneidensis* MR-1 metabolism reveals a previously uncharacterized machinery for lactate utilization. *Proc. Natl. Acad. Sci. U. S. A.* **2009**, *106* (8), 2874-2879.
269. Wu, S.; Fang, G.; Wang, Y.; Zheng, Y.; Wang, C.; Zhao, F.; Jaisi, D. P.; Zhou, D., Redox-active oxygen-containing functional groups in activated carbon facilitate microbial reduction of ferrihydrite. *Environ. Sci. Technol.* **2017**, *51* (17), 9709-9717.
270. Li, J.; Qiu, J.; Xu, J.; Chen, H.; Xia, X., The synergistic effect of Prussian-blue-grafted carbon nanotube/poly(4-vinylpyridine) composites for amperometric sensing. *Adv. Funct. Mater.* **2007**, *17* (9), 1574-1580.
271. Jiao, Y.; Newman, D. K., The *pio* operon is essential for phototrophic Fe(II) oxidation in *Rhodospseudomonas palustris* TIE-1. *J. Bacteriol.* **2007**, *189* (5), 1765.
272. Shi, L.; Rosso, Kevin M.; Zachara, John M.; Fredrickson, James K., Mtr extracellular electron-transfer pathways in Fe(III)-reducing or Fe(II)-oxidizing bacteria: a genomic perspective. *Biochem. Soc. Trans.* **2012**, *40* (6), 1261.
273. Emerson, D.; Field, E.; Chertkov, O.; Davenport, K.; Goodwin, L.; Munk, C.; Nolan, M.; Woyke, T., Comparative genomics of freshwater Fe-oxidizing bacteria: Implications for physiology, ecology, and systematics. *Front. Microbiol.* **2013**, *4*, 254.
274. Staudigel, H.; Hart, S. R.; Pile, A.; Bailey, B. E.; Baker, E. T.; Brooke, S.; Connelly, D. P.; Haucke, L.; German, C. R.; Hudson, I.; Jones, D.; Koppers, A. A. P.; Konter, J.; Lee, R.; Pietsch, T. W.; Tebo, B. M.; Templeton, A. S.; Zierenberg, R.; Young, C. M., Vailulu'u Seamount, Samoa: Life and death on an active submarine volcano. *Proc. Natl. Acad. Sci. U. S. A.* **2006**, *103* (17), 6448.
275. DiChristina, T. J.; DeLong, E. F., Design and application of rRNA-targeted oligonucleotide probes for the dissimilatory iron- and manganese-reducing bacterium *Shewanella putrefaciens*. *Appl. Environ. Microbiol.* **1993**, *59* (12), 4152-4160.
276. Bräuer, S. L.; Adams, C.; Kranzler, K.; Murphy, D.; Xu, M.; Zuber, P.; Simon, H. M.; Baptista, A. M.; Tebo, B. M., Culturable *Rhodobacter* and *Shewanella* species are abundant in estuarine turbidity maxima of the Columbia River. *Environ. Microbiol.* **2011**, *13* (3), 589-603.
277. Blöthe, M.; Wegorzewski, A.; Müller, C.; Simon, F.; Kuhn, T.; Schippers, A., Manganese-cycling microbial communities inside deep-sea manganese nodules. *Environ. Sci. Technol.* **2015**, *49* (13), 7692-7700.
278. Yli-Hemminki, P.; Jørgensen, K. S.; Lehtoranta, J., Iron–manganese concretions sustaining microbial life in the baltic sea: The structure of the bacterial community and enrichments in metal-oxidizing conditions. *Geomicrobiol. J.* **2014**, *31* (4), 263-275.

-
279. Wright, M. H.; Farooqui, S. M.; White, A. R.; Greene, A. C., Production of manganese oxide nanoparticles by *Shewanella* species. *Appl. Environ. Microbiol.* **2016**, *82* (17), 5402.
280. Soldatova, A. V.; Butterfield, C.; Oyerinde, O. F.; Tebo, B. M.; Spiro, T. G., Multicopper oxidase involvement in both Mn(II) and Mn(III) oxidation during bacterial formation of MnO₂. *JBIC J. Biol. Inorg. Chem.* **2012**, *17* (8), 1151-1158.
281. Wu, J.; Kim, K.-S.; Sung, N.-C.; Kim, C.-H.; Lee, Y.-C., Isolation and characterization of *Shewanella oneidensis* WL-7 capable of decolorizing azo dye Reactive Black 5. *J. Gen. Appl. Microbiol.* **2009**, *55* (1), 51-55.
282. Sinirlioglu, Z. A.; Sinirlioglu, D.; Akbas, F., Preparation and characterization of stable cross-linked enzyme aggregates of novel laccase enzyme from *Shewanella putrefaciens* and using malachite green decolorization. *Bioresour. Technol.* **2013**, *146*, 807-811.
283. Zimbardi, L. A.; Camargo, F. P.; Carli, S.; Aquino Neto, S.; Meleiro, P. L.; Rosa, C. J.; De Andrade, R. A.; Jorge, A. J.; Furriel, P. R., A high redox potential laccase from *Pycnoporus sanguineus* RP15: Potential application for dye decolorization. *Int. J. Mol. Sci.* **2016**, *17* (5), 672.
284. Shleev, S. V.; Ir Gvon, K.; Morozova, O. V.; Mazhugo, Y. M.; Khalunina, A. S.; Yaropolov, A. I., Phenylpyrazolones, novel oxidoreductase redox mediators for degradation of xenobiotics. *Appl. Biochem. Microbiol.* **2004**, *40* (2), 140-145.
285. Piontek, K.; Antorini, M.; Choinowski, T., Crystal structure of a laccase from the fungus *Trametes versicolor* at 1.90-Å resolution containing a full complement of coppers. *J. Biol. Chem.* **2002**, *277* (40), 37663-37669.
286. Höfer, C.; Schlosser, D., Novel enzymatic oxidation of Mn²⁺ to Mn³⁺ catalyzed by a fungal laccase. *FEBS Lett.* **1999**, *451* (2), 186-190.
287. Palma, C.; Martínez, A. T.; Lema, J. M.; Martínez, M. J., Different fungal manganese-oxidizing peroxidases: a comparison between *Bjerkandera* sp. and *Phanerochaete chrysosporium*. *J. Biotechnol.* **2000**, *77* (2), 235-245.
288. Okamoto, A.; Nakamura, R.; Hashimoto, K., In-vivo identification of direct electron transfer from *Shewanella oneidensis* MR-1 to electrodes via outer-membrane OmcA–MtrCAB protein complexes. *Electrochim. Acta* **2011**, *56* (16), 5526-5531.
289. Li, S.-L.; Yen, J.-H.; Kano, K.; Liu, S.-M.; Liu, C.-L.; Cheng, S.-S.; Chen, H.-Y., Using metabolic charge production in the tricarboxylic acid cycle (QTCA) to evaluate the extracellular-electron-transfer performances of *Shewanella* spp. *Bioelectrochemistry* **2018**, *124*, 119-126.
290. Han, L.; Xia, H.; Yin, L.; Petrenko, V. A.; Liu, A., Selected landscape phage probe as selective recognition interface for sensitive total prostate-specific antigen immunosensor. *Biosens. Bioelectron.* **2018**, *106*, 1-6.
291. Rodionov, D. A.; Yang, C.; Li, X.; Rodionova, I. A.; Wang, Y.; Obratsova, A. Y.; Zagnitko, O. P.; Overbeek, R.; Romine, M. F.; Reed, S.; Fredrickson, J. K.; Nealson, K. H.; Osterman, A. L., Genomic encyclopedia of sugar utilization pathways in the *Shewanella* genus. *BMC Genomics* **2010**, *11* (1), 494.
292. Chang, H.-C.; Osawa, M.; Matsue, T.; Uchida, I., A novel polyviologen electrode fabricated by electrochemical crosslinking. *J. Chem. Soc., Chem. Commun.* **1991**, (9), 611-612.
293. Okamoto, A.; Hashimoto, K.; Nealson, K. H.; Nakamura, R., Rate enhancement of bacterial extracellular electron transport involves bound flavin semiquinones. *Proc. Natl. Acad. Sci. U. S. A.* **2013**, *110* (19), 7856-7861.
294. Carmona-Martinez, A. A.; Harnisch, F.; Fitzgerald, L. A.; Biffinger, J. C.; Ringeisen, B. R.; Schröder, U., Cyclic voltammetric analysis of the electron transfer of

- Shewanella oneidensis* MR-1 and nanofilament and cytochrome knock-out mutants. *Bioelectrochemistry* **2011**, *81* (2), 74-80.
295. Richter, H.; Nevin, K. P.; Jia, H.; Lowy, D. A.; Lovley, D. R.; Tender, L. M., Cyclic voltammetry of biofilms of wild type and mutant *Geobacter sulfurreducens* on fuel cell anodes indicates possible roles of OmcB, OmcZ, type IV pili, and protons in extracellular electron transfer. *Energy Environ. Sci.* **2009**, *2* (5), 506-516.
296. Chi, Q.; Zhang, J.; Ulstrup, J., Surface microscopic structure and electrochemical rectification of a branched alkanethiol self-assembled monolayer. *J. Phys. Chem. B* **2006**, *110* (3), 1102-1106.
297. Silhavy, T. J.; Kahne, D.; Walker, S., The bacterial cell envelope. *Cold Spring Harb. Perspect. Biol.* **2010**, *2* (5), a000414.
298. Reichow, S. L.; Korotkov, K. V.; Hol, W. G. J.; Gonen, T., Structure of the cholera toxin secretion channel in its closed state. *Nat. Struct. Mol. Biol.* **2010**, *17* (10), 1226.
299. Prampolini, G.; Yu, P.; Pizzanelli, S.; Cacelli, I.; Yang, F.; Zhao, J.; Wang, J., Structure and dynamics of ferrocyanide and ferricyanide anions in water and heavy water: An insight by MD simulations and 2D IR spectroscopy. *J. Phys. Chem. B* **2014**, *118* (51), 14899-14912.
300. Koley, D.; Bard, A. J., Triton X-100 concentration effects on membrane permeability of a single HeLa cell by scanning electrochemical microscopy (SECM). *Proc. Natl. Acad. Sci. U. S. A.* **2010**, *107* (39), 16783.
301. Bird, L. J.; Bonnefoy, V.; Newman, D. K., Bioenergetic challenges of microbial iron metabolisms. *Trends Microbiol.* **2011**, *19* (7), 330-340.
302. Deplanche, K.; Caldelari, I.; Mikheenko, I. P.; Sargent, F.; Macaskie, L. E., Involvement of hydrogenases in the formation of highly catalytic Pd(0) nanoparticles by bioreduction of Pd(II) using *Escherichia coli* mutant strains. *Microbiology* **2010**, *156* (9), 2630-2640.
303. Deplanche, K.; Macaskie, L. E., Biorecovery of gold by *Escherichia coli* and *Desulfovibrio desulfuricans*. *Biotechnol. Bioeng.* **2008**, *99* (5), 1055-1064.
304. Srivastava, S. K.; Constanti, M., Room temperature biogenic synthesis of multiple nanoparticles (Ag, Pd, Fe, Rh, Ni, Ru, Pt, Co, and Li) by *Pseudomonas aeruginosa* SM1. *J. Nanopart. Res.* **2012**, *14* (4), 831.
305. Lloyd, J. R.; Yong, P.; Macaskie, L. E., Enzymatic recovery of elemental palladium by using sulfate-reducing bacteria. *Appl. Environ. Microbiol.* **1998**, *64* (11), 4607.
306. Ganesh, R.; Robinson, K. G.; Chu, L.; Kucsmas, D.; Reed, G. D., Reductive precipitation of uranium by *Desulfovibrio desulfuricans*: evaluation of cocontaminant effects and selective removal. *Water Res.* **1999**, *33* (16), 3447-3458.
307. Grady, J. K.; Chasteen, N. D.; Harris, D. C., Radicals from "Good's" buffers. *Anal. Biochem.* **1988**, *173* (1), 111-115.
308. Ferreira, C. M. H.; Pinto, I. S. S.; Soares, E. V.; Soares, H. M. V. M., (Un)suitability of the use of pH buffers in biological, biochemical and environmental studies and their interaction with metal ions – a review. *RSC Adv.* **2015**, *5* (39), 30989-31003.
309. Xu, H.; Tan, L.; Cui, H.; Xu, M.; Xiao, Y.; Wu, H.; Dong, H.; Liu, X.; Qiu, G.; Xie, J., Characterization of Pd(II) biosorption in aqueous solution by *Shewanella oneidensis* MR-1. *J. Mol. Liq.* **2018**, *255*, 333-340.
310. Lin, Y.-s. E.; Vidic, R. D.; Stout, J. E.; McCartney, C. A.; Yu, V. L., Inactivation of *Mycobacterium avium* by copper and silver ions. *Water Res.* **1998**, *32* (7), 1997-2000.
311. Valodkar, M.; Modi, S.; Pal, A.; Thakore, S., Synthesis and anti-bacterial activity of Cu, Ag and Cu–Ag alloy nanoparticles: A green approach. *Mater. Res. Bull.* **2011**, *46* (3), 384-389.

-
312. Cui, L.; Chen, P.; Chen, S.; Yuan, Z.; Yu, C.; Ren, B.; Zhang, K., In situ study of the antibacterial activity and mechanism of action of silver nanoparticles by surface-enhanced Raman spectroscopy. *Anal. Chem.* **2013**, *85* (11), 5436-5443.
313. Vardanyan, Z.; Trchounian, A., The effects of copper (II) ions on *Enterococcus hirae* cell growth and the proton-translocating F₀F₁ atpase activity. *Cell Biochem. Biophys.* **2010**, *57* (1), 19-26.
314. Wang, S.; Li, L.; Zhu, Z. H., Solid-state conversion of fly ash to effective adsorbents for Cu removal from wastewater. *J. Hazard. Mater.* **2007**, *139* (2), 254-259.
315. Xiong, L.; Chen, J.; Huang, Y.; Li, W.; Xie, J.; Yu, H., An oxygen reduction catalyst derived from a robust Pd-reducing bacterium. *Nano Energy* **2015**, *12*, 33-42.
316. Sun, H.; Cao, L.; Lu, L., Bacteria promoted hierarchical carbon materials for high-performance supercapacitor. *Energy Environ. Sci.* **2012**, *5* (3), 6206-6213.
317. Guo, Z.; Ren, G.; Jiang, C.; Lu, X.; Zhu, Y.; Jiang, L.; Dai, L., High performance heteroatoms quaternary-doped carbon catalysts derived from *Shewanella* bacteria for oxygen reduction. *Sci. Rep.* **2015**, *5*, 17064.
318. Kappe, C. O.; Dallinger, D., The impact of microwave synthesis on drug discovery. *Nat. Rev. Drug Discovery* **2006**, *5* (1), 51-63.
319. Egerton, R. F., *Physical principles of electron microscopy: An introduction to TEM, SEM, and AEM*. Springer US: 2005; p 1-202.
320. Wang, H.; Sun, Z.; Yang, Y.; Su, D., The growth and enhanced catalytic performance of Au@Pd core-shell nanodendrites. *Nanoscale* **2013**, *5* (1), 139-142.
321. Li, P.; Lv, W.; Ai, S., Green and gentle synthesis of Cu₂O nanoparticles using lignin as reducing and capping reagent with antibacterial properties. *J. Exp. Nanosci.* **2016**, *11* (1), 18-27.
322. Zheng, G.; Altman, E. I., The oxidation of Pd(111). *Surf. Sci.* **2000**, *462* (1), 151-168.

Appendix

Contributions made during the Ph.D. project are listed.

International Journals:

Zheng, Z.; Xiao, Y.; Wu, R.; Mølager Christensen, H. E.; Zhao, F.; Zhang, J., Electrons selective uptake of a metal-reducing bacterium *Shewanella oneidensis* MR-1 from ferrocyanide. *Biosens. Bioelectron.* 2019, *142*, 111571.

Zheng, Z.; Lee, E. L.; Yu, P.; Ma, L.; Engelbrekt, C.; Ulstrup, J.; Zhang, J., Efficient photothermal ablation of cancer cells by an ultra-thin CuS nanocrystal, (in preparation)

Tang, J.; Werchmeister, R. M. L.; Preda, L.; Huang, W.; **Zheng, Z.;** Leimkühler, S.; Wollenberger, U.; Xiao, X.; Engelbrekt, C.; Ulstrup, J.; Zhang, J., Three-dimensional sulfite oxidase bioanodes based on graphene functionalized carbon paper for sulfite/O₂ biofuel cells. *ACS Catalysis* 2019, *9* (7), 6543-6554.

Book chapter:

Zheng Z.; Xiao Y.; Zhao, F.; Ulstrup, J.; Zhang, J., Bacterially generated nanocatalysts and their applications. in *Novel catalyst materials for bioelectrochemical systems: Fundamentals and applications*. American Chemical Society, 2019 (in press).

Poster presentations at national and international conferences:

Zheng, Z.; Xiao, Y.; Wu, R.; Christensen, H. E. M.; Zhao, F.; Zhang, J., Inward Electron Transfer of a Metal Reducing Bacterium from High-Redox Potential Molecules. *Electrochemical Conference on Energy and the Environment: Bioelectrochemistry and Energy Storage*, July 2019, Glasgow, United Kingdom. (Oral presentation)

Tang, J.; Werchmeister, R. M. L.; Preda, L.; Huang, W.; **Zheng, Z.;** Leimkühler, S.; Wollenberger, U.; Xiao, X.; Ulstrup, J.; Zhang, J., Graphene-sulfite oxidase bioanodes for enzymatic biofuel cells. *XXV International Symposium on Bioelectrochemistry and Bioenergetics*, May 2019, Limerick, Ireland. (Oral presentation)

Zheng, Z.; Xiao, Y.; Christensen, H. E. M.; Zhao, F.; Zhang, J., Electrocatalytic oxidation of K₄[Fe(CN)₆] by metal-reducing bacterium *Shewanella oneidensis* MR-1. *Sustain*

Conference 2018: Creating technology for a Sustainable Society, November **2018**, Lyngby, Denmark. (Poster)

Zheng, Z.; Lee, L.; Yu, P.; Ma, L.; Engelbrekt, C.; Zhang, J., Copper sulfide nanocrystals for efficient photothermal ablation of tumor cells. *6th International Conference and Exhibition on Materials Science and Chemistry*, May **2018**, Rome, Italy. (Poster)

Ma, L.; Xu, H.; Lee, L. E.; Bandari, R. P.; Zhou, T.; Smith, J.; **Zheng, Z.**; Shen, F.; Zhang, J.; Yu, P., In vitro and in vivo evaluations of a high affinity and specificity photoacoustic nanoparticle targeting to cancer. *2018 World Molecular Imaging Congress*, November **2018**, Seattle, United States. (Oral presentation)

Zheng, Z.; Xiao, Y.; Wu, R.; Christensen, H. E. M.; Zhao, F.; Zhang, J., Electrocatalytic oxidation of $K_4[Fe(CN)_6]$ by metal-reducing bacterium *Shewanella oneidensis* MR-1. *Sustain 2017*, December **2017**, Lyngby, Denmark. (Poster)

Zheng, Z.; Xiao, Y.; Wu, R.; Christensen, H. E. M.; Zhao, F.; Zhang, J., Bacterial electrocatalysis of $K_4[Fe(CN)_6]$ oxidation. *The Sixteenth International Symposium on Electroanalytical Chemistry*, August **2017**, Changchun, China. (Oral presentation)

Zheng, Z.; Wu, R.; Xiao, Y.; Christensen, H. E. M.; Zhao, F.; Zhang, J., Electrochemical catalysis of inorganic complex $K_4[Fe(CN)_6]$ by *Shewanella oneidensis* MR-1. *Forth EuCheMS Inorganic Chemistry Conference (EICC-4)*, July **2017**, Copenhagen, Denmark. (Poster)

Attended workshops or seminars:

Workshop on HRTEM image analysis, **2018**, Lyngby, Denmark